ALTERATION SYSTEMATICS AND MINERALISING POTENTIAL OF THE PALINPINON GEOTHERMAL FIELD, NEGROS ISLAND, PHILIPPINES

by

Andrew J. Rae
MSc

Andrew John

CODES

UNIVERSITY OF TASMANIA

Submitted in fulfilment of the requirements
for the degree of Doctor of Philosophy

University of Tasmania
Australia
April, 2002

STATEMENT AND AUTHORITY OF ACCESS

This thesis contains no material which has been accepted for a degree or diploma by the University or any other institution and, to the best of my knowledge and belief, no material previously published or written by another person except where due acknowledgment is made in the text of this thesis.

Date: 13/05/02

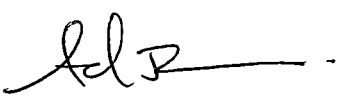

Andrew Rae

ABSTRACT

Palinpinon geothermal field (Negros Island, Philippines) is a high temperature, liquid-dominated geothermal system in an active volcanic island arc setting. Previous workers have made parallels between the geological setting, mineral deposition and hydrothermal alteration styles recognised at Palinpinon with those that characterise several types of magmatic-hydrothermal ore deposits (e.g., porphyry, skarn, and high and low sulphidation epithermal systems).

Igneous rock formations on southern Negros Island have medium K, calc-alkaline, basaltic to dacitic compositions. The Middle Miocene Lower Puhagan Volcanic Formation is part of a volcanic sequence that is traceable throughout the Visayas region. It formed during southeasterly-directed subduction of the Sulu Sea oceanic basin beneath the Sulu arc. Late Miocene to Early Pliocene times marked a period of regional subsidence and marine sedimentation during which a thick sequence (< 1500 m) of calcareous sediments was deposited (Okoy Formation). Locally in the southern Negros region, magmatism during Early Pliocene to Recent times produced a thick (< 2600 m) sequence of volcanic and volcaniclastic rocks (Southern Negros and Cuernos Volcanic Formations). During this time, diorites to quartz diorites of the Puhagan dikes ($^{40}Ar/^{39}Ar$ = 4.2-4.1 Ma) and the Nasuji Pluton ($^{40}Ar/^{39}Ar$ = 0.7-0.3 Ma) intruded the Middle Miocene, Late Miocene and Early-Late Pliocene rock units.

The igneous rocks at Palinpinon have adakitic geochemical signatures and are associated with Nb-enriched basalts. This is interpreted to indicate that magmatism in this region has been influenced by the melting of subducted oceanic basalt. Considering the regional tectonic history, the most likely scenarios for the generation of slab melts are considered to be: (1) melting of relatively young (< 20 Ma) oceanic crust during the Middle Miocene; (2) initiation of east-directed subduction along the Negros-Sulu Trench during Early Pliocene times; and (3) melting of young (< 10-20 Ma) oceanic crust during Late Pliocene times.

Hydrothermal alteration at Palinpinon is spatially associated with the Puhagan dikes and the Nasuji Pluton. Only incipient calc-silicate alteration is spatially associated with the Puhagan dikes. In the Nasuji-Sogongon region, the hydrothermal alteration assemblages spatially associated with the Nasuji Pluton are K-silicate (biotite), calc-silicate, hypogene advanced argillic, propylitic and distal illite assemblages. Fluid inclusion evidence indicates that magmatic-hydrothermal fluids associated with the final stages of magma crystallisation and the formation of a biotite alteration assemblage and associated veins had homogenisation temperatures of 267° to > 600°C and salinities of 26 to 56 eq.wt.% NaCl. PIXE analyses show that these fluids were endowed with base metals (e.g., up to 0.2 wt. % Cu). Age determinations on hydrothermal biotite ($^{40}Ar/^{39}Ar$ = 0.7-0.6 Ma), alunite (K/Ar = 0.9-0.8 Ma) and illite (K/Ar = 0.7 Ma) demonstrate that these assemblages all formed contemporaneously with the Nasuji

Pluton, implying a genetic link between intrusion emplacement and the formation of porphyry, high sulphidation epithermal and low sulphidation epithermal alteration assemblages.

The Early Pliocene age of the Puhagan dikes establishes they are not the heat source to the current geothermal system, which must be a much younger 'blind' intrusion situated beyond depths drilled in the Puhagan area. The emplacement of this intrusion, at depths greater than 2.5 km, occurred within the last 0.8 Ma and provides the heat source for present-day geothermal activity. Distinctive high temperature hypogene hydrothermal alteration types have developed at depths greater than 2 km and include calc-silicate and biotite alteration zones. Parts of the biotite alteration zone are in thermal equilibrium with the present-day geothermal system. The lack of a hypogene advanced argillic alteration zone in the Puhagan region is interpreted to indicate that the intrusion has been emplaced at depths great enough for lithostatic confining pressures to hinder or prevent magma degassing.

With ongoing hydrothermal convection, areas of propylitic alteration have developed as halos surrounding the Puhagan magmatic-hydrothermal alteration zones. At shallow crustal levels (< 2 km), low sulphidation (illite) alteration assemblages overprint the biotite and hypogene advanced argillic alteration types associated with the Nasuji Pluton and are in thermal equilibrium with the present-day geothermal system. Therefore, it is possible that biotite and illite alteration assemblages in the Puhagan region either have a protracted history of formation, or else have formed during two discrete time periods in the past 0.8 Ma. Lastly, perched aquifers of steam-heated acid sulphate water have altered regions above the water table to an advanced argillic (steam-heated) alteration assemblage. The percolation of these waters down near-vertical permeable structures (i.e., faults and joints), results in steeply dipping zones of steam-heated advanced argillic alteration.

The current geothermal hydrology at Palinpinon is grossly influenced by permeable zones related to faults and lithological boundaries. The upflow zone is situated at a fault intersection (Ticala and Lagunao Faults) and the main northeasterly outflow zone is parallel to NE-striking faults (Ticala and Puhagan Faults). The neutral chloride reservoir water chemistry is affected by boiling, mixing and conductive cooling. Boiling occurs close to the region of upflow and is mainly restricted to narrow zones of permeability. Mixing occurs peripherally to the upflow zone. The proposed end-member mixing solutions are steam-heated sulphate and meteoric waters. Steam-heated sulphate waters are sourced from perched aquifers in the vadose zone beneath areas of high elevation. Hybrid neutral chloride – sulphate waters have chemistries influenced by host rock dissolution and have not attained chemical equilibrium. In contrast, hybrid neutral chloride – meteoric waters have chemistries that are closer to chemical equilibrium with the host rock. Conductive cooling occurs in the northeasterly outflow zone and water chemistries influenced by this process are also close to chemical equilibrium with the host rock.

The occurrence of base and precious metal scale deposits in several geothermal wells demonstrates that the present-day deep reservoir fluid is capable of transporting and depositing base and precious metals. However, trace metal analysis of the deep reservoir fluids shows they are undersaturated with respect to gold (1-4 μg/kg). Chemical modelling of Palinpinon geothermal water predicts that boiling should be the most effective mechanism for base and precious metal deposition. Boiling of the neutral chloride water is predicted to produce sulphide assemblages similar to those seen in well scale deposits. Mixing with acid bearing sulphate waters can also produce these sulphide assemblages, but does so less efficiently, and the deposition of gold and silver is predicted to occur only at much lower temperatures (i.e., < 110°C). In terms of the mineralogy and the sequence of mineral deposition, mixing with meteoric water is predicted to produce the same results as conductive cooling of the neutral chloride water. Based on fluid modelling results, neither can be considered effective deposition mechanisms for base and precious metal mineralisation.

Despite indications that both the early magmatic-hydrothermal fluids and the modern hydrothermal fluids were, and are, capable of metal transportation, base and precious metal deposition is not strongly developed at Palinpinon. Geochemical assays of drillcore and drillcuttings show base and precious metal concentrations to be one to two orders of magnitude below ore grade (< 0.02 wt. % Cu, < 0.03 wt. % Pb, < 0.01 wt. % Zn, < 0.01 wt. % Mo, < 8 g/t Ag and <0.05 g/t Au). It may be that the geothermal wells drilled to date have failed to intersect mineralised ore zones. Alternatively, the lack of significant ore mineral deposition may imply that there has been, and still is, a lack of sufficient permeability to create a focus for fluid flow. High lithostatic pressures (i.e., > 0.6 kb) during emplacement of the intrusions may account for this apparent lack of permeability in the magmatic-hydrothermal domain. These elevated pressures would also hinder any metal-bearing magmatic brines from ascending to form ore at shallower levels. Therefore, for base and/or precious metal ore deposition to occur at Palinpinon, a resurgence of magmatism may be required, with an influx of metal-bearing brines and gases, and significant fault dilation and/or phreatic/phreatomagmatic breccia formation to provide favourable permeability for these fluids to escape and form mineralised ore horizons at shallow crustal levels.

ACKNOWLEDGEMENTS

Terry Leach started me on this voyage of discovery and put in a lot of work during the early days, initiating the project, arranging sponsors and locating a tertiary institution willing to take it on. Thank you Terry for all your efforts, without your initiative, support and enthusiasm this project would not have been possible.

The remaining members of the "supervisory board" are from CODES SRC, University of Tasmania, and the Geothermal Institute, University of Auckland. I am grateful for all the advice, encouragement, enthusiasm and support over the past five years from Dave Cooke, Bruce Gemmell, Stuart Simmons and Pat Browne. In particular a very big thanks to Dave for all his guidance, tutelage and assistance throughout the course of my study here at CODES. His thorough reviews and rapid turn-around time, especially during the last few weeks, have been greatly appreciated. Thanks alot, Dave. Stuart Simmons, put in a lot of effort reviewing manuscripts. Thanks for all your encouragement and constructive input Stuart. Both you and Pat have been important influences during the course of my education, right from the early days at the Geothermal Institute, and for that I thank you both very much.

Financial support for this project was provided by a University of Tasmania School Scholarship along with sponsorship from BHP (BHP-Billiton), Inmet, Newcrest, and North (Rio Tinto). I thank the following people for all their input: Jun Angeles, Bob Beeson, Colin Burge, Nick Cook, John Holliday, Nick Langsford, Arturo Ona, Stuart Smith and Noel White.

Of course this study would not have been possible without PNOC-EDC's permission to access drillcore, drillcuttings, maps, company files and reports. Thank you, Alfredo Troncales, Hermes Ferrer, Francisco (Jun) Delfin and Manuel Ogena. Also, Maribel Zaide-Delfin, Larry Bayrante, Noel Salonga, Rowena (Weng) Alvis-Isidro, Sylvia Ramos and the remaining PNOC-EDC staff members, in particular, the petrologists and geochemists at Ft. Bonifacio, Makati City, Manila. During my visits they all made "Manila madness" not only bearable, but enjoyable. In southern Negros, I thank all the scientific, technical and administrative staff at the Ticala offices of PNOC-EDC. In particular, thanks go to Oliver Jordan and Danny Hermoso.

Kevin Brown put aside a week from his hectic schedule and dropped by Dumaguete, on his way from somewhere in Latin America (I think) to somewhere in SE Asia (I think), bearing his "bazooka-looking" downhole water sampler. Thank you very much Kevin. I have always appreciated the help, support and enthusiasm you've given me during my PhD study.

I greatly appreciate the use of the Datamine software for rendering 3D images of the geothermal wells, geology and hydrology of the geothermal system. I thank Datamine for the free site licence. I am indebted to Jonathon Knight for initially allowing me to use his software licence

and computer, and also teaching me everything I needed to know about the program. He also assisted in arranging for CODES SRC to obtain a free site licence. Thank you, Jonathon.

Thanks go to: Wally Herrmann, Garry Davidson, Khin Zaw, Dima Kamenetsky, Tony Crawford and Peter Hollings who have all helped in various ways. I especially thank Tony and Peter for reviewing my manuscripts. Over the years I have received technical assistance from a number of people including: Kai Yang, Chris Ryan, Chris Yeats and Tin Tin Win at CSIRO, Nth. Ryde; Dave Phillips at PRISE, ANU, Canberra; Peter Wood and Andy Tulloch at IGNS, N.Z.; Ashley Townsend, Graham Rowbottom and David Steele, at CSL, University of Tasmania; Simon Stephens, Jun Pongratz, Peter Cornish, Phil Robinson, Darren Turner, Alistair Chilcott, Nilar Hlaing and Katie McGoldrick. A big thank you to Mike Blake for his assistance during the final stages of this thesis. Christine Higgins, Marilyn Feast, Di Steffens, Lynne Starr and Lynne Vaudry have all helped with administrative matters. Thanks to you all.

To my fellow post-graduate students I thank Michael Agnew, Steve Bodon, James Cannell, Robin Cantrill, Dene Carroll, Andrew Davies, Peter Frikken, Cathryn Gifkins, Oli Holm, Ben Jones, Roman Leslie, Vanessa Lickfold, Glen Masterman, Meng, Ali Raos, Catherine Reid, Kirstie Simpson, Briony Sinclair, Rick Squire, Alan Wilson and Rohan Wolfe. I especially thank my office mates, Sarah Jones and Karin Orth. Thank you both for all your support, encouragement and food.

Various friends have helped and provided encouragement outside of office hours and I thank them for it, Karen Tyler, Peter Cahill, Rachel Lawrence, Suzanne Cooper, Vanessa Bakker, Mike Piper and Scott Howard.

Lastly, I would like to thank the Rae diaspora – my extended, trans-Tasman family – especially Sylvia, John and Cilla for all their continued love, support and encouragement.

TABLE OF CONTENTS

LIST OF FIGURES

LIST OF TABLES

PREAMBLE

Palinpinon geothermal field, located on Negros Island in the western Visayas region, Philippines, has been developed for electricity production and is maintained by the Philippine National Oil Company - Energy Development Corporation (PNOC-EDC). It is part of the Southern Negros Geothermal Project area, a 1330 km^2 reservation comprising most of the southern peninsula of Negros Island (Figure i).

During development of the geothermal steamfield, PNOC-EDC and consulting geologists recognised parallels that could be drawn between the geological setting and hydrothermal alteration styles recognised at Palinpinon with those that characterise many types of magmatic-hydrothermal ore deposits (e.g., porphyry, skarn, high and low sulphidation epithermal systems). These parallels were reported by Leach and Bogie (1982) and Mitchell and Leach (1991) and have been summarised in Section 3.3 of this thesis.

For the purposes of this research project, the distribution of the host rock lithologies, isograd surfaces of characteristic minerals from the different hydrothermal alteration assemblages, present-day lithologies and the topography at Palinpinon, have been visualised using Datamine 3D imaging software. This was achieved by digitising the geological, alteration and stable downhole temperature data from 65 geothermal wells. The cross-sections presented in Sections 2, 3, and 4 of the thesis are modified 2D slices taken from the 3D Datamine models. Appendix 4 of this thesis is a CD-ROM that contains an unpublished Powerpoint presentation (Palinpinon.ppt), that the reader can use to access hyperlinked Datamine images and rotate through three dimensions. This provides an improved understanding of spatial relationships between the host rocks, hydrology, and alteration minerals at Palinpinon.

PROJECT AIMS AND OBJECTIVES

Geothermal systems have been long regarded as the active equivalents of many epithermal style ore deposits (Lindgren, 1933; White, 1955; White, 1981). Based on the principle of uniformitarianism, research done on these systems, in particular the geologic and structural settings, fluid chemistries and processes of fluid-rock interaction, can lead to a greater understanding of the processes of hydrothermal ore deposit formation.

For the purposes of understanding the formation of magmatic-hydrothermal ore deposits, such as porphyry, skarn and high sulphidation epithermal styles, modern equivalents may possibly be found in high temperature geothermal systems located in volcanic arc settings, as opposed to rift settings (Henley and Ellis, 1983). In terms of influencing the characteristics of the associated geothermal systems, general differences between the two tectonic settings have been discussed by Reyes (1995) who compared geothermal systems located in New Zealand (both arc- and rift-types) with those in the Philippines (mostly arc-type). A key difference is the depth to the

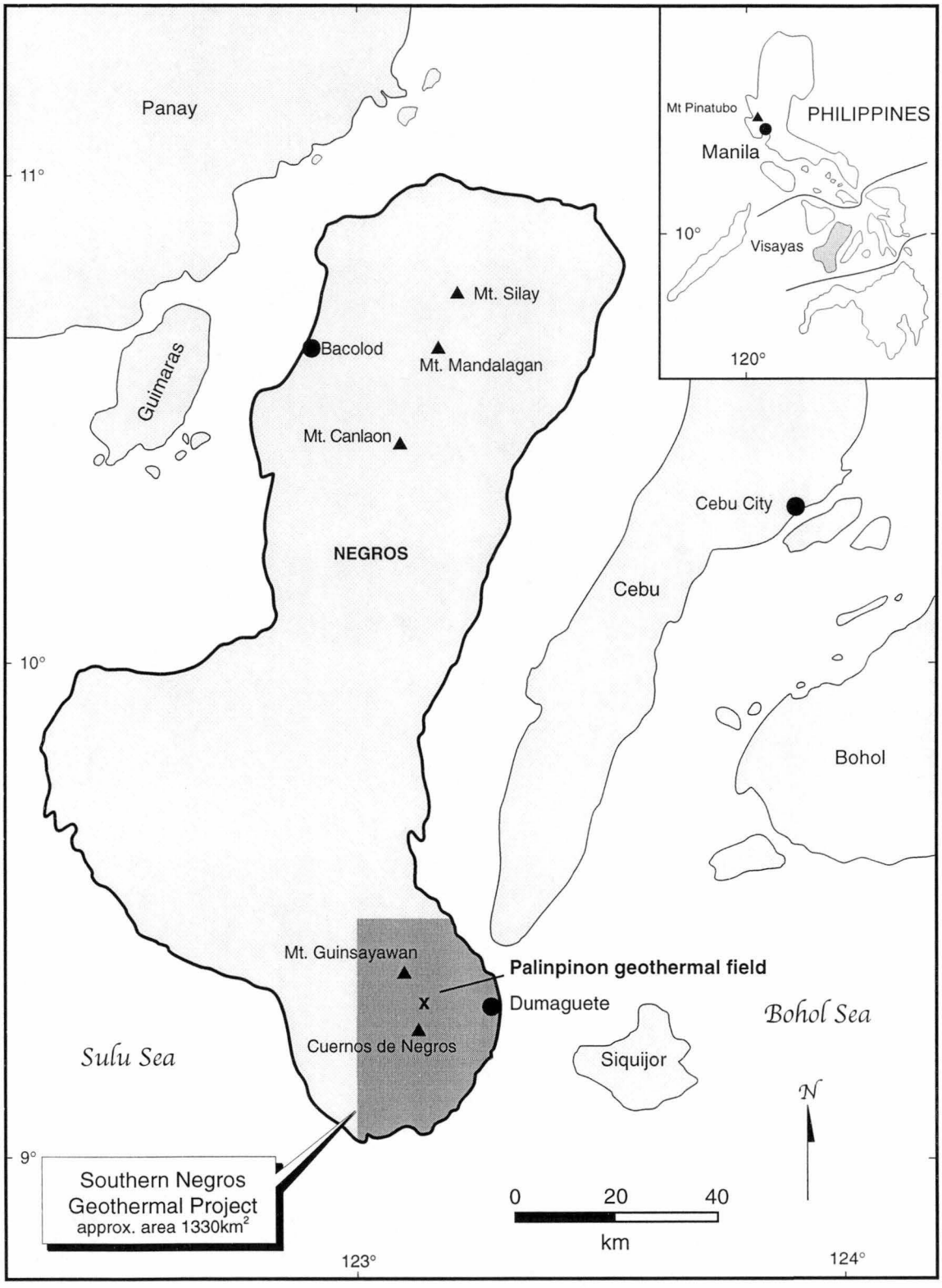

Figure i. Palinpinon geothermal field, southern Negros Island, Visayas region, Philippines.

degassing magma body. For Philippine geothermal systems it is relatively shallow (i.e., 2-3 km depth), whereas in New Zealand it can be greater than 4 km depth (Reyes, 1995). This results in steeper geochemical gradients in Philippine systems with a higher input of magmatic water (Philippine: > 40%; New Zealand: < 20%), higher salinities (Philippine: < 10000 mg/kg Cl^-; New Zealand: < 2400 mg/kg Cl^-), and higher gaseous components and higher maximum temperatures (Philippine: > 400° C; New Zealand: < 330° C). Also, high temperature magmatic-hydrothermal alteration assemblages (e.g., biotite, actinolite-tremolite, clinopyroxene) are more common in Philippine geothermal systems. Hence to gain greater insights into the formation of magmatic-hydrothermal ore deposits, research should possibly be focussed on high temperature geothermal systems located in volcanic arc settings, such as that at Palinpinon.

Previous work undertaken by geothermal scientists at Palinpinon has clearly established similarities with certain varieties of mineralised hydrothermal-magmatic ore systems (Leach and Bogie, 1982; Sillitoe and Gappe, 1984; Reyes, 1990; Mitchell and Leach, 1991; Reed, 1994). Despite all the previous work undertaken during development of the Palinpinon geothermal steamfield, none has involved investigation into base and precious metal mineral deposition. Only a few cores were ever assayed and these showed copper concentrations up to 500 ppm and rarely greater than 1000 ppm (Mitchell and Leach, 1991). With measured temperatures in approximate thermal equilibrium with some alteration mineralogies, the Palinpinon geothermal field represents a time-slice in the evolution of a magmatic-hydrothermal system and provides a natural laboratory and a unique opportunity to investigate processes involved in the formation of such a system at all levels.

This PhD research project addresses the issue of mineralisation in the active magmatic-hydrothermal system at Palinpinon. It includes a review of all previous work relating to geology, structure, geophysics, hydrology, water chemistry and hydrothermal alteration. Work undertaken for this thesis includes igneous petrology, petrography of hydrothermal alteration and ore mineral assemblages, fluid inclusion measurements, radiometric age dating, base and precious metal analyses of drillcores and drillcuttings, trace metal chemistry of geothermal water and the examination and analysis of geothermal well scale deposits.

This thesis consists of five sections, three of which are ultimately intended for publication in refereed journals (i.e., Sections 2-4). Previous work on Palinpinon by Leach and Bogie (1982) and Mitchell and Leach (1991), stimulated the undertaking of this PhD study. The contents of the main sections are as follows:

- Section 1 is a summary of the findings of previous studies at Palinpinon, together with a literature review of the regional and local geology. The hydrology and reservoir chemistry of the Palinpinon geothermal field, as known prior to this study, is documented. Water

types are classified in terms of their pH and dominant anions, and physical processes and reservoir conditions are interpreted from pre-existing data.

- Section 2 of this thesis is an igneous petrological and geochronological study which documents the geological setting and focuses on the geological features, namely the petrology of volcanic and intrusive lithologies, that influence the hydrology of the geothermal system. Along with radiometric age dating, this section provides the basis for a discussion of the petrogenetic evolution of magmatism in the district and also a context for the evolution of the hydrothermal system in terms of the intrusive history. The temporal and spatial relationships between the intrusions and the active geothermal system provide the framework for the following sections, and are important for insights into the possible locations of heat sources for the ancient and modern hydrothermal systems.

- Section 3 presents new petrographic analyses of hydrothermal alteration and mineralisation assemblages of drillcore samples from Palinpinon. This has led to clarification, and in some cases, the redefinition of previously defined hydrothermal alteration zones and establishes the distribution and association of sulphide mineralogies. Along with data collected from fluid inclusion measurements and radiometric dating of hydrothermal minerals, the history of the hydrothermal system, or systems, in terms of temporal variation in physiochemical conditions is established. Base and precious metal analyses of drillcuttings and drillcore provide insights into the distribution and intensity of base and precious metal mineralisation, allowing a discussion on the processes and mechanisms of mineralisation (or lack thereof). A major aim of Section 3 is to establish timing relationships and possible genetic links between the Palinpinon alteration types that are generally associated with porphyry (biotite), high sulphidation epithermal (advanced argillic) and low sulphidation epithermal (illite) mineralised systems.

- Section 4 investigates the mineralisation potential of the modern hydrothermal system at Palinpinon. This has been achieved by collecting downhole geothermal waters and analysing them for base and precious metals. The examination and analysis of geothermal well scales establishes whether these waters are capable of depositing metal sulphides. Chemical modelling is used to test responses to changes in physicochemical conditions (i.e., boiling, mixing, heating and cooling) and proposes viable mechanisms for the precipitation of base and precious metals at Palinpinon. Preliminary results of this were presented in Rae et al. (1998).

- Section 5 combines the results of the previous sections into a discussion of the implications for relationships between various alteration and mineralisation assemblages in magmatic-hydrothermal systems. Is the Palinpinon geothermal system now, or has it ever been, a mineralising hydrothermal system? If so, what were the predominating physical and chemical influences that resulted in ore mineral deposition? How do they relate to

alteration assemblages and fluid chemistry? If the hydrothermal system is barren, then just as importantly reasons for this need to be assessed in terms of the relative roles of depth of intrusion emplacement and physicochemical gradients. Another important aspect of this research is to test possible temporal and genetic links between the different hydrothermal alteration assemblages at Palinpinon, and to assess the implications for other hydrothermal systems.

1. PALINPINON GEOTHERMAL FIELD, NEGROS, PHILIPPINES: INTRODUCTION AND PREVIOUS WORK

1.1. INTRODUCTION

This section reviews the regional tectonic setting and describes the geologic framework of the western Visayas. This is followed by a summary of previous work by PNOC-EDC scientists on the geology, geophysics, hydrology and chemistry of geothermal fluids at the Palinpinon geothermal field. This work has been presented in published papers (Leach and Bogie, 1982; Urbino et al., 1986; Bogie et al., 1987; Bromley et al., 1987; Mitchell and Leach, 1991; Amistoso et al., 1993; D'Amore et al., 1993; Gerardo et al., 1993) and also unpublished PNOC-EDC company reports and files (mainly Glover, 1975; Ruaya, 1980; Jordan, 1983). Pre-existing chemical data from geothermal springs and wells are presented in geochemical discrimination diagrams (i.e., Cl^- vs enthalpy plots; Cl-SO_4-HCO_3 and K-Mg-Na triplots). Previously, only the geothermal well data has been presented in such a way (e.g., the Cl^- vs enthalpy diagram in Jordan, 1983; Gerardo et al., 1993). By compiling the pre-existing spring and well data from the geothermal field, this section is intended to illustrate how previous workers developed the hydrological model for the Palinpinon geothermal field.

1.2. REGIONAL GEOLOGY

1.2.1. Regional Tectonic Framework of the Philippine Archipelago

The Philippine archipelago occupies a complex plate boundary in the western Pacific (Figure 1.1). It is a region of opposing subduction zones between the western Eurasian plate and the eastern Philippine Sea plate. The region consists of accreted volcanic arcs, continental fragments, marginal basins and ophiolites, and has a complex history of subduction, collision and strike-slip faulting that has been ongoing since the late Mesozoic. The tectonic setting of the Philippines has been discussed by Hamilton (1979), Cardwell et al. (1980), Acharya and Aggarwal (1980) and many other workers. Models for the tectonic evolution of the archipelago have been proposed by Gervasio (1971), Mitchell et al. (1986) and Rangin et al. (1990), amongst others.

East of the archipelago, the Philippine Sea plate is being subducted westwards along the Philippine Trench and the East Luzon Trough (Figure 1.1, Hamilton, 1979; Cardwell et al., 1980). An associated active volcanic arc extends from southeastern Luzon to Leyte, and possibly into eastern Mindanao (Cardwell et al., 1980). Along the western boundary of the archipelago, eastward subduction of the South China, Sulu and Celebes Sea basins occurs respectively along the Manila, Negros and Cotabato Trenches (Figure 1.1). Arc volcanism is associated with each of these trenches (Hamilton, 1979; Cardwell et al., 1980).

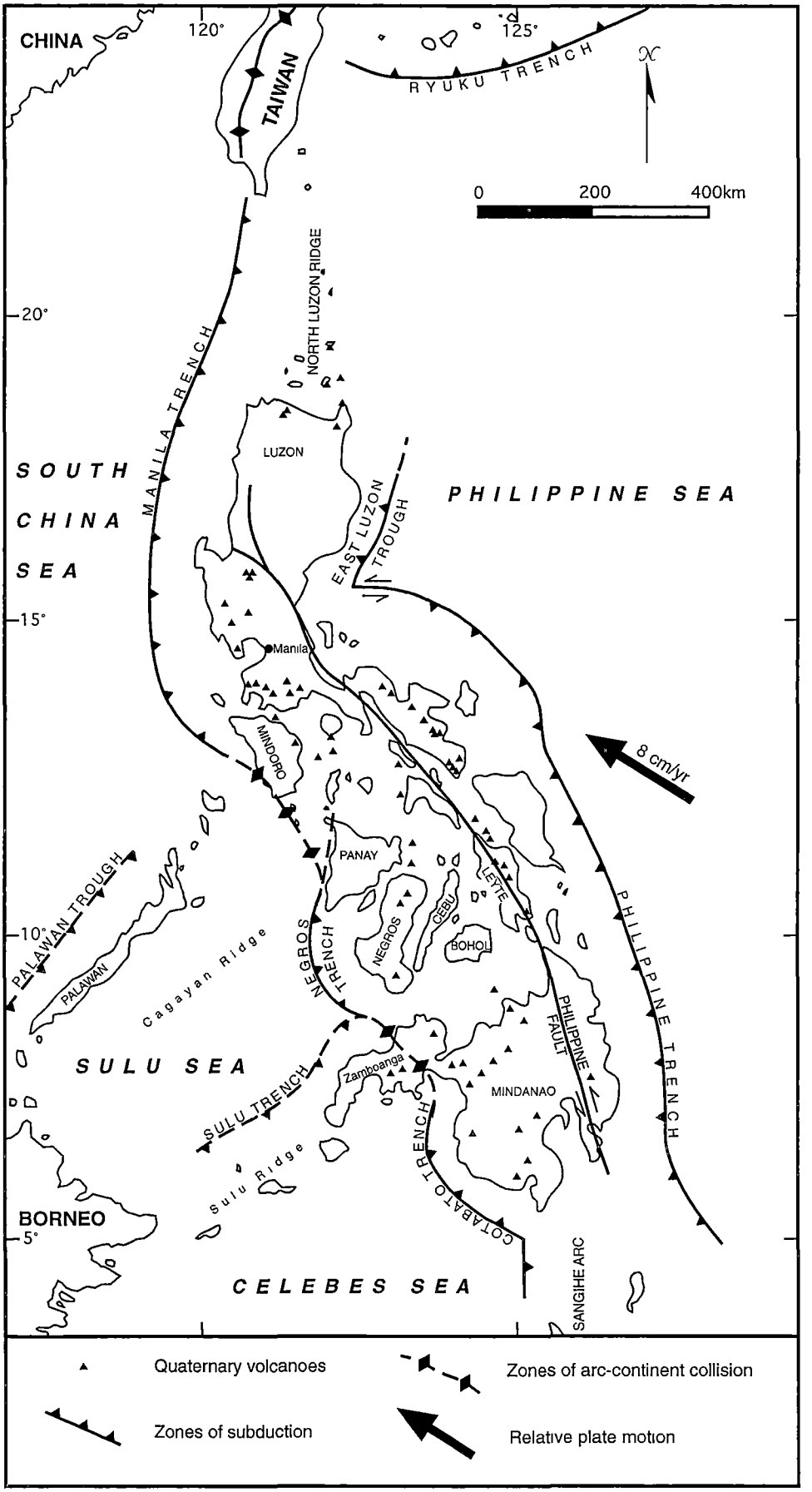

Figure 1.1. Regional tectonic map of the Philippine archipelago. From Cardwell et al. (1980), Sarewitz & Karig (1986b) and Barrier et al. (1991).

The tectonic framework of the western boundary of the archipelago is complicated by two zones of arc-continent collision connecting the three trenches: the Mindoro-Panay collision zone (McCabe et al., 1982; Rangin et al., 1985; Stephan et al., 1986; Sarewitz and Karig, 1986a; Sarewitz and Karig, 1986b) and the western Mindanao (Zamboanga) collision zone (Pubellier et al., 1991). In both zones, rifted Eurasia-derived continental crust has impinged onto the eastward-directed subduction zone.

Between the opposing subduction zones, in a region known as the Philippine Mobile Belt, is the Philippine Fault (Figure 1.1). This major left-lateral strike slip fault system accommodates the strike-slip component of oblique convergence of the Philippine and South China Sea basins (Aurelio et al., 1991; Barrier et al., 1991). Total displacement along the fault is uncertain but could exceed 200 km (Mitchell et al., 1986).

1.2.2. Geology of the Western Visayas, Central Philippines

The Visayas region, central Philippines, comprises the islands of Panay, Romblon, Negros, Cebu, Bohol, Leyte and Samar. The following discussion on the regional geology of the western Visayas focuses on the islands of Panay, Negros, Cebu and Bohol (Figure 1.2).

Subduction of the Sulu Sea at the Negros Trench is the salient influence on the Neogene regional geology of the western Visayas. Consequently, the region is broadly subdivided into the characteristic zones of island arc subduction. These being: accretionary wedge (western Panay), forearc basin (Iloilo Basin), backarc basin (northeastern Negros, Cebu, Bohol and adjacent seas) and volcanic arc (Negros volcanic arc; Figure 1.2; Rangin et al., 1989).

In the Antique Range of western Panay, the accretionary wedge is a complex package of imbricate thrust terranes of Late Oligocene-Middle Miocene island arc volcanics (Mt. Baloy and Valderrama volcanics). These lie unconformably upon Middle to Late Miocene carbonates and clastics and highly sheared Mesozoic ophiolites and mélanges (Rangin et al., 1989; Rangin, 1991). In northwest Panay, the arc volcanics are thrust onto the North Palawan block (Cuyo Platform) in an active arc-continent collision (Figure 1.2). The Pampanan volcanics (Late Oligocene-Early Miocene), which form the uppermost unit of the Antique Range and the basement of the forearc basin (Rangin, 1991), have been thrust over the younger Valderrama volcanics along the eastward-dipping Pampanan Thrust (Figure 1.2). East of the accretionary wedge, the forearc (Iloilo) basin is filled with more than 2 km of Late Oligocene to Recent sediments (McCabe et al., 1982; Rangin et al., 1989).

Negros Island comprises the volcanic arc (Figure 1.3) where calc-alkaline volcanism has occurred since the Pliocene (Rangin et al., 1989). The most prominent volcanoes are Cuernos de Negros in the south, and Mt. Canlaon, Mt. Mandalagan and Mt. Silay in the north. Only Mt. Canlaon has been active in historic times (von Biedersee and Pichler, 1995).

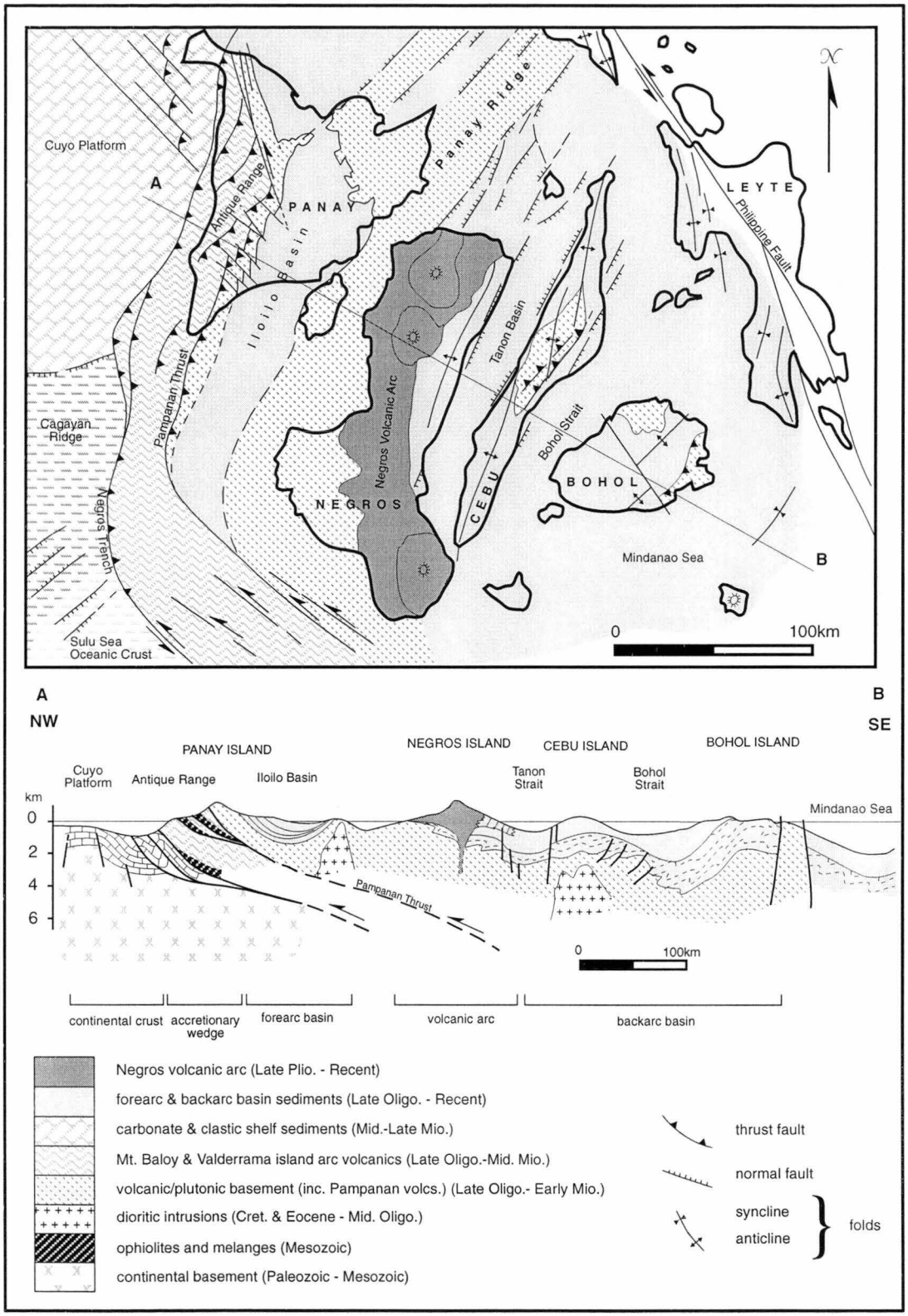

Figure 1.2. Regional geology of the western Visayas region, central Philippines. From Rangin et al. (1989).

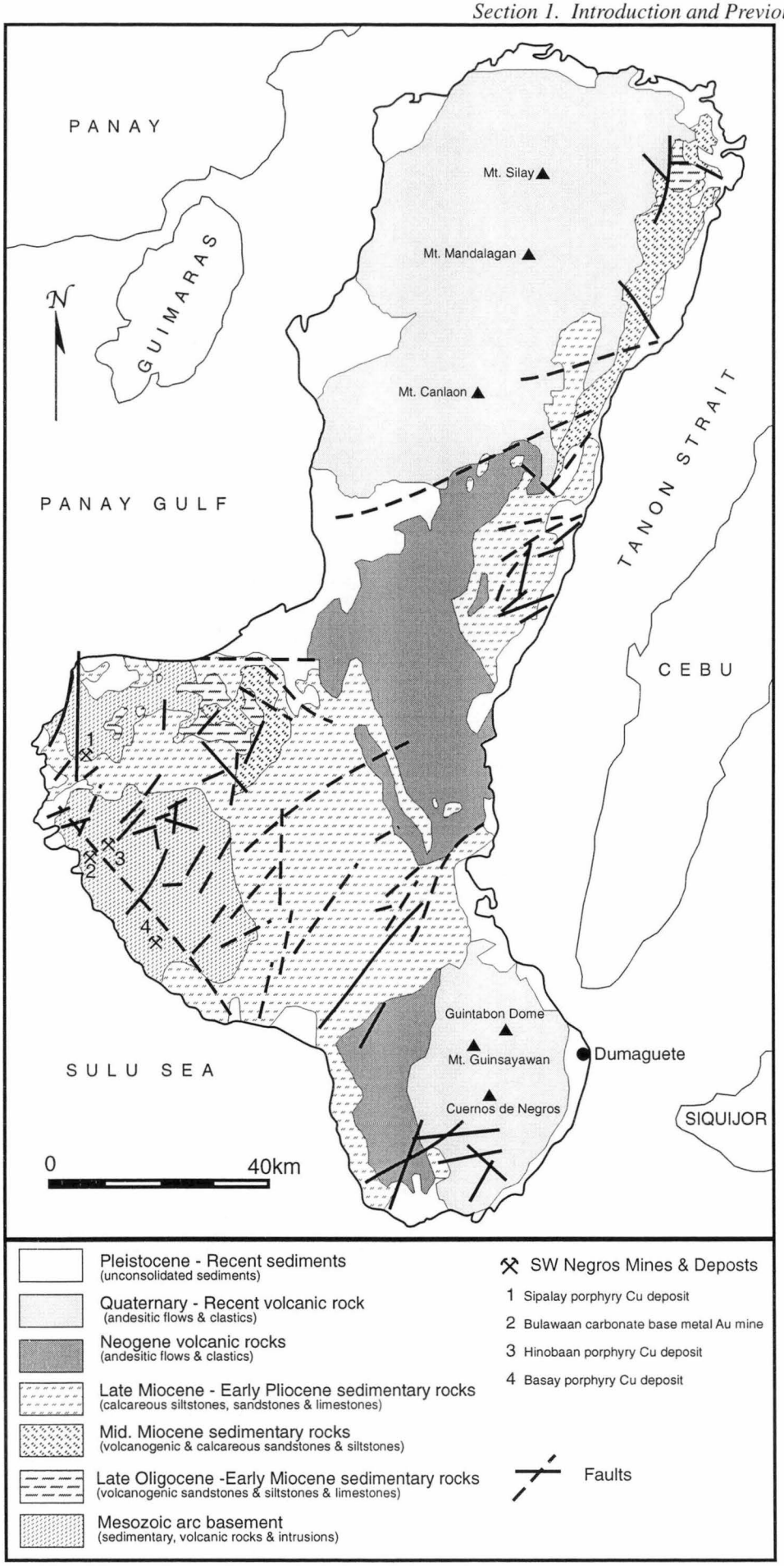

Figure 1.3. Geology of Negros Island showing the locations of the SW Negros Cu and Au deposits. From Porth et al. (1989) and Maglambayan et al. (1998).

Cretaceous to Early Tertiary rocks form the basement to both the volcanic arc and the back arc basin and crop out in southwest Negros and central Cebu (Figures 1.2 and 1.3). In southwest Negros, Late Cretaceous to Paleocene/Eocene metavolcanics and metasediments have been intruded by a quartz diorite batholith (Eocene-Middle Oligocene) and dacite porphyry stocks (Oligocene-Middle Miocene; Maglambayan et al., 1998). These intrusions have associated copper and base metal mineralisation and are part of the southwest Negros mineral district (Sillitoe and Gappe, 1984). Copper-molybdenum porphyry style mineralisation is associated with quartz diorite intrusions at Sipalay, Hinobaan and Basay. The dacite porphyry stocks have associated low sulphidation (carbonate-base metal-gold-silver) style mineralisation at the Bulawaan deposit (Maglambayan et al., 1998). In central Cebu, metavolcanics and metasediments of the Mesozoic basement are intruded by porphyritic diorites (108±1 my; Rangin et al., 1989) that have associated copper porphyry-style mineralisation (the Atlas mine district).

Tertiary sediments of the back arc basin lie unconformably upon Mesozoic basement. The Middle Miocene volcanic units in Cebu (Toledo Formation), Bohol (Carmen Formation) and northeast Negros (Malabago Formation; Figure 1.4) are coeval with the Valderrama volcanics in western Panay (Rangin et al., 1989). The Late Miocene to Early Pliocene folded basin sediments in Cebu (Barili Formation), Bohol (Sevilla Marl, Sierra Bullones Limestone) and Negros (Talave Formation) are calcareous siltstones, sandstones, limestones and tuffaceous sandstones and rest unconformably on the Middle Miocene volcanic sequences (Figure 1.4, Porth et al., 1989). The youngest formations of the back-arc basin are the Late Pliocene to Recent Negros arc volcanics, and reefal limestones of the Carcar Formation.

The backarc basin is believed to be undergoing intra-arc extension (Rangin et al., 1989; Pubellier et al., 1996). This has resulted in the formation of horst and graben structures parallel to the Negros Trench, most notably the Tañon Basin which separates the islands of Negros and Cebu (Figure 1.2). In the region of southern Negros Island, the Negros Trench trends NW-SE and hence extension direction normal to this would be NE-SW. Microseismic studies at Palinpinon by Bromley et al. (1987) show patterns of first motion consistent with this extension direction.

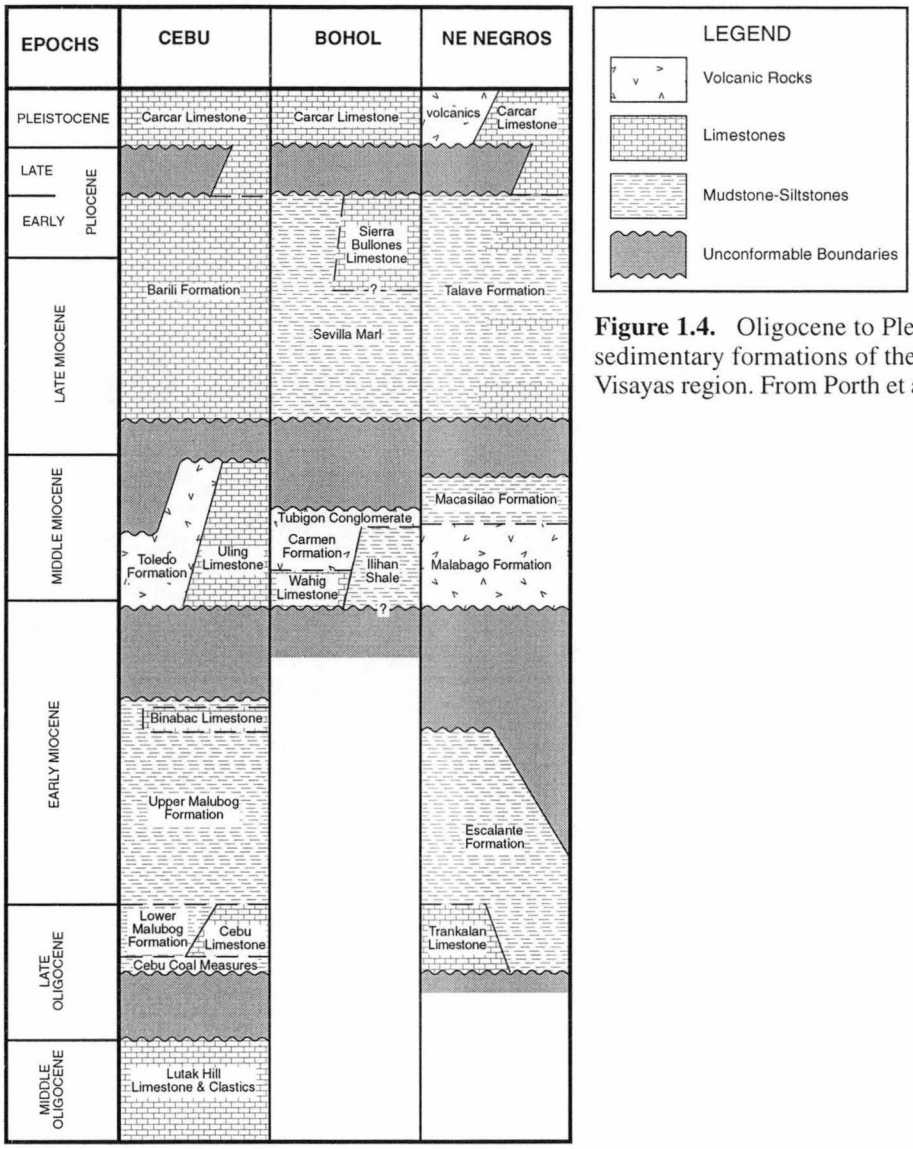

Figure 1.4. Oligocene to Pleistocene sedimentary formations of the western Visayas region. From Porth et al. (1989).

1.3. PALINPINON GEOTHERMAL FIELD, NEGROS, PHILIPPINES

Palinpinon geothermal field is located in the Okoy Valley, the watershed between two volcanic eruption centres, Mt. Guinsayawan (north) and Cuernos de Negros volcano (south; Figure 1.5). The geothermal steamfield occurs on the northern slopes of Cuernos de Negros volcano and consists of two production sectors (Figure 1.5). Palinpinon I (Puhagan) has a generating capacity of 112.5 MWe and was commissioned in May 1983. Palinpinon II (Nasuji-Sogongon) consists of 3 installed power plants with a combined capacity of 80 MWe that were commissioned in 1994 and 1995. Generated power is distributed on the Negros grid and via submarine cables to the neighbouring islands of Panay and Cebu. The steamfield has a total of 72 geothermal wells (Figure 1.5), 48 for steam production and 24 for the reinjection of waste water. Two vertical exploration geothermal wells have also been drilled on the southern and eastern flanks of Cuernos de Negros in the Baslay-Dauin area (Figure 1.5).

The stratigraphy of Palinpinon has been previously presented by Mitchell and Leach (1991) and consists of a Tertiary sequence of andesitic volcanic rocks and calcareous sandstones and limestones (Figure 1.6). Only volcanic rocks belonging to the Southern Negros Formation (Miocene-Pliocene; Mitchell and Leach, 1991) and the Cuernos Volcanic Formation (Recent; Mitchell and Leach, 1991) are exposed at surface. The western sequence has been intruded by a monzodiorite to granodiorite pluton (Nasuji Pluton) of possible Middle Miocene age (Mitchell and Leach, 1991) and along the eastern margin of this pluton, porphyritic stocks and dikes have been emplaced. These smaller intrusions, or their deeper equivalents, represent the possible heat source for the active geothermal system (Mitchell and Leach, 1991). The geology of Palinpinon is discussed in detail in Section 2.

1.3.1. Geophysics

Schlumberger resistivity traverses covering approximately 260 km^2 of the Southern Negros area were undertaken in 1977 (KRTA, 1977; Ward, 1980; Maunder et al., 1982). Rugged terrain and difficult access hindered surveys in the central and northern regions. Results of a resistivity survey are illustrated in Figure 1.7. An east-west trending region of low apparent resistivity (< 10 Ωm) occurs in the Okoy Valley, with the 10 Ωm contour enclosing an area of approximately 10 km^2. The apparent resistivity gradient is high along the southern edge of the anomaly and moderate to the north. This is interpreted to indicate that the geothermal reservoir has abrupt northern and southern boundaries and is largely confined beneath the Okoy Valley. There is a bifurcation at the western end of the anomaly, where the 20 Ωm contour extends to both the southwest and northwest towards the Mt. Guinsayawan area (Figure 1.7). To the east, the apparent resistivity gradient is low, with the 50 Ωm contour open to the coast (Figure 1.7).

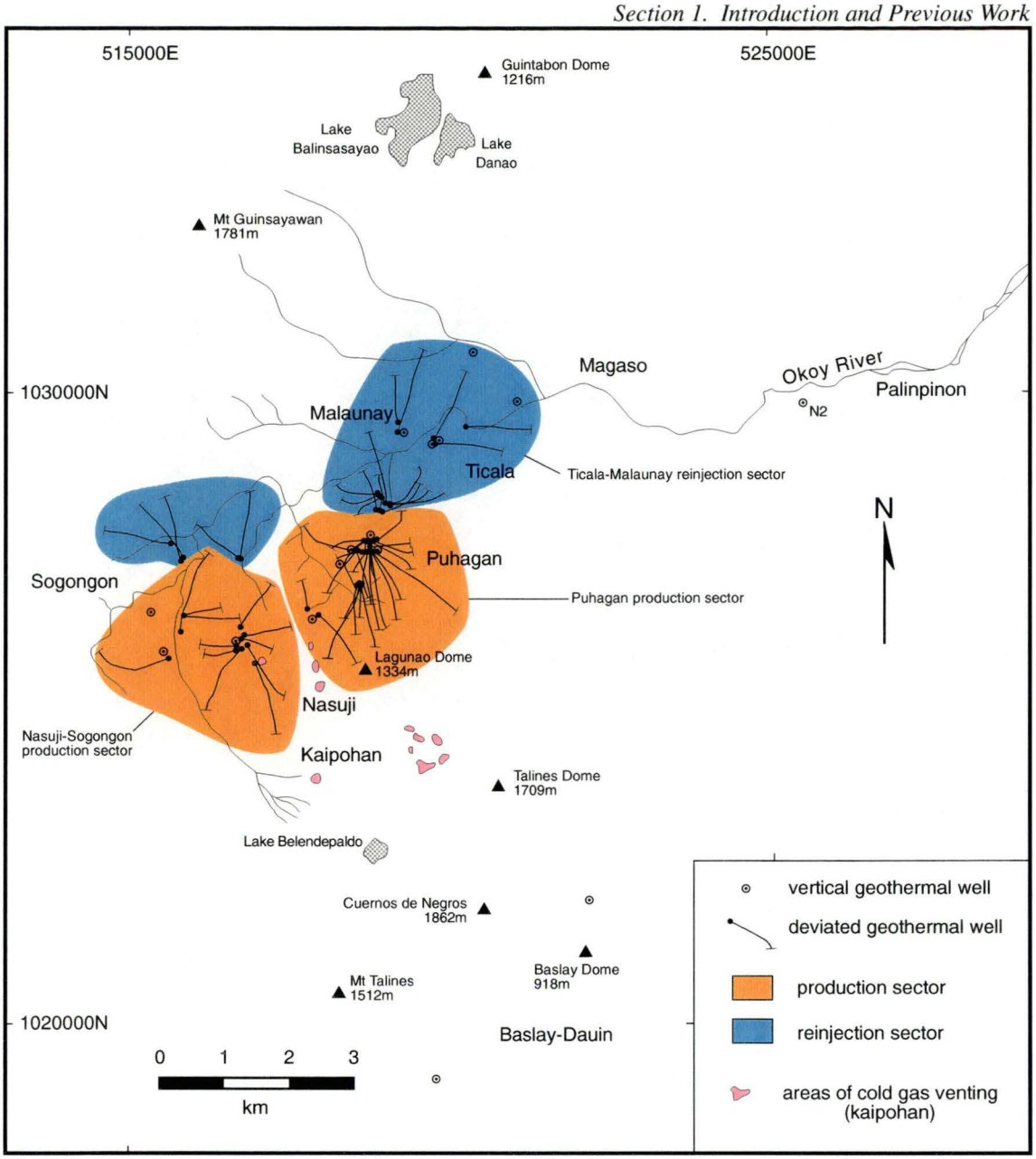

Figure 1.5. The Palinpinon geothermal field with the location of geothermal wells, production and reinjection sectors and some surface features.

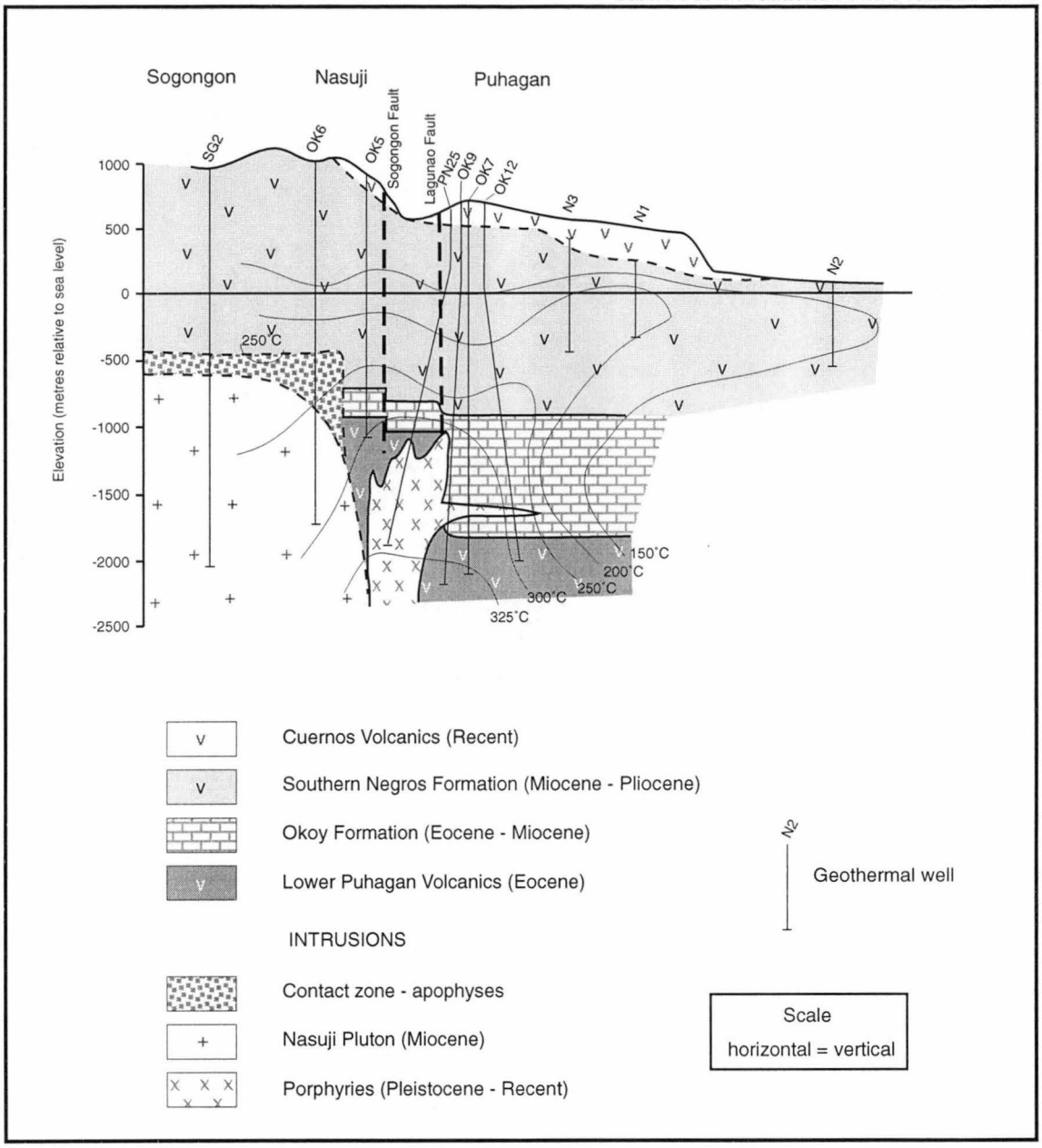

Figure 1.6. West-east cross section showing the subsurface geology and the distribution of isotherms in the Palinpinon geothermal field. From Mitchell & Leach (1991).

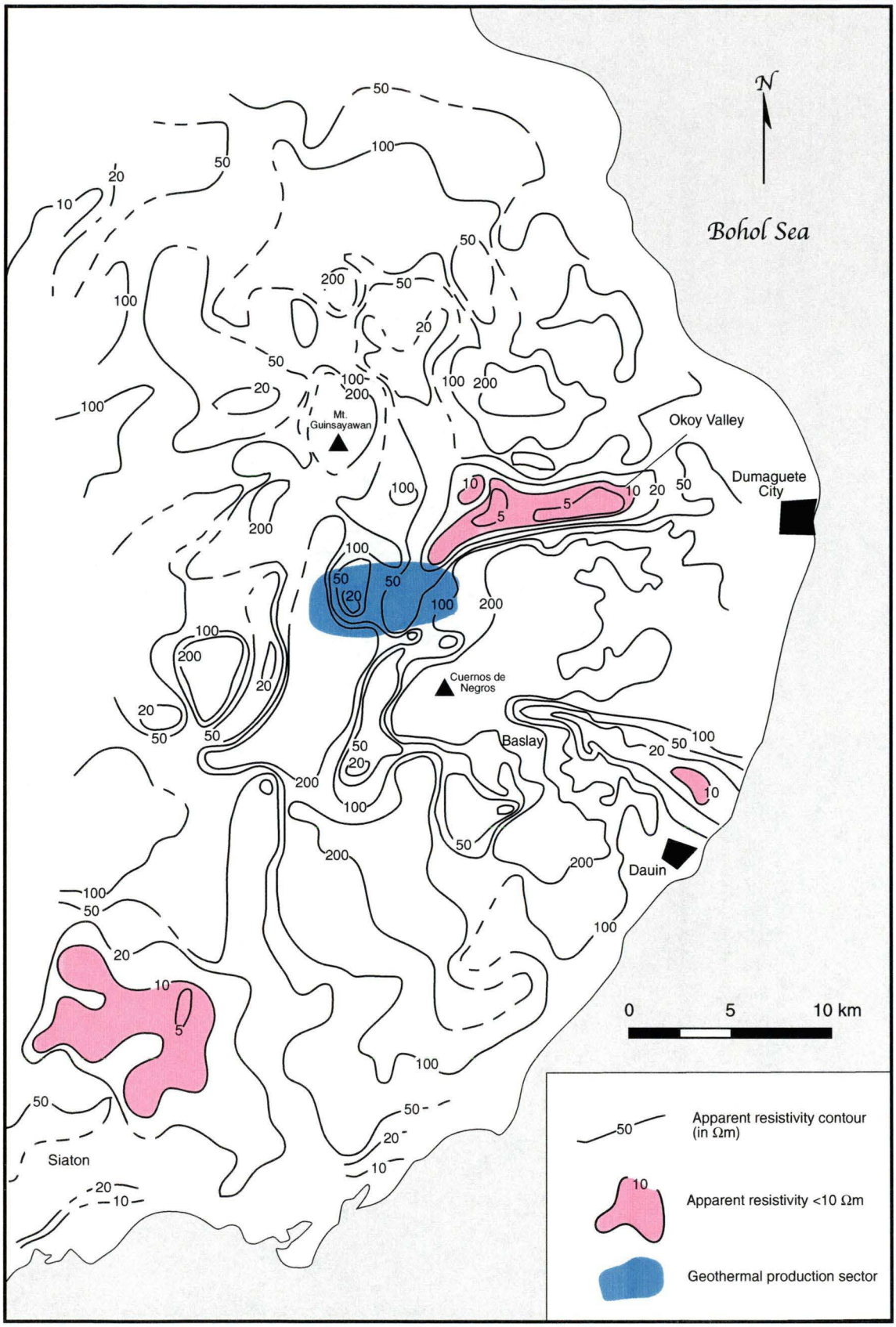

Figure 1.7. Apparent resistivity contours (AB/2=500m) of the southern Negros peninsula. From Maunder et al. (1982).

On the southeastern flanks of Cuernos de Negros, in the Baslay-Dauin region, an area of low apparent resistivity occurs beneath areas of hot spring discharges. The elongate anomaly trends WNW-ESE to the coast (Figure 1.7). In the southern parts of the geothermal project, near Siaton, another area of anomalous low apparent resistivity occurs, with the 10 Ωm contour enclosing approximately 21 km^2. However, only minor warm springs occur in the area, and the low resistivity gradient around the anomaly is probably related to factors other than a saline hydrothermal aquifer (KRTA, 1977). Attempts to further define these anomalies have resulted in the drilling of only two exploration wells in the Baslay-Dauin area.

In geothermal areas, regions of anomalously low apparent resistivity usually indicate either the presence of geothermal aquifers, or hydrothermally-altered country rock associated with such aquifers, past or present. The occurrence of discharging springs in regions of low apparent resistivity in the Okoy Valley and Baslay-Dauin region is interpreted to indicate lateral subsurface outflows presently occurring in these areas. These may be flowing radially from one or more upflow regions beneath the Cuernos de Negros massif. A possible outflow region, with associated wallrock alteration assemblages, may have once existed in the south, extending towards Siaton.

1.3.2. Hydrology and Reservoir Chemistry

Location and Chemistry of Geothermal Surface Features

The types of surface discharge features found at Palinpinon include steam and gas vents, together with hot and warm springs and seepages. Gas vents are found on the upper flanks of Cuernos de Negros, in the kaipohan areas (Figure 1.8), whereas steam vents and hot and warm springs and seepages are mainly found along the Okoy Valley. The hot and warm springs in the Baslay-Dauin area (Figure 1.8) are not discussed further.

Gas Vents (Kaipohans)

Areas of gas venting occur on the high slopes of Cuernos de Negros, at approximately 1200-1300 m elevation (Figure 1.8). Known as "kaipohan" (Bogie et al., 1987), these are areas of non-thermal gas emissions where CO_2 and H_2S are vented (Figures 1.9 and 1.10); warm or cold springs do not occur. There are 11 kaipohan areas within 6 km^2, the largest measuring 150 x 300 m and their distribution is possibly related to fault structures (Ruaya 1980; Bogie et al., 1987).

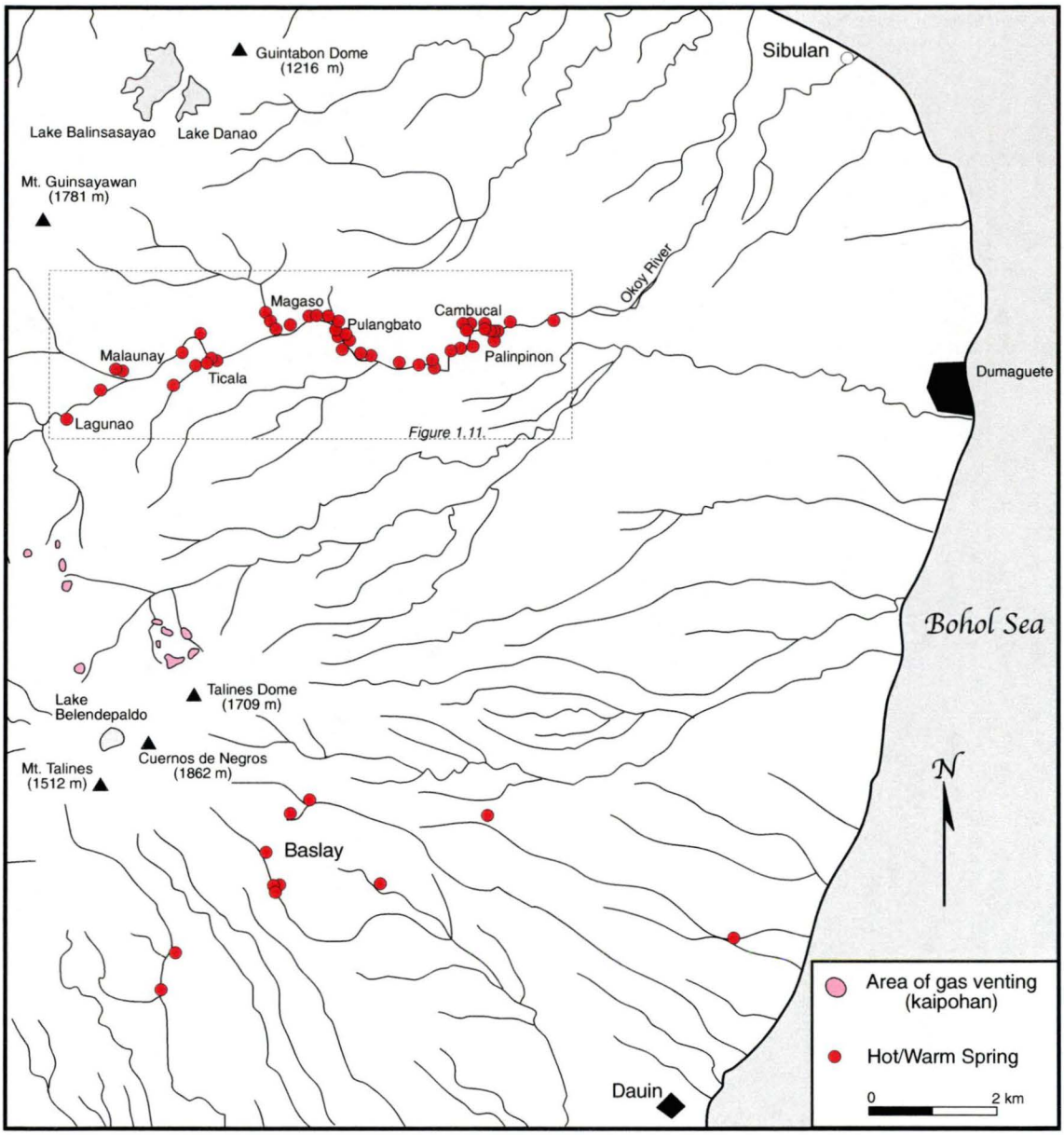

Figure 1.8. Patterns of drainage and the distribution of surface gas and geothermal water discharges in southern Negros (Glover, 1975).

Figure 1.9. Kaipohan. Date: 27.07.96. Energetic gas (CO_2 + H_2S) discharge is occurring through a pool filled with cold rainwater (before crouching figure). There is no water outflow from the pool. The amount of corrosion of the surrounding soil and rock substrate can be gauged by height of exposed roots on the dead tree (right).

Figure 1.10. Kaipohan (foreground). Date: 27.07.96. Gas sampling a large, gently bubbling, pool. There is no water outflow from the pool. The ephemeral nature of the kaipohan area is evident by the regrowth of scrubby vegetation in the middle distance.

Typical gas samples contain 5285 mmol/100mol CO_2 and 274 mmol/100mol H_2S (Ruaya, 1980). Rainwater collecting in surface depressions oxidises any H_2S that percolates through it, resulting in the formation of acidic waters (pH=1.9-2.8; Ruaya, 1980). These acidic surface waters have altered the rocks within the area to an advanced argillic assemblage of kaolinite, smectite, alunite, native sulphur and amorphous residual silica (Bogie et al., 1987). Dead vegetation within each area is indicative of the ephemeral nature of these discharges (Figures 1.9 and 1.10). The largest kaipohan area at Palinpinon was heavily vegetated until 1956 (Bogie et al., 1987). Conditions suitable for the formation of kaipohans include high gas flux, high relief, high rainfall and low rock permeability (Bogie et al., 1987). These are typical of geothermal systems located in volcanic arc terrains in tropical climes.

Steam Vents

Steam vents are found in the Magaso and Pulangbato areas (Figure 1.11) and usually discharge high up on the valley walls (Figure 1.12). The gas composition of these discharges is dominated by CO_2 with accessory H_2S. One analysed gas sample from Magaso by Glover (1975) contains 1810 mmol/100mol CO_2 and 57.6 mmol/100mol H_2S.

Springs and Seepages

This section summarises a chemical survey of the Okoy Valley springs (Table 1.1) undertaken prior to exploration drilling by Glover (1975). The data are used to illustrate relative boiling and mixing trends between springs and calculates reservoir temperatures using quartz adiabatic (Fournier, 1981), K-Mg and Na-K geothermometers (Giggenbach, 1988).

Springs and seepages along the Okoy Valley (Figure 1.11) are broadly categorized as chloride, sulphate and bicarbonate waters (Glover, 1975; Figure 1.13). Steam-heated waters (sulphate and bicarbonate) discharge in areas of high elevation, west of the Magaso area, whereas the chloride waters discharge from springs east of Magaso (Figure 1.11).

Sulphate spring waters are further characterised based on pH. Neutral sulphate springs occur in the upper reaches of the Okoy Valley, at Malaunay and Lagunao (Figures 1.11 and 1.13). These waters have measured temperatures between 32-53°C and near neutral pH (Table 1.1). An explanation for the occurrence of neutral pH sulphate waters in the upper valley is that acidity generated by H_2S condensation and subsequent oxidation has been neutralised by wall-rock interaction and that residence time of the sulphate water in perched shallow aquifers must be long enough for this to occur (Glover, 1975).

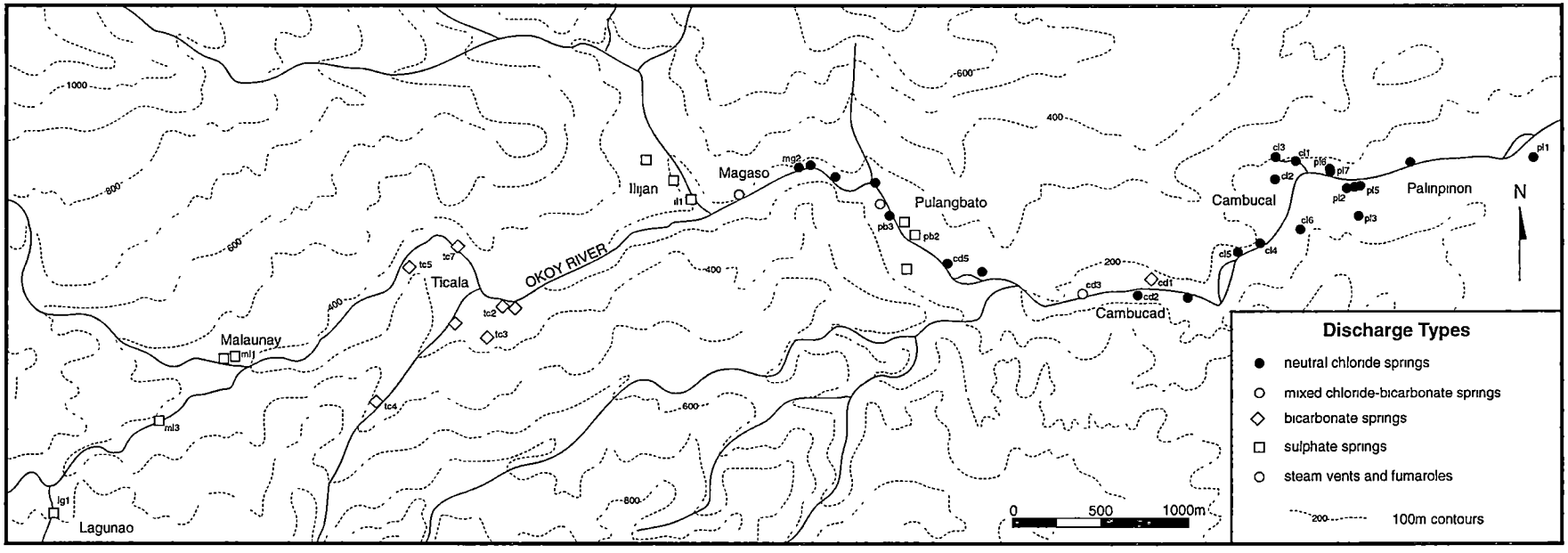

Figure 1.11. Location and types of spring and steam discharges along the Okoy Valley. From Glover (1975). Sampled springs (Table 1) are labelled. Sample prefixes: pl=Palinpinon; cl=Cambucal; cd=Cambucad; pb=Pulangbato; mg=Magaso; il=Ilijan; tc=Ticala; ml=Malaunay; lg=Lagunao.

Table 1.1. Water chemistry of the Okoy Valley springs and the Okoy River All data from Glover (1975).

Spring		Sample	T_{meas}	Enthalpy	pH	Li	Na	K	Rb	Cs	Ca	Mg	F	Cl	SO_4	B	SiO_2	HCO_3	CO_2(tot)	NH_3	Cl/B
		(Glover, 1975)	(°C)	(kJ/kg)									(mg/kg)								
Palinpinon1	pl1	M310	40	167.6	7.92	1.66	445	40	0.31	0.42	70	6.2	0 30	777	73	8.9	86	69	3	0.1	26 6
Palinpinon2	pl2	M312	98	410.6	7.85	8.30	2090	195	1.38	1 95	176	0.3	0 84	3647	63	40.7	195	22	3	5 2	27 3
Palinpinon3	pl3	M313	79.5	334.9	8.01	7.26	1851	143	1.03	1 85	174	3 9	0 90	3165	57	36.7	167	98	5	7.8	26 3
Palinpinon5	pl5	M314	48	201	8.48	1.37	421	37	0.28	0.42	18.1	0.5	1.02	471	15	6.4	225	64		0.1	22.4
Palinpinon6	pl6	M315	94	393.7	8.00	7.00	1747	179	1.28	1.80	161	3.8	0.66	2994	73	36.5	205	149	6	8.0	25.0
Palinpinon7	pl7	M316	77	322.3	8.03	7.66	1841	190	1.39	1 95	179	3 2	0.75	3278	64	37.8	224	131	6	8.3	26.4
Cambucal1	cl1	M317	92.5	389.5	7.87	7.91	1887	167	1.28	2 18	175	5.5	0.50	3490	64	40.4	175	58	2	13.0	26.3
Cambucal2	cl2	M318	86	360.1	7.75	5.93	1463	104	0.84	1.58	170	1.3	0.43	2703	43.5	31.0	147	27	4	10.5	26.6
Cambucal3	cl3	M319	85	355.9	8.00	4.10	1040	94	0.66	0.97	138	18.7	0.26	1836	27.5	21.8	155	281	5	6 2	25 7
Cambucal4	cl4	M320	83	347.5	7.80	9.38	2187	193	1.51	2.30	214	1.8	0.86	3823	77	44.7	187	42	3	13.5	26.1
Cambucal5	cl5	M321	77	322.3	7.95	7.92	1817	158	1.16	1.85	167	3.6	0.64	3204	52	37.5	218	126	5	12.0	26.1
Cambucal6	cl6	M322	54	226	-	7 92	1945	149	1.07	1 76	179	6.8	-	3278	75	-	159	-	-	-	-
Cambucad1	cd1	M323	47	196.8	7.93	0.01	23.6	5.6	0.03	-	28	8.6	0.17	9.2	2.9	0.10	127	169	5	0.1	-
Cambucad2	cd2	M324	58	242.8	7.88	3 85	932	80	0.66	0 97	96	12.2	0.38	1616	27	18.4	152	200	8	7.7	26.8
Cambucad3	cd3	M325	36	150.9	8.25	0.50	119	11.3	0.07	0.05	38	8.4	0.18	176	4.6	2.10	74	180		0.1	-
Cambucad5	cd5	M326	48	201	-	3.90	862	79	0.57	0.74	131	8.6	-	1539	70	-	120	-	-	-	-
Pulangbato2	pb2	M327	41	171.7	-	-	20	8.0	0.05	-	34	8.3	-	-	4.8	-	97	-	-	-	-
Pulangbato3	pb3	M328	46	192.6	7.90	5.56	1295	113	0.74	0.88	230	9.1	0.65	2214	284	24.9	115	150	7	0.1	27.1
Magaso2	mg2	M331	88.5	372.7	6.80	4.62	1120	148	1.07	0.97	159	8.8	0.83	1926	174	22.5	152	1.6	0.5	9.2	26.1
Iliyan1	il1	M332	39.5	167.6	2.83	0 05	14 5	2.6	0.02	-	60	7.1	0.00	0.3	480	0.13	85	-	-	0 3	-
Ticala2	tc2	M333	42.5	180.1	-	0 04	98	9.4	-	-	19	17.0	-	-	23	-	98	-	-	-	-
Ticala3	tc3	M334	32	134.1	8.15	0.01	15.9	2.8	-	-	32	9.4	0.11	1.9	4.0	0.02	77	172	2	0 3	-
Ticala4	tc4	M335	42	175.9	8.42	0.01	18.5	1.5	-	-	45	9.1	0.11	1.9	1.5	0.02	73	215	-	0.1	-
Ticala5	tc5	M336	53.5	226	-	0 02	70	5.5	-	-	23	12.4	-	-	28	-	100	-	-	-	-
Ticala7	tc7	M337	29	121.6	7.65	-	92	4.1	-	-	24	26.0	0.11	2.4	3 7	0.04	74	520	17	0.1	-
Malaunay1	ml1	M338	49	205.1	7.87	0.02	41	4.5	0.03	-	390	23 0	0.19	2.1	778	0.04	75	216	10	0.1	-
Malaunay3	ml3	M339	32	134.1	-	0 02	38	4.8	-	-	320	9.7	-	-	620	-	63	-	-	-	-
Lagunao1	lg1	M340	53	221.9	8 14	0 02	30	4.8	0.02	-	425	25.0	0.30	1.7	840	0.04	44	147	3	0 1	-
Okoy River		M341	24	100.7	7.60	0.01	7.6	2.0	-	-	45	4.5	0.12	1.2	103	-	47	39	1	0.1	-

Figure 1.12. Magaso, Okoy Valley.
Date: 13.06.96. Fumarolic activity (steam vents) high on the valley walls in the Magaso area.

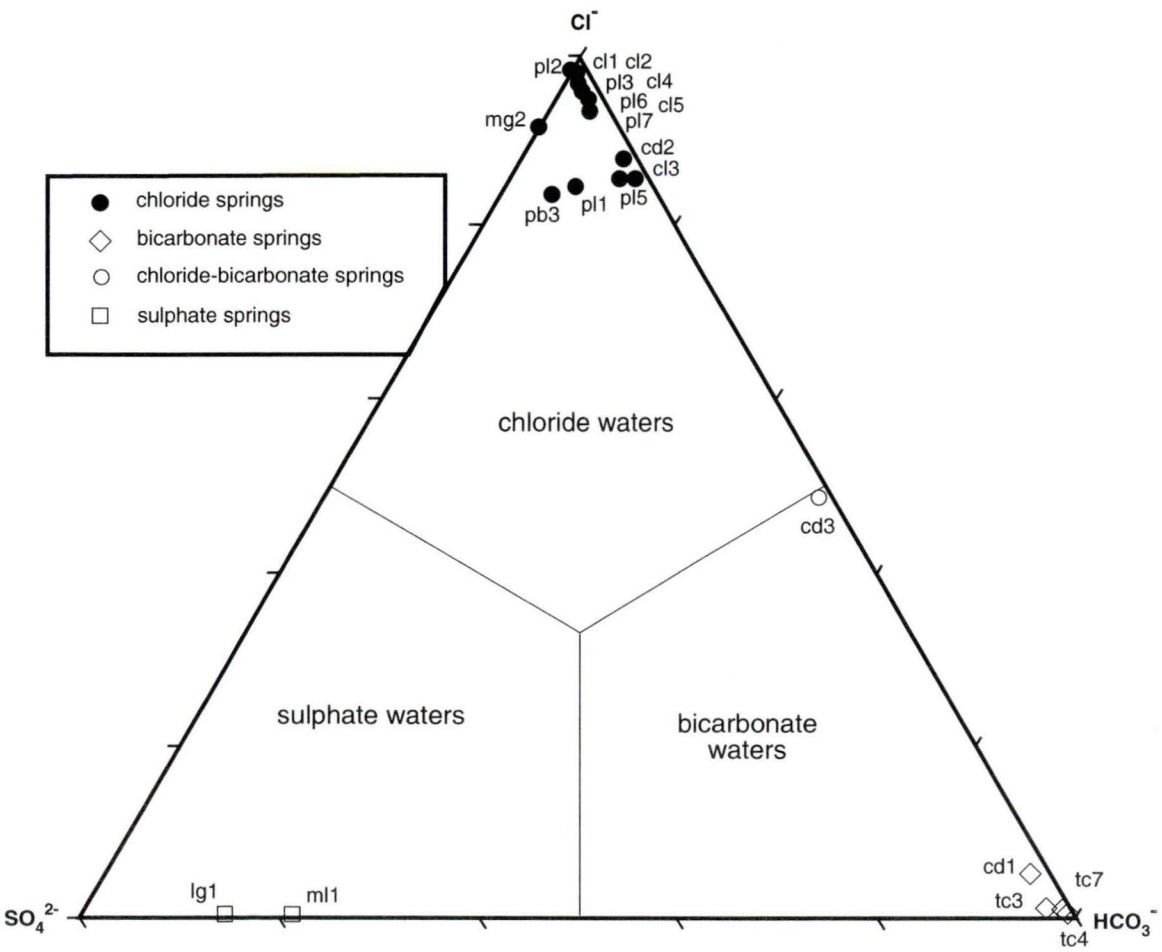

Figure 1.13. Relative SO_4^{2-}, HCO_3^- and Cl^- contents of Okoy Valley springs, showing different spring water types. Sample prefixes: pl=Palinpinon; cl=Cambucal; cd=Cambucad; pb=Pulangbato; mg=Magaso; tc=Ticala; ml=Malaunay; lg=Lagunao. Sample locations are shown in Figure 1.11.

Sulphate waters with acidic pH occur at lower elevations in the Ilijan area (Figures 1.11 and 1.14). For example, spring il1 has a pH of 2.8 (Table 1.1). In contrast to neutral sulphate waters, the acidic nature of the Ilijan sulphate springs and their close proximity to the steam vents (Figure 1.11) infers a closer proximity to subsurface steam separation and hence insufficient time for wall-rock interaction to neutralise the water before discharging at surface (Glover, 1975).

Bicarbonate waters (Figure 1.13) are found in the Ticala area, between areas of neutral sulphate and acid sulphate spring waters (Figure 1.11). Discharge temperatures of these springs range between 29-54°C, and the waters have neutral pH's (i.e., 7.7-8.4; Table 1.1).

Chloride spring waters with the highest chloride concentrations (2703-3823 mg/kg Cl^-) are located in the Palinpinon and Cambucal areas. Generally, springs with the highest discharge temperatures (40-98°C; Table 1.1) are located in these areas. The relative concentrations of chloride and boron, two "conservative" constituents of geothermal water, permit assessment of deep thermal inputs (Giggenbach and Goguel, 1989). Chloride waters of the Okoy Valley have consistent Cl/B ratios, between 25.7-27.3 (Table 1.1). An exception is spring pl5, the most dilute neutral chloride water (471 mg/kg), with a Cl/B value of 22.4. The consistency of the data is evidence for chloride waters discharging along the Okoy Valley being derived from a common reservoir (Glover, 1975). Using the composition of the chloride spring waters, Glover (1975) calculated reservoir temperatures between 182°-226°C using the Na-K geothermometer (Fournier and Truesdell, 1973) and 181°-213°C from the Na-K-Ca geothermometer (Fournier and Truesdell, 1973). Taking cold water mixing into account Glover (1975) concluded that reservoir temperatures at Palinpinon geothermal field were probably in the range 230°-260°C.

To establish the relationship between waters, in terms of boiling, mixing, cooling and heating processes, it is useful to compare the relationship between the temperature (expressed in terms of enthalpy) and chloride content of each spring (Figure 1.15). A mixing line has been drawn from Palinpinon meteoric water (represented by Okoy River water, Table 1.1) through the hottest and most dilute neutral chloride sample (pl5). Data points that plot beneath this mixing line indicate the relative amount of subsurface boiling each spring water has undergone prior to discharge (Figure 1.15). From this it is apparent that neutral chloride springs in the Palinpinon and Cambucal area discharge waters that have undergone the greatest amount of boiling and the least mixing. There is a general increase in dilution towards the west. The sulphate and bicarbonate waters discharging in the upper reaches of the Okoy Valley at Malaunay, Lagunao and Ticala, have the lowest chloride contents and lie above the mixing line (Figure 1.15). This is consistent with these waters being dilute and steam-heated.

Figure 1.14. Ilijan, Okoy Valley. Date: 13.06.96. A small, steam-heated acid sulphate spring discharging from the base of a cliff. The surrounding rock is altered to alunite-kaolinite-quartz.

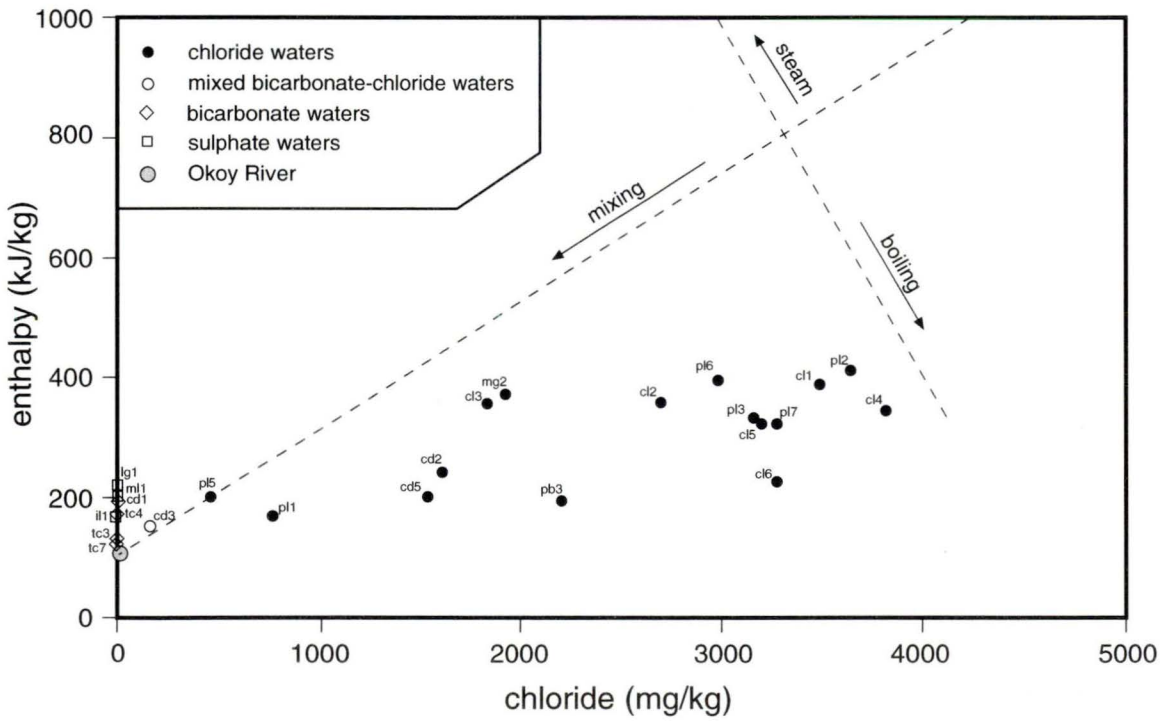

Figure 1.15. Chloride versus enthalpy plot for Okoy Valley springs. Data from Glover (1975).

The quartz adiabatic (Fournier, 1981) and K-Mg and Na-K (Giggenbach, 1988) solute geothermometers have been used to calculate reservoir temperatures (Table 1.2). Temperatures calculated using the quartz adiabatic geothermometer (Fournier, 1981) range from 98-175°C, with the neutral chloride waters between 126° and 175°C. The K-Mg geothermometer (Giggenbach, 1988) has a wider temperature range, 29-226°C, with the neutral chloride waters ranging from 107° to 226°C. Both of these geothermometers respond quickly to temperature changes and subsequent fluid-rock re-equilibration in the reservoir. Hence, their calculated temperatures reflect ongoing processes in the shallow reservoir (Giggenbach, 1988) and explain why the western, most dilute springs, generally have lower calculated temperatures (Table 1.2). The Na-K geothermometer (Giggenbach, 1988) responds more slowly and the calculated temperatures reflect equilibrium conditions in the hotter, deeper parts of the reservoir. The temperatures calculated using this geothermometer are between 175° and 374°C (Table 1.2), with the neutral chloride waters having a more restricted temperature range of 207-256°C. These temperatures indicate a higher reservoir temperature than those calculated by Glover (1975) using the Na-K-Ca geothermometer (Fournier and Truesdell, 1973). This relates to the Na-K-Ca geothermometer's sensitivity to mixing, which will affect calcium concentrations, but not the Na/K ratios (Fournier and Truesdell, 1973).

The spring waters are only suitable for geothermometer calculations if chemical equilibrium is attained between the fluid and the rock. A useful method of assessment is to combine the K-Mg and Na-K geothermometers (Giggenbach, 1988) and plot water compositions in terms of relative concentrations of Na, K and Mg (Figure 1.16). If equilibrium has been attained, calculated K-Mg and Na-K geothermometer temperatures for a particular water sample should be in close agreement and its position on the Na-K-Mg plot should lie along the line labelled "full equilibrium" (Figure 1.16). Only one water sample does so, pl2, which is one of the most saline chloride waters (Figure 1.15) and has approximately equal K-Mg and Na-K temperatures (T_{KMg}=226°C and T_{NaK}=227°C; Figure 1.16, Table 1.2). This implies that spring waters along the Okoy Valley are derived from a shallow reservoir with a temperature of approximately 225-230°C. Other chloride waters plot in a linear trend from the pl2 position towards the Mg apex, in the area of partial equilibrium, and some chloride waters, and the sulphate and bicarbonate waters, plot in the area labelled "immature waters". This indicates their compositions are affected by mixing with shallow derived, relatively Mg-rich water and emphasises their unsuitability for reservoir temperature assessment using solute geothermometers.

Table 1.2. Solute geothermometry calculations for Okoy Valley springs using data from Glover (1975).

Spring		Sample (Glover, 1975)	$T_{q\text{-}adi}$	T_{KMg} (°C)	T_{NaK}
Palinpinon1	pl1	M310	125.7	107.4	223.9
Palinpinon2	pl2	M312	166.7	226.0	226.8
Palinpinon3	pl3	M313	158.3	155.8	212.5
Palinpinon5	pl5	M314	174.8	143.0	222.2
Palinpinon6	pl6	M315	169.5	164.6	234.3
Palinpinon7	pl7	M316	174.5	170.2	234 8
Cambucal1	cl1	M317	160.8	155.2	222.7
Cambucal2	cl2	M318	151.7	164.1	206 5
Cambucal3	cl3	M319	154.4	116.2	224.4
Cambucal4	cl4	M320	164.4	182.7	222.5
Cambucal5	cl5	M321	173.0	160.9	221.4
Cambucal6	cl6	M322	155.8	147.4	211.9
Cambucad1	cd1	M323	144.3	55.0	312.2
Cambucad2	cd2	M324	153.4	117.8	220.4
Cambucad3	cd3	M325	119.0	70.9	228.2
Cambucad5	cd5	M326	141.5	122.7	225.4
Pulangbato2	pb2	M327	131.3	63.2	374.0
Pulangbato3	pb3	M328	139.4	133.2	221.7
Magaso2	mg2	M331	153.4	142.7	255.6
Ilijan1	il1	M332	125.2	41.4	283.7
Ticala2	tc2	M333	131.8	58.8	229.0
Ticala3	tc3	M334	120.8	40.1	281.9
Ticala4	tc4	M335	118.4	28.8	216.1
Ticala5	tc5	M336	132 7	50.8	213.8
Ticala7	tc7	M337	119.0	37.6	175.1
Malaunay1	ml1	M338	119.6	40 6	239.8
Malaunay3	ml3	M339	112.1	50.5	251.7
Lagunao1	lg1	M340	97.5	41.1	272.8

$T_{q\text{-}adi}$: quartz (adiabatic) geothermometer (Fournier, 1981)
T_{KMg} : K-Mg geothermometer (Giggenbach, 1988)
T_{NaK} : Na-K geothermometer (Giggenbach, 1988)

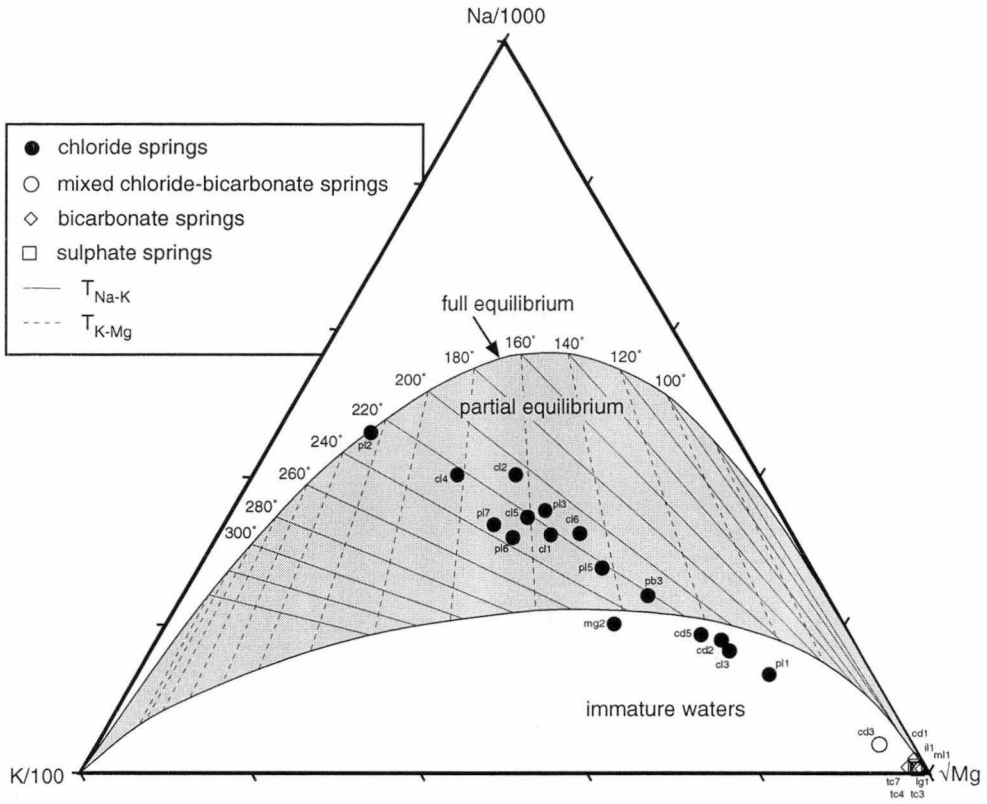

Figure 1.16. Relative concentrations of K, Mg and Na for the Okoy Valley spring waters and evaluation of Na-K and K-Mg geothermometers (Giggenbach, 1988). Solid lines represent Na-K geothermometer isotherms (T_{Na-K}), whereas dashed lines are K-Mg geothermometer isotherms (T_{K-Mg}). Points where the two coincide define the "full equilibrium" line and any sample plotting on this line can be considered to have attained water-rock equilibrium. Most chloride waters plot in the shaded area labelled "partial equilibrium" and the other spring water types plot close to, or at, the Mg apex. This indicates their composition is affected by shallow Mg-rich waters and they are far removed from water-rock equilibration and hence, unsuitable for solute geothermometry.

Summary of the Shallow Hydrology

As is typical for high temperature, liquid dominated geothermal systems located in high relief island arc settings (Henley and Ellis, 1983), the discharge spring chemistry at the Palinpinon geothermal field is largely controlled by elevation and geology. A reservoir of neutral chloride water with an approximate temperature of 225°-230°C exists beneath the Okoy River. Based on the modern day isotherms (Figure 1.6), this reservoir flows from west to east, away from an upflow zone located beneath western areas of high elevation. Steam venting and fumarolic activity in the Magaso and Pulangbato areas and the occurrence of acidic springs close by, in Ilijan (Figure 1.11), is an indication that this central area is closest to the hydrological upflow and zones of boiling in the neutral chloride reservoir. This area also marks the transition between steam-heated sulphate and bicarbonate springs to the west and neutral chloride springs to the east. Springs located furthest east at lowest elevation, in the Palinpinon and Cambucal area (Figure 1.11), discharge neutral chloride water that is least modified by fluid mixing and water-rock interaction.

Isothermal Structure and Permeability

Production wells at Palinpinon intersect multiple zones of permeability and discharge two phase fluid from a single phase liquid reservoir (Harper and Jordan, 1985; Urbino et al., 1986). Measured downhole temperatures range from 220°C to over 300°C, with the hottest temperature of 329°C measured at 1925 m below sea level (bsl) in well PN20D. Production temperatures are typically 280-295°C (D'Amore et al., 1993).

In terms of its isothermal structure, the deep hydrology at 500 m bsl is illustrated in Figure 1.17 (Amistoso et al., 1993). The area of highest heat, or upflow zone, is located south of the Puhagan production sector beneath the Lagunao Dome, where permeability is possibly provided by the northwest-trending Lagunao Fault (Figure 1.17). South and southeasterly-directed Puhagan wells were drilled to intersect aquifers connected to this zone. Outflow zones are towards Nasuji and Sogongon in the west, but predominantly to the northeast along the northeast-trending Puhagan and Ticala Faults, beneath the Okoy River (Figure 1.17). A constriction of the isotherms along the eastern boundary, as well as temperature reversals at depth in southeasterly drilled wells (OK10D, PN15D, PN17D and PN21D) provide evidence for a major inflow zone of cool meteoric water along the eastern edge of the reservoir. The isotherms northwest of Puhagan are less constricted (Figure 1.17) and temperature reversals are not present in the northwesterly drilled wells, implying that this area is an outflow region with less meteoric recharge. To the west, in the western Nasuji-Sogongon sector (Figure 1.17), a progressive decrease in temperature away from the upflow zone, with widely spaced isotherms, is consistent with diffuse outflow to the west. South of Nasuji, the shape of the isotherms are concave to the south (Figure 1.17), indicating a zone of meteoric recharge from the south, possibly along the Ticala Fault.

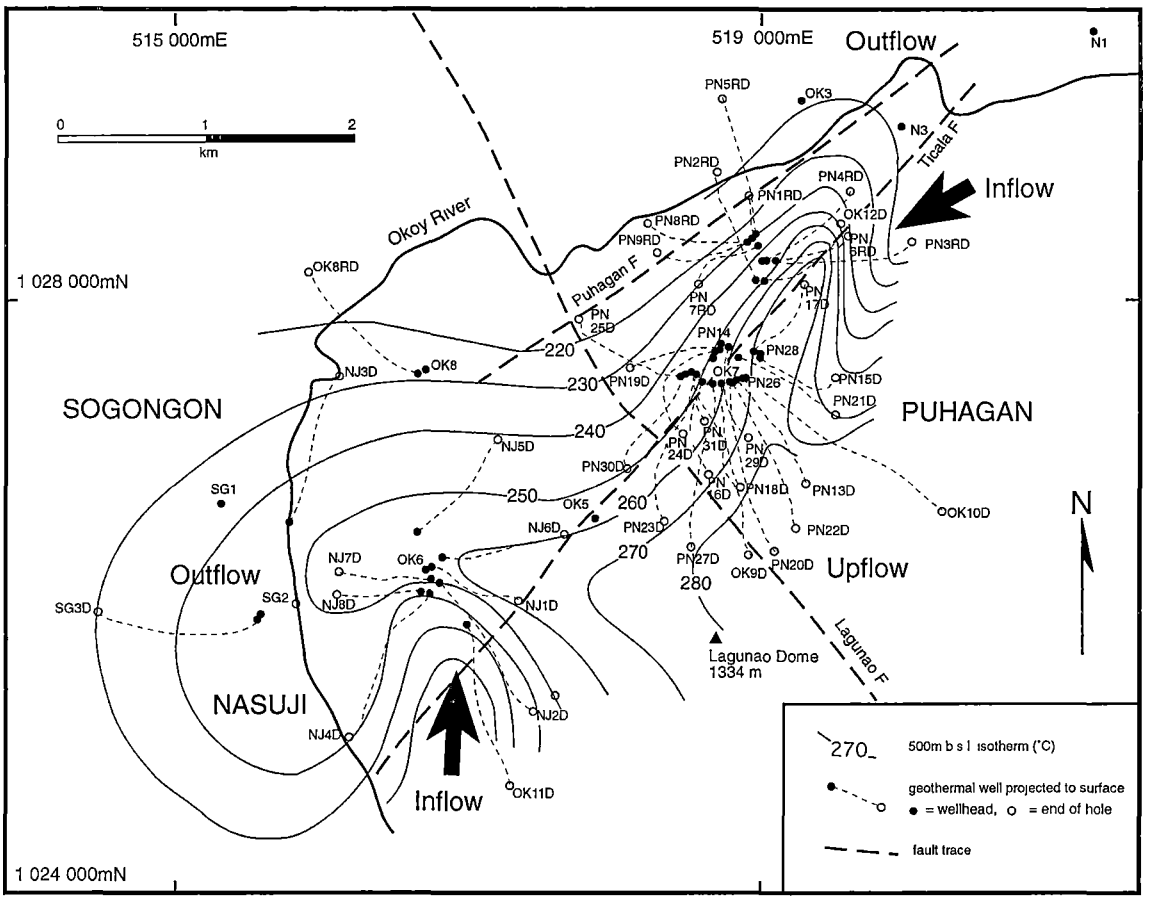

Figure 1.17. Geothermal well location map with the 500 m bsl isotherms (°C) and several faults. Zones of upflow, outflow and inflow of cool meteoric water are highlighted. After Amistoso et al. (1993).

Reservoir Chemistry

Major Element Chemistry

The chemistry of the pre-exploitation reservoir at Palinpinon has been presented and discussed in an unpublished PNOC-EDC report by Jordan (1983). Very little published data is available, but brief descriptions are provided by Amistoso et al. (1993), D'Amore et al. (1993) and Gerardo et al. (1993). Analyses from Jordan (1983) are reproduced in Table 1.3 and the following section summarises the results of his work.

Generally, geothermal production waters from Palinpinon are similar throughout the reservoir. At 20°C, they are typically neutral to slightly alkaline chloride waters with significant alkali metals, boron and silica. Evidence for a common reservoir for both Puhagan and Nasuji-Sogongon production sectors comes from the consistency of Cl/B ratios (21-31; Jordan, 1983). This is despite gross lithologic differences between the two sectors. Only the Nasuji-Sogongon wells NJ1D, NJ2D and OK11D (Figure 1.17) have distinct chemical compositions, for which chemical data were not presented by Jordan (1983). Water tapped from these wells are acidic under atmospheric conditions and characterised by high H_2S and SO_4 concentrations. These wells are less than 500 m from well OK6, which discharges neutral chloride waters. The different chemical compositions between adjacent wells led Jordan (1983) to conclude that fluid flow in the Palinpinon reservoir occurs largely along faults and fractures.

The chemistry of individual feed zones in the Palinpinon wells is difficult to define. However the results of discharge tests show that the fluid at shallow zones (i.e., 500-1000 m bsl) is generally more dilute and richer in gas than the deeper zones. Exceptions are wells PN26 and OK10D, where more saline and less gas-rich waters are produced from shallow zones.

The chloride-enthalpy plot from Jordan (1983) is presented in Figure 1.18 and shows water from PN26 to be the most saline. A boiling trend is defined by the line connecting PN26 with the enthalpy for pure steam (2799 kJ/kg). The parent reservoir fluid composition is represented by the intersection of the mixing and boiling lines (Figure 1.18). This yields a reservoir chloride concentration of 4150 mg/kg and a temperature of 328°C (Figure 1.18, Jordan, 1983), and compares favourably with the maximum measured temperature of 329°C in well PN20D.

Table 1.3. Chemistry of initial discharge water samples from selected geothermal wells. Data from Jordan (1983). W.H.P. & S.P. refer to wellhead pressure and sample pressure, respectively.

Well	Date	Enthalpy	W.H.P.	S.P.	pH	Li	Na	K	Rb	Cs	Ca	Mg	Cl	SO_4	B	SiO_2	CO_2T	H_2S	NH_3	Cl/B	Ion Balance
		(kJ/kg)	(bars atmos)		(T=20°C)	(mg/kg)															(% difference)
OK5	18-Dec-82	1772	28.9	1.0	7.73	16.10	3221	763	5.24	3.55	31.2	0.03	6037	47.2	77.1	1022	34.3	11.20	2.80	23.9	-2.3
OK6	8-Jan-82	1129	24.9	1.0	7 76	13.80	2839	576	3.62	2.63	29.8	0.07	5057	32.7	50.8	850	32.4	0.89	3.82	30.4	-0.5
OK7	19-Nov-82	1410	29.0	7.6	6.50	14.30	3213	789	4.41	2.97	69.4	0.12	5790	20.0	71.6	875	46.60	6.39	7 60	24.7	0.6
OK8	28-Apr-82	1285	8.2	1.0	8.00	14.40	2764	646	4.24	2.87	34.5	0.05	5319	48.8	68.6	974	8.8	2.56	-	23.6	-3.6
OK9D	21-Feb-81	1223	13.9	1.0	7 90	17.50	3532	767	4.27	3.56	100.0	0 26	6364	44.2	76.8	975	7.48	-	-	25.3	0.1
OK10D	20-May-81	1207	15.4	1.0	7.42	15.10	3342	687	4.08	3.49	129.0	0.94	6311	-	75.1	829	11.1	-	-	25.6	-1.8
OK12D	12-Sep-81	1089	15.5	10.9	6.70	10.70	2352	527	2 53	2.10	76.0	0.36	4361	32.0	49.2	532	59.8	62.60	-	27 0	-1.0
PN13D	20-Jan-82	1179	7.7	1.0	7.75	18.10	3578	707	3 87	3.04	81.9	0.53	6418	53.8	81.7	852	22 4	19.10	-	24 0	-0.4
PN14	24-Sep-82	1341	24 3	5.6	6.85	14.70	3160	858	4.41	2.80	59.2	0.06	6009	10.6	69.1	909	22.0	1.97	9.12	26.5	-1.5
PN15D	29-Mar-82	1190	11 6	1.0	7.10	11.40	2977	467	2.62	2 11	66.7	0.21	5035	46 0	50.4	683	86.0	2.56	16.00	30.5	1.2
PN16D	22-Oct-82	1309	28.4	1.0	7.60	15.40	3557	739	4.08	3.03	52.5	0.36	6035	18.0	74.5	1120	19.3	2.04	5.00	24.2	2 3
PN17D	16-Feb-82	1078	6.1	3.9	5.75	8.95	2671	453	2 65	2.30	73.3	0.41	4731	31.9	57 3	547	58.7	9.46	9.17	27.9	-0.5
PN19D	21-Oct-82	1196	8.7	7.3	7.00	12.10	3102	682	3.88	2.93	69.7	0.21	5495	26.9	65 9	693	11.9	2.70	7.10	25.4	0.7
PN20D	16-Dec-82	1375	32.5	32.3	5.68	11.20	2267	567	3.47	2.39	43.2	0.14	4246	25 7	52 7	710	132	13 60	7.90	24.2	-1.4
PN21D	5-Oct-82	1016	8.5	0.9	7.87	12.70	3427	514	2.91	2.92	117.0	0.84	5807	60 7	66.1	639	7.92	3 03	36.00	26.8	1.5
PN22D	12-Nov-82	1178	21.7	2.8	5.85	13.80	3000	676	3.80	2.75	74.4	0.22	5727	26.2	67 8	767	109	4 09	5.85	27.8	-2.7
PN24D	21-Dec-82	1322	18.5	17.9	5.00	11.80	2370	637	3.80	2 51	30.6	0.08	4668	27.0	57.1	822	94.2	12.90	6.00	24.9	-3.7
PN26	28-Dec-82	1167	27.5	5.8	6.95	15 40	3513	794	4.52	3.40	116.0	0.12	6704	28.7	78.5	743	38.3	4 77	6 10	26.1	-2.3
SG1	19-Nov-81	1126	10 8	1.0	7.74	12.20	2696	523	3 49	2.50	40.0	0.08	4765	30 8	59 3	737	40.9	0 94	-	24.5	-0.2
SG2	6-Jan-82	1197	26.5	1.0	7.71	12.30	2643	576	3.52	2.46	34.7	0.07	4893	38.4	60.3	807	9.5	4 94	-	24.8	-2.0

Wells with the highest aquifer chloride concentrations (4239-4922 mg/kg Cl^-; Jordan, 1983), which reflect boiling and/or evaporation processes in the reservoir, are located in the central Puhagan area (PN26, OK7, PN14, PN22D and PN19D; Figures 1.17 and 1.18). Waters with similar salinities but lower enthalpies than the parent fluid (e.g., PN13D, OK10D, PN15D) may have conductively cooled or alternatively, their compositions may be derived by a combination of mixing and boiling (Figure 1.18). The remaining well waters are less saline than the parent fluid and their compositions are predominantly influenced by mixing, along with less dominant processes of boiling and conductive cooling. It is apparent from Figure 1.18 that the Nasuji-Sogongon waters (OK6, OK8, SG1 and SG2) are more dilute than those from Puhagan. Because only a few wells define the high chloride zone, it is likely that boiling is occurring in only localised parts of the reservoir (e.g., along faults).

In summary, work by Jordan (1983) showed that the Palinpinon geothermal wells draw fluid from a single, common reservoir with an upflow zone beneath the Puhagan area and a composition of approximately 4150 mg/kg Cl^- and a temperature of 330°C. Boiling, mixing and conductive cooling all appear to be influences on the aquifer chemistries. Wells located in the central Puhagan area discharge water closest to the parent fluid composition, with some Nasuji-Sogongon wells having more dilute compositions. Distinct chemical differences between closely spaced wells and the constriction of the isotherms towards the northeast are consistent with the interpretation that faults are zones of boiling and high permeability.

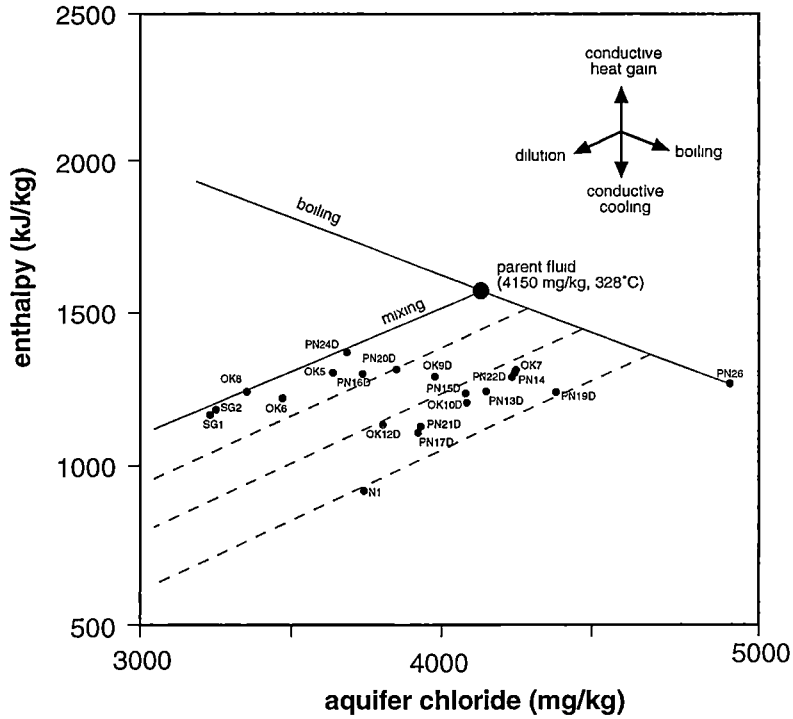

Figure 1.18. Chloride vs. enthalpy plot of Palinpinon geothermal well waters showing possible mixing and boiling trends, and a postulated parent fluid composition, as inferred by Jordan (1983).

Oxygen and Hydrogen Isotope Chemistry

Oxygen and hydrogen isotope compositions of Palinpinon geothermal and local meteoric waters were analysed by Gerardo et al. (1993). Their data for pre-exploitation conditions are reproduced in Table 1.4.

The geothermal waters have $\delta^{18}O$ values ranging from -6.8 to -3.6‰ and δD values ranging between -51 and -41‰. When presented on a $\delta^{18}O$ vs. δD diagram, the geothermal water data defines a linear trend (Figure 1.19) that Gerardo et al. (1993) attributed to mixing between Southern Negros meteoric water and an isotopically heavier water. They proposed that this heavier end-member water is compositionally similar to the magmatic water associated with andesitic volcanism, as described by Giggenbach (1992; i.e., $\delta^{18}O = +10 \pm 2$; $\delta D = -20 \pm 10$). The intersection of the mixing line with the meteoric water line defines an end-member meteoric water with a $\delta^{18}O$ value of -8.5‰ and a δD value of -54‰, corresponding to an average recharge altitude of 1000 m above sea level (Gerardo et al., 1993). Figure 1.19 illustrates that waters from the Puhagan wells generally plot further from the meteoric water line ($\delta D = 8\delta^{18}O + 14$) than the more dilute Nasuji-Sogongon waters. That is, the Puhagan waters are isotopically heavier than the Nasuji-Sogongon waters and may have a greater magmatic input. The Puhagan waters possibly contain 12-25% andesitic water, whereas at Nasuji-Sogongon it is less (10-15%, Gerardo et al., 1993).

Three alternative explanations for the isotopic composition of the Palinpinon geothermal waters exist. Firstly, they may be influenced by wallrock compositions, with the shift to higher $\delta^{18}O$ values for the Puhagan waters related to isotopic exchange with igneous wallrocks during meteoric convection. Secondly, the isotopic differences may relate to different wallrock lithologies in the two sectors. The Puhagan lithology comprises andesitic volcanic rock types and a calcareous sedimentary formation (Okoy Formation), whereas the Nasuji-Sogongon lithology consists of andesitic and dioritic igneous rock types. Thirdly, the data may reflect isotopic exchange with two isotopically distinct meteoric waters. The Puhagan waters may be influenced by interaction with isotopically heavier meteoric water (i.e., ~-7.5‰ $\delta^{18}O$, ~-40‰ δD), and Nasuji-Sogongon waters by interaction with isotopically lighter meteoric water (i.e., ~-8.0‰ $\delta^{18}O$, ~-50‰ δD). Any future isotope work undertaken at Palinpinon needs to address the influence, if any, of wallrock and meteoric water composition on the isotopic composition of the geothermal waters.

Table 1.4. a) Reservoir isotope data; **b)** Meteoric water isotope data. From Gerardo et al. (1993)

a) Well	Date	$\delta^{18}O_{td}$	δD_{td}	$\delta^{18}O_{td\ ave}$	$\delta H_{td\ ave}$
		(‰)			
PN14	5/10/82	-3.6	-45	-3.7	-44.0
		-3.7	-43		
PN17D	12/1/83	-6.0	-48	-6.0	-48.0
PN18D	11/3/83	-4.5	-44	-4.6	-43.5
	15/3/83	-4.6	-43		
PN19D	3/10/82	-4.1	-43	-4.2	-43.5
	13/10/82	-4.0	-43		
	21/10/82	-4.2	-43		
	22/9/83	-4.4	-45		
PN20D	19/1/83	-4.3	-49	-4.5	-47.5
	28/9/83	-4.7	-46		
PN21D	28/8/82	-4 6	-44	-4.4	-42.3
	31/8/82	-4.3	-41		
	8/9/83	-4.4	-42		
PN22D	24/11/81	-4.8	-46	-4.8	-46.0
	20/11/83	-4.7	-46		
PN23D	9/3/83	-5.0	-46	-5.0	-46.0
PN24D	24/12/82	-4.4	-43	-4.5	-42.0
	29/12/82	-4.5	-41		
	4/1/83	-4.5	-42		
PN26	28/12/82	-3.9	-42	-3.9	-42.0
PN27D	3/9/83	-5.3	-49	-5.3	-49 0
PN30D	11/10/83	-4.4	-46	-4.4	-46.0
OK10D	23/9/83	-4.7	-44	-4.7	-44.0
OK6	8/1/82	-6.7	-50	-6.4	-49.5
	12/3/83	-6.0	-49		
OK8	15/1/82	-6.8	-51	-6.8	-51.0
SG1D	26/12/82	-5.6	-45	-5.6	-45.0
SG3D	21/4/83	-6.4	-48	-6.4	-48.0
NJ1D	7/11/83	-5.9	-47	-5.9	-47.0
NJ3D	10/8/83	-5.9	-48	-5.9	-48.0
NJ4D	10/8/83	-5.7	-47	-5.7	-47.0

b) Source (above sea level)	Date	$\delta^{18}O$	δD
		(‰)	
Creeks			
Sogongon River	1-Apr-90	-7.7	-46
Puhagan River (900m)	1-Apr-90	-7 3	-42
Ticala Creek (450m)	18-May-90	-7.3	-43
Okoy River	1-Apr-90	-7.1	-44
Pulangtubig Creek (1000m)	10-Jun-91	-7.0	-44
Kagolkol Gamay Creek (950m)	10-Jun-91	-7.8	-47
Lagunao Right Creek (900m)	10-Jun-91	-7.2	-44
Springs			
Cantieso coldspring (500m)	10-Jun-91	-7.7	-49
Lagunao coldspring (1000m)	7-Jun-91	-8.1	-49
Halasan coldspring (450m)	2-Aug-91	-7.6	-47
Casiroro coldspring (700m)	2-Aug-91	-7 3	-47
Groundwater Wells			
Camanjac <55m depth (50m)	13-Aug-91	-7.0	-44
Rotary5 <55m depth (10m)	13-Aug-91	-7.4	-47
Okoy Bridge <55m depth (20m)	13-Aug-91	-7.1	-42
Talay Bliss 142m depth (80m)	13-Aug-91	-7.6	-45
Palinpinon water supply	13-Aug-91	-7.5	-41
Rainwater			
Ticala	July-Sept. 91	-7.3	-48
Puhagan	July-Sept. 91	-7.7	-52
Balas-Balas	July-Sept. 91	-8.4	-56
Nasuji	July-Sept. 91	-8.6	-56

td : total discharge composition
td ave : average total discharge composition

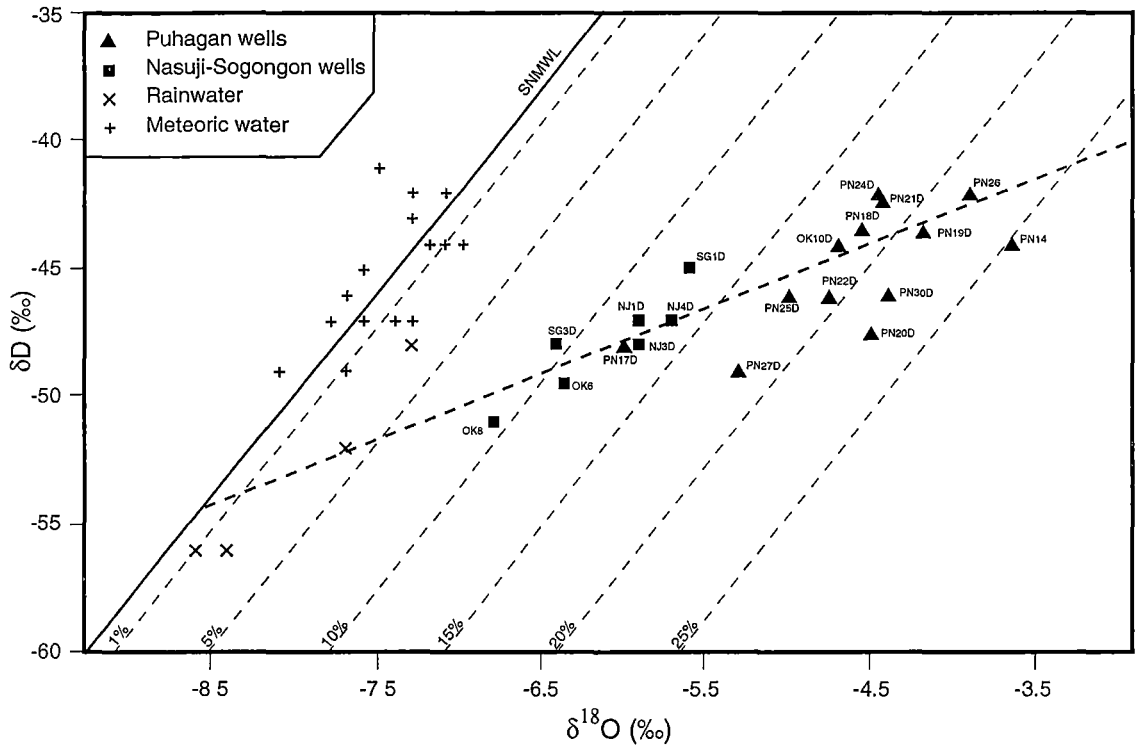

Figure 1.19. Stable isotope compositions of Palinpinon well waters, shallow and cold groundwater and rain water (from Gerardo et al., 1993). The line through the Palinpinon geothermal waters is defined by the relationship $\delta D=2.55\delta^{18}O-32.5$. The Southern Negros Meteoric Water Line (SNMWL) is defined by the equation $\delta D=8\delta^{18}O+14$. Dashed lines parallel to the SNMWL indicate the possible percent contribution of magmatic waters to Palinpinon geothermal waters.

Table 1.5. Gas chemistry in total discharge and mole % for selected wells. Data from Jordan (1983).

Well	Date	W.H.P.	Hmeas.	CO_2	H_2S	NH_3	R	CO_2	H_2S	NH_3	R	CO_2/H_2S
		(bars at.)	(kJ/kg)	mmol/100mol total discharge				(mol. %)				
NJ1D	24/4/82	2.2	1195	103	24.0	1 15	2.37	78.9	18.4	0.88	1.82	4 3
NJ2D	2/12/82	3.9	1243	124	93.0	0 04	5.87	55.6	41 7	0.02	2.63	1.3
OK5	9/10/82	28.7	1752	216	9.1	0.91	9.54	91.7	3.9	0.39	4.05	23.7
OK6	17/10/82	25.3	1282	143	2.2	0.70	1.88	96 8	1.5	0.47	1.27	65 9
OK7	16/6/82	32.4	1441	330	8.3	1.29	5.31	95.7	2.4	0.37	1.54	40 0
OK8	14/4/82	8.1	1286	130	2.8	-	1.55	96.7	2.1	-	1.15	46.1
PN13D	17/6/82	17.4	1210	286	9.2	-	4.13	95.6	3.1	-	1.38	31 2
PN14	24/9/82	24.3	1341	655	9.6	1.30	6.52	97.4	1.4	0.19	0.97	68.3
PN15D	29/3/82	11.6	1190	223	2.8	2.02	4.73	95.9	1.2	0.87	2.03	81.1
PN16D	25/10/82	29.1	1336	336	9.3	1.18	8.13	94.8	2.6	0.33	2.29	36 2
PN17D	28/1/82	13.4	1067	315	3.4	-	5 78	97.2	1.1	-	1.78	92.1
PN19D	16/10/82	18.4	1070	56.4	1 3	0 53	0.61	95.9	2.2	0.90	1.04	44.1
PN20D	11/1/83	35.9	1411	334	14.0	0.71	4.44	94.6	4.0	0.20	1.26	23 9
PN21D	2/11/82	12.7	977	82.2	2.3	0.79	1.72	94.5	2.6	0.91	1.98	36.2
PN22D	20/11/82	23.4	1170	147	5.3	0.57	1.20	95 4	3.4	0.37	0.78	27.8
PN24D	21/12/82	18.8	1377	252	7.0	0.74	11 30	93.0	2.6	0.27	4.17	36.0
PN26	28/12/82	27.5	1167	113	3.9	1.04	5.96	91.2	3.1	0 84	4.81	29.1
SG1	14/12/81	14.9	1129	85	1.7	0.58	1.39	95.8	1.9	0.65	1.57	49.4
SG2	22/1/82	10.4	1271	102	1.7	0 32	2.81	95.5	1.6	0.30	2.63	61.4

R . residual gases (includes H_2, N_2, CH_4)
W.H.P. : Well Head Pressure in bars atmosphere (bars at.)
Hmeas. : measured enthalpy

Gas Chemistry

Palinpinon gas chemistry data, in total discharge concentrations and mole % (Table 1.5), shows that CO_2 is the dominant gas component, making up 94-98% of the non-condensable gases in the steam phase from most wells. The remainder are H_2S, NH_3 and residual gases (including H_2, N_2 and CH_4; Jordan, 1983). The discharge gas compositions from all Palinpinon wells are similar throughout, with the only exceptions from the southern Nasuji wells, NJ1D and NJ2D. These wells have much higher H_2S components of 18 and 42 mole %, respectively (Table 1.5).

With the exception of wells NJ1D and NJ2D, Jordan (1983) noted that the lowest CO_2/H_2S ratios are found in wells south of Puhagan in the upflow region. As H_2S has a higher solubility in the boiling liquid than CO_2 (Giggenbach, 1980), this trend may indicate that fluids peripheral to the upflow zone have undergone more boiling (Hedenquist, 1990). Alternatively, Jordan (1983) explained it as being possibly due to the preferential removal of H_2S from fluids as a response to longer migration times and water-rock interaction.

Summary and Discussion

Based on this review and reinterpretation of previous work (Glover, 1975; Jordan, 1983; Amistoso et al., 1993), a schematic diagram illustrating important aspects of the Palinpinon hydrology is presented in Figure 1.20. As discussed by Henley and Ellis (1983), with geothermal systems located in areas of steep terrain, topography is the dominant influence on spring water chemistry and the location of spring water types relative to the zone of hydrothermal upflow. This is the case at Palinpinon. Neutral chloride spring waters occur at

the lowest elevation of distances up to 10 km east of the upflow region. Steam-heated sulphate and bicarbonate spring waters occur in the western part of the field at higher elevation.

The hydrological structure of the reservoir is apparently grossly influenced by fault structures (Amistoso et al., 1993). Upflowing neutral chloride water uses zones of permeability associated with the northwest-trending Lagunao Fault in the area south of Puhagan. The main outflow zone beneath the Okoy River is localised along permeable zones associated with the northeast-trending Ticala and Puhagan Faults.

In the upflow zone, as hydrostatic pressure decreases, the single phase liquid reservoir undergoes boiling. This causes dissolved gases (mainly CO_2 and H_2S) and steam to separate and permeate the overlying rock. Due to the high relief, it is probable that boiling zones are mainly restricted to localised zones, such as permeable faults, where pressure decreases can facilitate upflow and phase separation. Oxidation of separated H_2S gas to SO_4^{2-} and steam condensation results in the formation of perched, steam-heated sulphate aquifers (Figure 1.20). Initially these aquifers will have an acidic pH, but with ongoing wall-rock interaction they are neutralised by hydrolysis reactions and discharge as neutral pH springs in the Lagunao and Malaunay areas (Figure 1.20; Glover, 1975). Some of these aquifers must be saturated with respect to dissolved H_2S and CO_2 for these gases to permeate through and vent at the surface in the kaipohan areas (Figure 1.20).

Subsurface water flow becomes topography driven as it cools and moves away from the region of hydrological upflow (Figure 1.20). Condensation of CO_2 into the outflowing water produces bicarbonate-rich waters that discharge at springs in the Ticala area (Figure 1.20). With decreasing elevation towards the northeast, the outflowing neutral chloride reservoir draws progressively closer to the surface, resulting in steam and gases venting at surface in the Magaso and Pulangbato areas. Oxidised, steam-heated sulphate springs in the Ilijan area retain their acidicity due to insufficient wall-rock interaction to the point of discharge (Glover, 1975). After modification by boiling and mixing with shallow-derived waters and/or cooling, the easterly flowing neutral chloride reservoir waters discharge at low elevations, east of Magaso in the Cambucal and Palinpinon areas (Figure 1.20).

Production wells at Palinpinon intersect multiple zones of permeability and discharge two phase fluids from a liquid dominated reservoir. The waters have a uniform composition across the field and are classified as neutral to alkaline chloride waters. Mixing and boiling models intimate that the upflowing waters are sourced from a single "parent" reservoir fluid with approximately 4000 mg/kg Cl^- and a temperature of 328°C (Jordan, 1983). The central Puhagan wells discharge water closest to this composition with divergences brought about by combinations of boiling and mixing, and/or conductive cooling (Jordan, 1983). In the western Nasuji-Sogongon area geothermal waters are generally more dilute and have compositions mainly influenced by mixing. Faults are the major zones of permeability and boiling.

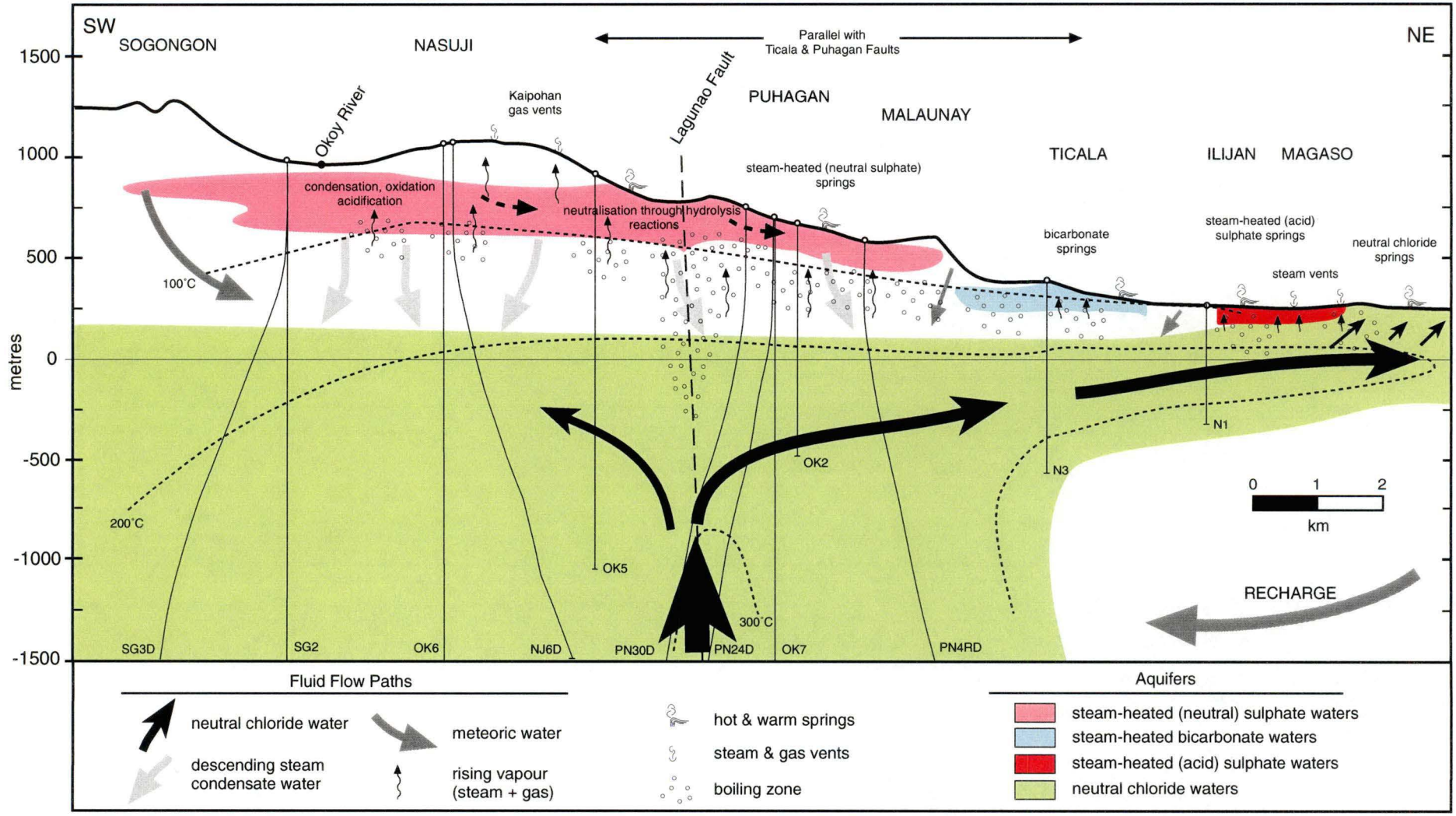

Figure 1.20. Hypothetical hydrological cross-section through the Palinpinon geothermal field showing fluid flow paths for neutral chloride, meteoric and steam-heated condensate waters. The diagram shows the relationship between the deep hydrology and surface discharges. Downflowing meteoric waters and those derived from shallow steam-heated aquifers dilute the upwelling waters. Due to the high relief, boiling zones may be localised and restricted to faults.

2. THE NATURE OF MAGMATISM AND ITS IMPLICATION FOR GEOTHERMAL ACTIVITY AND REGIONAL TECTONICS

2.1. INTRODUCTION

High temperature geothermal systems occur in areas where convective circulation leads to anomalously high geothermal gradients (i.e., > 30°C/km). They are defined by rock temperatures greater than 225°C at approximately 1 km depth and their heat source is typically a magmatic body (Hochstein and Browne, 2000). The size, geometry, depth of emplacement and composition of the magma(s), influence the development and sustainability of the hydrothermal system.

This section of the thesis documents the history of magmatism and volcanism at Palinpinon, to assess possible genetic relationships between intrusion and geothermal circulation. Geochemical and petrological analyses of the igneous rocks are used to discuss the petrogenetic evolution of magmatism in the district. The temporal and spatial relationships between subvolcanic intrusions and the active geothermal system at Palinpinon presented here provide the framework for later papers that document the water chemistry, hydrothermal alteration and mineralisation within the geothermal system. To gain a better understanding of the spatial relationships between the various rock types, structure and the hydrology, the reader is referred to the 3D Datamine images, hyperlinked in the Powerpoint file (Palinpinon.ppt) in Appendix 4.

2.2. STRATIGRAPHY

The geology of the Palinpinon geothermal field, along with some whole rock geochemistry, has been documented previously by Philippine National Oil Company - Energy Development Corporation (PNOC-EDC) scientists and consultants in unpublished company reports and files (Castro et al., 1979; Seastres, 1982; Wood, 1982; Pornuevo, 1984). Brief stratigraphic descriptions have been published in Leach and Bogie (1982) and Mitchell and Leach (1991). Absolute and relative ages (K-Ar radiometric and palaeontologic) were presented in an unpublished company report by Zaide (1984), and Sajona et al. (2000a) presented K-Ar whole rock dates for seven surface volcanic samples from Cuernos de Negros.

The surface geology (Figure 2.1) is dominated by Pleistocene volcanic units (Pornuevo, 1984). There are at least four recognised eruptive centres in the area: Mt. Guinsayawan, Guintabon Dome, Cuernos de Negros and Mt. Talines. South of the Okoy River, volcanic units sourced from Cuernos de Negros are exposed, together with the underlying Late Pliocene volcanic rocks (Southern Negros Formation), which crop out along some valley floors (Figure 2.1, Pornuevo, 1984).

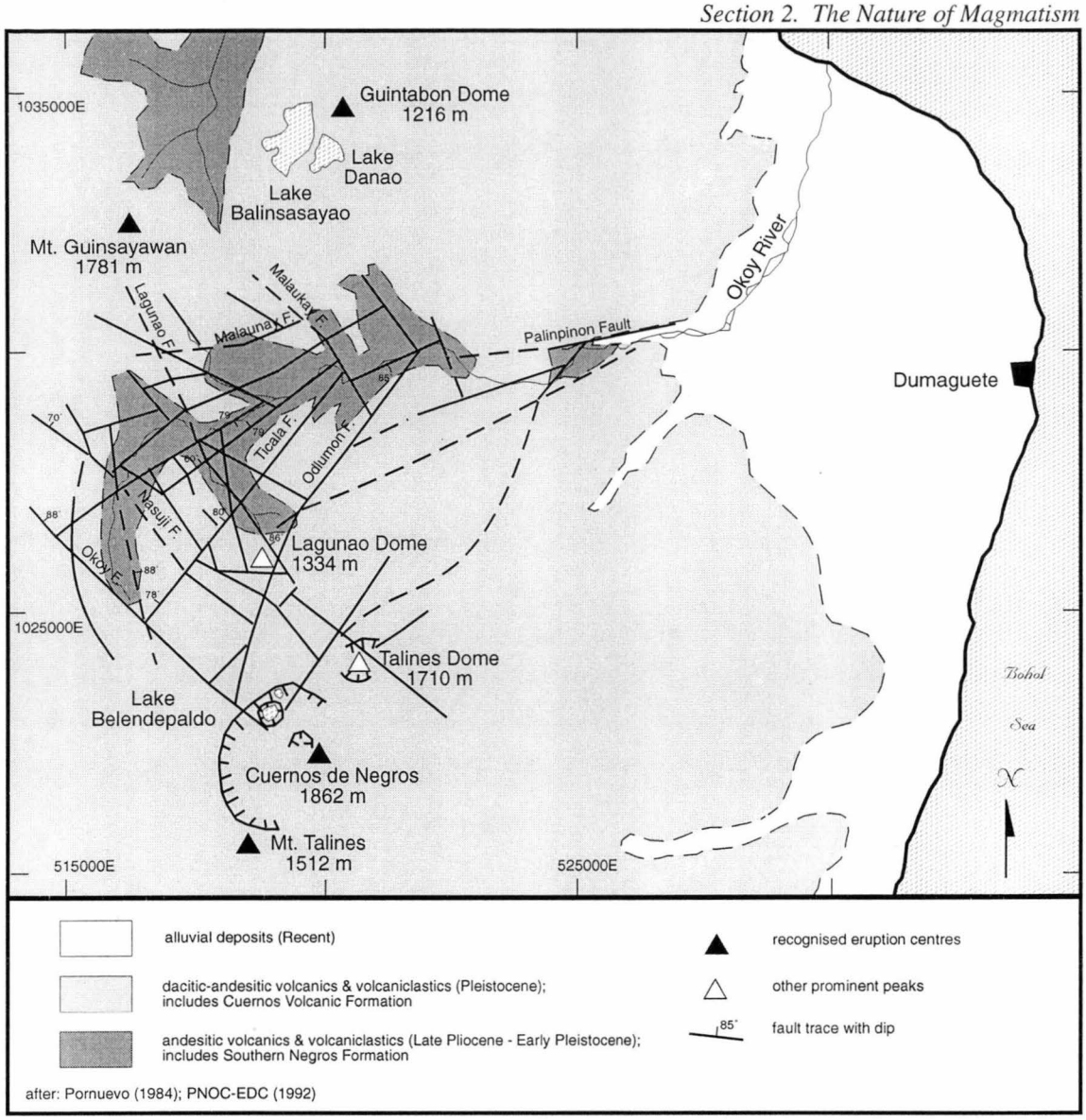

Figure 2.1. Surface geology and fault traces in the Palinpinon geothermal field. After Pornuevo (1984) and PNOC-EDC (1992).

A complex fault array in the Palinpinon area (Figure 2.1) is the dominant influence on the drainage pattern of the Okoy Valley (PNOC-EDC, 1992). Steeply-dipping (> 60°) normal faults have NE- and NW-trends (Bromley et al., 1987). This fault array may have been affected by a pluton situated between 1000-1500 m depth in the western field area (Nasuji Pluton). Important faults in terms of their influences on the hydrology are the Lagunao, Ticala, Puhagan and Nasuwa Faults (Figure 2.2).

A revision of the stratigraphy as originally proposed by Mitchell and Leach (1991; Figure 1.6), in particular the location of the dikes beneath the Puhagan area (henceforth referred to as the Puhagan dikes), is illustrated in Figures 2.2 and 2.3 (see also Appendix 4). The revised section is based on detailed petrographic examination of 170 drillcores from 56 geothermal wells, augmented with petrographic descriptions of drillcuttings from 62 unpublished PNOC-EDC geothermal well logs. No lithologic contacts have been observed in any of the drillcores examined in this study.

The Lower Puhagan Volcanic Formation has been intersected at depth beneath the Puhagan area (Figure 2.3) and is at least 780-900 m thick. Geothermal wells do not penetrate the underlying strata. This sequence of volcaniclastic breccias, microbreccias and volcanogenic sedimentary rocks is possibly of Middle Miocene age (Zaide, 1984). The contact between the Lower Puhagan Volcanic Formation and the overlying Okoy Formation is between 1400 m and 2000 m bsl (Figure 2.3).

The Okoy Formation, more than 1000 m thick (Figure 2.3), is a sequence of well to poorly bedded fossiliferous and calcareous siltstones, sandstones and limestones and sedimentary breccias. Microfossil assemblages suggest a bathyal environment of deposition and a Late Miocene to Middle Pliocene age (Zaide, 1984).

The Southern Negros Formation is the most widely distributed rock formation at Palinpinon and has been intersected by all geothermal wells. It occurs between the underlying Okoy Formation and the overlying Cuernos Volcanic Formation and is 1500-2000 m thick (Figure 2.3). The Southern Negros Formation is a sequence of hornblende andesites and andesitic breccias/volcaniclastics. Intense hydrothermal alteration has prevented accurate radiometric age determinations of this formation, but field relationships suggest an age of Late Pliocene to Early Pleistocene. At the surface, rocks of the Southern Negros Formation crop out along the Okoy Valley (Figure 2.1) where it has been described by Wood (1982) as a sequence of poorly sorted volcaniclastic conglomerates with interbedded sandstones and siltstones. A paleosol layer reported by Seastres (1982), cropping out along the lower Okoy River, may be the contact between the Southern Negros Formation and the overlying Cuernos Volcanic Formation. A paleosol in a similar stratigraphic position was also identified in some geothermal wells (e.g. PN26, Hermoso, 1983; PN16D, Fragata, 1983a; PN18D, Fragata, 1983b).

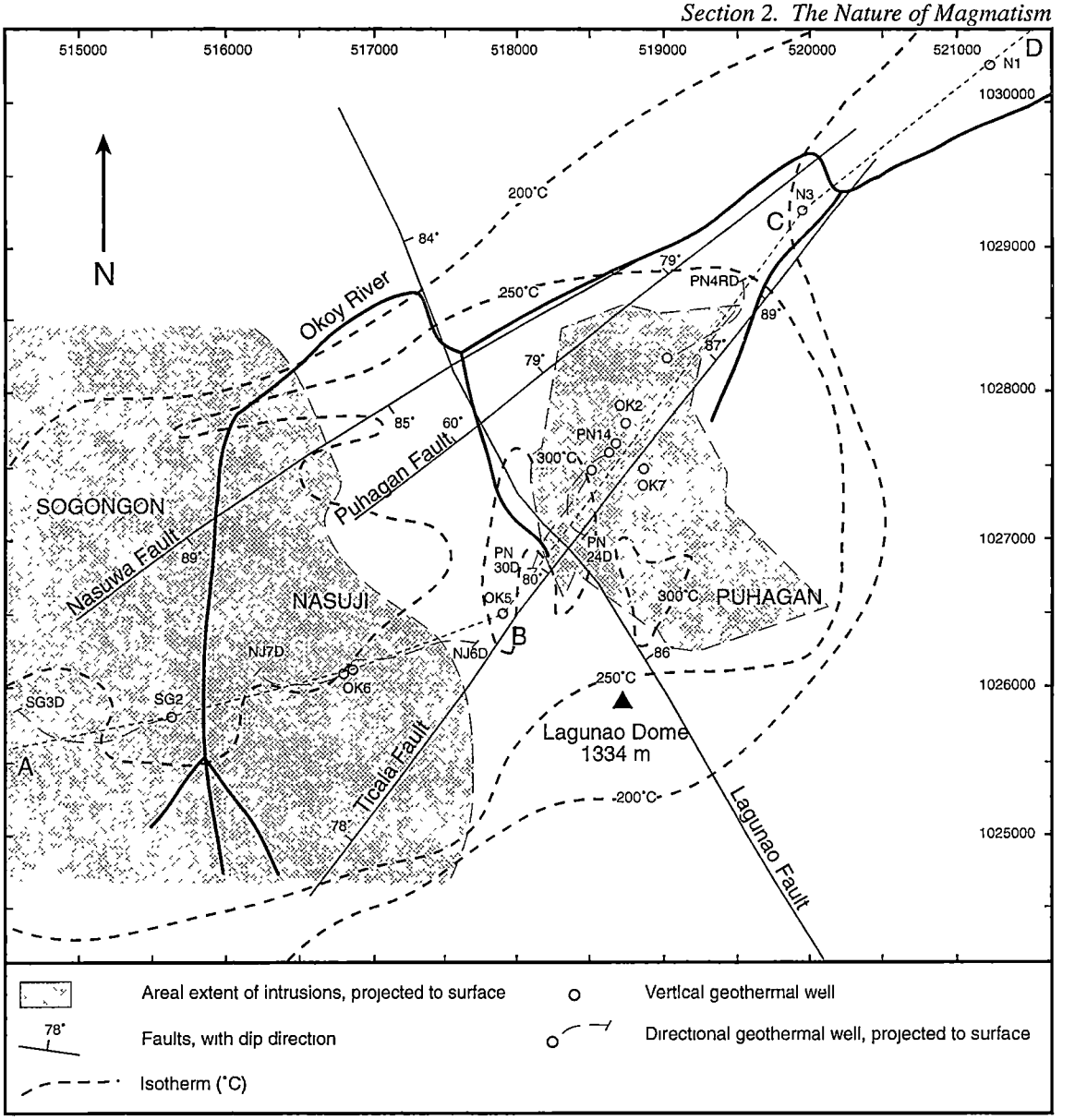

Figure 2.2. Plan view of the Palinpinon geothermal field showing the areal extent of the intrusions (western Nasuji Pluton; eastern Puhagan dikes), the distribution of major faults, the distribution of isotherms at 1500 m bsl and the location of geothermal wells used to draw the cross-section (along line A-B-C-D) shown in Figure 2.3.

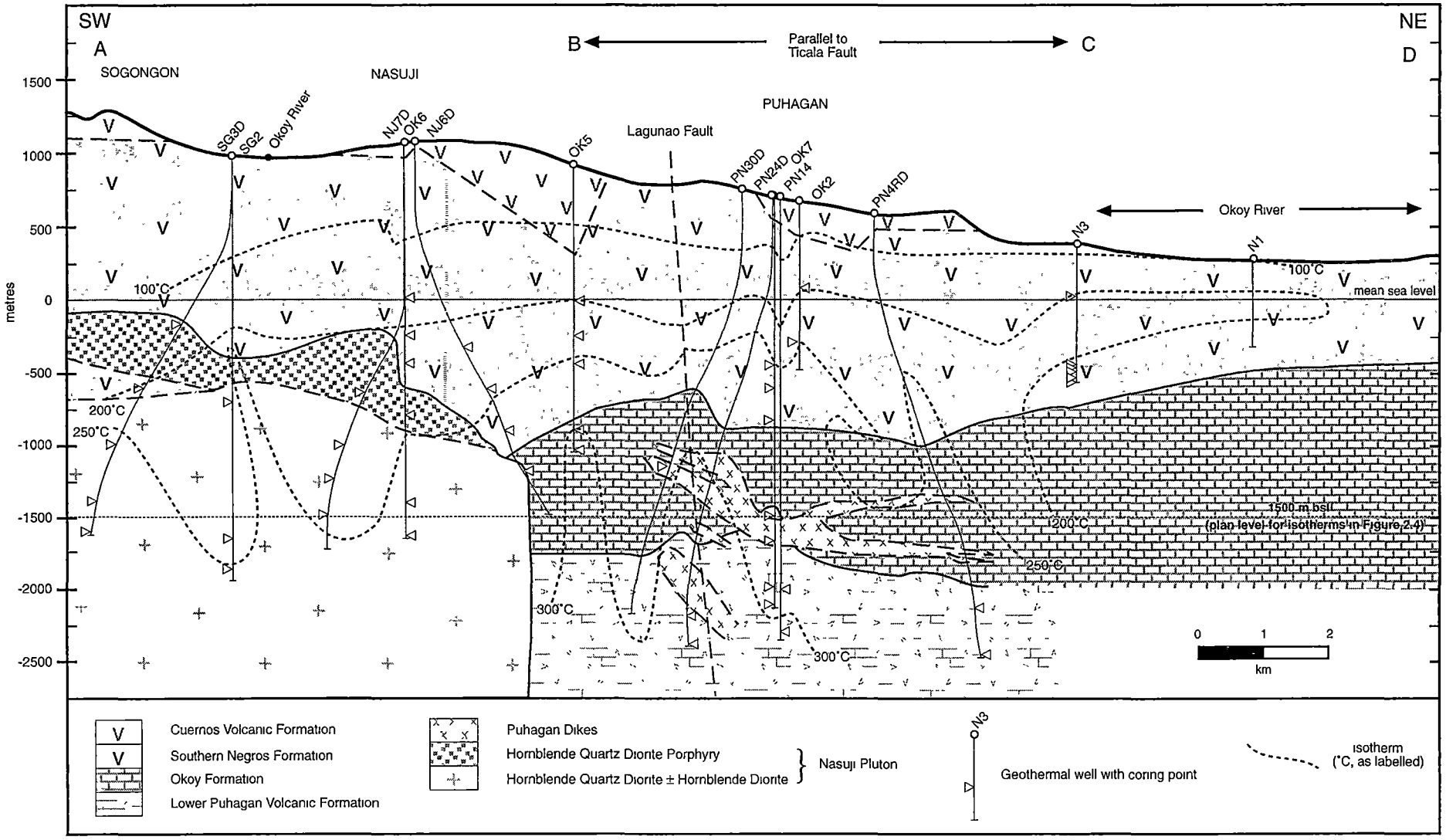

Figure 2.3. Geological cross-section through the Palinpinon geothermal field, along line A-B-C-D in Figure 2.2, showing the distribution of isotherms in the hydrothermal system.

Volcanic and sedimentary rocks in the western geothermal field have been intruded by the Nasuji Pluton (Figure 2.3). Above the pluton, the Southern Negros Formation has been contact metamorphosed. At its shallowest, the Nasuji Pluton lies between 1000 and 1500 m below ground surface at approximately 60 m bsl (Figure 2.3). Geothermal wells encountered up to 1500 m of intrusive rocks and none intersected its base. Only the eastern margin of the intrusion has been defined by drilling. A negative aeromagnetic anomaly with an E-W elongation in the western part of the geothermal field has been modelled by Bromley et al. (1984) as a manifestation of the Nasuji Pluton. It suggests that the intrusion extends approximately 10 km further west of the drilled regions, but no more than a few hundred metres beyond drilled depths to the north and south.

The Nasuji Pluton consists of equigranular hornblende diorite and equigranular and porphyritic hornblende quartz diorite. The most abundant rock type is an equigranular hornblende quartz diorite, which comprises most of the pluton. The porphyritic hornblende quartz diorite occurs at the top of the Nasuji Pluton, apparently above, and in direct contact with the underlying equigranular hornblende quartz diorite (Figure 2.3). To the southwest, the porphyritic diorite occurs as a dike that has intruded Southern Negros Formation. Geochemical analyses from the Nasuji Pluton are presented in Section 2.7.

Radiometric K-Ar ages of separated hornblendes from the Nasuji Pluton range from 10.5 Ma to 5.6 Ma (Zaide, 1984). However, these dates are discrepant with field relationships, because contact metamorphism and hydrothermal alteration of Southern Negros Formation rocks imply that the intrusion is no older than Late Pliocene. New $^{40}Ar/^{39}Ar$ hornblende age determinations of this unit have been undertaken as part of the current study and are discussed in Section 2.5.

East of the Nasuji Pluton, the Puhagan dikes have intruded the upper portions of the Lower Puhagan Volcanic Formation and the lower Okoy Formation, between 940 m and 2330 m bsl (Figure 2.3). Their proximity to the intersection of the NW-trending Lagunao Fault and NE-trending Ticala Fault (Figure 2.2) suggests that these faults may have localised the sites of intrusion. Close to the fault intersection the dikes extend to greater depths and are relatively steeply dipping, whereas away from the intersection they are sills, subparallel with stratigraphy (Figure 2.3). This dike-sill complex could either represent lateral extensions, peripheral to the larger Nasuji intrusion, or separate unrelated intrusions. The relationship between the Puhagan dikes and the Nasuji Pluton is discussed in Section 2.5.

The youngest formations on southern Negros Island are volcanic rocks erupted from the four eruptive centres (Figure 2.1, Pornuevo, 1984). In the Okoy Valley, where the geothermal wells are located, the youngest volcanic rocks were erupted from Cuernos de Negros (Cuernos Volcanic Formation). The Cuernos Volcanic Formation has a variable thickness with a maximum of 620 m intersected in well OK5 (Seastres, 1985; Figure 2.3). Previous PNOC-EDC workers (Castro et al., 1979; Seastres, 1982) described the Cuernos Volcanic Formation as

comprising a lower andesite (K-Ar: 870 000 yr. BP, Zaide, 1984), a middle dacite (C^{14}: 14 000 yr. BP, Zaide, 1984) and an upper andesite unit of unknown age (< 14 000 yr. BP). Older K-Ar whole rock ages were reported by Sajona et al. (2000a), ranging between 1.97±0.05 Ma and 0.31±0.08 Ma. However, no sample descriptions and locations were provided and it is possible that the oldest rocks dated by Sajona et al. (2000a) belong to the Southern Negros Formation.

The lower andesite of the Cuernos Volcanic Formation rests unconformably on the Southern Negros Formation and is estimated to be 200 m thick (Castro et al., 1979). It is an aphanitic to porphyritic andesite with phenocrysts of pyroxene, hornblende and plagioclase (labradorite) in a hypocrystalline groundmass with subparallel feldspar microlites (Castro et al., 1979). This andesite is overlain by dacitic flows and breccias. The dacites are leucocratic and porphyritic, with hornblende and plagioclase (albite) phenocrysts in a groundmass comprising plagioclase microlites and intersertal glass. They are estimated to be 150-200 m thick (Castro et al., 1979). The youngest volcanic unit occurs mainly on the high flanks of Cuernos de Negros, and was described by Castro et al. (1979) as an aphanitic to porphyritic andesite with phenocrysts of plagioclase (andesine) and pyroxene in a crystalline groundmass of plagioclase microlites. These authors did not report a thickness range for the upper andesite.

2.3. Spatial Relationships Between Intrusions and Geothermal Hydrology

The hydrologic structure of the geothermal system is reflected by the distribution of isotherms shown in Figures 2.2 and 2.3 (see also Appendix 4), which are based on downhole measured temperatures. The upflow zone, represented by the 300°C isotherm, is focused close to the intersection of the Ticala and Lagunao Faults, and to the southwest near the eastern margin of the Nasuji Pluton. The 250°C isotherm mantles the 300°C isotherm, with vertical plumes extending to shallower levels in proximity to wells SG2 and PN4RD. The locations of outflow zones, or regions of lateral flow away from the upflow, are intimated by a northeast elongation of the 200°C isotherm along the Puhagan and Nasuwa Faults and also by a southwest elongation of the 250°C isotherm along the Ticala Fault into the southern portions of the Nasuji Pluton (Figure 2.3). The 200°C isotherm defines a lateral plume to the northeast with lower temperatures in the deeper portions of wells N3 and N1 (Figure 2.3), consistent with a major outflow zone extending northeast beneath the Okoy River.

It is doubtful whether any of the intrusions intersected by the geothermal wells provide heat for the modern hydrothermal system. The location of the 300°C isotherm adjacent to a fault intersection and intrusive margin is consistent with hydrothermal fluids utilising these structures as vertical pathways to shallow crustal levels. Although the upflow zone is close to the Puhagan dikes, they are of such small volume that it is unlikely that they could have maintained a

hydrothermal system for any geologically significant period of time. They would probably take less than 10^3 years to cool conductively, and considerably less time would be required with convective cooling (Cathles et al., 1997). It is more likely that another intrusion, which is situated beyond depths drilled beneath the Puhagan area (Figure 2.3), is the causative heat source. This deeper intrusion may or may not be a feeder intrusion to the Puhagan dikes.

2.4. IGNEOUS PETROGRAPHY

2.4.1. Volcanic Rocks

Lower Puhagan Volcanic Formation

Breccias and microbreccias of the Lower Puhagan Volcanic Formation are both clast- and matrix-supported. Clasts are subangular to rounded and range in size from less than one millimetre to several centimetres (Figure 2.4a). The dominant clast types are porphyritic clinopyroxene + plagioclase andesites (Figure 2.4b). Andesite clasts containing hornblende phenocrysts are subordinate. The groundmass of individual clasts varies from holocrystalline, containing flow-aligned feldspar microlites, to holohyaline with recognisable perlitic (Figure 2.4c) and pumiceous textures. Calcareous sedimentary clasts and marine microfossils (foraminifera) are rare (Figure 2.4d). The primary matrix of the breccias and microbreccias has been completely replaced by secondary hydrothermal alteration products.

Volcanogenic sedimentary rock types range from fine-grained sandstones to siltstones (Figures 2.4e and 2.4f). These are moderately to well sorted with a sub-millimetre detrital framework of angular plagioclase, clinopyroxene and sporadic hornblende. Weak bedding is present in some samples (Figure 2.4f). Areas interstitial to the detritus are filled with secondary hydrothermal minerals, which have also replaced the detrital crystal fragments.

Southern Negros Formation

Most of the studied petrological samples from the Southern Negros Formation are drillcore specimens, but two surface samples were also investigated (Figure 2.5). This formation consists of polymictic volcaniclastic breccias and coherent volcanic rocks (Figures 2.6a and 2.6b).

Clast- and matrix-supported breccias (Figures 2.6c and 2.6d) have subangular to rounded porphyritic andesite fragments ranging in size from submillimetre to several centimetres (Figure 2.6a). Clasts contain phenocrysts of clinopyroxene, hornblende, magnetite and plagioclase (Figures 2.6c and 2.6d). Their groundmasses vary between holocrystalline to holohyaline. Some vesicular clasts exist.

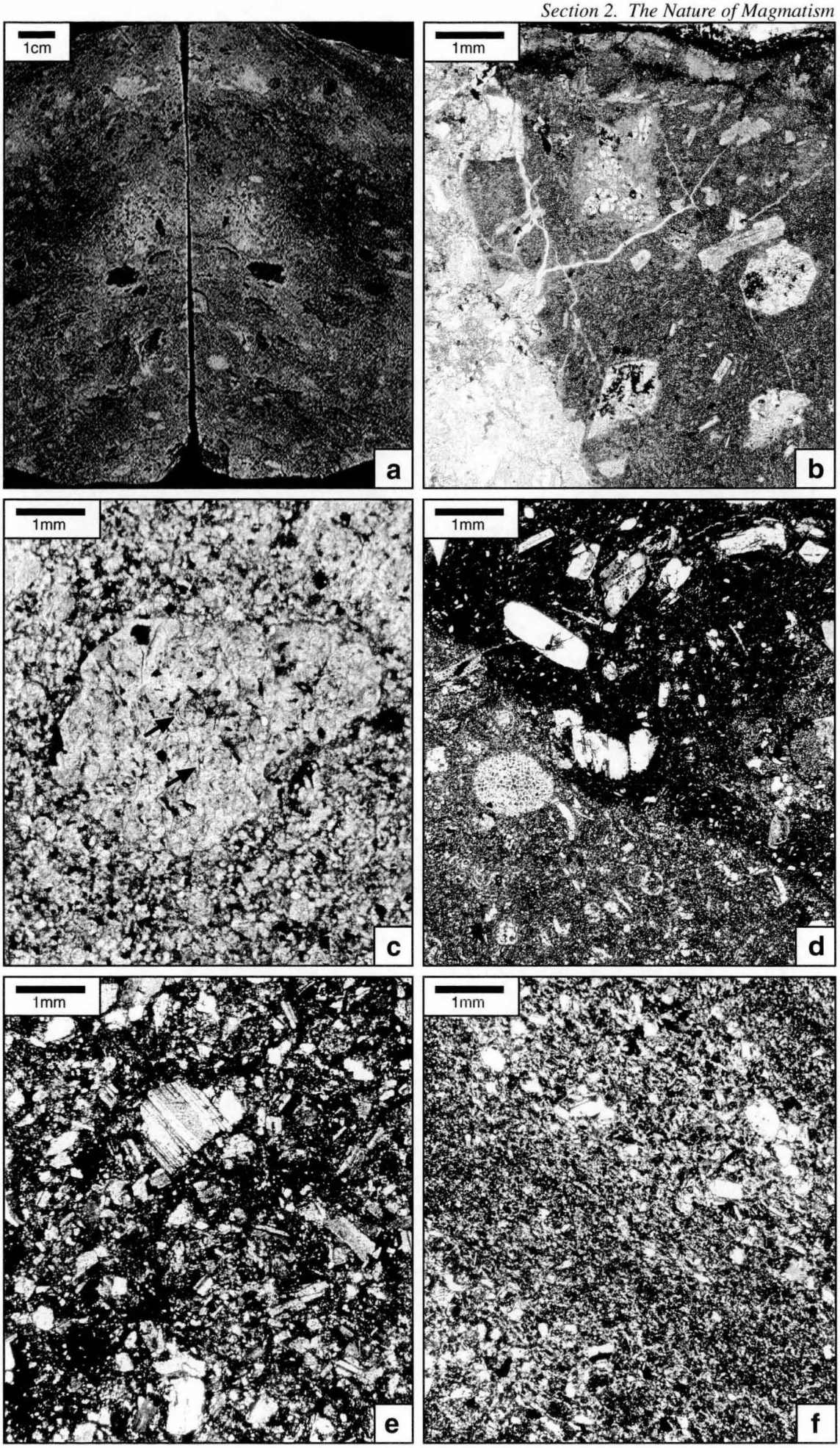
1cm
a
1mm
b
1mm
c
1mm
d
1mm
e
1mm
f

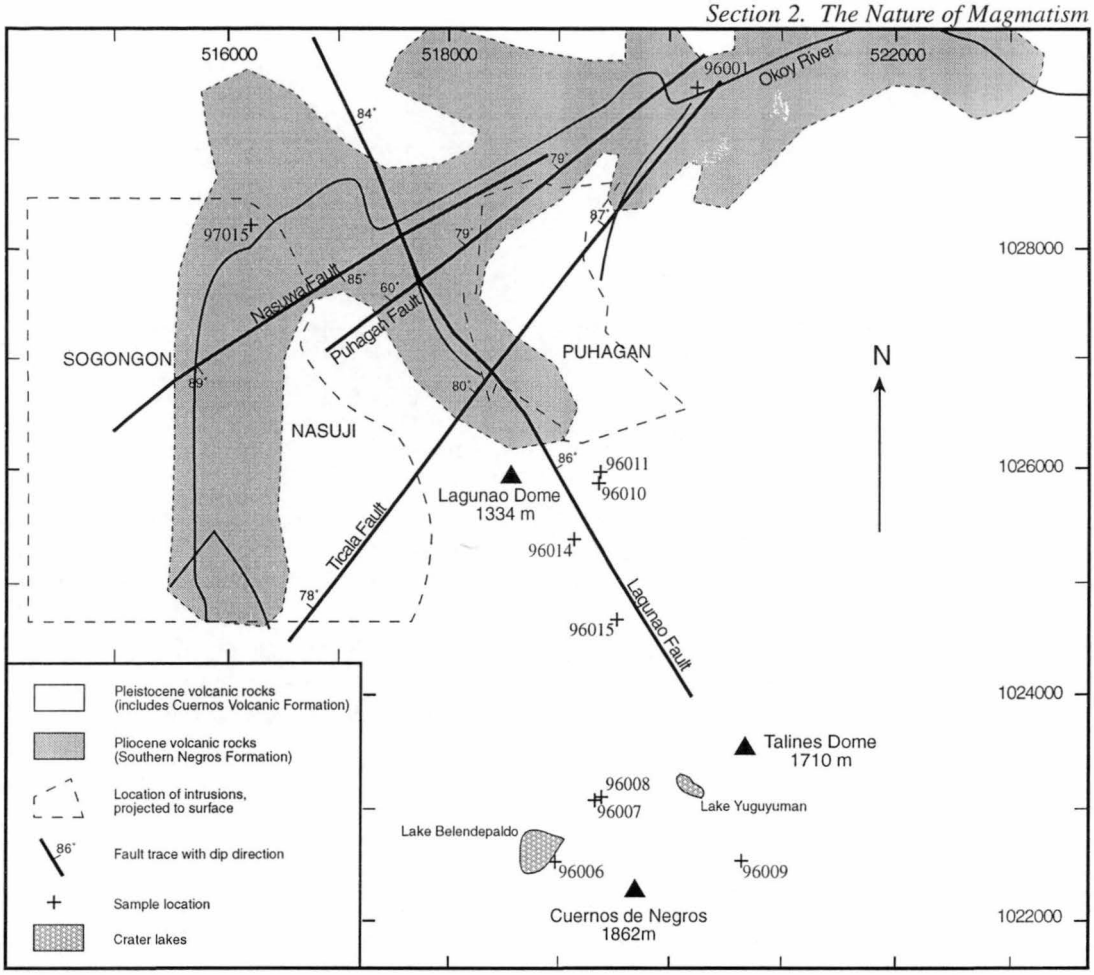

Figure 2.5. Geologic map of the Palinpinon geothermal field (PNOC-EDC, 1982; Pornuevo, 1984) showing surface sample locations and the areal extent of the intrusions projected to the surface.

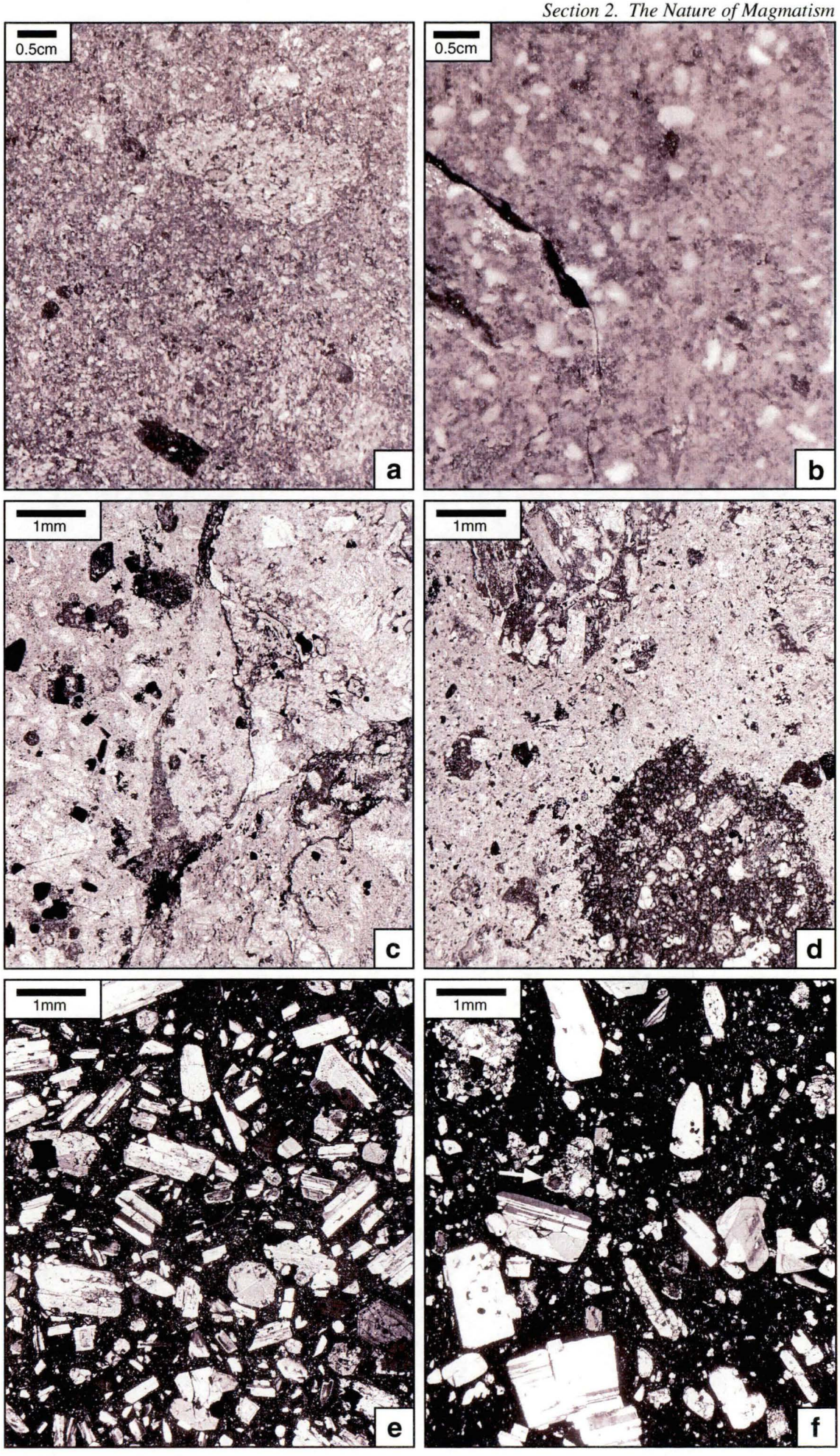
0.5cm
a
0.5cm
b
1mm
c
1mm
d
1mm
e
1mm
f

Coherent, porphyritic volcanic rocks include clinopyroxene + orthopyroxene + plagioclase andesites (Figure 2.6e) along with porphyritic olivine + clinopyroxene + hornblende + plagioclase basaltic andesites (Figure 2.6f). Both contain phenocrysts in a microcrystalline groundmass of flow-aligned feldspar microlites. In the basaltic andesites, olivine phenocrysts are rimmed by fine-grained crystals of clinopyroxene (Figure 2.6f). Hornblende phenocrysts have been completely replaced by opacite, an aggregate of fine-grained (<10 μm) orthopyroxene, clinopyroxene, plagioclase and FeTi-oxide, which has formed from products of amphibole breakdown produced by dehydration during magma ascent (Rutherford and Hill, 1993).

Cuernos Volcanic Formation

Eight surface samples were collected from the upper slopes of Cuernos de Negros (Figure 2.5). Seven are porphyritic andesites and one is a basaltic andesite.

The andesites (Figure 2.7a) have a phenocryst assemblage of oxyhornblende, clinopyroxene, plagioclase (An_{45-53}) and magnetite (Figure 2.7b). Four samples contain minor rounded quartz phenocrysts (Figures 2.7c and 2.7d), some with reaction rims of fine clinopyroxene. Oxyhornblende phenocrysts display strong pleochroism (pale yellow to dark, reddish brown) and are typically lined with, or completely replaced by, opacite. The groundmass of most samples contains feldspar microlites in volcanic glass. One sample has a holohyaline groundmass (Figure 2.7b).

The basaltic andesites have a different mineralogy than that of the andesites (Figure 2.7e). They contains phenocrysts of plagioclase, hornblende, clinopyroxene and olivine. Plagioclase phenocrysts are more calcic (An_{70}) than those in the andesites and are normally zoned to An_{40} rims. Their cores have a corroded or porous appearance (Figure 2.7e). Olivine phenocrysts are anhedral and rimmed by hornblende (Figure 2.7e). The groundmass comprises hornblende, clinopyroxene and plagioclase crystals in volcanic glass. There are a few rounded quartz crystals rimmed by clinopyroxene.

Given their sample localities, these eight rocks were probably collected from the youngest, upper, andesite described by Castro et al. (1979). However, these authors describe a porphyritic rock with pyroxene and plagioclase phenocrysts, and neither hornblende, quartz or olivine phenocrysts were described. Castro et al. (1979) do not give sample locations or how many samples were collected from each unit. The results of this study shows that there is considerably more compositional variation than previously documented in the Cuernos Volcanic Formation.

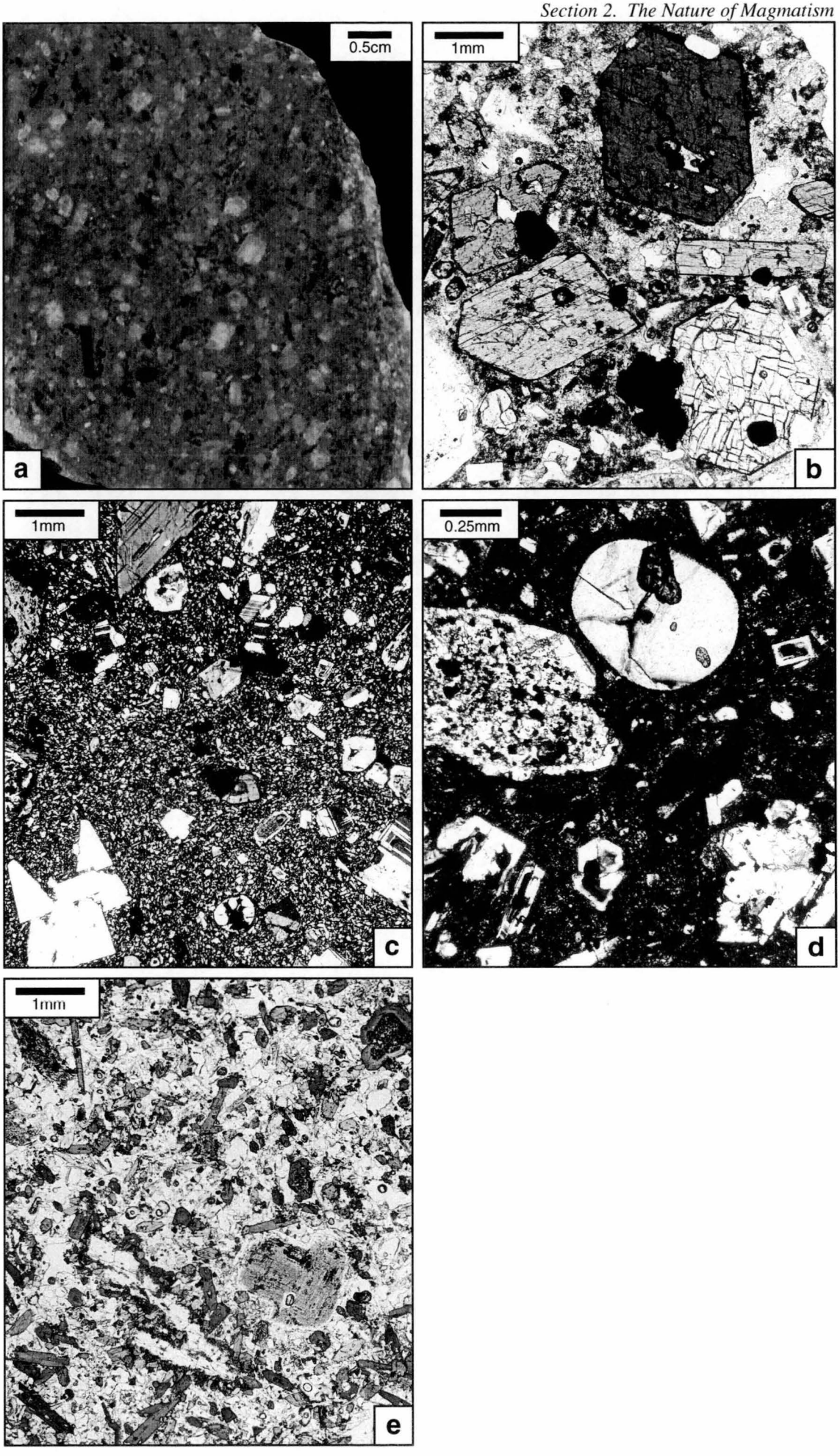
0.5cm
a
1mm
b
1mm
c
0.25mm
d
1mm
e

2.4.2. Intrusive Rocks

Nasuji Pluton

Rocks belonging to the Nasuji Pluton are leucocratic, equigranular to porphyritic and range from hornblende diorite to hornblende quartz diorite (Figures 2.8a to 2.8f). Hornblende crystals are commonly flow aligned and occur in a framework of plagioclase, with variable amounts of orthoclase and quartz.

The most common rock type, an equigranular hornblende quartz diorite (Figure 2.8a), has euhedral hornblende and plagioclase crystals in an equigranular framework of anhedral orthoclase and quartz (Figure 2.8b). Micrographic intergrowths exist between quartz and orthoclase. Plagioclase crystals (An_{30-40}) are oscillatory zoned, and hornblendes are pleochroic (green, yellow green, olive green). Magnetite and sphene are common accessory minerals. Magnetite is associated with hornblende, and sphene is interstitial to quartz and orthoclase. Clinopyroxene is rare. Igneous quartz crystals contain vapour-rich and hypersaline, liquid-rich fluid inclusions that contain daughter salts and opaque minerals.

The porphyritic hornblende quartz diorite is mineralogically equivalent to the equigranular hornblende quartz diorite. It is finer grained than the equigranular variety (Figure 2.8c) and contains phenocrysts of hornblende, plagioclase, quartz and magnetite in a fine-grained (< 0.1mm), equigranular, felsic groundmass (Figure 2.8d). Quartz phenocrysts are anhedral, rounded (Figure 2.8d) and commonly embayed.

The hornblende diorite is an equigranular rock with a framework of hornblende and plagioclase laths (Figures 2.8e and 2.8f). Plagioclase (An_{50-60}) is more calcic than in the hornblende quartz diorite. Magnetite is commonly associated with hornblende. Quartz and orthoclase occur in interstices, but never comprise more than 1 modal %. It is possible that either or both minerals are the products of hydrothermal alteration.

Puhagan Dikes

Rocks belonging to the Puhagan dikes are porphyritic hornblende diorites and clinopyroxene-hornblende diorites. In hand specimen they are leucocratic and porphyritic, with white feldspar and black hornblende and clinopyroxene phenocrysts in a pale grey groundmass (Figures 2.9a and 2.9c). The groundmass is holocrystalline with plagioclase laths (Figures 2.9b and 2.9d) that are variably flow aligned and randomly oriented. Due to the intensity of hydrothermal alteration, the igneous versus hydrothermal origin of quartz and alkali feldspar in the groundmass cannot be distinguished.

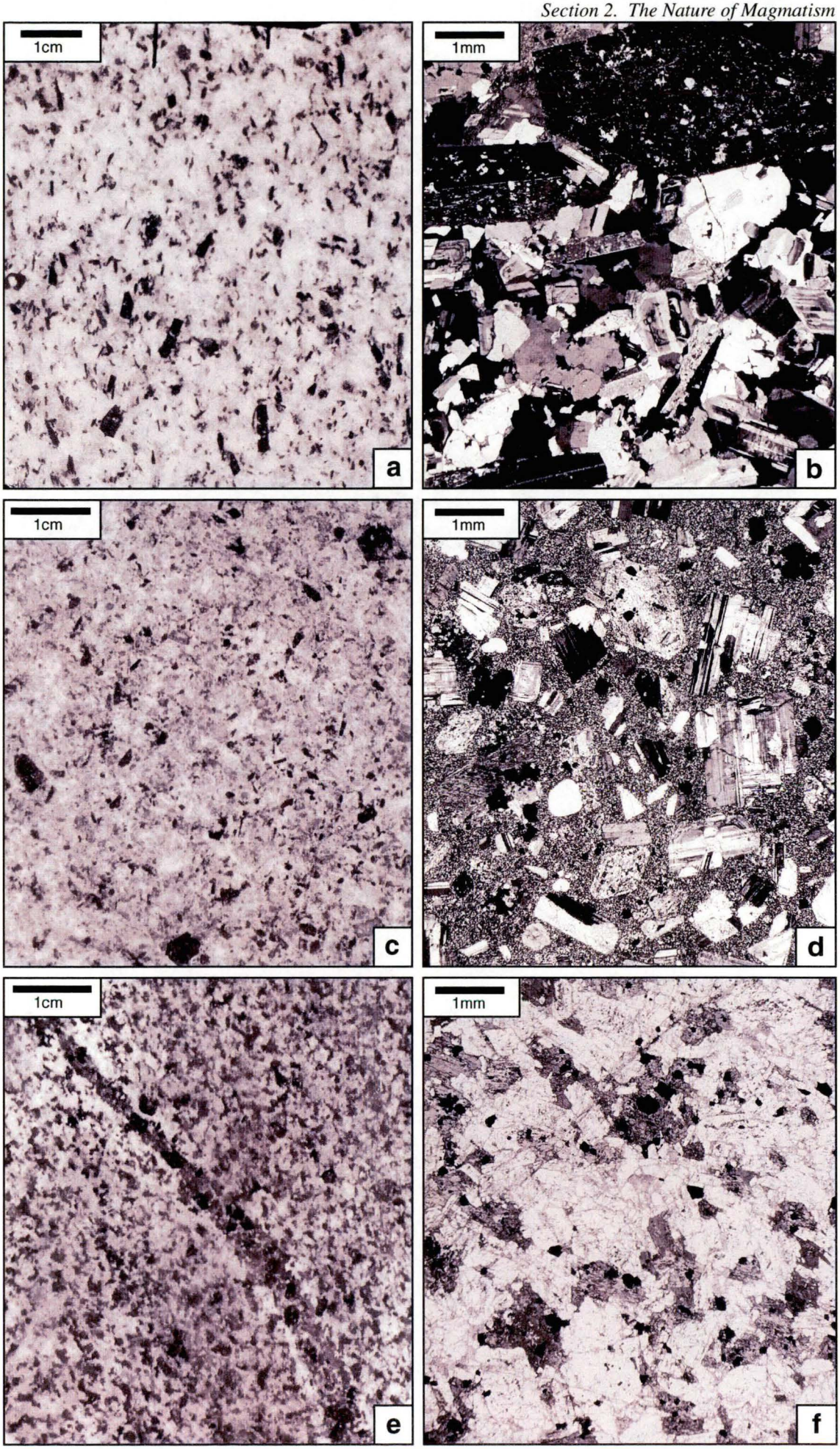

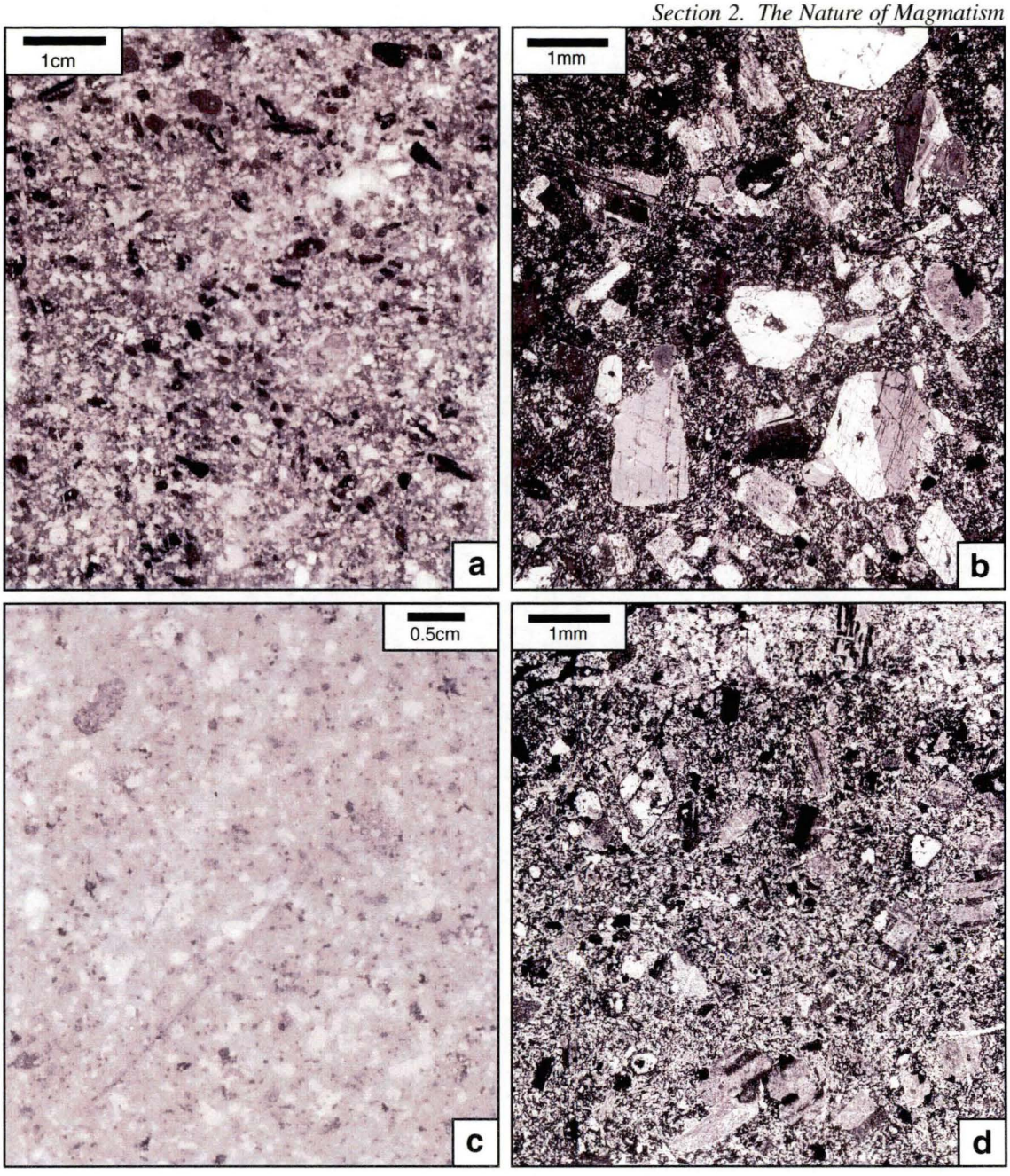

Figure 2.9 : Puhagan Dikes

a. *Sample PN21D/4.* Porphyritic hornblende-clinopyroxene diorite. Black hornblende, clinopyroxene, and white plagioclase crystals are enclosed in a pale grey groundmass of fine grained feldspar.

b. *Sample PN21D/4. Photomicrograph taken under crossed polarised light.* Photomicrograph of a porphyritic hornblende-clinopyroxene diorite. Euhedral hornblende (lower left & lower right), clinopyroxene (centre) and plagioclase phenocrysts are enclosed in a fine grained, holocrystalline groundmass of plagioclase feldspar. Hornblende and clinopyroxene crystals are unaltered, whereas plagioclase is altered to albite.

c. *Sample PN30D/1.* Porphyritic hornblende diorite. A porphyritic hornblende diorite with white plagioclase and grey hornblende phenocrysts enclosed in a pale grey groundmass of fine grained feldspar.

d. *Sample PN30D/1. Photomicrograph taken under crossed polarised light.* Photomicrograph of a strongly altered porphyritic hornblende diorite. Phenocrysts of plagioclase are enclosed in a felsic groundmass comprised of flow aligned plagioclase laths. Plagioclase phenocrysts are altered to albite. Hornblende phenocrysts are completely replaced by alteration minerals (calcite, titanite, epidote, chlorite). A relict euhedral amphibole is upper left.

2.5. RADIOMETRIC ($^{40}Ar/^{39}Ar$) DATING OF INTRUSIONS

2.5.1. Sample Descriptions

$^{40}Ar/^{39}Ar$ ages of hornblende from two samples were obtained, one from the Nasuji Pluton and one from the Puhagan dikes. Only samples with the least hydrothermal alteration were analysed. Description of the analytical procedures are presented in Appendix 1.1.

Sample NJ2D/1 is an equigranular hornblende quartz diorite belonging to the Nasuji Pluton. This rock contains approximately 1 modal % of 3-4 mm long hornblende crystals. Wallrock alteration is restricted to alteration haloes surrounding widely spaced quartz-adularia-anhydrite veins (< 1 mm), in which hornblende crystals been partially replaced by chlorite. Hornblende crystals collected away from these haloes are unaltered. Sample PN21D/4 is a porphyritic hornblende-clinopyroxene diorite with 1-2 modal % 1-2 mm hornblende phenocrysts. Hornblende phenocrysts are unaltered and occur in a holocrystalline groundmass of plagioclase laths that have been altered to albite (Figure 2.9b).

Collection depths for these samples are 1582 m bsl and 1916 m bsl, for sample NJ2D/1 and PN21D/4, respectively. Both occur at measured downhole temperatures of approximately 250°C, below the radiogenic argon closure temperature for hornblende of ~500°C (McDougall and Harrison, 1999).

2.5.2. $^{40}Ar/^{39}Ar$ Results

Analytical results of the two irradiated hornblende samples are listed in Table 2.1 and illustrated as stepwise release spectra in Figure 2.10. From these, an age is determined by the recognition of a 'plateau' that has been defined by Fleck et al. (1977) as: "that part of an age spectrum diagram composed of contiguous gas fractions that together represent more than 50% of the total ^{39}Ar released from the sample and for which no difference in age can be detected between any two fractions at the 95% confidence level".

Analysis of the hornblende from the Nasuji Pluton (NJ2D/1) yielded a flat age spectrum, with a plateau age of 0.54 ± 0.09 Ma (1σ; Figure 2.10a). Relatively large errors associated with the individual steps are due to the release of small quantities of radiogenic argon (< 5%). If a 2σ error is used, the age range would be between ~0.7 and 0.3 Ma. The hornblende from the Puhagan dikes (PN21D/4) has a more reliable age (Figure 2.10b). Its plateau age is estimated to be 4.17 ± 0.05 Ma (1σ).

Table 2.1. Step heating Ar isotopic data and apparent ages for hornblende samples from the Puhagan dikes (PN21D/4) and the Nasuji Pluton (NJ2D/1).

Temp. (°C)	Cum. ^{39}Ar	$^{40}Ar/^{39}Ar$	$^{37}Ar/^{39}Ar$	$^{36}Ar/^{39}Ar$	Vol. ^{39}Ar ($x10^{-14}$mol)	%Rad. ^{40}Ar	Ca/K	$^{40}Ar^*/^{39}Ar$	Age (Ma±1σ)
NJ2D/1 Hornblende, Mass = 138.00 mg, J-value = 0 0007557 ± 0.0000038									
1. 600	0.0084	534.9	2.259	1.7881	0.1822	1.2	4.3	6.694	9.10±8.56
2. 700	0.0331	193.7	0.610	0.6501	0.5359	0.8	1.2	1.560	2.13±2.62
3. 800	0.0839	146.7	0.455	0.4895	1.1040	1.4	0.9	2.077	2.83±1.74
4. 900	0 1415	43.31	1.479	0.1452	1.2520	1.1	2.8	0.487	0.66±0.51
5. 1000	0.1723	67.13	9.916	0 226	0 6751	1.8	19.0	1.245	1 70±0.90
6. 1050	0.2880	16.94	9.237	0.0586	2.5290	2 6	17.7	0.437	0.60±0 25
7 1060	0 4840	11.08	8.707	0.0394	4.2840	1.8	16.7	0 200	0.27±0 17
8. 1080	0.6977	9.88	8.726	0.0348	4.6720	3.6	16.7	0.360	0.49±0.16
9. 1130	0.9096	13.62	9.698	0.0471	4.6350	4.2	18 6	0.577	0.79±0.19
10 1220	0.9606	34.65	12.379	0.1199	1.1180	1.0	23.7	0 352	0.48±0 61
11 1350	0.9989	38.43	13.577	0.1329	0.8404	1.0	26.1	0.392	0.54±0.74
12. 1450	1.0000	491.4	11.785	1.6498	0.0234	1.0	22.6	5.002	6.81±34.90
Total		34.09	8.316	0.1159	21.8500			0.594	0.81±0.52
PN21D/4 Hornblende, Mass = 151.68 mg, J-value = 0.0007669 ± 0.0000038									
1 600	0.0010	3040.9	24.098	10.1160	0.029	1.8	46.7	54.46	73.8±156 80
2. 700	0.0026	1075.6	52.866	3.6070	0.045	1.4	105.0	15.41	21.2±21.50
3. 800	0.0045	2201.6	20.342	7.3763	0.055	1.1	39.3	24.00	32.9±110.60
4. 900	0.0073	483.1	21.166	1.6347	0.782	0.4	40.9	1.95	2.70±18.66
5. 1000	0.0380	61.55	15.043	0.2035	0.868	4.5	28.9	2.83	3.92±0.82
6. 1050	0.1744	16.77	12.591	0.0507	3.840	17.4	24 2	2.95	4.08±0.15
7 1070	0.3945	10.68	12.533	0.0296	6.195	28.9	24.1	3.12	4.30±0 09
8. 1090	0.6712	8.91	12.521	0.0242	7.792	32.3	24.0	2.91	4 02±0 10
9. 1105	0.7959	9.82	12.497	0.0270	3.508	30.3	24.0	3.01	4.15±0 09
10. 1125	0.8533	19.13	12.542	0.0577	1.617	16.8	24.1	3.24	4.48±0.31
11. 1160	0 9384	17.88	12.667	0 0530	2.396	18.8	24.3	3.40	4.70±0.32
12 1220	0.9832	21.86	13.553	0.0691	1.261	12.2	26.0	2.71	3.74±0.40
13. 1300	0.9988	40.31	13.984	0 1288	0.442	8.7	26.9	3.56	4.91±1.12
14. 1420	1.0000	550.4	13.790	1.8348	0.033	1.7	26.5	9.46	13 0±39.7
Total		25.607	12.805	0.0800	28.16			3.15	4 35±0.69

Notes:

i) Errors are one sigma uncertainties and exclude uncertainties in the J-value.

ii) Data are corrected for mass spectrometer backgrounds, discrimination and radioactive decay.

iii) Interference corrections are: $(^{36}Ar/^{37}Ar)_{Ca} = 3.2x10^{-4}$; $(^{39}Ar/^{37}Ar)_{Ca} = 7.86x10^{-4}$; $(^{40}Ar/^{39}Ar)_{K} = 5.10x10^{-2}$

iv) J-value is based on an age of 27.95 Ma for the Fish Canyon Tuff biotite monitor

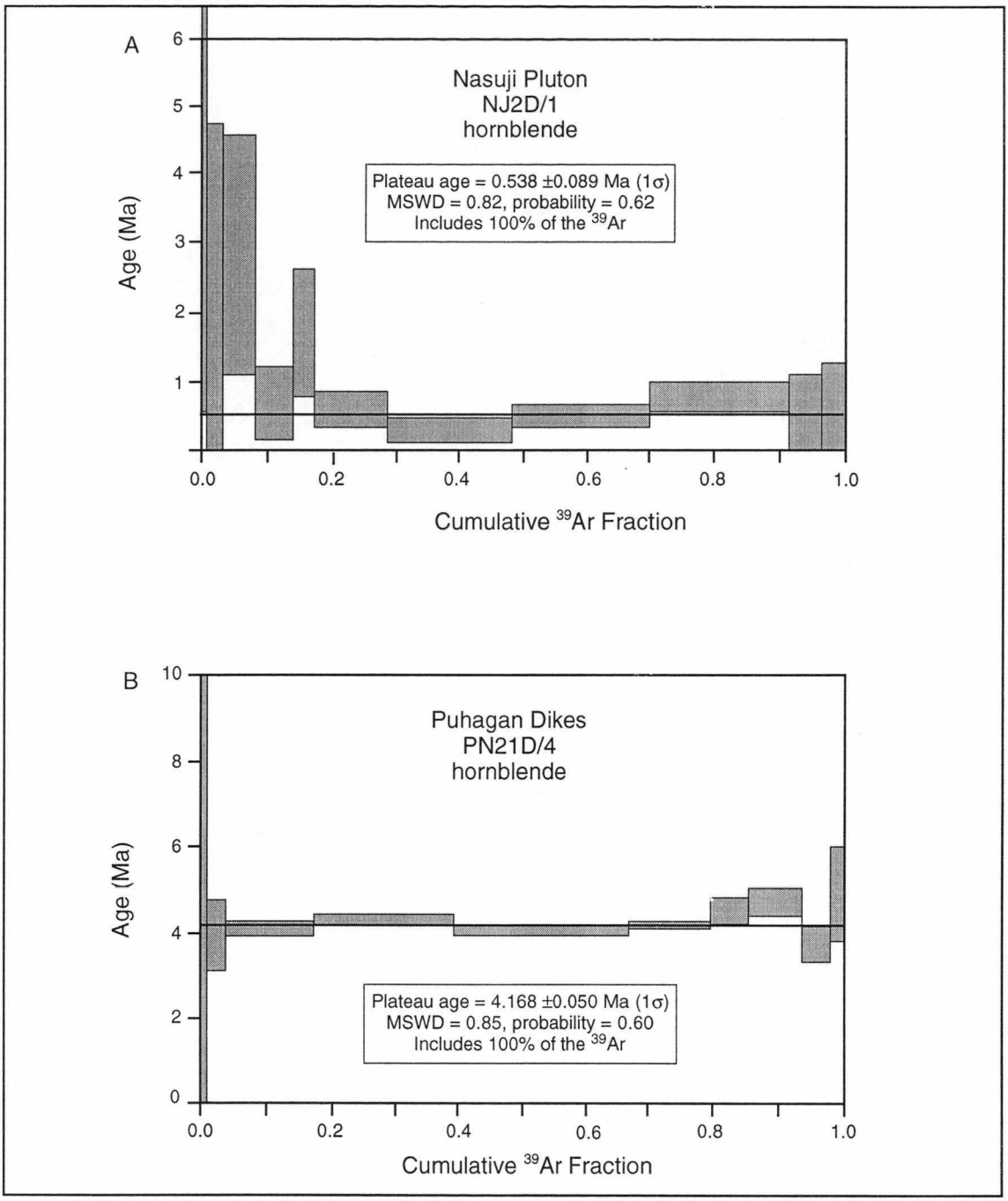

Figure 2.10. $^{40}Ar/^{39}Ar$ apparent age spectra for hornblendes from the Nasuji Pluton (A) and the Puhagan Dikes (B). See text for discussion and Table 2.1 for the primary isotopic data and calculated ages.

2.6. REGIONAL STRATIGRAPHIC CORRELATION AND IMPLICATIONS OF THE RADIOMETRIC AGE DETERMINATIONS

Based on the formation ages proposed by Zaide (1984), a correlation with the Visayas stratigraphy (Porth et al., 1989) is presented in Figure 2.11. The Middle Miocene age assigned to the Lower Puhagan Volcanic Formation by Zaide (1984) makes it coeval with the other Middle Miocene volcanic and volcaniclastic formations of the Visayas basin (Figure 2.11). These volcanic rocks are thought to be time equivalent to the Valderrama volcanic arc of western Panay (Figure 1.2; Rangin, 1989). According to Zaide (1984), the palaeontological evidence for a Late Miocene to Early Pliocene age for the Okoy Formation is reliable and accurate. This age correlates well with the Talave Formation of NE Negros (Porth et al., 1989) and other calcareous sedimentary formations of Cebu and Bohol (Figure 2.11). The nature of the contact between the Okoy Formation and the underlying Lower Puhagan Volcanics is not known, but the regional Middle/Late Miocene unconformity (Figure 2.11) implies a non-conformable contact between these two rock types. The Southern Negros Formation overlies the Okoy Formation and hence is younger than Early Pliocene age. It is a product of arc volcanism which has been ongoing since Pliocene times, when subduction of Sulu Sea basin initiated at the Negros-Sulu Trench (Rangin, 1989).

The calculated $^{40}Ar/^{39}Ar$ ages of the Nasuji Pluton and the Puhagan dikes are 0.7-0.3 Ma and 4.2-4.1 Ma, respectively. These data indicate that the Nasuji Pluton is considerably younger than the age estimated by K-Ar methods (10.5-5.6 Ma; Zaide, 1984). This younger age is consistent with the observation that the pluton was emplaced into the Late Pliocene Southern Negros Formation. The anomalously old ages determined by K-Ar methods could be explained by the presence of excess ^{40}Ar.

The large age difference between the Nasuji and Puhagan intrusions verifies that they are not genetically related. The Early Pliocene age for the Puhagan dikes confirms that they are too old to be the heat source for the modern hydrothermal system. This implies that a much younger intrusion, unrelated to the Puhagan dikes, is situated beyond depths drilled in the Puhagan region.

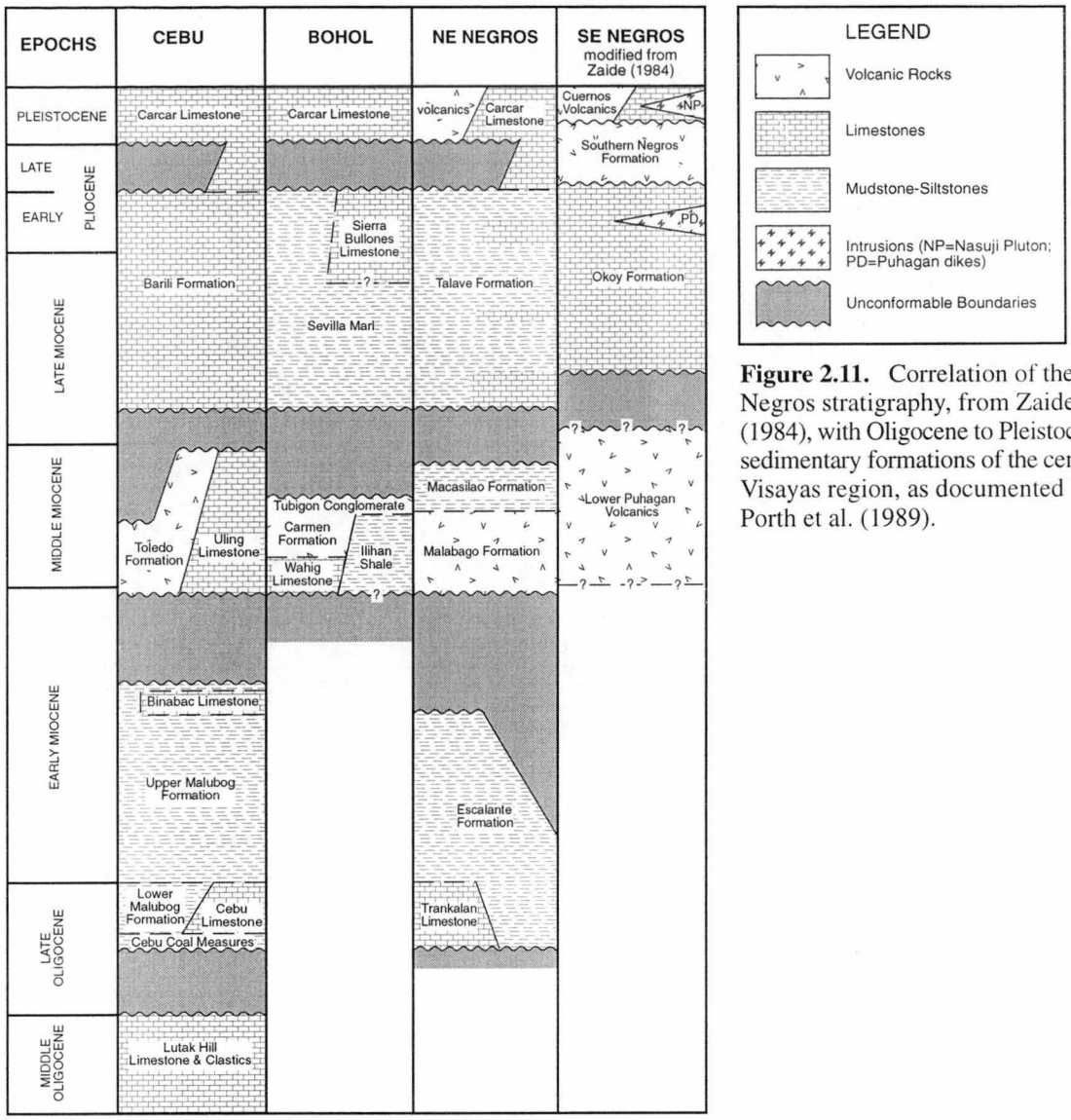

Figure 2.11. Correlation of the SE Negros stratigraphy, from Zaide (1984), with Oligocene to Pleistocene sedimentary formations of the central Visayas region, as documented by Porth et al. (1989).

2.7. IGNEOUS ROCK GEOCHEMISTRY

The geochemistry of volcanic rocks from Negros Island has been documented by von Biedersee and Pichler (1995), but their study focused mainly on rocks from the northern Negros volcano, Mt. Canlaon (Figure 1.3). However, their data includes whole rock major and partial trace element analyses of ten volcanic samples from southern Negros. Two are shallow drillcore samples of the Southern Negros Formation and six are surface samples belonging to the Cuernos Volcanic Formation (von Biedersee and Pichler, 1995). Data from these eight samples are incorporated into the following discussion.

Sajona et al. (2000a) discussed the origin of island arc magmas based on Negros Island volcanic rocks. Their data includes rock analyses from four Negros volcanoes: Mt. Silay, Mt. Mandalagan, Mt. Canlaon and Cuernos de Negros (Figure 1.3). Descriptions and locations of the 17 Cuernos de Negros samples are not presented and hence this data is not included here.

In the current study, thirty six igneous rocks were selected for whole rock geochemical analyses of their major and trace element compositions in order to classify the different igneous rock types and to assess their magmatic affinities. Care was taken to analyse only the least hydrothermally altered specimens.

2.7.1. Major Elements

Igneous rocks from southern Negros Island (Table 2.2) have SiO_2 concentrations between 49 and 66 wt %. On a K_2O vs SiO_2 classification diagram (Figure 2.12, Peccerillo and Taylor, 1976), the compositions range from basalt to dacite, with the majority falling in the medium-K, calc-alkaline field. Many samples fall outside this field, but potassium mobility during hydrothermal alteration may explain the wide scatter in K_2O values (0.3 to 4.6wt %).

Two samples belonging to the Lower Puhagan Volcanic Formation (NJ5D/5, PN25D/2) have basaltic compositions (49-52wt % SiO_2). The Southern Negros Formation samples show a compositional range from andesite to dacite (57-65wt % SiO_2). Cuernos Volcanic Formation samples are basaltic andesite to andesite (52-63wt % SiO_2). The Nasuji Pluton and Puhagan dikes have equivalent compositional ranges, 52-66wt % and 51-64wt % SiO_2 respectively, spanning basaltic to dacitic compositions.

Major element vs SiO_2 variation diagrams are shown in Figure 2.13. All major element abundances are typical for orogenic medium K, calc-alkaline rocks of the SW Pacific (Ewart, 1982). There are linear trends of increasing SiO_2 with concomitant depletion in TiO_2, Fe_2O_3, MgO and CaO, and enrichment in Na_2O and K_2O (Figure 2.12). The fields for the Nasuji Pluton and Puhagan dikes are congruent. The most mafic (and the only olivine-bearing) Cuernos Volcanic sample (96008) has the highest MgO value (9.1wt %; Figure 2.13).

Table 2.2. Major (wt%) and trace (ppm) element analyses for southern Negros igneous rocks. RF=Rock Formation; CV=Cuernos Volcanic Formation; SNF=Southern Negros Formation; LPV=Lower Puhagan Volcanic Formation; NP=Nasuji Pluton; PD=Puhagan dikes.

Samp./Well	96006	96008	96010	96014	96001	NJ5D	NJ5D	PN25D	NJ2D	NJ4D	NJ7D
Core						5	5	2	1	2	1
RF	CV	CV	CV	CV	SNF	LPV	LPV	LPV	NP	NP	NP
SiO_2	59.42	52.33	60.67	62 46	56.58	48.97	48.78	51.87	65.56	63.60	63.51
TiO_2	0.57	0.68	0.51	0.44	0.73	0.95	0.94	1.01	0.35	0.37	0.39
Al_2O_3	17.95	14.94	18.07	18.24	18.97	18 17	17.86	17.61	16.61	17.44	17 25
Fe_2O_3*	5 79	8.15	6 48	5.43	6.73	9.98	10 26	9.08	3.96	4.44	4 81
MnO	0.12	0.14	0.09	0.18	0.11	0.17	0.18	0.14	0.08	0.09	0.13
MgO	3.32	9.11	2.76	2.15	2.94	5.97	6.26	7 00	1.50	1.74	1 70
CaO	7.20	10.15	5.76	5.54	8.43	12.24	12.36	10.15	4 97	5.69	5.65
Na_2O	3 65	3.03	3.55	3 64	3.34	2.93	2 72	2.22	4.04	4.18	4.11
K_2O	1.75	1.31	1.94	1.76	1.89	0.25	0.29	0.62	2.75	2.24	2.24
P_2O_5	0.23	0.15	0.18	0.15	0.28	0.37	0.35	0.29	0.17	0.20	0 21
LOI	1.02	1.37	3.27	2.17	1.83	1.50	0.97	0.82	0.46	1 10	0.39
Total	100.00	100.00	100.00	100.00	100.00	100.00	100.00	100.00	100 00	100.00	100 00
Sb	-	-	-	-	-	-	-	2.4	-	-	-
Nb	3.85	2.03	3 23	3.48	3.89	2.03	2 72	9.06	4.53	4.85	4.13
Zr	94	77	109	93	119	38	39	112	107	116	122
Sr	782	500	504	571	793	842	798	757	508	616	580
Ba	279	192	337	345	385	80	86	164	340	369	385
Sc	21 4	38.1	18.2	13.0	23.8	47.9	46.3	36.6	9.1	10.1	10.6
V	185	270	156	147	276	374	378	249	96	110	116
Cr	9.5	385.3	125.0	7.2	9 8	66.4	64.6	179.2	6.8	7.2	6.5
Ni	10.0	105.3	41.7	4.7	7 9	22.7	26.1	41.8	3.9	2.7	2.9
La	12.8	8.3	25.2	12.6	17.0	10.4	7.3	10.3	16.1	13.9	15.7
Y	13.1	12.2	34.7	18.2	17.0	16.1	15.4	15.8	11.5	13.3	12.7
Rb	30.5	23.3	40.0	35 2	23.8	3.6	4.9	17.4	62.0	44.2	44 1
As	-	-	-	-	-	3.6	3.1	-	-	-	-

Well	OK11D	OK8RD	SG1	SG2	SG3RD	NJ1D	NJ3D	NJ5D	NJ5D	NJ5D	NJ6D
Core	3	2	1	5	1	5	1	3	4	4	4
RF	NP	NP	NP	NP	NP	NP	NP	NP	NP	NP	NP
SiO_2	62.85	63.60	56.74	64.51	63.80	62.23	51.82	58.94	55.39	56.02	56.83
TiO_2	0 41	0.40	0.75	0.38	0.38	0.44	0.78	0.52	0.51	0.52	0.61
Al_2O_3	17.54	17.28	18.83	16.98	17.34	17.78	19.11	18.20	19.82	19.58	18.89
Fe_2O_3*	4.83	4.59	6.43	4.39	4.42	3.07	8.89	5 89	6.72	6.25	7.54
MnO	0.13	0.10	0.10	0.07	0.10	0.05	0.26	0.10	0.10	0.10	0.19
MgO	1.69	1.70	3.57	1.57	1.61	2.21	5.43	3.43	3.13	3.23	2.73
CaO	5.78	5.52	4.44	5.45	5.58	7.72	9.15	7.53	8.94	8.85	9.24
Na_2O	4.23	4.17	4.28	4.01	4.46	3.80	3.72	4 03	3 89	3.83	3 06
K_2O	2.33	2.43	4.56	2.45	2 10	2.49	0 65	1.13	1 20	1.33	0 56
P_2O_5	0 20	0.20	0.32	0.19	0.21	0.21	0.19	0.23	0.30	0.30	0.36
LOI	1.05	0.55	1.48	0.55	0.55	2.21	2.96	4.21	3.16	3.42	1.80
Total	100.00	100.00	100.00	100.00	100.00	100.00	100.00	100.00	100.00	100.00	100.00
Sb	-	-	-	-	-	-	-	-	-	-	-
Nb	4.57	4.62	4.49	4.41	4.22	5.21	2 17	3.88	3.52	3.31	6.11
Zr	120	117	117	115	116	127	58	110	100	104	108
Sr	615	573	591	559	610	1055	682	652	811	792	686
Ba	408	345	419	397	352	390	149	254	240	236	150
Sc	11.0	11.6	7.9	9.5	9.4	13.7	33.8	20.3	17.9	18.3	19.1
V	118	113	99	107	104	166	291	198	177	180	202
Cr	12.4	4.0	5.0	5.9	5.8	7.9	21.6	28 4	9.0	8 7	5 1
Ni	4.0	2.7	2.5	3.2	2.0	3.1	13.9	11.1	6.8	6.0	5.7
La	15.3	16.3	16.4	15.0	17.9	14.0	7.6	11.4	11.7	14.3	14.2
Y	12.6	14.1	12.4	12.8	12.2	14.4	15.4	14.3	15.5	15.7	16 0
Rb	42.0	46.2	48.3	42.1	34.2	45.8	16.2	24.4	24.3	26.0	12 3
As	-	-	-	-	-	-	-	-	-	-	-

Table 2.2. Major (wt%) and trace (ppm) element analyses for southern Negros igneous rocks. RF=Rock Formation; CV=Cuernos Volcanic Formation; SNF=Southern Negros Formation; LPV=Lower Puhagan Volcanic Formation; NP=Nasuji Pluton; PD=Puhagan dikes.

Well	NJ7D	NJ3D	SG1RD	SG1RD	OK7	PN21D	PN31D	PN1RD	PN1RD	OK10D
Core	1	3	1	1	7	4	4	3	6	6
RF	NP	NP	NP	NP	PD	PD	PD	PD	PD	PD
SiO_2	65.05	62.83	52.68	52.62	51.39	55.68	51.49	51.25	61.32	62.56
TiO_2	0.36	0.33	0.79	0.79	0.75	0.60	0.79	0.73	0.43	0 45
Al_2O_3	16.80	16.74	18.02	18.30	19.08	18.82	19.74	20.24	17.53	17 44
$Fe_2O_3^*$	4.43	4.50	9.14	9.24	8.82	7.49	9.00	9.30	5.17	5.17
MnO	0.07	0.09	0.22	0.24	0.15	0.16	0.16	0.15	0.11	0.12
MgO	1.42	1.68	4.23	4.25	5 61	3.80	5.52	4.03	2.47	1.90
CaO	4.95	6.64	9.37	9.56	9 62	8.00	7.79	8.58	6.67	3.25
Na_2O	3.93	4.02	3.31	3.24	3 43	4.11	4.16	4.65	3 96	7.01
K_2O	2.81	2.97	1.81	1.35	0.98	1.13	1.19	0.82	2.10	1.88
P_2O_5	0.17	0.20	0.44	0 40	0.18	0.21	0.18	0.24	0.23	0.22
LOI	1.06	3.37	1.28	0.55	2.97	3.91	3.34	4.18	2.38	3.17
Total	100.00	100.00	100.00	100.00	100.00	100.00	100.00	100.00	100.00	100.00
Sb	-	-	2.2	2.9	-	-	-	-	-	-
Nb	4.07	4.35	4.26	5.05	2.68	5.10	2.59	3.48	4.65	5.99
Zr	119	116	64	66	48	80	50	66	127	129
Sr	540	643	854	837	792	804	850	1035	950	813
Ba	423	434	719	569	216	302	321	235	356	447
Sc	7.7	9.2	25.5	25.2	29 9	22.2	33.4	22.5	14.0	8.6
V	102	110	238	243	289	197	300	232	144	111
Cr	5 4	5.7	9.7	10.8	36.5	20.0	30.2	7 1	56.9	3.8
Ni	2.8	3.4	10.0	9.9	23.9	12.6	21.0	6.3	17.6	2.5
La	17.9	20.5	12.6	11.9	5.8	8.8	4 4	7.4	13.4	13.8
Y	12.3	17.1	16.4	16.8	13.8	14.5	13.3	15.9	14.0	15.0
Rb	58.6	53.5	25.8	17.7	14.1	21.2	18.2	11.5	34.5	34.8
As	-	-	5.8	8.0	-	-	-	-	-	-

Well	OK9	PN30D	PN20D	PN20D
Core	6	1	2	2
RF	PD	PD	PD	PD
SiO_2	62.99	64.14	58.64	56.79
TiO_2	0.45	0.44	0.74	0.74
Al_2O_3	17.38	17.01	17.53	18.79
$Fe_2O_3^*$	5.05	4.98	6.66	6.39
MnO	0 10	0.17	0.11	0.09
MgO	1.85	2.00	3.90	3.59
CaO	3.40	3.81	4.35	4.48
Na_2O	6.49	6.85	4.23	4.30
K_2O	2.06	0.40	3.51	4.51
P_2O_5	0.22	0.21	0.32	0.32
LOI	2.91	3.47	2.14	2.04
Total	100.00	100.00	100.00	100.00
Sb	-	-	-	-
Nb	5.66	5.72	13.49	14.54
Zr	127	126	201	217
Sr	792	787	1297	1498
Ba	505	189	830	1190
Sc	8.5	8.9	17.0	16.5
V	102	97	127	141
Cr	3.8	3.0	21.8	19.6
Ni	2.0	2.9	6.8	6.9
La	12.9	14.8	16.9	20.5
Y	15.2	14.7	22.3	22.2
Rb	39.4	8.9	62.8	78.0
As	-	-	-	-

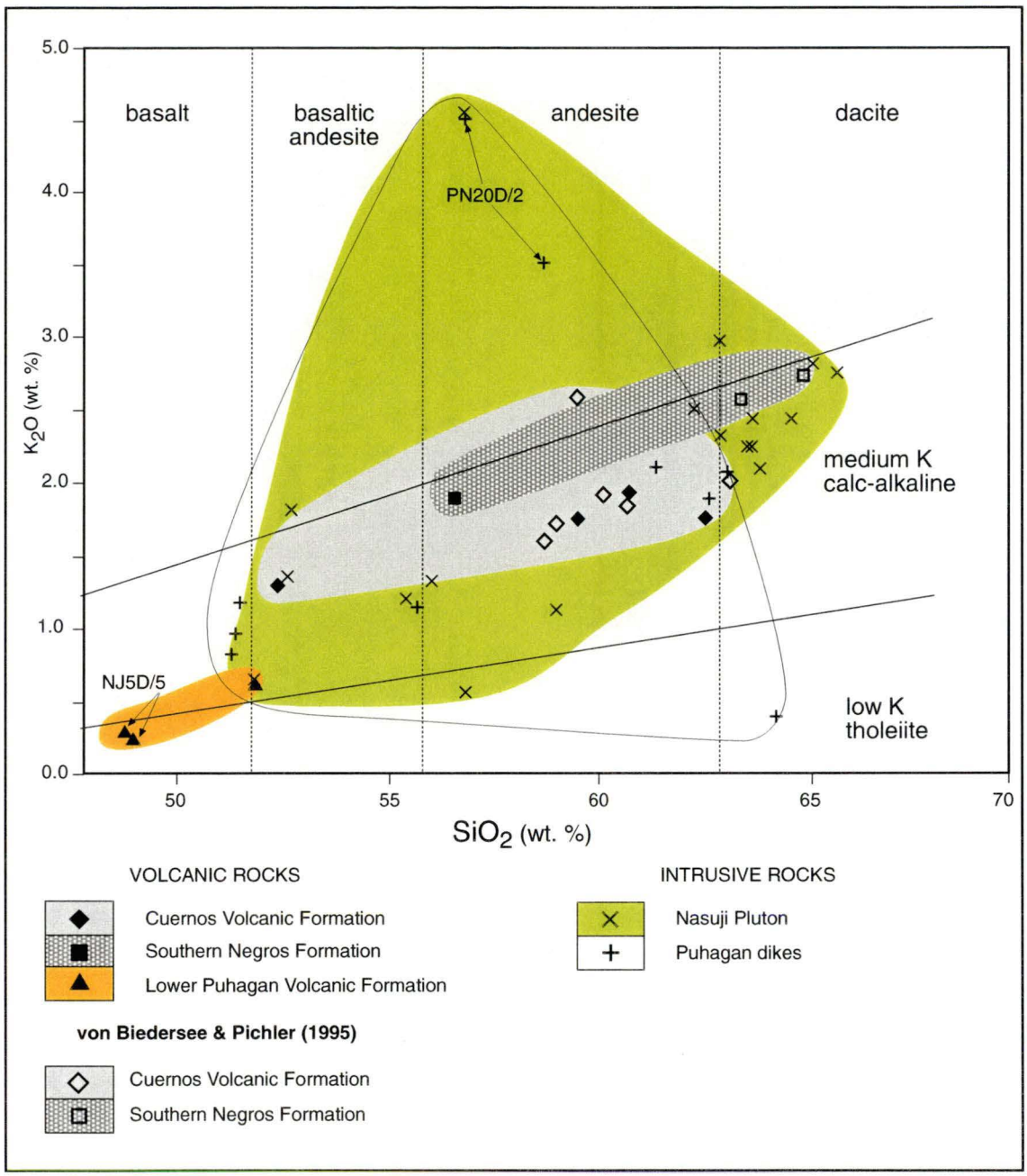

Figure 2.12. SiO_2 vs K_2O classification diagram of Peccerillo & Taylor (1976) for southern Negros rocks, incorporating data from von Biedersee & Pichler (1995). The southern Negros rocks plot mainly in the medium K calc-alkaline field and range in composition from basalt to dacite.

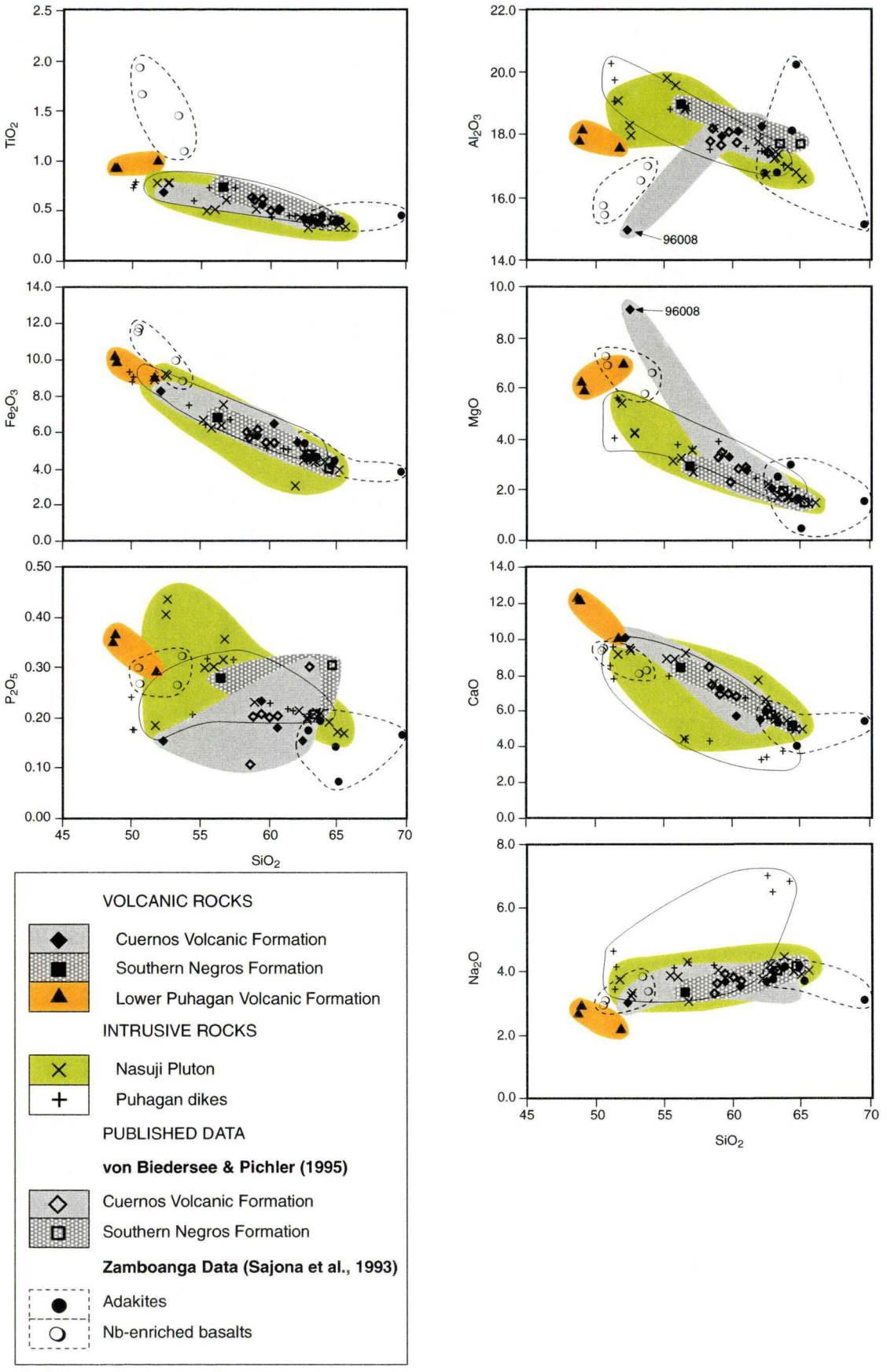

Figure 2.13. Major element vs. SiO_2 variation diagrams for southern Negros rocks, including analyses from von Biedersee & Pichler (1995), and comparisons with adakites and Nb-enriched basalts from Zamboanga, Mindanao (Sajona et al., 1993).

Compared with the other major elements, Al_2O_3 and P_2O_5 values are more erratic. With increasing SiO_2, Al_2O_3 has a negative trend for all fields except for the Cuernos Volcanic Formation, which has a positive slope (Figure 2.13) that is possibly caused by plagioclase fractionation.

2.7.2. Trace Elements

Trace element compositions are listed in Table 2.2 and illustrated as a function of SiO_2 content on Figure 2.14. Concentrations are generally typical for medium-K, calc-alkaline rocks of the SW Pacific (Ewart, 1982). However, most rocks from southern Negros Island have abnormally high Sr (500-1498 ppm) compared to typical SW Pacific calc-alkaline rocks (527-661 ppm; Ewart, 1982). Also, some of the Y concentrations (12-22 ppm) are lower than typical SW Pacific calc-alkaline rocks (18.7-26.0 ppm; Ewart, 1982). An exception is Cuernos Volcanic andesite 96010, which is Y enriched (35 ppm; Figure 2.14). The olivine-bearing Cuernos Volcanic basaltic andesite (96008) contains higher Cr (385 ppm) concentrations compared to other southern Negros Island rocks with equivalent SiO_2 contents (Table 2.2; Figure 2.14).

Primitive mantle-normalised, multi-element variation diagrams (Figure 2.15) have slopes with LILE enrichment and depletions for the HFSE, Nb and Ti. Both features are characteristic of island arc magmas (Gill, 1981). However, two samples have high Nb concentrations. Samples PN25D/2 and PN20D/2 contain 9.1 ppm and 14.0 ppm Nb, respectively, compared to 4.3 to 6.8 ppm Nb for typical SW Pacific calc-alkaline rocks (Ewart, 1982). Sample PN25D/2, a basalt from the Lower Puhagan Volcanic Formation, has a relatively flat trace element pattern that lacks a negative Nb anomaly (Figure 2.15b). Sample PN20D/2, a diorite from the Puhagan dikes, contains the highest Nb concentration (14.0 ppm) and has a steeper trace element pattern with a more pronounced LILE enrichment (Figure 2.15d). Along with Nb, this sample also has the highest concentrations of Zr, Sr, Ba and Rb (Table 2.2).

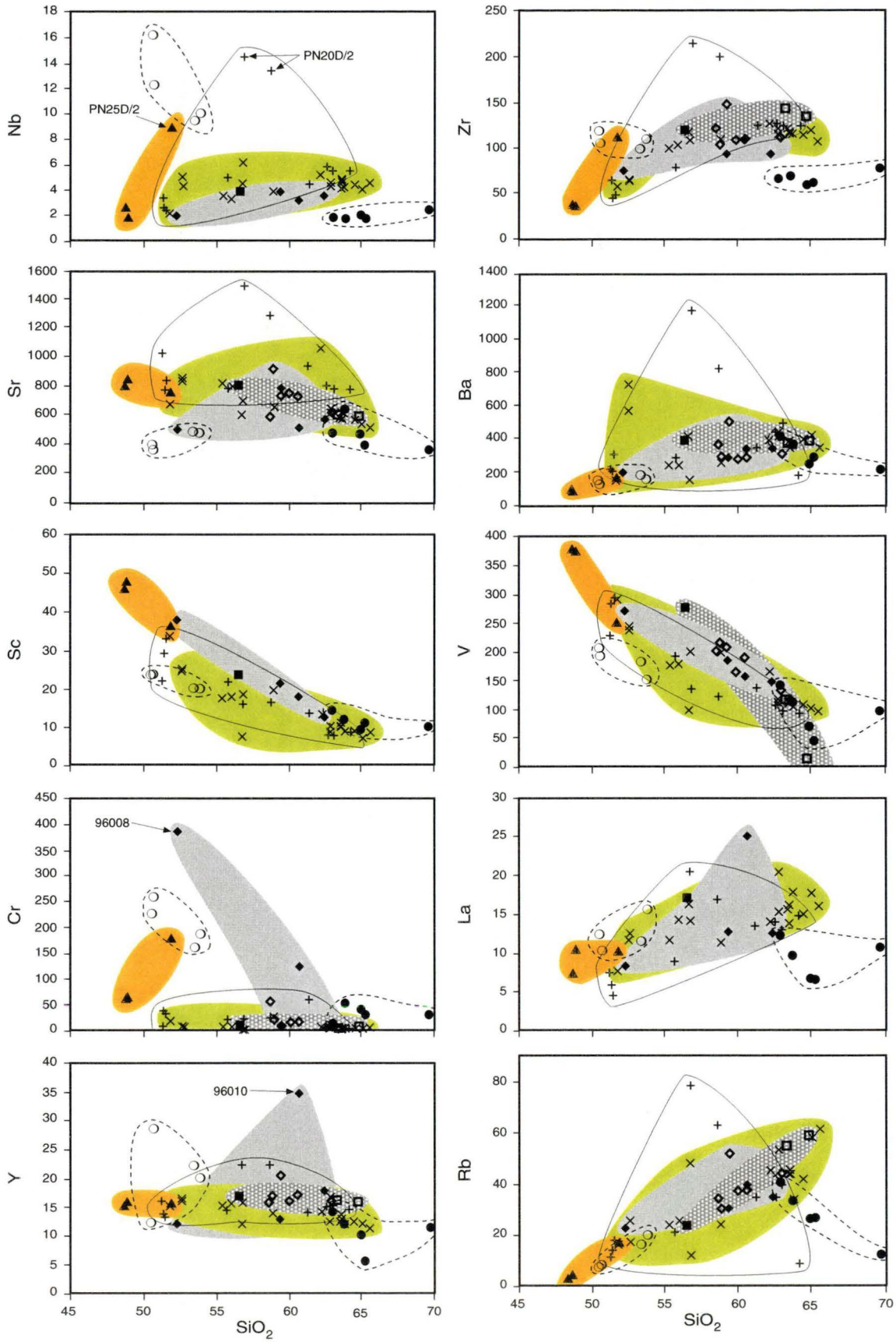

Figure 2.14. Trace element vs. SiO_2 variation diagrams for southern Negros igenous rocks with comparisons to adakites and Nb-enriched basalts from Zamboanga, Mindanao (Sajona et al., 1993). Some data from von Biedersee & Pichler (1995) are also shown. Symbols and shaded fields as for Figure 2.13.

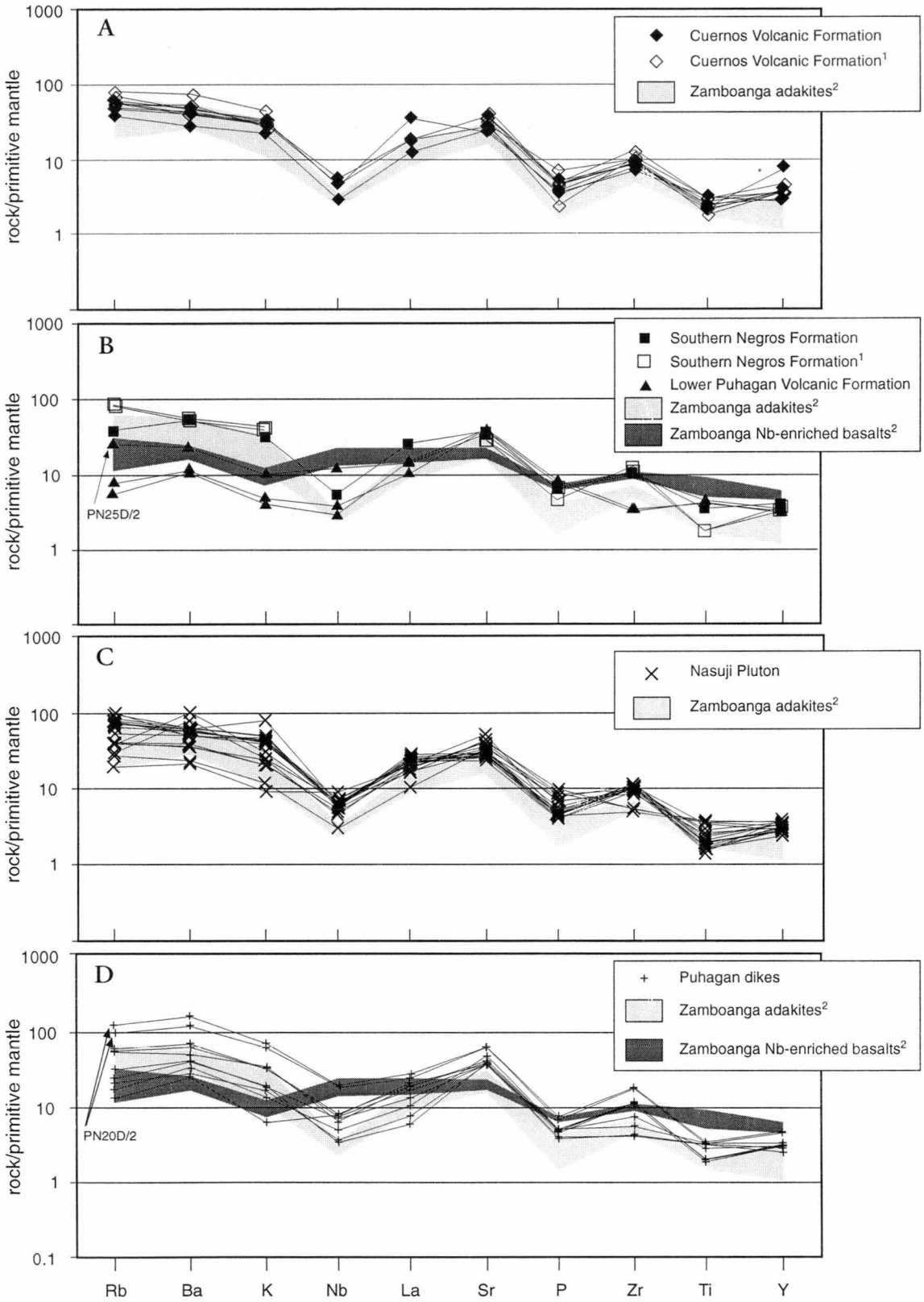

Figure 2.15. Primitive mantle normalised multi-element variation diagrams for southern Negros igneous rocks with comparisons to adakites and Nb-enriched basalts from Zamboanga. **A.** Cuernos Volcanic Formation. **B.** Southern Negros Volcanic and Lower Puhagan Volcanic Formations. **C.** Nasuji Pluton. **D.** Puhagan dikes. Sources of published data : [1] von Biedersee & Pichler (1995); [2] Sajona et al. (1993).

2.8. DISCUSSION

2.8.1. Petrogenesis

Studies of volcanic arc magmas have drawn attention to a unique rock type termed adakites (Defant and Drummond, 1990), after they were first documented from Adak Island, Alaska (Kay, 1978). They are volcanic or intrusive rocks characterised by $SiO_2 \geq 56\%$, $Al_2O_3 \geq 15\%$, MgO usually < 3%, low Y ($\leq$ 18 ppm), low HREE (e.g., Yb $\leq$ 1.9 ppm), high Sr (rarely < 400 ppm) and $^{87}Sr/^{86}Sr < 0.7040$ (Defant and Drummond, 1990). Petrographically, they are indistinguishable from typical calc-alkaline andesites and dacites with phenocrysts of plagioclase and amphibole in all but MgO-rich varieties. Other phenocrysts which may be present are clinopyroxene, orthopyroxene, biotite and FeTi-oxides. Adakitic andesites and dacites have been described in many subduction-related settings, e.g. western Aleutians (Kay, 1978; Yogodzinski et al., 1995), Panama-Costa Rica (Defant et al., 1991a; 1991b; 1992), northern Kamchatka (Kepezhinskas, 1989; Hochstaedter et al., 1994), the Cascades, western USA (Defant and Drummond, 1993), southern South America (Kay et al., 1993; Stern and Kilian, 1996; Gutscher et al., 2000), Hunter Ridge, Fiji (Verbeeten, 1996), and the islands of Luzon, Negros, Mindanao, Catanduanes, Camiguin and Batan, Philippines (Sajona et al., 1993; 1994; 2000a; 2000b; Schiano et al., 1995; Sajona and Maury, 1998; Castillo et al., 1999; Yumul et al., 2000).

The origin of adakitic magmas has been attributed to the partial melting of subducted oceanic basalt that has undergone eclogite facies metamorphism (Kay, 1978; Defant and Drummond, 1990; Drummond and Defant, 1990), implying subducted slab temperatures in excess of 700°C at relatively shallow depths (75-85 km; Sajona et al., 1993). The model commonly proposed to account for these high temperatures at shallow levels is subduction of oceanic crust that is young (i.e., < 25 Ma) and hence, still hot (Defant and Drummond, 1990; Sajona et al., 1993; Peacock et al., 1994). However, it is possible more than one tectonic setting is capable of generating slab melts and alternative settings have been proposed. These are: initiation and cessation of subduction (Sajona et al., 2000b); subduction associated with high shear stresses (> 100 MPa; Peacock et al., 1994); and subduction of oceanic crust at a low angle (i.e., < 30°; Gutscher et al., 2000).

Many adakite occurrences are temporally and spatially associated with high-Nb basalts (Reagan and Gill, 1989; Defant et al., 1992; Defant and Drummond, 1993; Prouteau et al., 2000). This association has been noted in Costa Rica (Reagan and Gill, 1989), northern Kamchatka (Hochstaedter et al., 1994), Fiji (Verbeeten, 1996) and Mindanao, Philippines (Sajona et al., 1993; 1994; 1996; Prouteau et al., 2000). Unlike typical island arc magmas, high-Nb basalts are enriched in HFSE and have low LILE/HFSE ratios, high Nb (> 20 ppm) and TiO_2 (1-2%), and mantle-normalised La/Nb $\{(La/Nb)_{MN}\}$ ratios < 2 (Sajona et al., 1996). Their

mantle-normalised trace element plots typically lack a negative Nb anomaly. The basalts associated with adakites from Zamboanga Peninsula, Mindanao, have lower Nb concentrations, 7 to 16 ppm, and Sajona et al. (1993) termed these rocks Nb-enriched basalts. The adakite – high-Nb basalt association suggests a petrogenetic link and it has been proposed that magmas high, or enriched, in Nb are generated from a mantle lithosphere that has been metasomatised by slab melts (Defant et al., 1992; Defant and Drummond, 1993).

The trace element chemistry of the southern Negros Island rocks are compared with the adakites and Nb-enriched basalts from Zamboanga in Figure 2.15. Most rocks from southern Negros Island show similar trace element patterns to the Zamboanga adakites with low Nb, P, Ti and Y, and high Sr concentrations (Figure 2.15). The Sr/Y vs Y plot illustrated in Figure 2.16, is a useful adakite discrimination diagram (Defant et al., 1991b) and shows that most southern Negros Island rocks lie within the adakite field. An exception is the Cuernos Volcanic andesite, 96010, which plots well outside the adakite field within the field for typical calc-alkaline island arc magmas derived from fractionation of mantle-derived basalts (Figure 2.16; Defant et al., 1991b). Adakites from Cuernos de Negros have been documented previously by Sajona et al. (2000a), who showed that they can be derived by batch partial melting of an eclogitic N-MORB-like source. This is supported by their Sr, Nd and Pb isotopic compositions, which fall within the range for a MORB source (Castillo, 1996).

The two samples with high Nb concentrations, sample PN25D/2 (9.1 ppm Nb) and PN20D/2 (14.0 ppm Nb), have Nb values within the range for the Nb-enriched basalts of Zamboanga (7-16 ppm; Sajona et al., 1996) and $(La/Nb)_{MN}$ ratios < 2 (PN25D/2 = 1.2 and PN20D/2 = 1.4). The trace element patterns for these two rocks are compared with the Nb-enriched basalts from Zamboanga in Figures 2.15b and 2.15d. The relatively flat trace element pattern of the Lower Puhagan Volcanic Formation sample (PN25D/2) closely matches that of the Zamboanga Nb-enriched basalts (Figure 2.15b). The steeper trace element pattern for Puhagan dike sample PN20D/2 closely mirrors the adakite pattern but with higher concentrations for all the trace elements in Figure 2.15d.

The results of this current study show that adakitic and Nb-enriched magmas have been generated in this region since Middle Miocene times. However, the complex tectonic history of the Philippine Archipelago makes it difficult at present to rule out any one of the processes responsible for the generation of such magmas. After the following discussion of the regional tectonics, the most likely scenarios are presented Section 2.9.

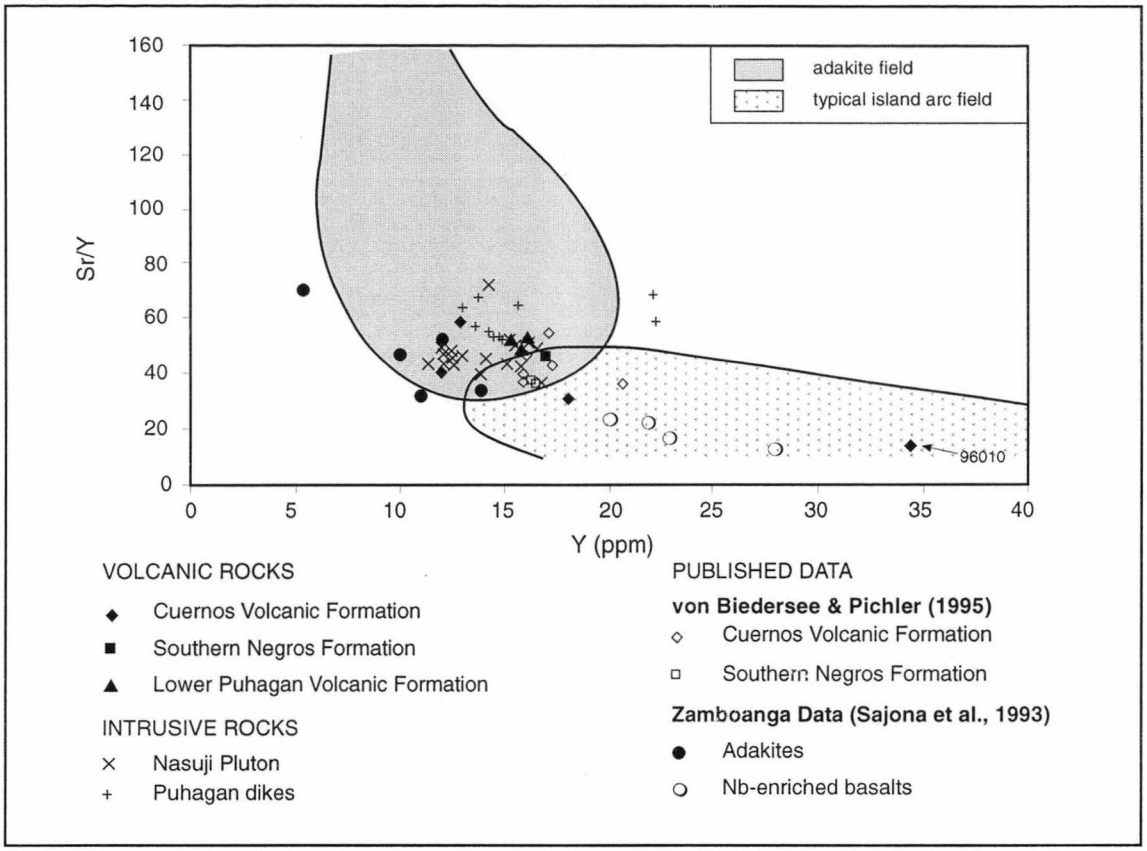

Figure 2.16. Sr/Y vs. Y diagram for southern Negros and Zamboanga igneous rocks. Data are from this study, von Biedersee & Pichler (1995) and Sajona et al. (1993). Also shown are fields defined by Defant et al. (1991) for adakites and typical island arc andesite-dacite-rhyolite rocks.

2.8.2. Regional Tectonic History

The three volcanic formations of southern Negros Island are products of island arc magmatic activity that occurred during Middle Miocene (Lower Puhagan Volcanics) and Late Pliocene (Southern Negros Formation) to Pleistocene (Cuernos Volcanic Formation) times. This magmatic activity also resulted in the emplacement of intrusions during the Early Pliocene (Puhagan dikes) and Pleistocene (Nasuji Pluton). Despite the different ages and emplacement styles (i.e., intrusive or extrusive), the igneous rocks of southern Negros all have medium K, calc-alkaline, basaltic to dacitic compositions. A lack of contrasting fractionation trends between the different igneous rock formations simply reflects a regional tectonic setting influenced by island arc magmatism during Late Tertiary and Quaternary times. The recognition that all igneous rock formations have adakitic, and some with Nb-enriched basaltic, affinities implies that island arc magmatism in this region has been influenced by the melting of subducted oceanic basalt.

The Middle Miocene was a period of widespread volcanic activity in the Visayas region (Rangin, 1989) and volcanic rocks of this age are distributed from Zamboanga (Sajona et al., 1993) in the south, and northwards to the central Visayas region (Figure 2.11) and the Valderrama Volcanics of western Panay (Figure 1.2; Rangin, 1989). Volcanism at this time produced adakites and Nb-enriched basalts on southern Negros Island and Zamboanga Peninsula (Figure 2.17; Sajona et al., 1993). The occurrence of marine microfossils as bioclasts in the Middle Miocene Lower Puhagan Volcanic breccias and sediments indicates deposition in a subaqueous environment.

Middle Miocene volcanic activity is believed to be related to southeasterly-directed subduction of the Sulu Sea oceanic basin beneath the Sulu arc (Rangin and Silver, 1991; Silver and Rangin, 1991). The Sulu Sea oceanic basin apparently opened in a back-arc position behind the Cagayan Ridge volcanic arc (Figure 2.17; Silver and Rangin, 1991) during either Early Oligocene (Roeser, 1991) or Early Miocene (Rangin and Silver, 1991) times. By the Middle Miocene an arc-continent collision, involving the Palawan continental fragment, halted subduction at the Cagayan Ridge and the southeasterly-directed subduction transferred south to the Sulu arc (Rangin and Silver, 1991). Consequently the subduction of the Sulu Sea basin during Middle Miocene times involved oceanic crust no older than 20 Ma and was conducive to the generation of adakitic and Nb-enriched basaltic magmas (Defant and Drummond, 1990; Sajona et al., 1993). This Middle Miocene volcanic activity was relatively short-lived, as subduction ceased during Late Miocene times with the collision of the Cagayan Ridge at Panay (Figure 2.17; Rangin and Silver, 1991).

The adakitic and Nb-enriched Puhagan dikes were emplaced during Early Pliocene times, a period when evidence for major regional volcanism is lacking (Rangin et al., 1989).

Nevertheless, about this time subduction of the Sulu Sea basin began along the Negros-Sulu Trench after the continental Zamboanga terrane collided with central Mindanao (Pubellier et al., 1991). Therefore, it is possible that generation of adakitic and Nb-enriched magmas at this time is related to the initiation of subduction along the Negros-Sulu Trench (Sajona et al., 2000b).

South and eastward subduction of the Sulu Sea basin along the Negros-Sulu trench system continued into Late Pleistocene and Recent times. This produced arc-related igneous rocks on southern Negros Island and Zamboanga Peninsula with the chemical characteristics of adakites, Nb-enriched basalts and typical calc-alkaline island arc magmas (Figure 2.17; Sajona et al., 1993; 1996; 2000a). On southern Negros Island this magmatism produced a thick sequence (> 2000 m) of volcanic and volcaniclastic rocks (Southern Negros and Cuernos Volcanic Formations) and an intrusion (Nasuji Pluton). These igneous rocks have adakitic geochemical characteristics, but the Cuernos Volcanic Formation also contains rocks with normal calc-alkaline island arc chemistry derived by fractionation of typical mantle-derived arc basalts.

The age of the Sulu Sea crust currently subducted beneath the region is either approximately 10 Ma, based on magnetic lineations (Roeser, 1991), or 20 Ma based on palaeontological evidence (Rangin and Silver, 1991). Heat flow studies in the southeast Sulu Sea basin reveal thermal gradients as high as 200°C/km (Hinz and Block, 1990), which may account for the aseismic nature of subduction along the Sulu Trench (Pubellier et al., 1991). Thus, the occurrence of Late Pliocene to Pleistocene adakites and Nb-enriched basalts/basaltic andesites in Zamboanga and southern Negros Island can be explained by the abnormally high thermal regime of the subducted oceanic crust, conditions that are conducive for slab melting to occur (Sajona and Maury, 1998; Prouteau et al., 2000).

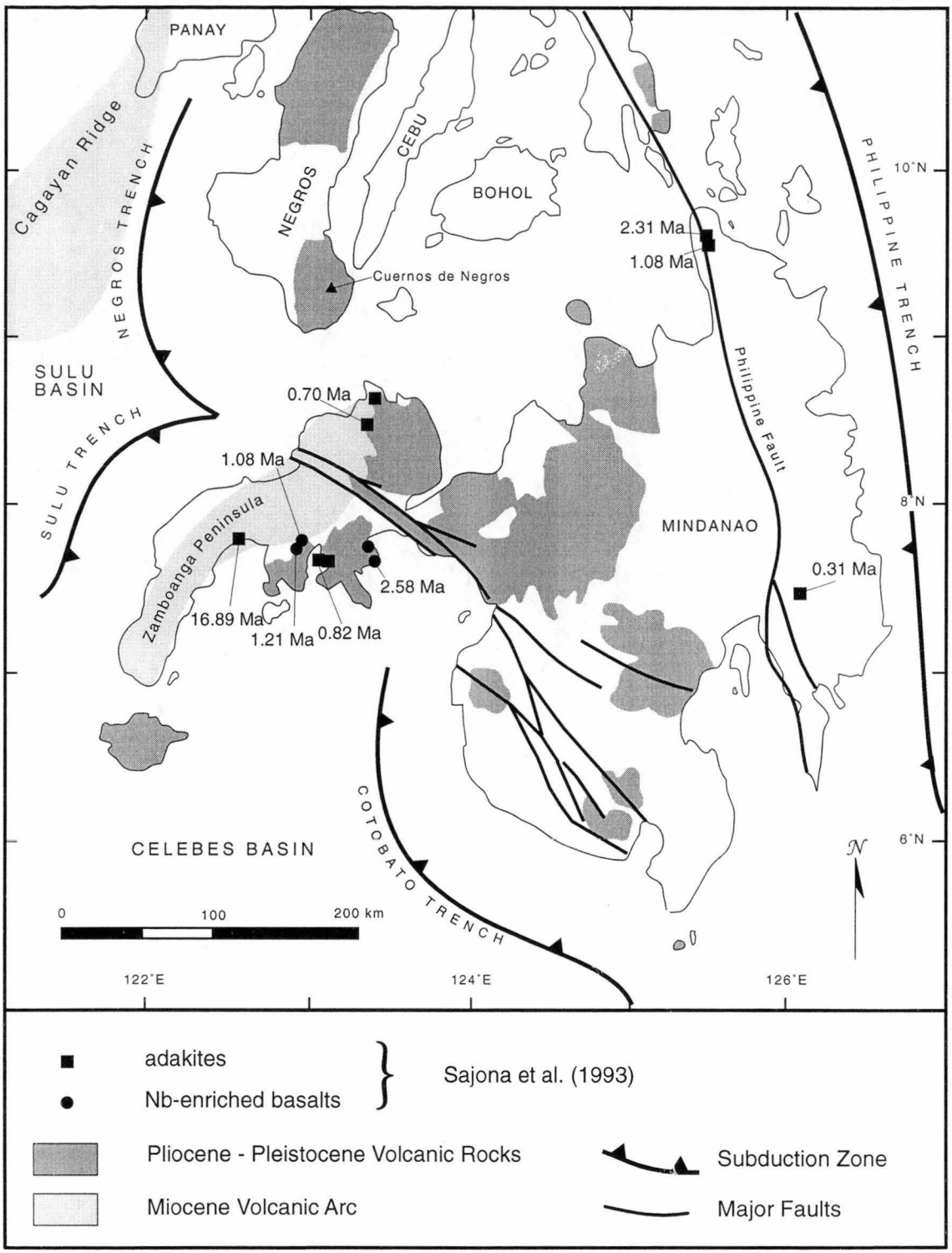

Figure 2.17. Tectonic setting of Mindanao and Negros Islands showing the sample locations of the Zamboanga adakites and Nb-enriched basalts. The adakites of eastern Mindanao are believed to be related to subduction along the Philippine Trench (Sajona et al., 1993).

2.9. SUMMARY AND CONCLUSIONS

Correlation of Palinpinon rock formations with Visayas stratigraphy constrains the formation ages and provides the regional geological context for the Palinpinon geothermal field. Igneous rock formations in southern Negros Island are the products of regional island arc magmatism that occurred during the Middle Miocene and since Early Pliocene times. The oldest formation (Lower Puhagan Volcanic Formation) is part of a volcanic sequence that is traceable throughout the Visayas region and is a product of Middle Miocene arc volcanism. In southern Negros, this volcanism resulted in deposition of basaltic breccias and sediments in a subaqueous environment. Late Miocene to Early Pliocene times marked a period of regional subsidence and marine sedimentation (Porth et al., 1989; Rangin et al., 1989) and a thick sequence of calcareous sediments (Okoy Formation) was deposited. Resurrection of magmatism in Early Pliocene to Recent times coincided with commencement of subduction at the Negros-Sulu Arc. This produced basaltic andesites and andesites belonging to the Southern Negros and Cuernos Volcanic Formations. The lack of any observed marine sedimentary clasts in the Southern Negros Formation breccias may imply it is the product of subaerial volcanism. Hence, there may have been a regional evolution from submarine (Lower Puhagan Volcanic Formation) to subaerial (Southern Negros Formation) volcanism, with a transitional shallow marine sequence (Okoy Formation). This evolution implies uplift and/or growth and emergence of the volcanic edifice with time.

The Puhagan dikes and the Nasuji Pluton intruded Middle Miocene, Late Miocene and Early-Late Pliocene formations. The radiogenic age difference between the Puhagan dikes (4.2-4.1 Ma) and the Nasuji Pluton (0.7-0.3 Ma) confirms that they are not genetically related.

Adakites have been produced in the southern Negros region since Middle Miocene times. Rocks with Nb-enriched basaltic affinities were produced during Middle Miocene and Early Pliocene times, whereas typical island arc calc-alkaline volcanic rocks were erupted only during Pleistocene times. The complex tectonic history of the region, with many phases of subduction, oceanic basin formation and island arc ridge collision, implies that slab melts may have been generated by: the subduction of young oceanic crust; subduction initiation or cessation; subduction at low angle due to the collision of buoyant arc ridge segments; or perhaps the least likely, subduction associated with high shear stresses. However, considering the regional tectonic history the most likely scenarios are: (1) during the Middle Miocene, slab melts were generated by the melting of relatively young (< 20Ma) oceanic crust; (2) during Early Pliocene times by the initiation of subduction along the Negros-Sulu Trench; and (3) during Late Pliocene times, by the melting of young (< 20-10 Ma) oceanic crust.

The total duration of geothermal activity in the region is unknown. It may have been occurring for as long as there has been magmatic activity. Although spatially related, the 4 Ma age of the

Puhagan dikes rules them out as the heat source for the active geothermal system. Evidence shows the hydrology is controlled by a complex array of faults and a heat source that is situated beyond depths drilled in the Puhagan area.

3. HYDROTHERMAL ALTERATION AND MINERALISATION

3.1. INTRODUCTION

Alteration mineral assemblages associated with active or extinct hydrothermal systems provide important insights into the physicochemical nature of the fluids responsible. The zonal distribution patterns and overprinting relationships of alteration assemblages can show how fluid chemistry has evolved both spatially and temporally in a given system.

Previous workers (Leach and Bogie, 1982; Reyes, 1990; Mitchell and Leach, 1991; Corbett and Leach, 1998) have drawn parallels between the types of alteration recognised at Palinpinon and mineralised magmatic-hydrothermal ore systems (specifically, porphyry Cu deposits). However, a detailed and systematic investigation of base and precious metal mineral occurrences at Palinpinon has never previously been attempted.

This section of the thesis describes the different hydrothermal alteration types at the Palinpinon geothermal field, their distribution and the extent of any associated base and precious metal mineral occurrences. This has led to clarification and in some cases the redefinition of zones of alteration originally defined by Leach and Bogie (1982). For each alteration assemblage, the associated sulphide mineralogy is documented. This provides a basis for a discussion on the evolution of the Palinpinon hydrothermal system and the genetic links between contrasting types of hydrothermal alteration and any related base and/or precious metal mineral assemblages.

3.2. METHODS

For this research project, hydrothermal alteration and sulphide mineral assemblages at the Palinpinon geothermal field have been investigated mostly by petrographic examination of drillcore. During drilling of the Palinpinon geothermal wells, drillcore samples were recovered typically from the deeper regions of the stratigraphic sequence (i.e., below sea level) and so most of the petrographic information obtained from core samples pertains to these deeper regions. In total, 171 drillcore from 58 geothermal wells were examined using polished thin section microscopy and infrared absorption spectroscopy (Portable Infrared MicroAnalyser: PIMA and Fourier Transform InfraRed: FTIR). Drillcuttings, collected from 24 wells at 100 m depth intervals, were also investigated using infrared spectroscopy and this provided the petrographic information for the shallow regions of the geothermal system (i.e., above sea level). For geothermal wells for which drillcores and/or cuttings were no longer available (i.e. either missing or not able to be collected), petrographic information was collated from unpublished PNOC-EDC company well-log files. PNOC-EDC and consulting geologists compiled their petrographic information using thin section petrography, coupled with XRD

analysis. Extending the information collected from the drillcores and drillcuttings, samples from areas of surface alteration were also examined using polished thin section microscopy and infrared absorption spectroscopy.

To gain a better understanding of the spatial relationships between the hydrothermal alteration assemblages, intrusions, and downhole measured temperatures, the reader is referred to the 3D Datamine images hyperlinked in the PowerPoint file (Palinpinon.ppt) in Appendix 4. The relevant images contain isograd surfaces (or wireframes) of the shallowest occurrences of a few characteristic minerals (e.g., biotite, garnet, epidote, illite, alunite) from the hydrothermal alteration assemblages described in this section.

To determine the character and extent of precious and base metal mineral occurrences, polished thin section microscopy was augmented with bulk rock XRF analysis of drillcores and drillcuttings. Drillcuttings from three geothermal wells were analysed as composites from 100 m intervals. In addition, 25 drillcore samples from 20 geothermal wells were included in the analytical sample suite to test the quality of the cuttings XRF data.

Radiogenic ($^{40}Ar/^{39}Ar$, K/Ar) geochronology of potassium-bearing alteration phases has been used to establish temporal relationships between biotite and advanced argillic alteration types and the intrusions. Aluminium-phosphate-sulphate (APS) minerals in the hypogene advanced argillic alteration assemblage were identified by scanning electron microscope imaging (SEM) and qualitative energy dispersive X-ray analysis (EDAX). Fluid inclusion heating and freezing measurements were carried out on quartz vein material to detect any systematic variation in fluid temperature and composition across the hydrothermal system. Analysis of a few fluid inclusions by Proton Induced X-ray Emission (PIXE) was undertaken to quantify metal concentrations.

3.3. PREVIOUS WORK

Extensive work on the hydrothermal alteration at Palinpinon was undertaken by PNOC-EDC and consulting geologists during the development of the geothermal steamfield. This was mostly presented in unpublished company reports and well-log files, but was then synthesised in Leach and Bogie (1982), Reyes (1990), Mitchell and Leach (1991) and Corbett and Leach (1998).

Leach and Bogie (1982) proposed two episodes or regimes of hydrothermal alteration. A 'relict' hydrothermal alteration regime that is spatially related to the Nasuji Pluton and a later, more recent event associated with the active geothermal system. These 'recent' assemblages have overprinted earlier-formed hydrothermal mineral assemblages, and are in approximate thermal equilibrium the modern geothermal system.

Early-formed potassic, advanced argillic, phyllic and propylitic alteration zones have been distinguished by Leach and Bogie (1982) at Palinpinon (Figure 3.1). Rocks belonging to the Cuernos Volcanic Formation are not affected by these alteration styles, implying that a relict hydrothermal system was active prior to formation of these surface volcanics (i.e., < 14 000 yr. BP.; Mitchell and Leach, 1991). The temperatures and fluid chemistries required for the formation of the associated mineral assemblages in the relict suite of alteration assemblages are different than the conditions within the present geothermal system (Leach and Bogie, 1982). The relict nature of these alteration zones is more obvious where high temperature mineral assemblages have been exposed at the surface, but their origin is less certain at depth. It is particularly difficult to discriminate relict phyllic and propylitic alteration assemblages from those related to the present alteration regime.

The potassic alteration zone occurs at the top of the Nasuji Pluton, extending into the overlying volcanics of the Southern Negros Formation (Figure 3.1). Advanced argillic alteration is restricted to the western part of the geothermal field above the potassic zone (Figure 3.1). East of the advanced argillic alteration zone, a phyllic zone occurs from about 1000 m elevation to approximately 400 m bsl (Figure 3.1). Propylitic alteration occurs distally to the Nasuji Pluton and main geothermal upflow zone. It occurs mainly east of the phyllic zone in the Southern Negros Formation beneath the Puhagan area (Figure 3.1). The propylitic assemblage appears to have been overprinted by phyllic alteration mineral assemblages (Leach and Bogie, 1982).

In contrast to the 'relict' assemblages, 'recent' alteration assemblages occur in rocks belonging to the Cuernos Volcanic Formation (Figure 3.2). The Cuernos Volcanic Formation and upper levels of the Southern Negros Formation are affected by a 'low grade alteration' assemblage (smectite, interlayered smectite-illite, illite; Leach and Bogie, 1982). At depths approximately greater than 600 m bsl, a propylitic alteration assemblage occurs in apparent thermal equilibrium with measured downhole temperatures. This zones grades with depth into a zone of skarn, or 'lower propylitic' (Leach and Bogie, 1982; Mitchell and Leach, 1991) alteration, developed in the calcareous sediments and underlying volcanics at temperatures in excess of 300° C. At greatest depths and temperatures, the occurrence of biotite indicates a zone of potassic alteration (Figure 3.2; Leach and Bogie, 1982). In the Nasuji-Sogongon area, the relict potassic zone is overprinted by lower temperature phyllic and propylitic alteration assemblages.

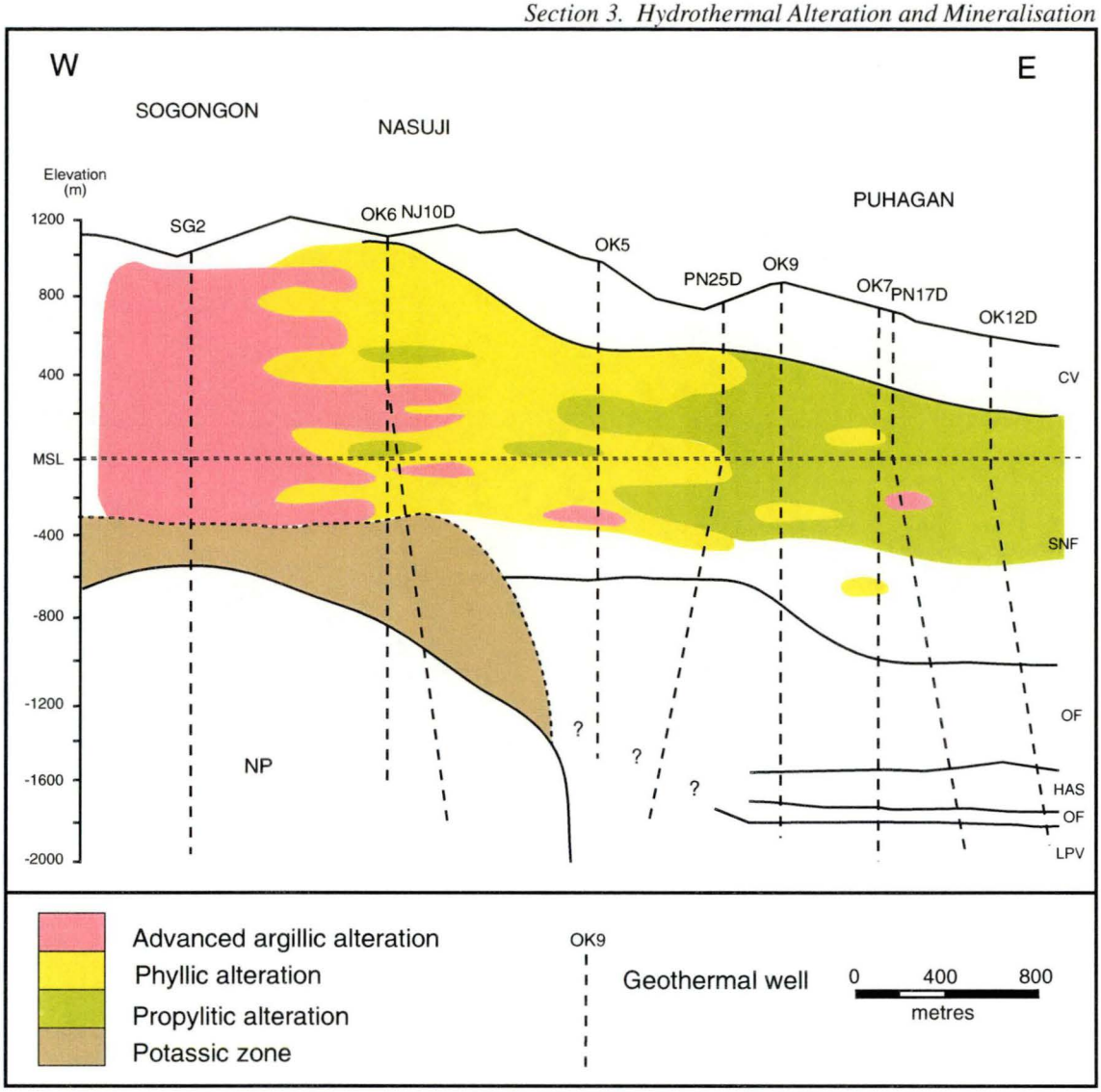

Figure 3.1. West-east cross section through the Palinpinon geothermal field showing the zones of relict alteration. Solid lines represent lithologic boundaries : CV=Cuernos Volcanics; SNF=Southern Negros Formation; OF=Okoy Formation; HAS=hornblende andesite sill; LPV=Lower Puhagan Volcanics; NP=Nasuji Pluton. From Leach & Bogie (1982).

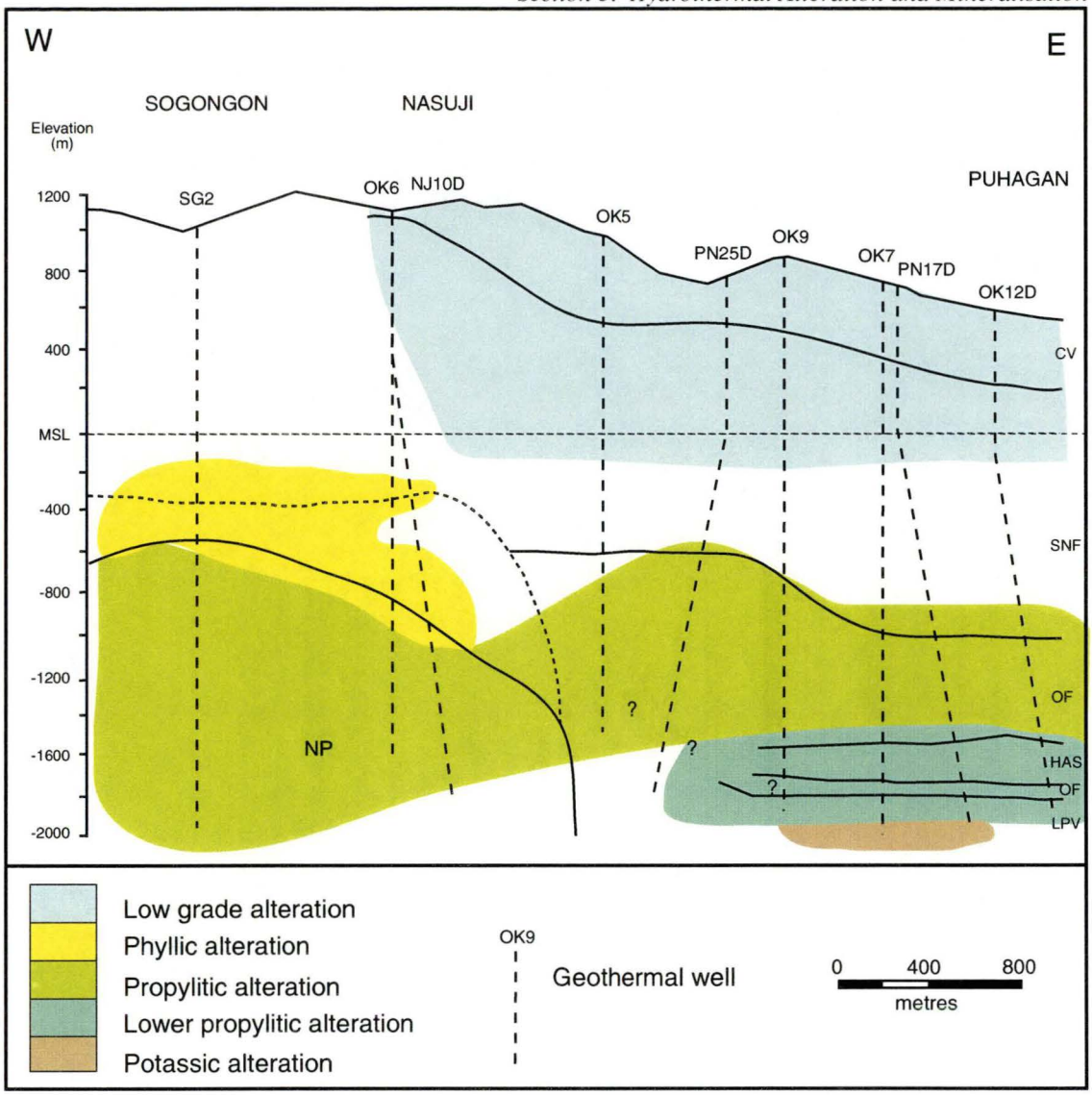

Figure 3.2. West-east cross section through the Palinpinon geothermal field showing the zones of recent alteration. Solid lines represent lithologic boundaries : CV=Cuernos Volcanics; SNF=Southern Negros Formation; OF=Okoy Formation; HAS=hornblende andesite sill; LPV=Lower Puhagan Volcanics; NP=Nasuji Pluton. From Leach & Bogie (1982).

Investigations into areas of surface alteration in the Okoy Valley and the kaipohan areas were undertaken by Celenk et al. (1987) and Bogie et al. (1987), respectively. In the Okoy Valley, areas of propylitic (chlorite, epidote, illite), advanced argillic (kaolinite, alunite, sulphur, jarosite, ± cristobalite, ± tridymite, ± opal) and silicic alteration (quartz, illite) are present (Celenk et al., 1987). Propylitic alteration has affected rocks in the headwaters of the Okoy Valley in Nasuji-Sogongon, covering an area approximately 2 x 3 km. It is overprinted by silicification and advanced argillic alteration types. Areas of advanced argillic alteration and silicification occur as prominent ridges along the length of the valley (Figure 3.3), some of which are associated with thermal springs and steam discharges (Celenk et al., 1987). Rocks in the kaipohan areas are pervasively altered to an advanced argillic assemblage of amorphous silica, kaolinite, smectite, alunite and native sulphur (Bogie et al., 1987).

A geochemical survey of the alteration zones in the Okoy Valley was undertaken using stream sediment, soil and rock samples (Celenk et al., 1987). The results showed that metal occurrences are poorly developed and sporadic. Some of the propylitically-altered rocks were found to be elevated in Cu (150-1270 ppm), Mo (2-27 ppm) and Mn (> 1000 ppm). Rocks from silicified zones are enriched in Au (≤ 1.3 ppm) and Ag (≤ 19 ppm), but with appreciable quantities of Sb (> 10 ppm), Hg (> 0.5 ppm) and Bi (> 10 ppm), whereas advanced argillic altered rocks were found to have high As (> 100 ppm) and Tl (1-3 ppm).

3.4. WALLROCK ALTERATION AND MINERALISATION

3.4.1. Alteration and Mineralisation Types and Their Distribution

The following description of the hydrothermal alteration types at Palinpinon uses a nomenclature (Meyer and Hemley, 1967; Titley, 1982) based on the predominant mineral, or group of minerals that characterises each alteration assemblage, to classify a particular alteration type. The five alteration types that have been distinguished at Palinpinon are biotite, calc-silicate, propylitic, illite and advanced argillic. The following section defines and describes the mineralogy and distribution of each alteration type. Comparisons are made between hydrothermal mineral stability temperatures (Table 3.1) and the current downhole measured temperatures to gain further insights into the evolution of the hydrothermal system. Mineral stability temperatures were determined empirically by Reyes (1990) based on their observed mineral occurrences in several Philippine geothermal systems.

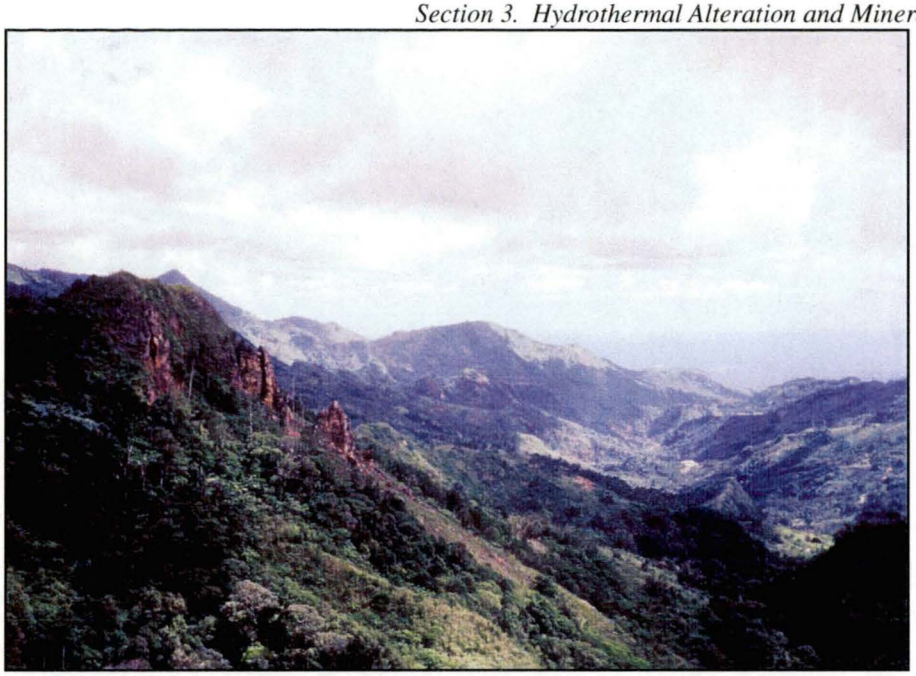

Figure 3.3. View looking eastward down the Okoy Valley from the Nasuji-Sogongon area. Alunite ridges and bluffs occur on the northern valley slopes and can be seen in the left foreground and in the middle distance.

Table 3.1. Mineral stability temperatures for hydrothermal alteration minerals at Palinpinon. Temperature ranges were determined empirically from several Philippine geothermal systems by Reyes (1990).

Minerals	Temperature 100°C	200°C	300°C
Tremolite-actinolite (>280°C)			
Biotite (>270°C)			
Epidote (>250°C)			
Prehnite (250-310°C)			
Wairakite (220-320°C)			
Illite (220-310°C)			
Albite (170-320°C)			
Chlorite (>120°C)			
Smectite (20-200°C)			
Kaolinite (20-200°C)			
Alunite (40-290°C)			
Diaspore (>110°C)			
Dickite (120-280°C)			
Pyrophyllite (200-300°C)			
Zunyite (250-300°C)			
Andalusite (>260°C)			

Geothermal well locations, with their deviated traces projected to the surface, are illustrated in Figure 3.4. Also shown are the projected locations of the Nasuji Pluton and Puhagan dikes, along with surface sample locations and areas where surface alteration has been recognised. Three cross-sections have been drawn through the geothermal field (Figures 3.5 to 3.7) and the locations of each are indicated in Figure 3.4. The cross-sections show the distribution of rock units and alteration types. Also shown is the hydrology, in terms of the 100°C, 200°C, 250°C and 300°C isotherms, based on stabilised downhole measured temperatures. The difficulty when plotting deviated geothermal wells onto a cross-section is that well traces and their drillcore locations, need to be projected onto the plane of cross-section. Attempts have been made to keep projection distances to a minimum, but in some places they can be as much as 500 m. The three orientations of the drillhole traces, along with the location of mineral isograds relative to the intrusions and downhole measured temperatures can be seen in Appendix 4.

Biotite Alteration

Biotite alteration assemblages occur within and above the Nasuji Pluton and below the Puhagan dikes (Figure 3.5). Hydrothermal biotite is the diagnostic mineral of this assemblage but other minerals that are present locally include magnetite, quartz, anhydrite, orthoclase, albite, tremolite-actinolite, hematite, pyrite and chalcopyrite. Biotite alteration is manifested as a pervasive wallrock replacement (Titley, 1982), and is also confined to narrow breccia zones (< 50 mm) and veinlets (< 5 mm).

Pervasive biotite alteration has resulted in the host rock being altered to fine grained (< 0.1mm) biotite and orthoclase, along with disseminated magnetite and minor amounts (< 0.1 modal %) of pyrite and chalcopyrite. Where it is most intense, pervasive biotite alteration has obscured primary host rock textures (Figure 3.8a).

Small breccia zones associated with biotite alteration contain comminuted wallrock fragments (< 10mm) that are enclosed in a hydrothermally-altered matrix (Figures 3.8b and 3.8c). This matrix and the associated veinlets consist of fine grained (< 0.1 mm) biotite, quartz, anhydrite, ± orthoclase, ± albite, ± magnetite, ± hematite, ± pyrite ± chalcopyrite (Figure 3.8d). Hornblende in the wallrock adjacent to the breccia zones and veinlets has been selectively altered to fine grained biotite (Figure 3.8e) and plagioclase has been altered to orthoclase.

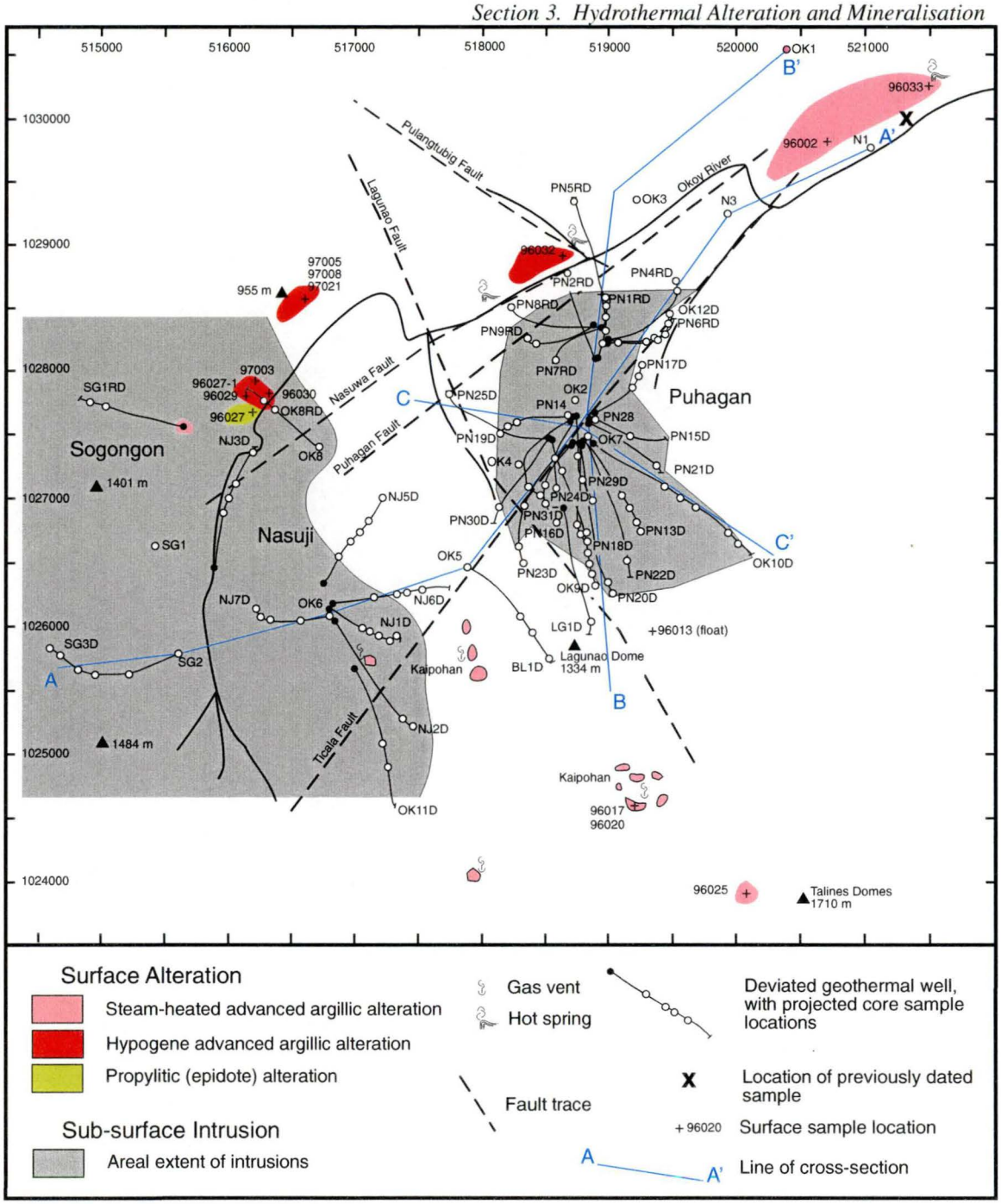

Figure 3.4. A geothermal well location map that shows the orientation of three cross-sections (A-A', B-B', C-C'; Figures 3.5 to 3.7, respectively), along with surface features, including fault traces, areas of hydrothermal alteration and active geothermal discharge features. Also shown is the location of a previously dated (K/Ar) illite-bearing sample (Zaide, 1984). The locations of the Nasuji Pluton (western sector) and the Puhagan dikes (central sector) are projected to surface. Figure 3.5 shows the subsurface extent of the intrusions.

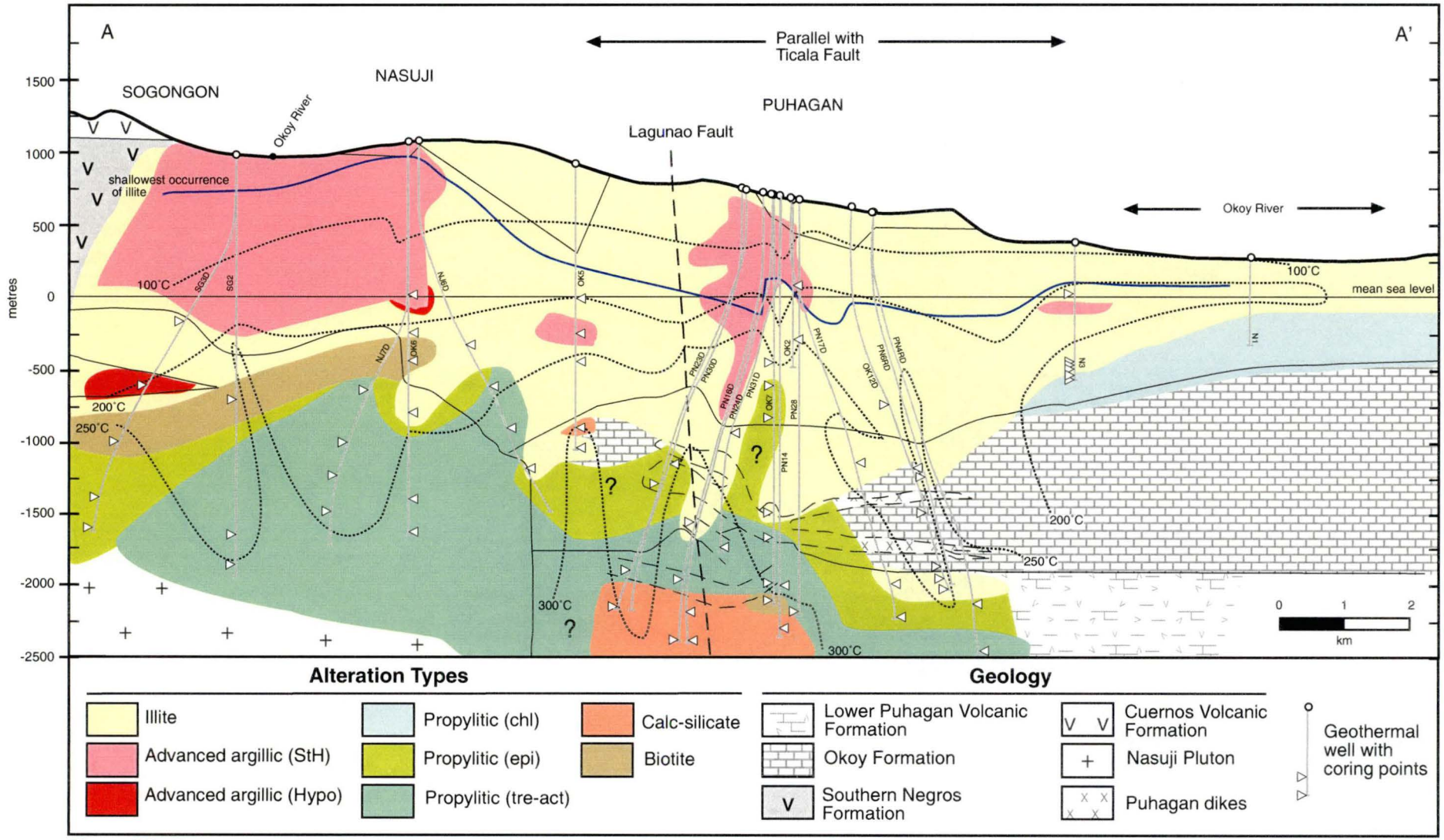

Figure 3.5. Cross-section along line A-A' (Figure 3.4) showing the distribution of alteration types relative to the geology and hydrology, as defined by the 100°, 200°, 250° and 300°C isotherms (dotted lines). The thin dashed lines represent the Puhagan dike contacts. All geologic contacts are inferred. See Figure 2.3 for the geology along the same cross-section line. The blue line shows the shallowest occurrence of illite in the illite alteration assemblage. At shallower depths smectite is the dominant phyllosilicate mineral. Alteration type abbreviations: chl = chlorite; epi = epidote; tre-act = tremolite-actinolite; StH = steam-heated; Hypo = hypogene.

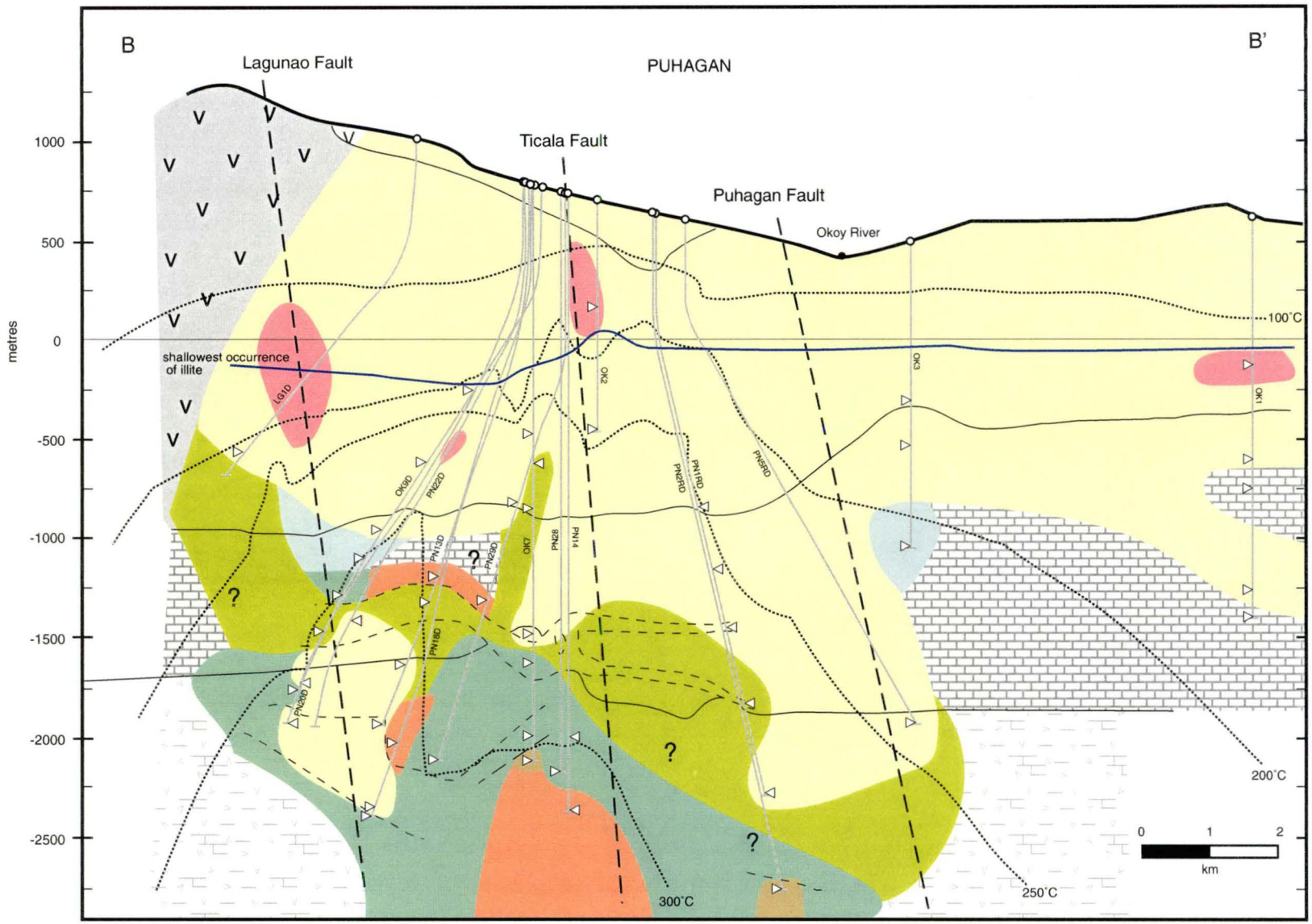

Figure 3.6. Cross-section along line B-B' (Figure 3.4) showing the distribution of alteration types relative to the geology and hydrology, as defined by the 100°, 200°, 250° and 300°C isotherms (dotted lines). The thin dashed lines represent the Puhagan dike contacts. All geologic contacts are inferred. The blue line shows the shallowest occurrence of illite in the illite alteration assemblage. At shallower depths smectite is the dominant phyllosilicate mineral. See Figure 3.5 for a legend to the alteration types and geology.

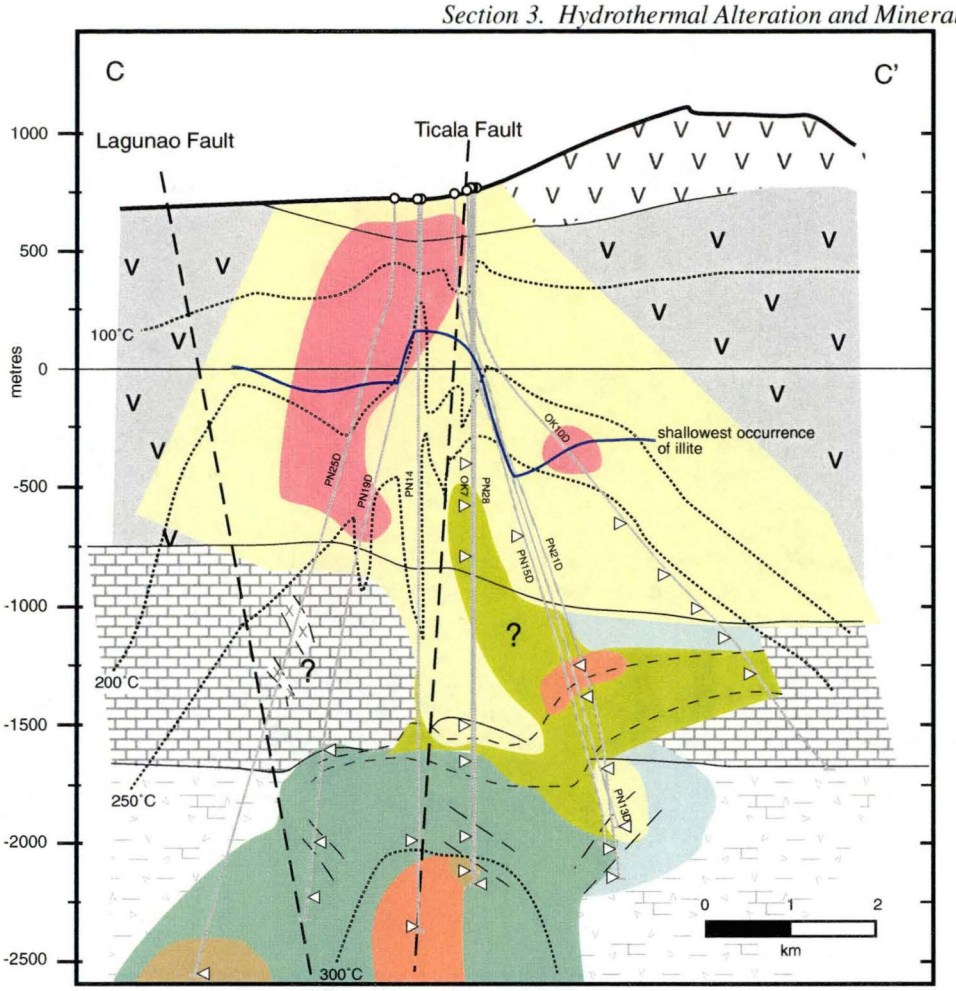

Figure 3.7. Cross-section along line C-C' (Figure 3.4) showing the distribution of alteration types relative to the geology and hydrology, as defined by the 100°, 200°, 250° and 300°C isotherms (dotted lines). The thin dashed lines represent the Puhagan dike contacts. All geologic contacts are inferred. The blue line shows the shallowest occurrence of illite in the illite alteration assemblage. At shallower depths smectite is the dominant phyllosilicate mineral. See Figure 3.5 for a legend to the alteration types and geology.

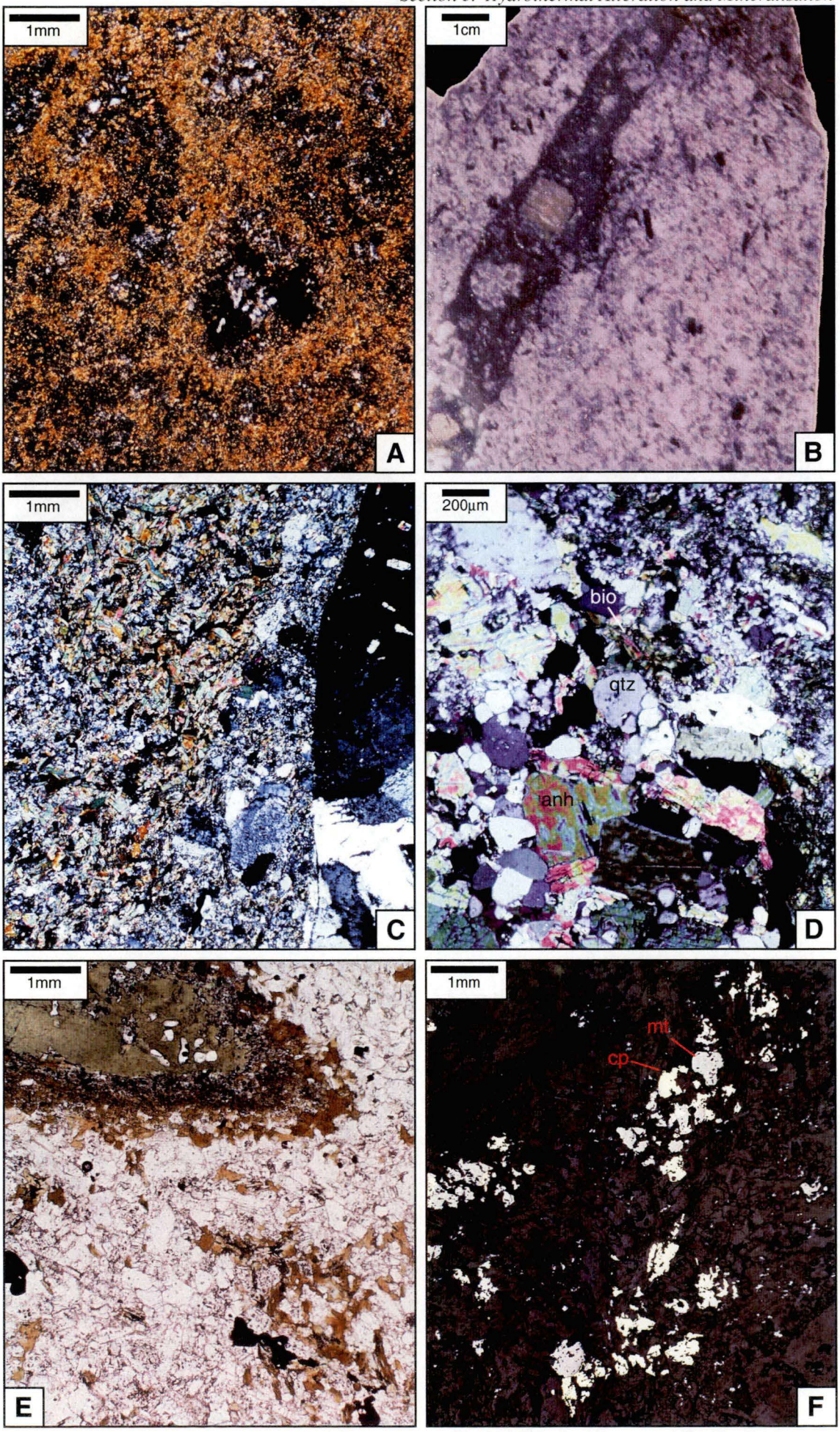
1mm
A
1cm
B
1mm
C
200µm
bio
qtz
anh
D
1mm
E
1mm
mt
cp
F

Base Metal Sulphide Minerals

Chalcopyrite and pyrite are the only sulphide minerals associated with the biotite alteration assemblage. They are minor components, never comprising more than 0.1 modal % of the total rock in the samples examined in this study. The sulphides occur in quartz-magnetite-anhydrite-veinlets as late stage minerals, filling interstitial spaces and enclosing hydrothermal magnetite crystals (Figure 3.8f).

Distribution and Relationships to Measured Temperatures

A major zone of biotite alteration occurs in the upper regions of the Nasuji Pluton (Figure 3.5), where the intrusive wallrock is cut by biotite veinlets and breccia zones. Above the pluton, pervasive biotite alteration has affected the country rock (Figure 3.5). This zone of biotite alteration is spatially associated with present-day downhole temperatures that are below the lower limit of biotite stability (i.e. < 270°C; Figure 3.5; Appendix 4).

In the Puhagan sector, zones of biotite alteration have been intersected at the bottom of wells OK7, PN2RD and PN25D (i.e., > 2000 m bsl; Figures 3.6 and 3.7). These alteration zones are proximal to fault structures (i.e., the Ticala, Puhagan, Nasuwa and Lagunao Faults; Figures 3.4 to 3.7). They occur either above, or close to, the isotherm that defines the lower thermal limit of biotite stability (i.e., 270°C, Table 3.1; Figures 3.5 to 3.7; Appendix 4).

Calc-Silicate Alteration

The calc-silicate alteration assemblage at Palinpinon is defined by the presence of the diagnostic skarn minerals garnet, clinopyroxene and scapolite. Tremolite-actinolite, epidote, wairakite, prehnite, albite, pyrite, chalcopyrite and pyrrhotite may also be present. Pervasive calc-silicate alteration has destroyed the primary textures and affected both sedimentary and igneous rocks. Anhedral garnet, with anomalous birefringence, contains small inclusions of prismatic clinopyroxene crystals (Figure 3.9a). Scapolite occurs as coarse (< 7 mm) bladed crystals, either having altered plagioclase or containing inclusions of tremolite-actinolite and albite-altered feldspar crystals (Figure 3.9b). The birefringence of scapolite (δ < 0.02) implies its composition is closest to the Na-Cl-bearing end-member, marialite. With the exception of scapolite, calc-silicate alteration minerals also occur in veinlets (< 20 mm across; Figures 3.9c-e).

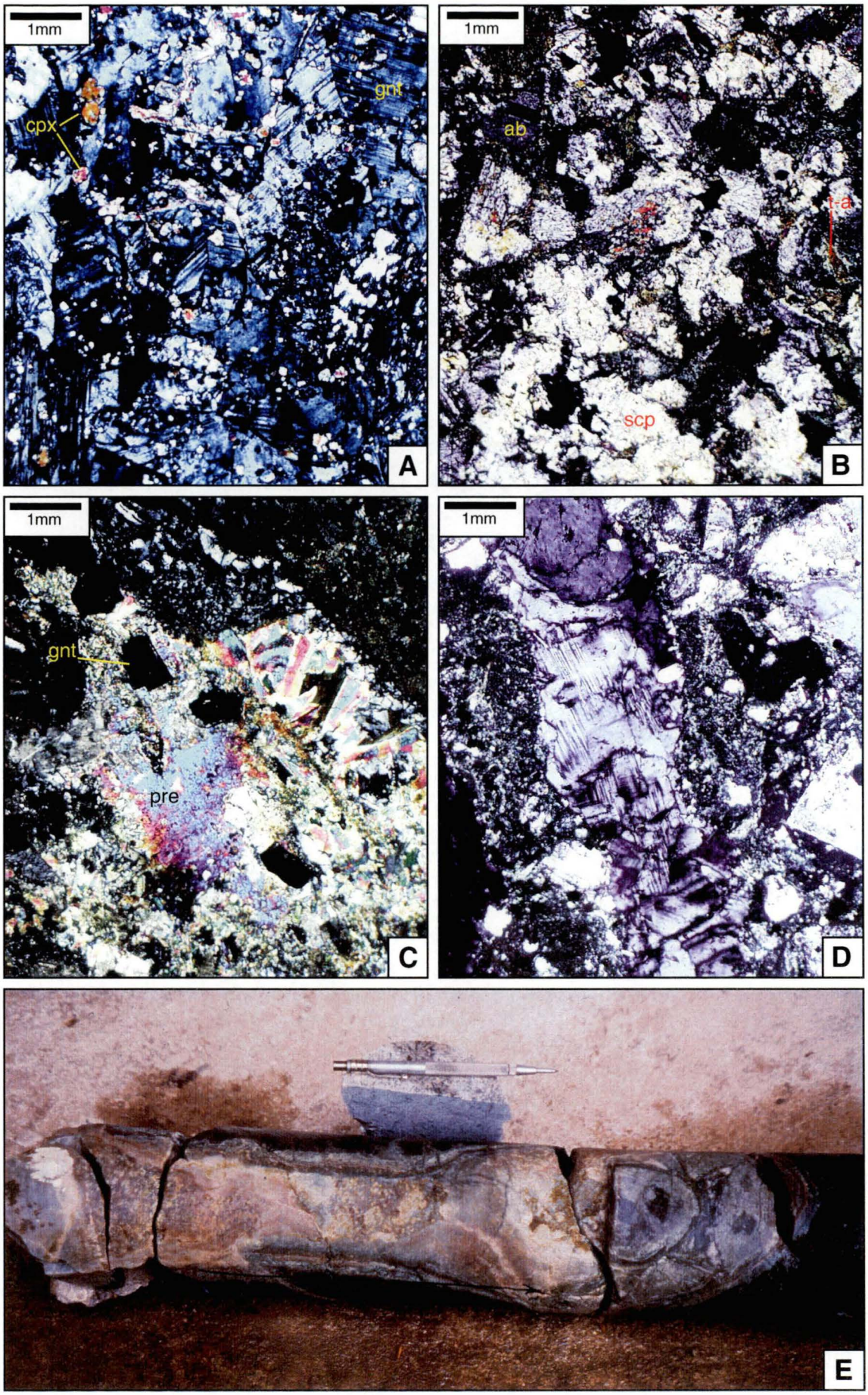
1mm
gnt
cpx
A
1mm
ab
t-a
scp
B
1mm
gnt
pre
C
1mm
D
E

Base Metal Sulphide Minerals

Small crystals of chalcopyrite, sphalerite and galena (< 50 μm) are negligible components (< 0.1 modal %) of this alteration type and only occur as sparse disseminations in the samples studied.

Distribution and Relationships to Measured Temperatures

Beneath Puhagan, in the upflow zone, the most intense development of calc-silicate alteration (garnet, clinopyroxene, scapolite) occurs in drillcore retrieved from the deepest portions of wells PN23D, PN16D, PN24D, OK7, PN14 and PN9RD (i.e., > 2000 m bsl; Figures 3.4 to 3.7). These wells were drilled beneath the Puhagan dikes into regions proximal to the Lagunao and Ticala Fault intersection, and also between the Puhagan and Nasuwa Faults (Figure 3.4; Appendix 4). Calc-silicate alteration is also sporadically and incipiently developed where the Puhagan dikes are in contact with rocks belonging to the Okoy and Lower Puhagan Volcanic Formations (Figures 3.6 and 3.7).

In the Nasuji-Sogongon region, calc-silicate alteration has been observed in a few drillcore retrieved from areas adjacent to the Nasuji Pluton margin. In one sample, limestone from the Okoy Formation is cut by garnet-prehnite veins (Figure 3.9c). Also, a sample of a porphyritic volcanic rock from the Lower Puhagan Volcanic Formation has been pervasively altered to biotite and is cut by garnet-clinopyroxene veins (Figure 3.9e).

Temperatures required to stabilise garnet and clinopyroxene are estimated to be in excess of 400°C, at approximately 1 kb pressure (Tracy and Frost, 1991). Such temperatures are well above the present measured downhole temperatures (< 330°C; Figures 3.5 to 3.7; Appendix 4), implying that the hydrothermal system has cooled at least 70°-100°C since the formation of the calc-silicate alteration zones.

Propylitic Alteration

Minerals that characterise propylitic alteration assemblages at Palinpinon are tremolite-actinolite, epidote and chlorite. These minerals occur with albite, orthoclase, quartz, pyrite ± chalcopyrite ± bornite ± titanite ± leucoxene ± calcite. The propylitic alteration zone has been subdivided into three subzones: (1) a tremolite-actinolite subzone defined by the presence of tremolite-actinolite ± epidote ± chlorite (Figures 3.5 to 3.7); (2) an epidote subzone (epidote ± chlorite; Figures 3.4 to 3.7); (3) a chlorite subzone (chlorite; Figures 3.5 to 3.7).

The propylitic assemblage is developed as a pervasive alteration style (Titley, 1982) with the hydrothermal mineralogy strongly influenced by the primary mineralogy of the protolith. Thus, even with the most intense propylitic alteration, it is still possible to discern primary rock textures (Figures 3.10a and b). In the volcanic rocks, the feldspar phenocrysts have been

altered to albite ± orthoclase ± epidote ± calcite, whereas (depending on the subzone) hornblende and clinopyroxene phenocrysts have been replaced by tremolite-actinolite, epidote and/or chlorite.

Propylitic alteration of the Puhagan dikes has resulted in the pervasive albitisation of feldspar phenocrysts and groundmass laths, and the ferromagnesian phenocrysts are pseudomorphed by epidote ± tremolite-actinolite ± chlorite (Figure 3.10b). Veinlets (< 10 mm) that have crosscut albitised intrusive wallrock contain quartz, epidote ± tremolite-actinolite ± pyrite ± chalcopyrite. In these veinlets, radial aggregates of acicular epidote typically occur both interstitial to and enclosed by euhedral quartz, and are interpreted to be due to co-precipitation of quartz and epidote (Figure 3.10c).

Propylitic alteration of the Nasuji Pluton is developed as alteration haloes (< 1 mm) surrounding quartz, epidote ± tremolite-actinolite veinlets (< 2 mm; Figure 3.10d). Partial albite ± orthoclase alteration of primary feldspars and replacement of primary hornblendes by tremolite-actinolite or epidote is typical. In the equigranular quartz diorites, away from the veins, propylitic alteration is incipiently developed and tremolite-actinolite, epidote and sphene have filled interstitial spaces between primary quartz and orthoclase (Figure 3.10e).

Base Metal Sulphide Minerals

Chalcopyrite and bornite are associated with the propylitic alteration assemblage. Both are relatively rare (< 0.1 modal %) and occur as sparse disseminations (< 100 μm), typically associated with epidote. Bornite is only found in propylitic-altered rocks of the Nasuji Pluton as intergrowths with chalcopyrite. These chalcopyrite-bornite aggregates have overgrown and enclosed tremolite-actinolite and/or epidote (Figure 3.10f).

Distribution and Relationships to Measured Temperatures

The tremolite-actinolite subzone occurs in the deepest parts of the geothermal field (Figures 3.5 to 3.7). In the Puhagan sector, it surrounds biotite and calc-silicate alteration zones. In the Nasuji-Sogongon, tremolite-actinolite alteration has affected rocks adjacent to the flanks of the intrusion and extends into the deepest portions of the Nasuji Pluton. This subzone mostly occurs where present-day temperatures are between 250° and 300°C. However, in the core of the upflow zone temperatures are greater than 300°C, implying that in this area tremolite-actinolite is in close thermal equilibrium with the present measured temperatures.

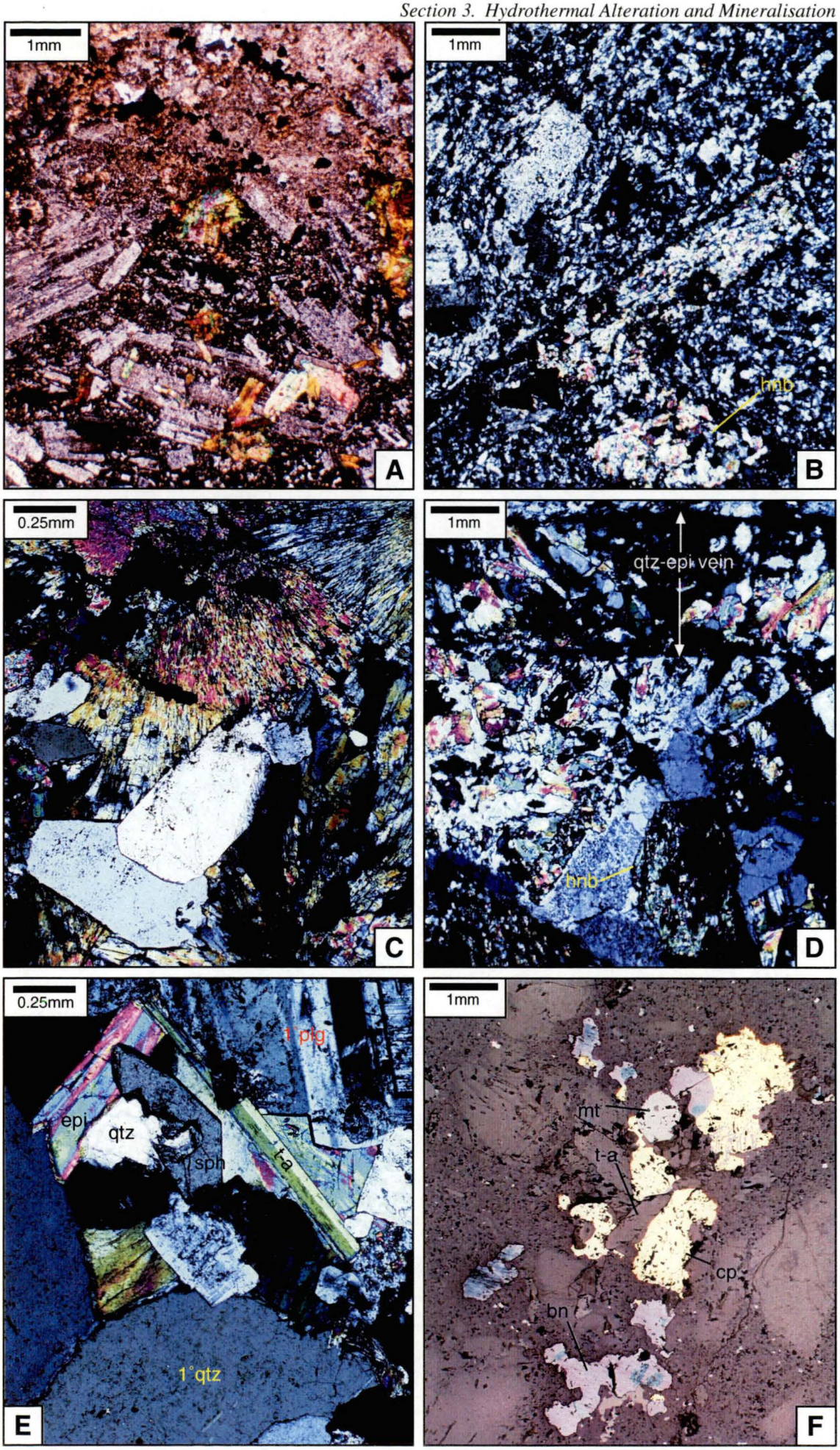
1mm
A
1mm
hnb
B
0.25mm
C
1mm
qtz-epi vein
hnb
D
0.25mm
1 plg
epi
qtz
sph
t-a
1 qtz
E
1mm
mt
t-a
cp
bn
F

The epidote subzone occurs above the tremolite-actinolite subzone. In Puhagan, it mainly occurs either in the Lower Puhagan Volcanic Formation or the Puhagan dikes. However, close to the upflow zone, epidote development extends into the Southern Negros Formation (well OK7; Figures 3.5 to 3.7). In Nasuji-Sogongon, the epidote subzone occurs in the upper portions of the Nasuji Pluton and extends into the overlying Southern Negros Formation. As reported by Celenk et al. (1987), propylitically altered rocks belonging to the epidote subzone crop out in the Nasuji-Sogongon area (Figure 3.4). Reyes (1990) noted that in Philippine geothermal systems, epidote is only stable at temperatures greater than 250°C (Table 3.1), and hence can only be in thermal equilibrium with its surroundings in the deeper Puhagan and Nasuji-Sogongon occurrences (Figures 3.5 and 3.7). At higher elevations, the geothermal system must have cooled markedly since the time of epidote formation.

The chlorite subzone occurs above the epidote subzone and at depth on the margins of the upflow zone (Figure 3.7). It is also present in the outflow zone, where the deeper regions of the Southern Negros Formation have been chloritised (Figure 3.5). Empirically, the chlorite stability temperature is greater than 120°C (Table 3.1) and hence is in equilibrium with measured temperatures in most occurrences at Palinpinon (Figures 3.5 to 3.7).

Illite Alteration

The occurrence of either illite or smectite, with or without chlorite, defines the illite alteration assemblage. Other minerals that are present locally include quartz, leucoxene, anhydrite, calcite, pyrite, chalcopyrite, sphalerite and galena. This alteration assemblage is developed pervasively and tends to have obscured the primary rock textures. It has mainly affected igneous rocks and is most strongly developed as haloes around quartz-anhydrite-sulphide and calcite-quartz veins (Figures 3.10a, 3.11a and b). Primary feldspar is selectively replaced by illite or smectite, whereas primary hornblende is altered to chlorite and leucoxene, and magnetite to leucoxene. With increasing alteration intensity, replacement of the groundmass by illite, quartz, anhydrite, chlorite, leucoxene, calcite, pyrite and chalcopyrite results in obliteration of the primary rock textures (Figure 3.11d).

Base Metal Sulphide Minerals

Chalcopyrite, sphalerite and galena are present in minor amounts (< 0.5 modal %). They occur in quartz – anhydrite ± calcite veins as minor disseminations (< 200 μm) either lining the vein walls or enclosed by coarse anhydrite (Figures 3.11e and f).

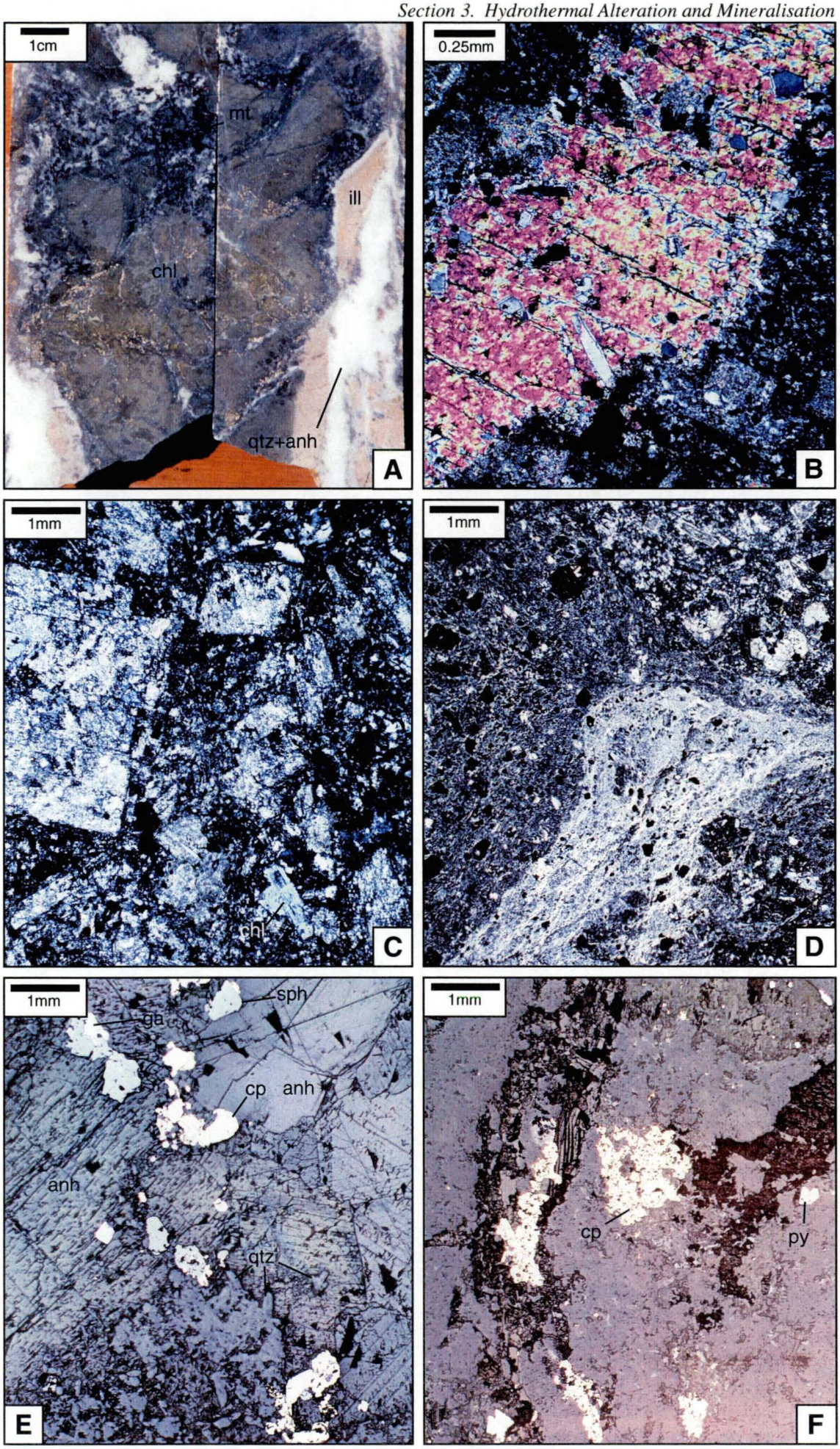
1cm
mt
ill
chl
qtz+anh
A
0.25mm
B
1mm
chl
C
1mm
D
1mm
sph
ga
cp
anh
anh
qtz
E
1mm
cp
py
F

Distribution and Relationships to Measured Temperatures

This is the most extensively developed alteration assemblage and occurs across the geothermal field from the surface to depths greater than 500 m bsl (Figures 3.5 to 3.7; Appendix 4). At the surface, the predominant phyllosilicate is smectite, but with increasing depth this decreases in abundance and illite predominates. The approximate transition from smectite dominant to illite dominant is illustrated on each of the cross-sections (Figures 3.5 to 3.7). In Nasuji-Sogongon and parts of the eastern outflow zone, the shallowest occurrence of illite occurs at temperatures well below its stability range (220°-310°C; Figures 3.5 and 3.6), whereas in Puhagan illite occurs in approximate equilibrium with its temperature of stability (Figures 3.5 to 3.7). Beneath Puhagan, narrow zones of illite alteration extend to greater depths close to steeply-dipping fault zones (Figures 3.5 to 3.7) and deep zones of illite alteration occur beneath the Okoy Formation on the margins of the upflow zone (Figures 3.5 to 3.7).

Advanced Argillic Alteration

Advanced argillic alteration mineral assemblages form from highly acidic solutions. Such waters can be generated by either the oxidation of sulphide-rich host rocks (supergene), steam-heated waters occurring above the water table in a hydrothermal system, or from the absorption of vapours released from a degassing intrusive body at shallow depths (hypogene; Rye et al., 1992). Because sulphide-rich host rocks are not present at Palinpinon, the zones of advanced argillic alteration must have formed either through interaction with steam-heated waters or via hypogene processes.

Hypogene Advanced Argillic Alteration

An advanced argillic assemblage consisting of pyrophyllite, diaspore, dickite, tabular alunite, zunyite $\{Al_{13}Si_5O_{20}F_2(OH,F)_{16}Cl\}$, quartz, aluminium-phosphate-sulphate (APS) minerals, ± andalusite has been recognised. The occurrence of zunyite implies this assemblage must have formed from a volatile-rich, saline solution at temperatures greater than 250°C (Table 3.1; Hsu, 1986; Reyes, 1990). Based on this implication and the tabular habit of alunite (Hedenquist et al., 2000), it is most likely that this assemblage formed under hypogene conditions.

Alteration of the porphyritic volcanic rocks has resulted in the replacement of phenocrysts by pyrophyllite ± zunyite (Figure 3.12a) ± tabular alunite. The groundmass of these rocks is pervasively altered to pyrophyllite, tabular alunite, diaspore, dickite, silica, ± andalusite. Tabular alunite crystals commonly contain fine grained (< 20 μm) APS mineral inclusions (woodhouseite, $CaAl_3(PO_4)(SO_4)(OH)_6$; Figure 3.12b). The dominant sulphide mineral occurring with this assemblage is pyrite, but marcasite and rare covellite are also present. Where it is most intense, advanced argillic alteration of porphyritic volcanic rocks has resulted in the formation of a 'vuggy' quartz rock (Figure 3.12c).

Alunite breccias are associated with the hypogene advanced argillic alteration assemblage. These breccias are either clast- or cement-supported with clasts consisting of angular wallrock fragments (10-200 mm; Figure 3.12d). The clasts were originally a porphyritic rock that has been completely altered to vuggy quartz. The breccia cement consists of coarse (< 2 mm), tabular alunite crystals (Figure 3.12e) which enclose fine grained (< 70 μm), anhedral woodhouseite inclusions.

Steam-heated Advanced Argillic Alteration

Quartz or amorphous silica, kaolinite, pseudocubic alunite (Figure 3.12f), APS minerals, ± native sulphur ± diaspore ± pyrophyllite ± dickite comprise a second advanced argillic assemblage at Palinpinon. The presence of kaolinite or amorphous silica implies temperatures of formation were less than 200°C or 120°C, respectively (Table 3.1). Based on this low temperature mineralogy and the pseudocubic habit of alunite (Hedenquist et al., 2000), this assemblage is interpreted to have formed in shallow oxidised zones during interaction with steam-heated waters.

In most cases, the steam-heated advanced argillic mineral assemblage at Palinpinon is pervasively developed (Figure 3.12f). Pseudocubic alunite locally contains fine grained inclusions of cubic APS minerals (svanbergite, $SrAl_3(PO_4)(SO_4)(OH)_6$). The sulphide minerals occurring with this assemblage are pyrite and marcasite.

Base Metal Sulphide Minerals

Very minor covellite (< 0.1 modal %; < 500 μm) has been observed in hypogene advanced argillic altered rocks exposed at the surface in the Nasuji-Sogongon area. These rocks have been altered to a pyrophyllite + diaspore ± dickite ± alunite mineral assemblage.

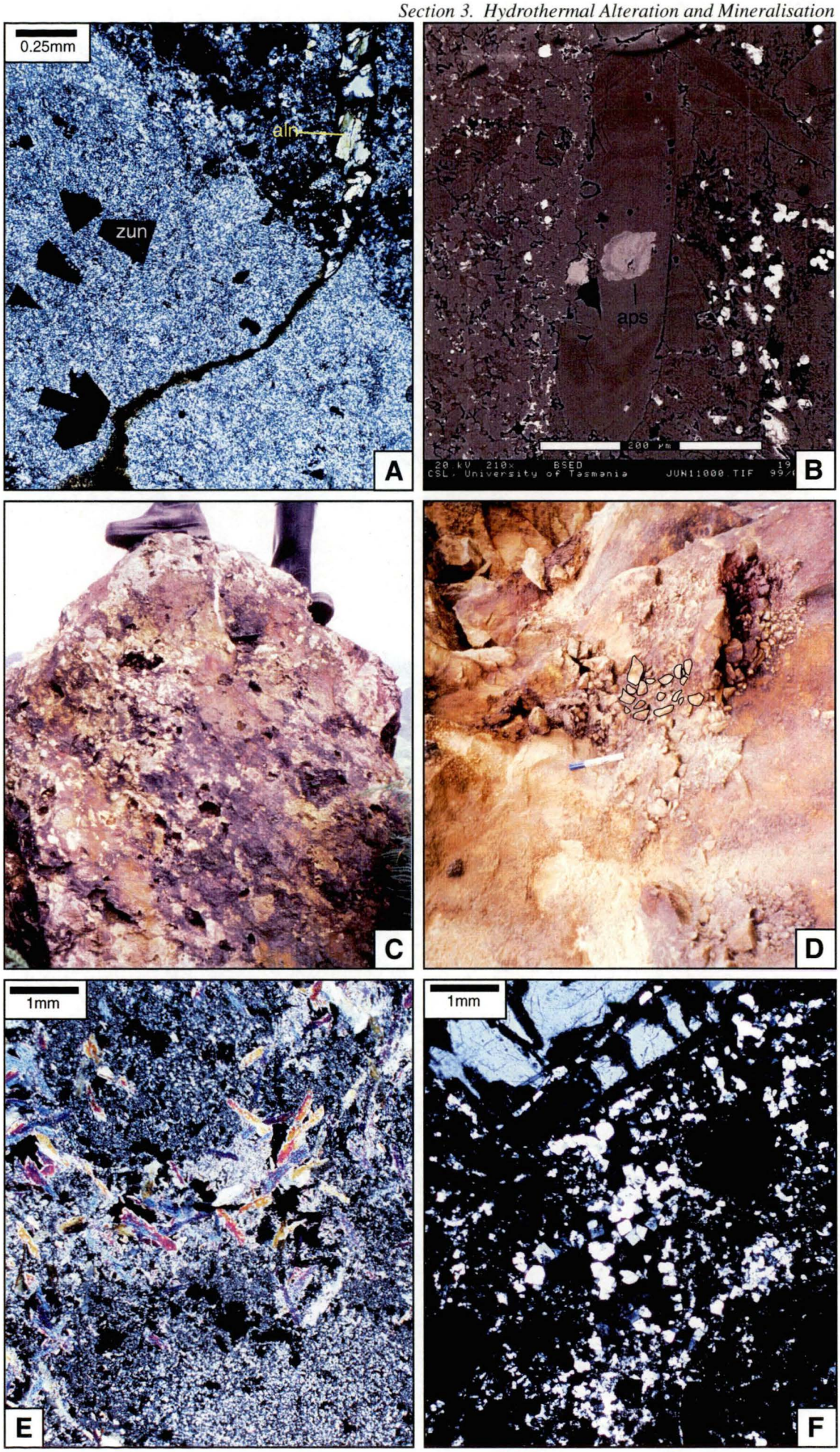
0.25mm
aln
zun
A
aps
200 µm
20 kV 210× BSED
CSL, University of Tasmania JUN11000.TIF
B
C
D
1mm
E
1mm
F

Distribution and Relationships to Measured Temperatures

Advanced argillically altered rocks crop out at the surface (Celenk et al., 1987) and the location of samples collected for this study are indicated in Figure 3.4. A series of north-east striking ridges occur along the northern side of the Okoy Valley (Figures 3.4 and 3.7). These ridges are relatively resistant to erosion due to advanced argillic alteration of the volcanic country rock to alunite ± quartz. The maximum gold grade reported by Celenk et al. (1987) comes from these ridges (1-3 ppm Au). At the south-western end of the ridges, the surface rocks have been altered to a hypogene advanced argillic assemblage (pyrophyllite, diaspore, tabular alunite, ± zunyite, ± dickite, ± APS minerals). Alunite breccias crop out at the base of the ridge, in the bed of the Okoy River, and also approximately 500 m to the north-east (Figure 3.4). Approximately half way along the strike of the ridge, advanced argillic alteration has produced fine grained (< 0.2 mm) alunite (Figure 3.4). Rocks that crop out at the north-eastern end of the ridges (Figure 3.4) are altered to a steam-heated advanced argillic assemblage (pseudocubic alunite, silica, kaolinite). At the base of this ridge, geothermal springs discharge steam-heated acid sulphate water (Figure 1.14).

Surface samples collected from higher elevations to the south of Puhagan are also altered to advanced argillic assemblages. Rocks in areas of active gas discharge (i.e., kaipohan areas; Figures 1.9 and 3.4) are undergoing alteration to a steam-heated assemblage of amorphous silica, ± kaolinite, ± native sulphur. However, areas of fossil advanced argillic alteration also occur in this region. For example, a sample of stream float (Figure 3.4) is altered to an assemblage of tabular alunite, pyrophyllite, diaspore, dickite and woodhouseite (Figure 3.12b). Also, rocks cropping out in area south-east of the kaipohan (Figure 3.4) are altered to a steam-heated assemblage of amorphous silica, pseudocubic alunite and svanbergite (Figure 3.12f).

In the Nasuji-Sogongon area, a thick (< 1200 m) zone of advanced argillic alteration extends from the surface to approximately the top of the Nasuji Pluton (Figure 3.5; Appendix 4). Along with the hypogene assemblage at the surface, andalusite ± diaspore occur in the deeper parts of this zone (Figure 3.13a). Measured temperatures in this region are well below the temperatures needed to stabilise andalusite (> 260°C; Table 3.1) and zunyite (> 250°C; Table 3.1) and their occurrence is interpreted to reflect an earlier hydrothermal regime that involved high temperature saline acidic fluids derived from a degassing intrusion. Elsewhere, most of the subsurface Nasuji-Sogongon advanced argillic zone consists of alunite, pyrophyllite, diaspore and dickite. This assemblage is also present beneath the Puhagan area as a narrow zone extending to deeper levels (i.e., below 500 m bsl; Figures 3.5 and 3.7). It is also sporadically developed towards the northeast in the eastern outflow zone (Figures 3.5 and 3.6). Pyrophyllite is not a reliable temperature indicator, because its stability is dependent on silica saturation and it can form in association with active hot springs (Reyes, 1990). Therefore, it may be that these minerals were deposited under steam-heated conditions, at temperatures less

than 200°C, in equilibrium with the present-day prevailing physicochemical conditions in the Nasuji-Sogongon, Puhagan and eastern outflow areas. The perched steam-heated aquifers (Figure 1.20) are a reservoir of acid-sulphate water that can alter the host rocks to an assemblage of diaspore, alunite, pyrophyllite, dickite ± kaolinite. These steam-heated acidic waters can also percolate to deeper levels along near-vertical permeable pathways, such as faults (Reyes, 1990) and could, at least partly, explain the presence of the subvertical advanced argillic alteration zone in the Puhagan area (Figures 3.5 to 3.7).

3.4.2. Alteration Timing Relationships Based on Textural Evidence

Overprinting and crosscutting relationships observed during petrographic examination of the drillcore samples provide important evidence for understanding the timing relationships between some contrasting alteration types.

In Nasuji-Sogongon, it is apparent that zones of biotite alteration are amongst the earliest to develop. Biotite altered rocks are overprinted by propylitic (epidote) alteration and vein assemblages (Figure 3.13b) and also by an illite alteration assemblage (Figure 3.10a). The hypogene advanced argillic alteration assemblage (andalusite ± diaspore) also predates the illite assemblage, as indicated by corroded andalusite crystals that are enclosed and partially replaced by illite, anhydrite and quartz (Figure 3.13a). The propylitic (epidote) alteration assemblage is interpreted to predate illite alteration because epidote + quartz veins have been cut by anhydrite + quartz veins associated with illite alteration assemblages (Figure 3.13c).

In Puhagan, unambiguous textural relationships are rarely observed. However, as seen in Nasuji-Sogongon, the illite alteration assemblage has apparently overprinted the propylitic (epidote) assemblage (Figures 3.10a and 3.13d).

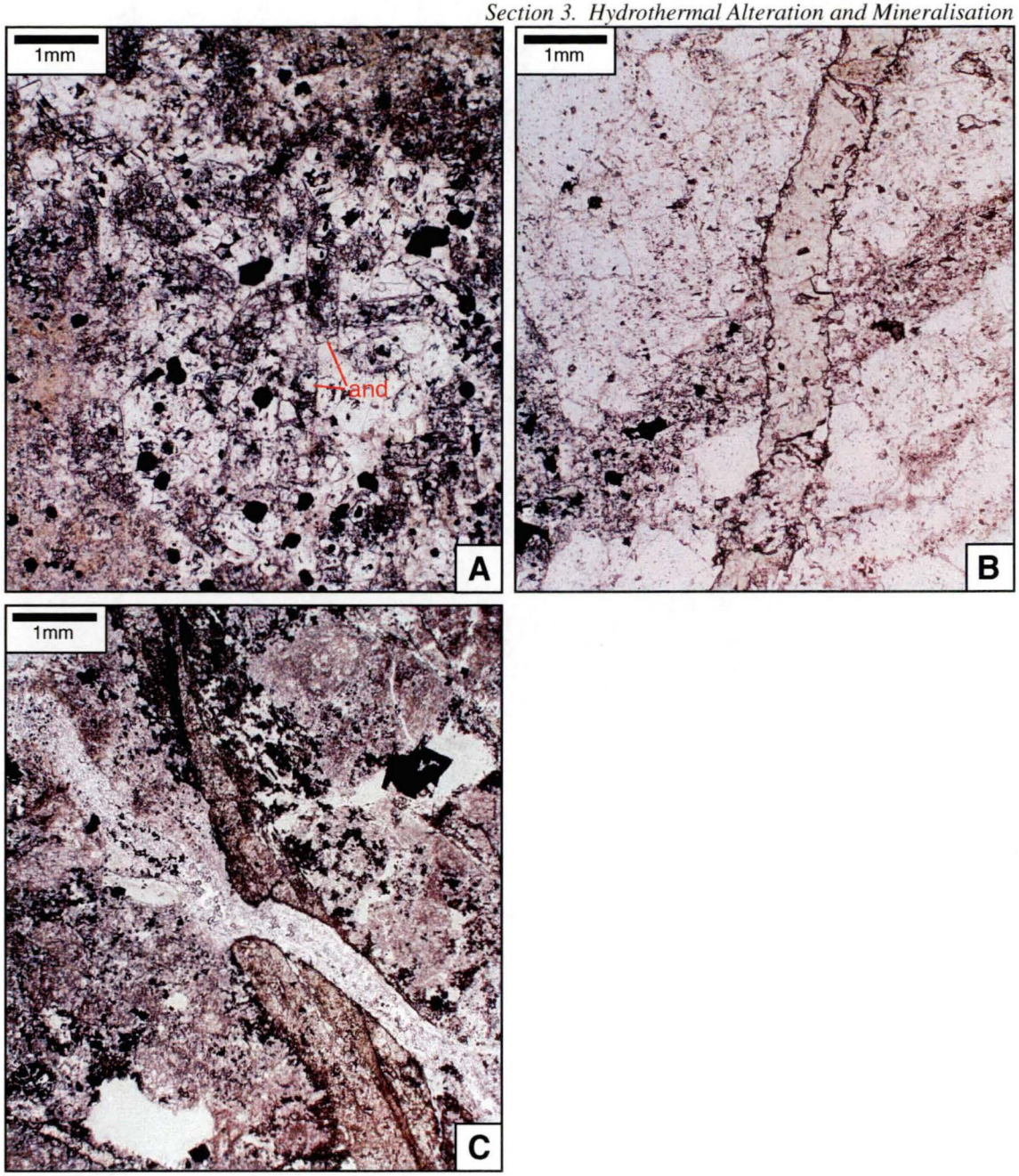

Hydrothermal Alteration Textural Relationships - Photomicrographs

Figure 3.13a. *Sample OK6/1. Plane Polarised Light.*
Interpreted timing relationship : **Hypogene advanced argillic alteration -> Illite alteration**
Corroded and embayed tabular andalusite crystals (and) are enclosed and partially altered by illite, anhydrite and quartz. The wallrock (upper right, lower left) is altered to illite, quartz, pyrite (opaque mineral).

Figure 3.13b. *Sample SG1/3. Plane Polarised Light.*
Interpreted timing relationship : **Biotite alteration -> Propylitic (epidote) alteration**
A vein containing biotite + quartz + orthoclase (lower left to upper right) is cut by an epidote vein (top to bottom).

Figure 3.13c. *Sample NJ6D/4. Plane Polarised Light.*
Interpreted timing relationship : **Propylitic (epidote) alteration -> Illite alteration**
An epidote vein (upper left to lower right) is cut by a vein of anhydrite + quartz (upper left to lower right).

3.4.3. Base and Precious Metal Mineralisation

Bulk rock base and precious metal analyses were carried out on drillcuttings and drillcores from three geothermal wells OK1, OK4 and SG2, along with an additional 25 drillcore samples from 20 other geothermal wells. For comparative purposes, five unaltered surface samples from the Cuernos Volcanic and Southern Negros Formations were included in the sample suite. The results are presented in Appendix 1.2 and summarised in Table 3.2 and Figure 3.14. The three wells are from the upflow zone (OK4), the western outflow zone (Nasuji-Sogongon area, SG2) and the eastern outflow zone (OK1; Figures 3.4 and 3.14).

The results show that base and precious metal concentrations are one to two orders of magnitude below ore grade. Cu is mostly < 0.02 wt. %, with Pb < 0.03 wt. %, Zn < 0.01 wt. %, Mo < 0.01 wt. %, Ag < 8 g/t, Au < 0.05 g/t. Gold is only above detection (5 ppb) in six of the 100 samples analysed and is most anomalous in the silicified surface samples analysed by Celenk et al. (1987). Silver is highest in rocks of the Okoy Formation but there is no apparent difference in silver grades between altered and unaltered samples. In conjunction with gold ore, 8 g/t silver is considered economic in some low sulphidation epithermal deposits. Copper is highest in rocks affected by biotite or propylitic (tremolite-actinolite) alteration. A weakly anomalous Cu-Au zone occurs above the Nasuji Pluton in drillhole SG2 associated with biotite and illite alteration. It overlies a weakly anomalous Mo zone (Figure 3.14). This is comparable to metal zonation in some porphyry deposits that contain a Mo-enriched halo enclosed by a Cu-Au halo (Jones, 1992). The sample with the highest detected copper concentration (0.1 wt. % Cu; Table 3.2; Appendix 1.2) is a porphyritic hornblende quartz diorite from the Nasuji Pluton that has been altered to a propylitic (tremolite-actinolite) assemblage (Figure 3.10f).

Table 3.2. Summary of base and precious metal analyses of drillcuttings and drillcore from 3 geothermal wells, along with an additional 25 drillcore from 20 geothermal wells.

		Cu	Pb	Zn	Mo	Ag	Au
		(wt%)				(g/t)	
OK1	Max	0.02	0.02	0.01	<0.01	8.0	b.d.
n=26	Min	<0.01	b.d.	<0.01	<0.01	b.d.	b.d.
	Ave.	0.01	<0.01	0.01	<0.01	4.4	b.d.
OK4	Max	0.02	0.01	0.01	<0.01	4.3	0.01
n=26	Min	<0.01	b.d.	<0.01	b.d.	b.d.	b.d.
	Ave.	0.01	<0.01	0.01	<0.01	2.9	0.01
SG2	Max	0.02	0.03	0.01	<0.01	3.0	0.01
n=18	Min	<0.01	<0.01	<0.01	b.d.	b.d.	b.d.
	Ave.	0.01	0.01	0.01	<0.01	2.5	0.01
Drillcore	Max	0.10	<0.01	0.01	<0.01	2.6	0.05
n=25	Min	<0.01	b.d.	<0.01	b.d.	b.d.	b.d.
	Ave.	0.01	<0.01	0.01	<0.01	2.6	0.05

b.d. = below detection limit.
Ave. = average of samples above detection limits
n = number of samples

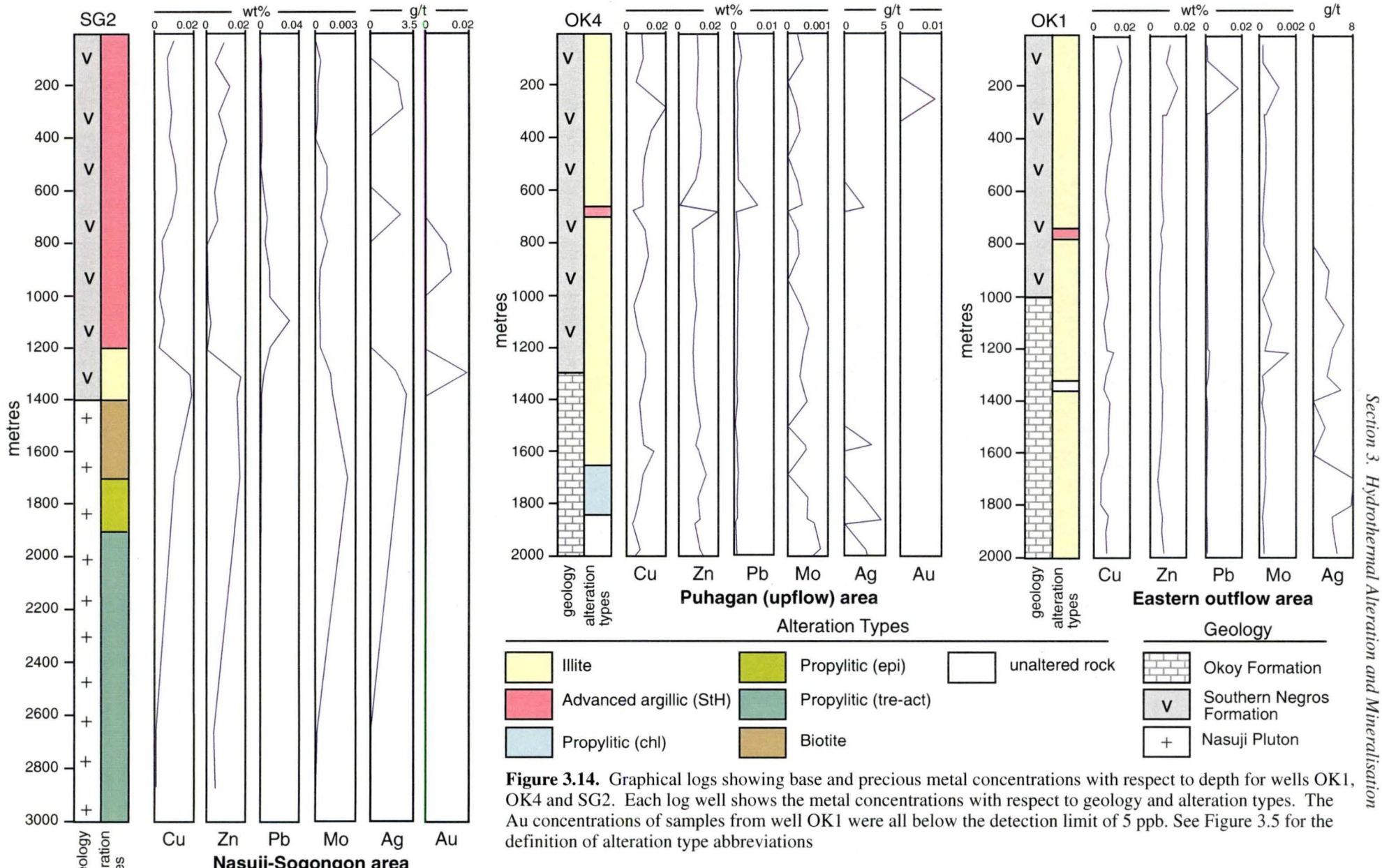

Figure 3.14. Graphical logs showing base and precious metal concentrations with respect to depth for wells OK1, OK4 and SG2. Each log well shows the metal concentrations with respect to geology and alteration types. The Au concentrations of samples from well OK1 were all below the detection limit of 5 ppb. See Figure 3.5 for the definition of alteration type abbreviations

3.5. RADIOMETRIC ($^{40}Ar/^{39}Ar$, K/Ar) DATING OF HYDROTHERMAL MINERALS

3.5.1. Introduction

For this study, radiometric dating of hydrothermal biotite and alunite was carried out at the Research School of Earth Sciences, Australian National University, by the Precise Radiogenic Isotope Services (PRISE) group. Biotite was dated using the $^{40}Ar/^{39}Ar$ method, whereas the alunite age was determined using the K/Ar method. The reason for using the K/Ar technique for dating the alunite is because of its high volatile component. Corrosive vapours released during sample heating can cause damage to the internal mechanisms of the mass spectrometer. The PRISE group has a line connected to the mass spectrometer dedicated solely for the heating of such minerals. In this way, damage to the internal mechanisms of the mass spectrometer can be minimised. Descriptions of the analytical procedures are presented in Appendix 1.1.

Previous radiometric dating of hydrothermal minerals from Palinpinon has been reported by Zaide (1984). K/Ar geochronology was used to date the illite and biotite. The illite was from a 'phyllically' altered volcanic rock (Southern Negros Formation) from the lower Okoy Valley (Figure 3.4). Biotite was from two drillcore samples retrieved from biotite alteration zones beneath the Puhagan and Nasuji-Sogongon areas (OK6/3, OK7/10; Figure 3.5).

3.5.2. Sample Descriptions

Samples of hydrothermal biotite and alunite were submitted for radiometric dating from the biotite and advanced argillic alteration zones spatially associated with the Nasuji Pluton.

The alunite was taken from an alunite breccia that crops out in the Okoy River bed (Figure 3.4). The breccia cement contains fine to coarse grained (0.2-2 mm) interlocking tabular alunite crystals that comprise approximately 95 modal % of the cement (Figure 3.12e). Fine grained (40 μm) quartz is the only other component of the breccia cement.

Hydrothermal biotite from a biotite altered sample of the Nasuji Pluton hornblende diorite was selected for $^{40}Ar/^{39}Ar$ geochronology. This specimen is a porphyritic hornblende diorite with an alteration assemblage of biotite, orthoclase, albite, quartz, anhydrite and magnetite. Plagioclase crystals are partially altered to albite and orthoclase, whereas hornblende crystals are replaced by fine grained biotite flakes. Disseminated biotite (< 0.1-0.3 mm) is variably distributed throughout the sample, comprising between 5-20 modal % of the specimen. This sample (NJ3D/1) is from a depth of approximately 1300 m bsl where the measured downhole temperature is approximately 200°C. This temperature is below the radiogenic argon closure temperature of 300°-350°C for biotite (McDougall and Harrison, 1999).

3.5.3. Radiometric Dating Results

Calculated apparent K/Ar ages of the alunite are listed in Table 3.3a. Duplicate analyses were found to be reproducible within the calculated analytical errors. The average shows that alunite from the advanced argillic hydrothermal breccia has an age of 0.85 ± 0.02 Ma (1δ).

The results of the irradiated biotite are presented in Table 3.3b, the stepwise release spectrum is illustrated in Figure 3.15. The analysis yielded a reliable flat age spectrum with a plateau age (Fleck et al., 1977) of 0.65 ± 0.01 Ma (1δ).

Table 3.3a. K-Ar analysis of hydrothermal alunite from the hydrothermal breccia (96030).

Sample No.	Sample	K (wt %)	Radiogenic ^{40}Ar (10^{-12} mol/g)	Radiogenic ^{40}Ar (%)	Calculated Age (± 1 s.d.)
96030	Alunite	3.436	5.123	7.20	0.855 ± 0.028 Ma
		3.471	5.108	7.18	0.853 ± 0.021 Ma

Table 3.3b. Step-heating Ar isotopic data and the apparent age of hydrothermal biotite (NJ3D/1), from the biotite alteration zone spatially associated with the Nasuji Pluton.

Temp (°C)	Cum ^{39}Ar	$^{40}Ar/^{39}Ar$	$^{37}Ar/^{39}Ar$	$^{36}Ar/^{39}Ar$	Vol. ^{39}Ar ($x10^{-14}$mol)	%Rad. ^{40}Ar	Ca/K	$^{40}Ar^*/^{39}Ar$	Age (Ma±1δ)
NJ3D/1 Biotite, Mass = 38.34 mg, J-value = 0.0007557 ± 0.0000038									
1. 550	0.0019	98.14	0.0984	0.3209	0.268	3 3	0.187	3.266	4.45±1.88
2. 600	0.0069	26.04	0.1314	0.0819	0.703	6.9	0.250	1.795	2.45±0.32
3. 650	0.0164	20.62	0.0819	0.0636	1.335	8.6	0.156	1.776	2.42±0.23
4. 690	0.0325	14.65	0.0214	0.0443	2.263	10 4	0.041	1.521	2 07±0.18
5. 720	0.0590	8.86	0.0093	0.026	3.720	12.8	0.018	1.133	1.54±0.09
6. 750	0.0936	5.99	0.006	0.0168	4.864	16.1	0.011	0.964	1.31±0.06
7. 780	0.1277	4.50	0.0053	0.0117	4.796	21.9	0.010	0.986	1.34±0.04
8. 810	0.1563	3.77	0.0069	0.0095	4.020	24.2	0.013	0.912	1 24±0.07
9. 850	0.1889	3.28	0.0076	0.0085	4.592	21.5	0.015	0.705	0.96±0.04
10. 900	0.2313	2.76	0.0081	0.0073	5.947	19.6	0.015	0.539	0.74±0.03
11. 950	0.2975	2.27	0.0098	0.0057	9.312	24.0	0.019	0.545	0.74±0.04
12. 1000	0.4716	1.56	0.0068	0.0035	24.470	31.6	0.013	0.494	0.67±0.02
13. 1050	0.7791	1.19	0.0056	0.0023	43.240	39.7	0.011	0.473	0.65±0.01
14. 1100	0.9647	1.12	0.0108	0.002	26.090	42.5	0.021	0.478	0 65±0.02
15. 1200	0.9950	2.52	0.0369	0.0068	4.885	19.0	0.070	0.479	0.65±0.03
16. 1300	1.0000	166.42	0.2532	0.5501	0.075	2.3	0.481	3.761	5 12±5.35
Total		2.849	0.0104	0.0074	140.6			0.600	0.82±0.04

Notes:
i) Errors are one sigma uncertainties and exclude uncertainties in the J-value.
ii) Data are corrected for mass spectrometer backgrounds, discrimination and radioactive decay.
iii) Interference corrections are: $(^{36}Ar/^{37}Ar)_{Ca} = 3.2x10^{-4}$; $(^{39}Ar/^{37}Ar)_{Ca} = 7.86x10^{-4}$; $(^{40}Ar/^{39}Ar)_{K} = 5.10x10^{-2}$
iv) J-value is based on an age of 27.95 Ma for the Fish Canyon Tuff biotite monitor

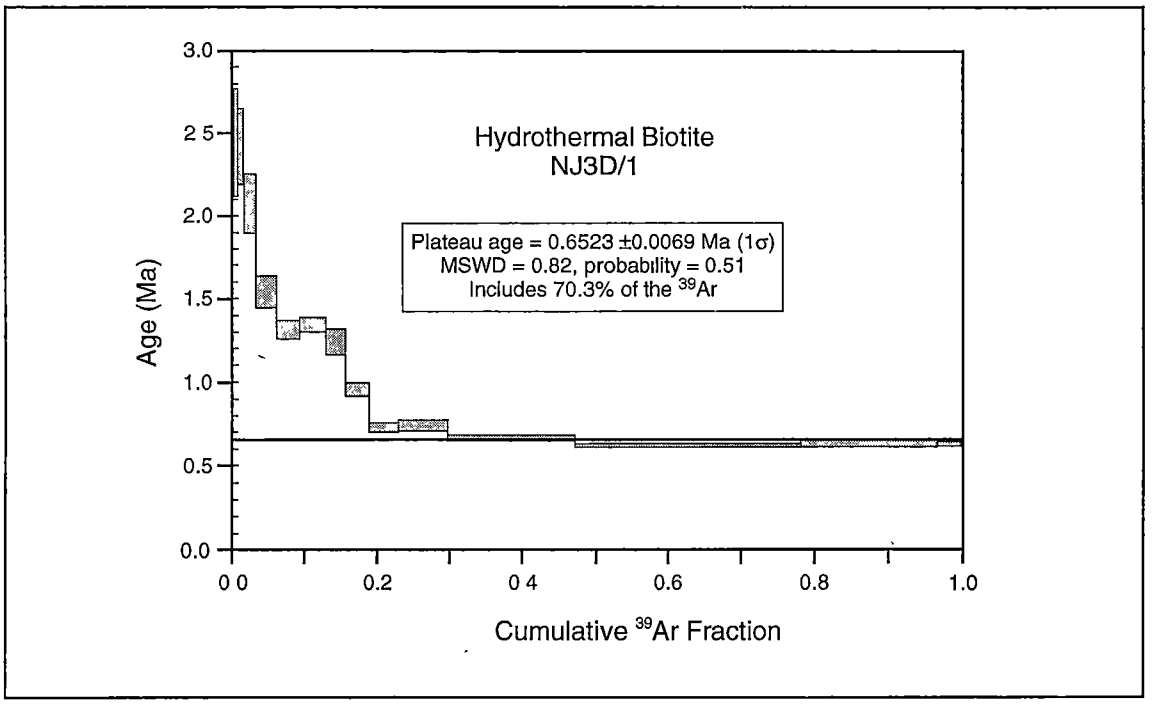

Figure 3.15. $^{40}Ar/^{39}Ar$ apparent age spectrum for hydrothermal biotite (NJ3D/1) from the biotite alteration zone near the top the Nasuji Pluton. See Table 3.3b for the primary isotopic data.

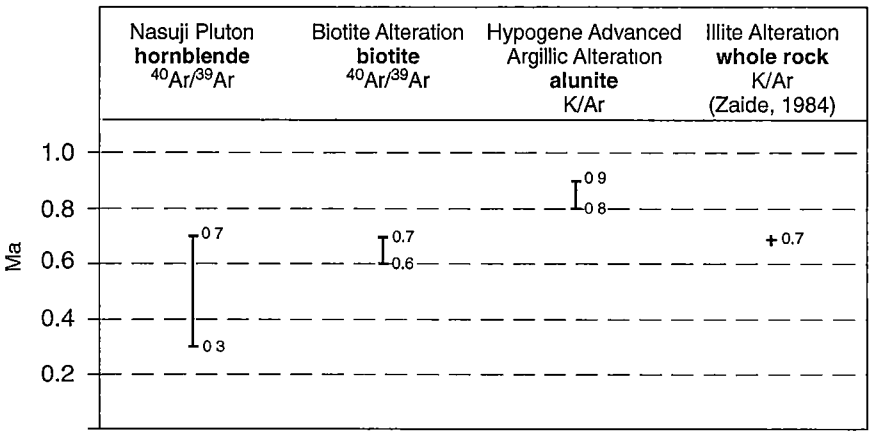

Figure 3.16. Summary of the radiometric ages of the Nasuji Pluton (NJ2D/1; this study) and associated alteration types : hydrothermal biotite (NJ3D/1), alunite (96030; both this study) and a whole rock age from an illite altered volcanic rock from the Southern Negros Formation (Zaide, 1984; see Figure 3.4 for sample location).

3.5.4. Summary and Discussion of the Radiometric Dating

Radiometric ages of primary and secondary K-bearing minerals undertaken during the course of this PhD study are summarised in Figure 3.16. Also shown is the K/Ar age of an illite-altered volcanic rock (Southern Negros Formation) reported by Zaide (1984).

The age of the biotite alteration zone (0.7-0.6 Ma) spatially associated with the Nasuji Pluton falls within the age range of the Nasuji Pluton, also determined in this study by $^{40}Ar/^{39}Ar$ methods (0.7-0.3 Ma). The K/Ar age of the hypogene advanced argillic alteration zone (0.9-0.8 Ma) situated at the surface, directly above the Nasuji Pluton also indicates a close temporal relationship between the intrusion and advanced argillic alteration. These close temporal relationships imply a genetic relationship between the intrusion of the Nasuji Pluton and the biotite and hypogene advanced argillic alteration zones. However, compared to the hornblende and biotite samples, the alunite sample collected from the surface is the least likely to have been affected by thermal resetting and its date (0.9-0.8 Ma) is probably a better reflection of the time of intrusion emplacement.

Previous radiometric studies of hydrothermal minerals at Palinpinon have been reported by Zaide (1984). A whole rock K/Ar age of a porphyritic volcanic rock (Southern Negros Formation; Figure 3.4) that was intensely altered to an assemblage of illite, quartz, chlorite, calcite and dolomite was determined to be 0.71 ± 0.01 Ma (Zaide, 1984). This date was regarded by Zaide (1984) to be the age of the illite formation and has been interpreted to indicate that a hydrothermal alteration system had developed away from the Nasuji Pluton (approximately 5 km north-northeast; Figure 3.4) close to the time of intrusion emplacement (Figure 3.16). However, it is difficult to place this dated sample of illite into the context of the alteration types discussed in this thesis because illite can be a component of the alteration haloes associated with hypogene advanced argillic alteration assemblages (Arribas, 1995). The occurrence of the dated sample adjacent to an area of steam-heated advanced argillic surface alteration (Figure 3.4) raises questions as to whether this dated sample is associated with the advanced argillic assemblage or the widespread illite alteration assemblage that appears to be in thermal equilibrium with the present-day geothermal system.

Two other hydrothermal mineral dates from Palinpinon have been previously reported. Whole rock age determinations were obtained on biotite from the Nasuji-Sogongon and Puhagan biotite alteration zones (Figures 3.5 to 3.7). Both specimens were reported to have an age of 1.4 Ma (Zaide, 1984). However, a subsequent short communication by Hulston (1984) expresses concerns about the significance of these dates and a more complete error analysis was reported. The recalculated age of the Nasuji-Sogongon biotite is 1.43 ± 0.83 Ma (Hulston, 1984). This date overlaps the biotite age (0.7-0.6 Ma) determined during this study. Two recalculated dates obtained from the Puhagan biotite zone were reported as 0.49 ± 0.34 Ma and 1.14 ± 0.22 Ma (Hulston, 1984). However, the validity of any age obtained on biotite using

argon geochronology from the Puhagan biotite zone must be questioned because present measured temperatures in this zone (Figures 3.5 to 3.7) are close to the lower limit of the biotite closure temperature for argon (i.e., 300°-350°C, McDougall and Harrison, 1999). This overlap of present measured temperature with biotite closure temperature could possibly account for the two discordant ages.

3.6. FLUID INCLUSIONS

3.6.1. Introduction

Microthermometric measurements of fluid inclusions provide important information on the prevailing physicochemical conditions of the fluid during mineral precipitation. Such information lends insights into the thermal history and chemical evolution of the hydrothermal system. A study of fluid inclusions in vein quartz from as many different alteration types as possible was undertaken for this study. Also included in the sample suite were primary quartz crystals from porphyritic (i.e., quartz phenocrysts) and equigranular Nasuji Pluton hornblende quartz diorite.

Fluid inclusion studies at Palinpinon were previously undertaken during development of the geothermal steamfield. These were done on fluid inclusions in quartz, anhydrite and calcite. In most cases, only heating measurements were recorded (i.e., no salinity estimates) and these were obtained for the purpose of determining a thermal history of the geothermal reservoir. The results, reported in PNOC-EDC files, showed that homogenisation temperatures were generally either approximately equal to, or higher than current measured temperatures, implying that the Palinpinon geothermal system is thermally waning. However, much of this data was collected over a period of several years by many different workers and the respective internal reports commonly lack important petrographic information such as mineral occurrence, associated alteration types and detailed descriptions of the coexisting fluid inclusion types and populations. The inconsistencies of these reports, along with the difficulties of placing the fluid inclusion samples into the context of the alteration types described in this study, make correlations with the previous data difficult. Thus no attempt was made to do so for this study, although it is noted that the temperatures reported by previous workers are consistent with those obtained here.

3.6.2. Analytical Methods

Suitable quartz vein material was found from zones of illite, propylitic, and biotite alteration. Fluid inclusions in primary quartz from porphyritic and equigranular Nasuji Pluton quartz diorites were also measured. Samples from 19 drillcore specimens were selected, from which 54 doubly polished thick sections (or wafers) were prepared. From these, 239 temperature

measurements were made, including liquid-vapour homogenisation, daughter salt dissolution, freezing point depressions and first melting of ice. All fluid inclusion results are tabulated in Appendix 2.

Microthermometry was carried out on a USGS heating/freezing stage (Werre et al., 1979; Woods et al., 1981) manufactured by Fluid Inc., and a Linkam MDS600 heating/freezing stage, manufactured by Linkam Scientific Instruments Ltd. Both stages have upper temperature limits of 600°C. They were calibrated using synthetic fluid inclusions supplied by Synflinc Inc., and the precision of measured temperatures are ± 1.0°C for heating and ± 0.3°C for freezing.

Salinities were determined as either NaCl or $CaCl_2$ equivalent weight percent (eq.wt.% NaCl or eq.wt.% $CaCl_2$, respectively). For halite-undersaturated inclusions these were calculated from freezing point depression temperatures using the method by Potter et al. (1978). Those inclusions that contained undersaturated solutions of H_2O-NaCl-$CaCl_2$, eq.wt.% NaCl and $CaCl_2$ were determined using the method described by Shepherd et al. (1985). For halite-saturated inclusions, salinities were calculated from the halite dissolution temperatures using the algorithm of Bodnar et al. (1989). Only a first approximation of the salinity of multiphase inclusions is provided by this method, as it ignores the contributions to the total salinity of salts other than NaCl and KCl. However, for halite- and sylvite-saturated inclusions, with two daughter salts, salinities were calculated using the computer program SALTY (Bodnar et al., 1989).

3.6.3. Fluid Inclusion Types

Based on observations made at room temperature, the following six fluid inclusion types (Table 3.4 and Figure 3.17) are recognised:

Type 1a : two-phase liquid-rich inclusions that homogenise to a liquid.

Type 1b : three-phase liquid-rich inclusions that contain an unknown opaque and/or translucent daughter minerals. Upon heating the vapour bubble disappears and the daughter minerals do not dissolve.

Type 2 : two-phase vapour-rich inclusions that either homogenise by vapour expansion or apparently do not homogenise during heating.

Type 3a : hypersaline three-phase inclusions with a halite daughter crystal. They homogenise either by vapour bubble disappearance (subtype **3al**) or halite dissolution (subtype **3ad**).

Type 3b : hypersaline multi-phase inclusions with a halite daughter crystal and an unknown opaque and/or translucent daughter minerals in addition to liquid and a vapour bubble. They homogenise either by vapour bubble disappearance (subtype **3bl**) or halite dissolution (subtype **3bd**). The unknown daughter minerals do not dissolve.

Type 4 : hypersaline multi-phase inclusions with two daughter salt crystals (halite and sylvite), along with unknown opaque and/or translucent daughter minerals. Upon heating, sylvite dissolves prior to disappearance of the vapour bubble and homogenisation is reached by dissolution of the halite daughter salt.

Only primary and secondary fluid inclusions were identified. These were distinguished using the criteria established by Roedder (1984). Primary fluid inclusions occur in crystal growth zones or as isolated and solitary inclusions. Secondary fluid inclusions occur along planes, or healed fractures.

Table 3.4. Summary of the fluid inclusion types with their contained phases at 25°C and behaviour upon homogenisation.

Fluid Inclusions		**Phases at 25°C**			**Homogenisation**
Type	**Subtype**	**Number**	**Dominant**	**Types**	**Behaviour**
1a	a	2	liquid	liquid + vapour	vapour disappears
1b	b	3-4	liquid	liquid + vapour + (± opaque ± unknown)	vapour disappears
2		2	vapour	vapour + liquid	no response observed on heating
3a	3al	3	liquid	liquid + vapour + halite	vapour disappears
	3ad	3	liquid	liquid + vapour + halite	salt dissolution
3b	3bl	3-5	liquid	liquid + vapour + halite + (± opaque ± unknown)	vapour disappears
	3bd	3-6	liquid	liquid + vapour + halite + (± opaque ± unknown)	salt dissolution
4		4-7	daughter minerals	liquid + vapour + halite + sylvite + (± opaque ± unknown)	salt dissolution

Number = the number of phases present in the fluid inclusion

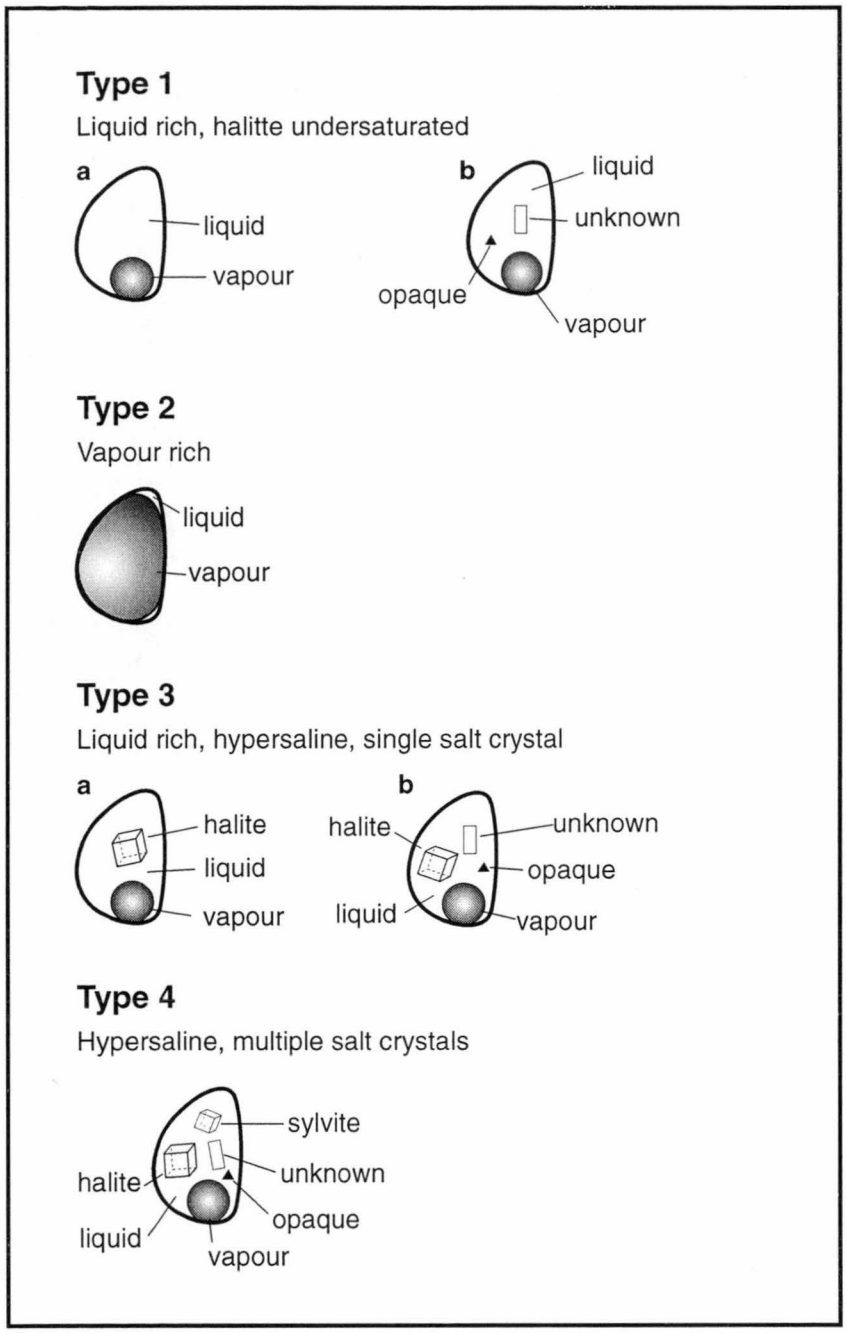

Figure 3.17. A summary of fluid inclusion types with phases present at 25°C.

3.6.4. Fluid Inclusion Populations

Fluid inclusions have been grouped into three populations. Table 3.5 summarises each population in terms of their range of homogenisation temperatures, salinities, inclusion types (in order of decreasing abundance), and where applicable, the associated alteration types and vein mineral assemblages.

Population A fluid inclusions consist of types 3a + 3b + 2 + 1a + 1b + 4 and occur both in quartz veins and in primary quartz from the Nasuji Pluton quartz diorite. Population A fluid inclusions in quartz veins are associated with biotite and propylitic (tremolite-actinolite) alteration. Biotite altered rocks have veins that contain quartz, biotite, anhydrite, magnetite ± tremolite-actinolite ± chalcopyrite ± hematite. In these veins, quartz crystals have equant anhedral habits that form an interlocking mosaic texture (Figure 3.8d). Two of the samples that contain population A fluid inclusions are from the biotite alteration zone associated with the Nasuji Pluton and are overprinted by illite alteration (Figure 3.5; Appendix 2). The other biotite altered specimen that contains population A fluid inclusions is from the biotite zone in the Puhagan area (Figure 3.7; Appendix 2). A propylitically (tremolite-actinolite) altered sample from the Puhagan area (Figure 3.6) contains population A fluid inclusions within discontinuous veins of euhedral quartz that has been overgrown by tremolite-actinolite needles (Appendix 2). Primary quartz crystals in porphyritic and equigranular quartz diorite contain secondary population A fluid inclusions. Fluid inclusions in quartz crystals from the porphyritic and equigranular hornblende quartz diorite have been measured, in order to compare their compositions with vein quartz from the biotite and propylitically (tremolite-actinolite) altered samples.

Coexisting type 1a and 2 inclusions (Figure 3.18a) comprise population B and occur in quartz veins associated with illite and propylitic (epidote + tremolite-actinolite) alteration assemblages. Samples containing population B inclusions are from wells located both close and peripherally to the upflow zone (Figure 3.19). Illite alteration quartz veins with population B inclusions contain anhydrite and minor calcite with rare illite, adularia, pyrite, chalcopyrite, sphalerite and galena. Veins associated with propylitic (epidote + tremolite-actinolite) alteration contain quartz and any of the following: bladed calcite, wairakite, epidote, tremolite-actinolite, adularia, pyrite, chalcopyrite and calcite. The presence of coexisting type 1a and 2 primary fluid inclusions in the same region of the crystal, suggests that the quartz precipitated from a two phase fluid with phase separation (i.e., boiling) occurring either at the site of entrapment and/or at greater depths (Roedder, 1984). Evidence for boiling occurring at the site of entrapment is provided by samples that have population B fluid inclusions in quartz occurring interstitial to bladed calcite (Figure 3.18b).

Inclusions belonging to population C consist exclusively of type 1a and occur in quartz veins associated with illite and propylitic (chlorite) alteration zones. Quartz veins associated with

illite alteration contain anhydrite and/or calcite with minor amounts of pyrite and rare chalcopyrite. Quartz veins associated with propylitic (chlorite) alteration have wairakite, adularia, illite, pyrite and rare chalcopyrite (Table 3.5). Samples containing population C inclusions are from wells located outside the upflow zone (Figure 3.19).

Table 3.5. Summary of the fluid inclusion populations with associated vein mineralogies, alteration and inclusion types and the range of homogenisation temperatures and salinities (eq.wt.% NaCl, KCl & $CaCl_2$). Fluid inclusion populations A, B and C are in quartz veins, and their respective associated alteration types are listed. Population A inclusions also occur in primary quartz from porphyritic and equigranular hornblende quartz diorite (Nasuji Pluton).

Inclusion Population	Vein Mineralogy	Alteration Type	Inclusion Types	Homog. Temp. (°C)	NaCl (eq.wt.%)
A	qtz ± anh ± bio ± mt ± tr/at ± cp	biotite, propylitic (tremolite-actinolite)	3a + 3b + 2 + 1a + 1b ± 4	267° to >600°C	34.3 to 61.6 (KCl = 11.8 to 19.9)
B	qtz ± epi ± tr/at ± anh ± cc ± wai ± adu ± py ± sph ± ga ± cp	illite, propylitic (epidote + tremolite-actinolite)	1a + 2	214° to 356°C	0.0 to 10.5 ($CaCl_2$ = 3.8)
C	qtz ± anh ± cc ± wai ± adu ± py ± cp	illite, propylitic (chlorite)	1a	189° to 345°C	0.0 to 4.5

Mineral abbreviations : adu = adularia; anh = anhydrite; bio = biotite; cc = calcite; cp = chalcopyrite; epi = epidote; ga = galena; mt = magnetite; py = pyrite; qtz = quartz; sph = sphalerite; tr/at = tremolite-actinolite; wai = wairakite.

Homog. Temp. = homogenisation temperature.

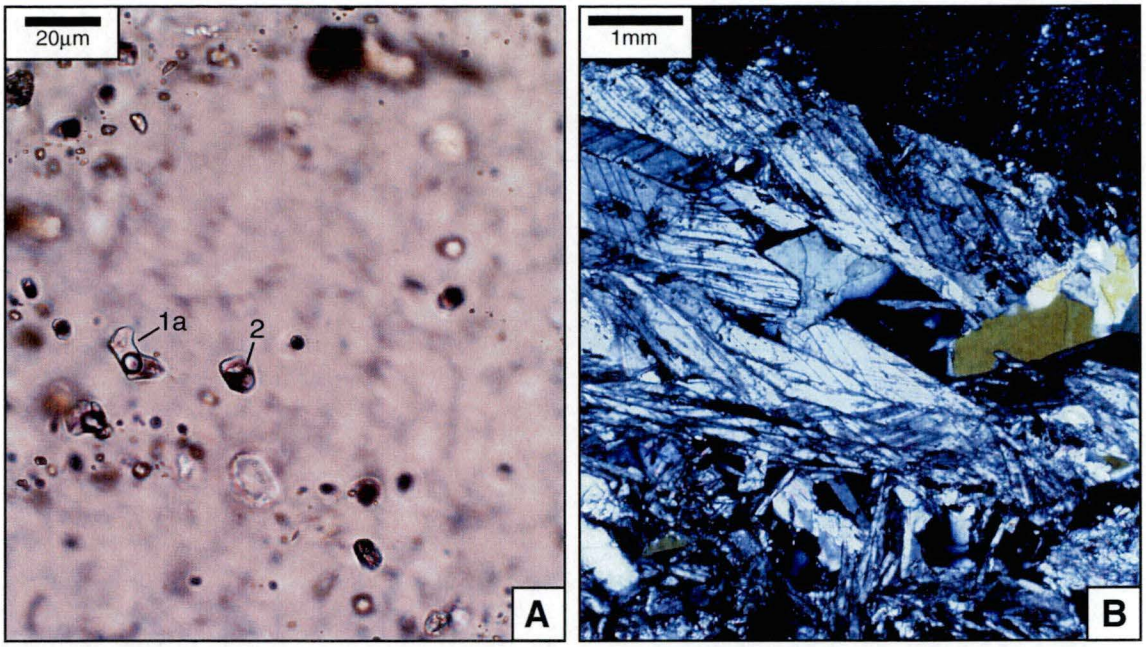

Figure 3.18. a. *Sample PN16D/2 Photomicrograph taken under plane polarised light.* Coexisting liquid-rich (Type 1a) and vapour-rich (Type 2) fluid inclusions in vein quartz associated with propylitic (epidote) alteration (population B). **b.** *Sample PN1RD/2. Photomicrograph taken under crossed polarised light.* A vein containing platey calcite and quartz filling interstitial cavities. Quartz contains population B (coexisting type 1a & 2) inclusions.

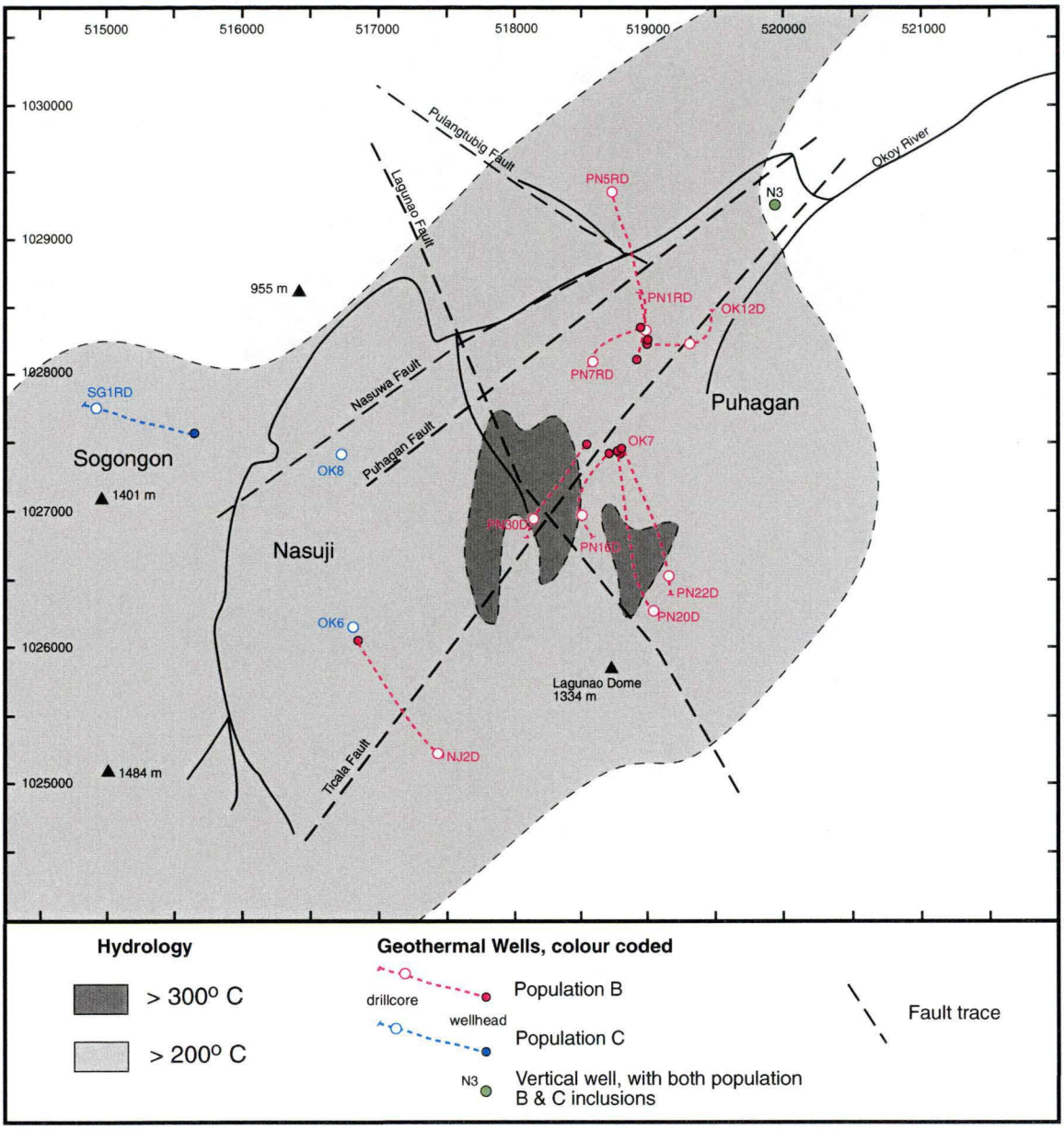

Figure 3.19. The location of wells and drillcore samples containing vein quartz with population B and C fluid inclusions. Deviated wells and drillcores are projected to the surface and colour coded with respect to the type of fluid inclusion population. Also represented is the hydrology, as defined by the 200° and 300°C isotherms.

3.6.5. Microthermometric Analyses

Population A

Population A fluid inclusions range in size between less than 5 μm and 40 μm. Temperatures of homogenisation are between 267° and greater than 600°C (Figure 3.20a). For the type 3 fluid inclusions, salt dissolution temperatures ranged between 244° and 537°C, indicating apparent salinities between 34.3 and 60.7 eq.wt.% NaCl (Figure 3.20b). For type 4 fluid inclusions, the halite and sylvite dissolution temperatures (463°-576°C; 80°-268°C, respectively) correspond to calculated concentrations ranging between 48.9-61.6 eq.wt.% NaCl and 11.8-19.9 eq.wt.% KCl (Bodnar et al., 1989). This implies that the type 4 fluid inclusions contain solutions with salinities between 60.7 and 79.4 eq.wt.% NaCl and KCl (Figure 3.20b).

Population B

Fluid inclusions range in size from less than 5 μm to 80 μm. Homogenisation temperatures are between 214° and 356°C, with 63% of the measurements between 280° and 320°C (Figure 3.20a). Two temperatures of first melting (-19° and -23°C) indicate that most of the solutions can be treated as simple H_2O-NaCl or H_2O-NaCl-KCl salt solutions with apparent salinities ranging between 0.0 and 10.5 eq.wt.% NaCl (Table 3.5; Figure 3.20b). However, some first melting temperatures ranging between -55.8° and -69.1°C were recorded, indicating that some fluid inclusions contain solutions with a chemistry belonging to the H_2O-NaCl-$CaCl_2$ salt system. In such inclusions, antarcticite ($CaCl_2.6H_2O$) was recognised to initially melt at approximately -69°C with a final melt temperature at -28.8°C, while ice finally melted at -3.2°C. This melting sequence and measured temperatures indicate that these inclusions contain solutions with 1.6 eq.wt.% NaCl and 3.8 eq.wt.% $CaCl_2$.

Population C

Population C inclusions range in size from less than 5 μm to 30 μm. Type 1a homogenisation temperatures are between 189° and 345°C, with 80% of the measurements between 201° and 270°C (Figure 3.20a). Four temperatures of first melting were observed and ranged between -23.5° and -27.9°C. Salinity estimates were between 0.0 and 4.5 eq.wt.% NaCl (Figure 3.20b). Secondary population C fluid inclusions from samples OK8/5 and OK6/2 (which contain primary population A fluid inclusions) have temperatures and salinities consistent with the primary data shown in Figures 3.20a and 3.20b.

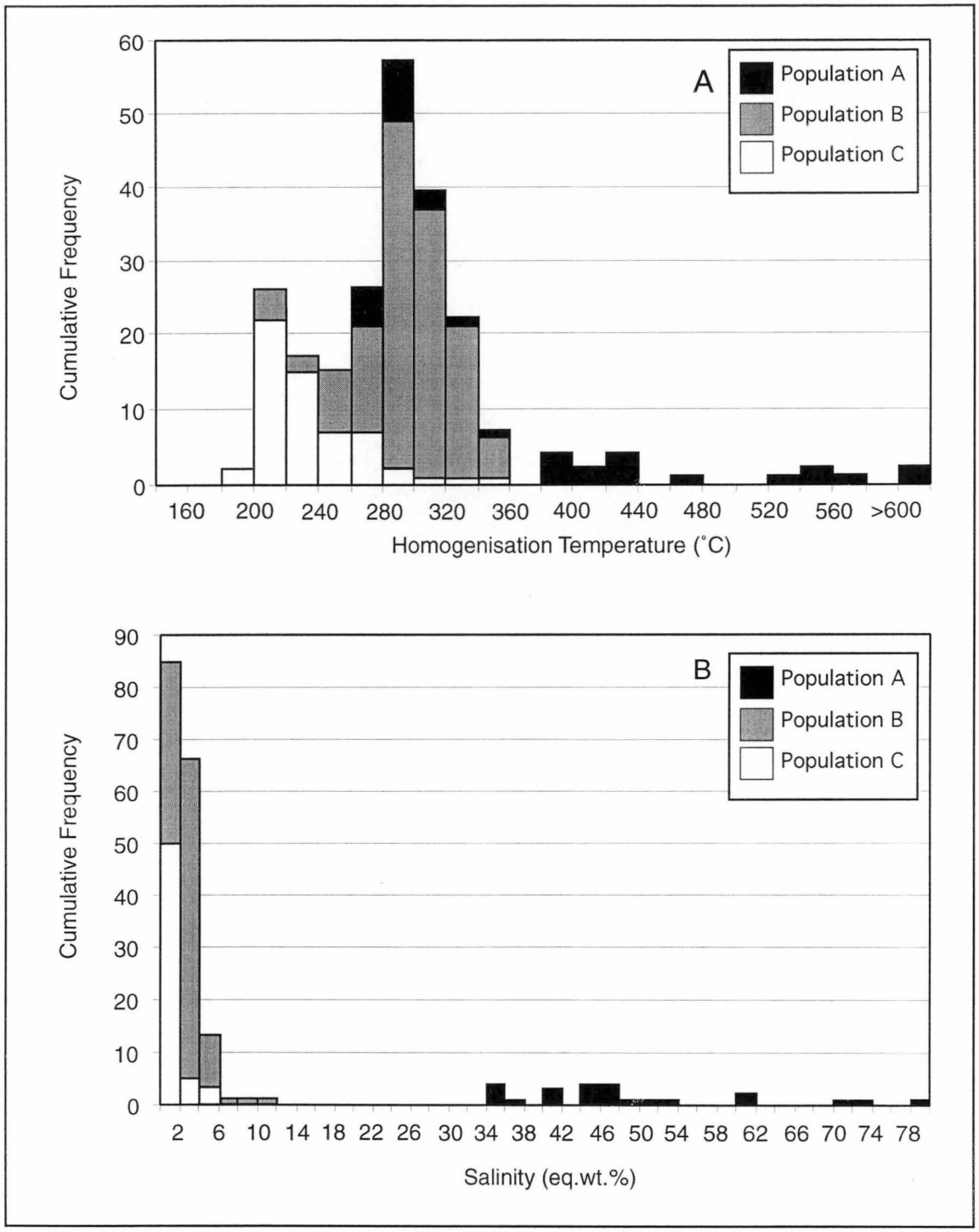

Figure 3.20. Histograms summarising : (A) homogenisation temperature measurements; (B) calculated salinities as eq.wt. % NaCl for population B and C fluid inclusions, and as eq.wt.% NaCl + KCl for type 4 fluid inclusions.

3.6.6. PIXE Analyses

Fluid inclusions from two samples were analysed by proton induced X-ray emission (PIXE) using the CSIRO-GEMOC Nuclear Microprobe housed at CSIRO, North Ryde, Sydney. PIXE analysis provides a nondestructive method for acquiring the chemical constituents of individual fluid inclusions. The microprobe can focus a 3 MeV proton beam with a 1.3 μm beam size for fluid inclusion analysis and beams for mineral imaging at 1.8 μm resolution (Ryan et al., 2001). Metal concentrations of the fluids were determined using the methodology of Heinrich et al. (1992)

Four type 3b and one type 2 (population A) fluid inclusions from sample NJ3D/3 and one type 1a (population B) fluid inclusion from OK7/7 were analysed. The PIXE results, along with microthermometric information for each fluid inclusion, are presented in Table 3.6 with the PIXE spectra illustrated in Figure 3.21 and element distribution images presented in Figure 3.22.

Sample NJ3D/3

This sample is a quartz phenocryst from a porphyritic hornblende quartz diorite (Nasuji Pluton). The range of homogenisation temperatures for the four type 3b inclusions is between 318° and 430°C and salinities range between 41.5 and 47.6 eq.wt.% NaCl. There was no apparent homogenisation during heating of the vapour-rich (type 2) inclusion (Table 3.6).

The results of the PIXE analyses shows that the chemical contents of all the fluid inclusions in these quartz crystals have an appreciable metal component (Table 3.6; Figures 3.21a-e). The four type 3b fluid inclusions measured have average concentrations of 6.0 wt.% Fe, 0.7 wt.% Zn, 0.3 wt.% Pb and 930 ppm Cu. There is however, a wide range of Cu concentrations with one fluid inclusion containing 0.2 wt.% Cu (Table 3.6). The type 2 fluid inclusion also contains considerable concentrations of Fe (3.4 wt.%), Zn (0.22 wt.%) and Cu (654 ppm).

Element distribution images have been reproduced in Figures 3.22a, b. The diffuse patterns of Pb and Zn implies that these metals are most likely residing in the saline solution at room temperature, whereas the more concentrated distribution patterns of Fe and Cu suggests they occur in minute daughter minerals. A small opaque daughter mineral can be seen beneath the bubble in Figure 3.22b.

Sample OK7/7

This specimen is from an epidote-quartz vein in a propylitically (epidote) altered porphyritic hornblende diorite (Puhagan dikes). The type 1a fluid inclusion has a homogenisation temperature of 288°C and based on the freezing measurements, the trapped fluid is a H_2O-NaCl-$CaCl_2$ solution with 1.6 eq.wt.% NaCl and 3.8 eq.wt.% $CaCl_2$ (Table 3.6).

The results of the PIXE analysis shows that the fluid inclusion contains 2.0 wt.% Ca and 3.2 wt.% Mn (Table 3.6). Unfortunately, Na concentrations could not be quantified, but elevated concentrations can be seen in the element distribution image (Figure 3.22c). High concentrations of Fe (0.22 wt.%), Zn (0.14 wt.%) and Pb (0.05 wt.%; Table 3.6) were detected. However of these, only Fe and Zn are discernible in the element distribution images (Figure 3.22c).

Table 3.6. Results of PIXE analyses

Sample	Type	T_H[1] (°C)	NaCl[2] (wt%)	Cl	K	Ca	As	Br	Ti	Mn	Fe	Zn	Pb	Cu	Rb	Sr
				(wt%)										(ppm)		
NJ3D/3																
i	3b	430	41.5	-	-	-	-	0.28	1.61	3.65	6.89	0.73	0.32	770	612	541
ii	3b	417	47.6	-	-	-	-	0.26	1.07	3.27	5.94	0.93	0.32	418	674	450
iii	3b	385	44.7	-	5.34	2.19	-	0.28	0.43	4.03	6.26	0.96	0.27	283	376	598
iv	3b	381	44.3	30.90	3.76	0.16	-	0.05	0.18	1.71	4.79	0.07	0.17	2250	620	-
Average		*403*	*44.5*	*30.9*	*4.6*	*1.2*	-	*0.2*	*0.8*	*3.2*	*6.0*	*0.7*	*0.3*	*930*	*571*	*530*
v	2	-	-	-	3.09	0.91	-	0.07	1.39	1.07	3.35	0.22	-	654	422	-
OK7/7																
i	1a	288	1.6 (3.8)[3]	-	0.46	2.02	0.01	0.06	-	0.31	0.22	0.14	0.05	-	114	500

1 = homogenisation temperature determined from fluid inclusion microthermometric measurements
2 = eq.wt.% NaCl determined from fluid inclusion microthermometric measurements
3 = OK7/7 inclusion contains 1.6 eq.wt.% NaCl and 3.8 eq.wt.% $CaCl_2$
- = inclusion was too deep for analysis

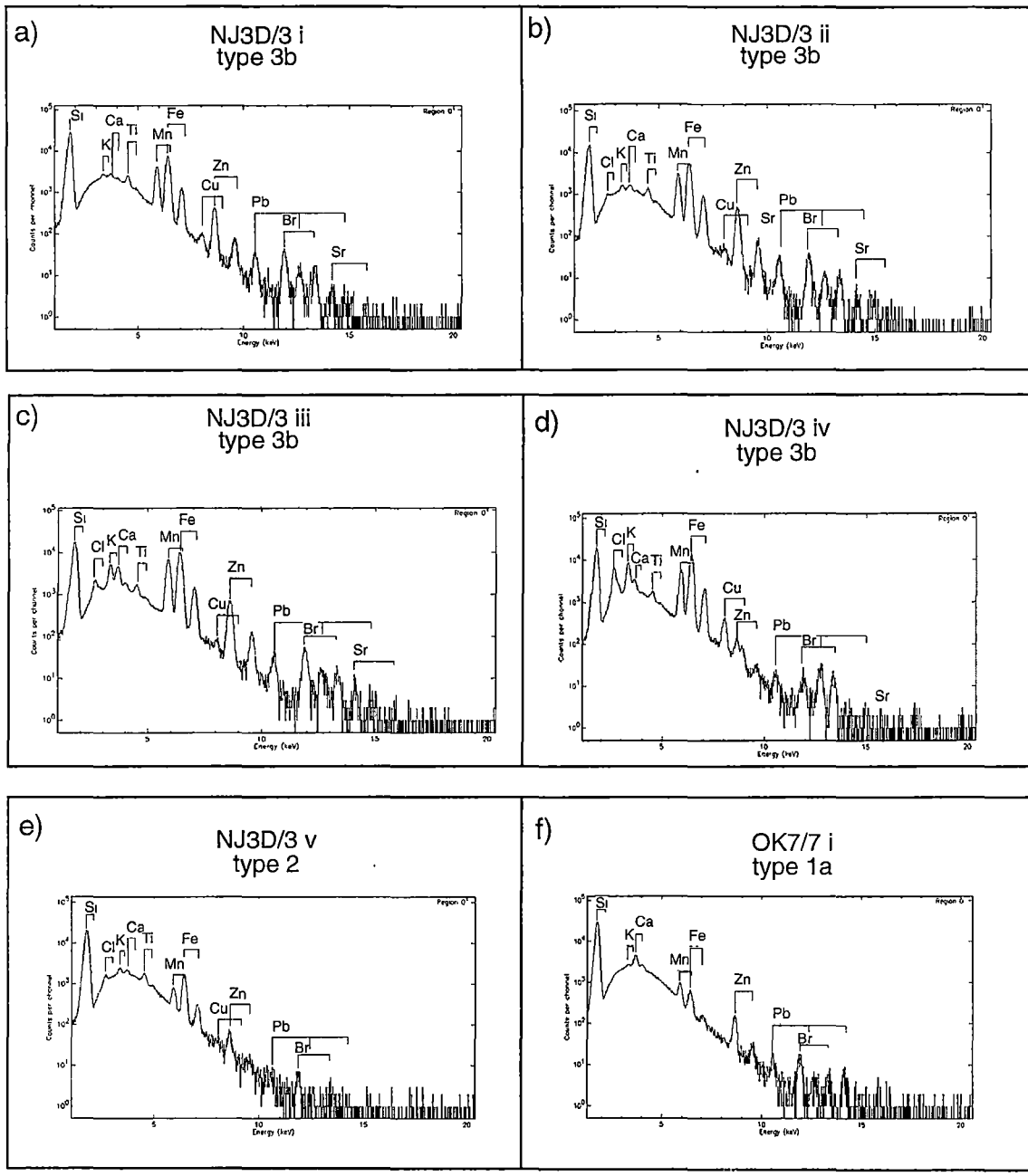

Figure 3.21. PIXE analytical spectra. **a-e)** five fluid inclusions from a quartz phenocryst in the porphyritic hornblende quartz diorite (NJ3D/1; Nasuji Pluton); **f)** one inclusion from vein quartz in a propylitically (epidote) altered porphyritic hornblende diorite (OK7/7; Puhagan dike).

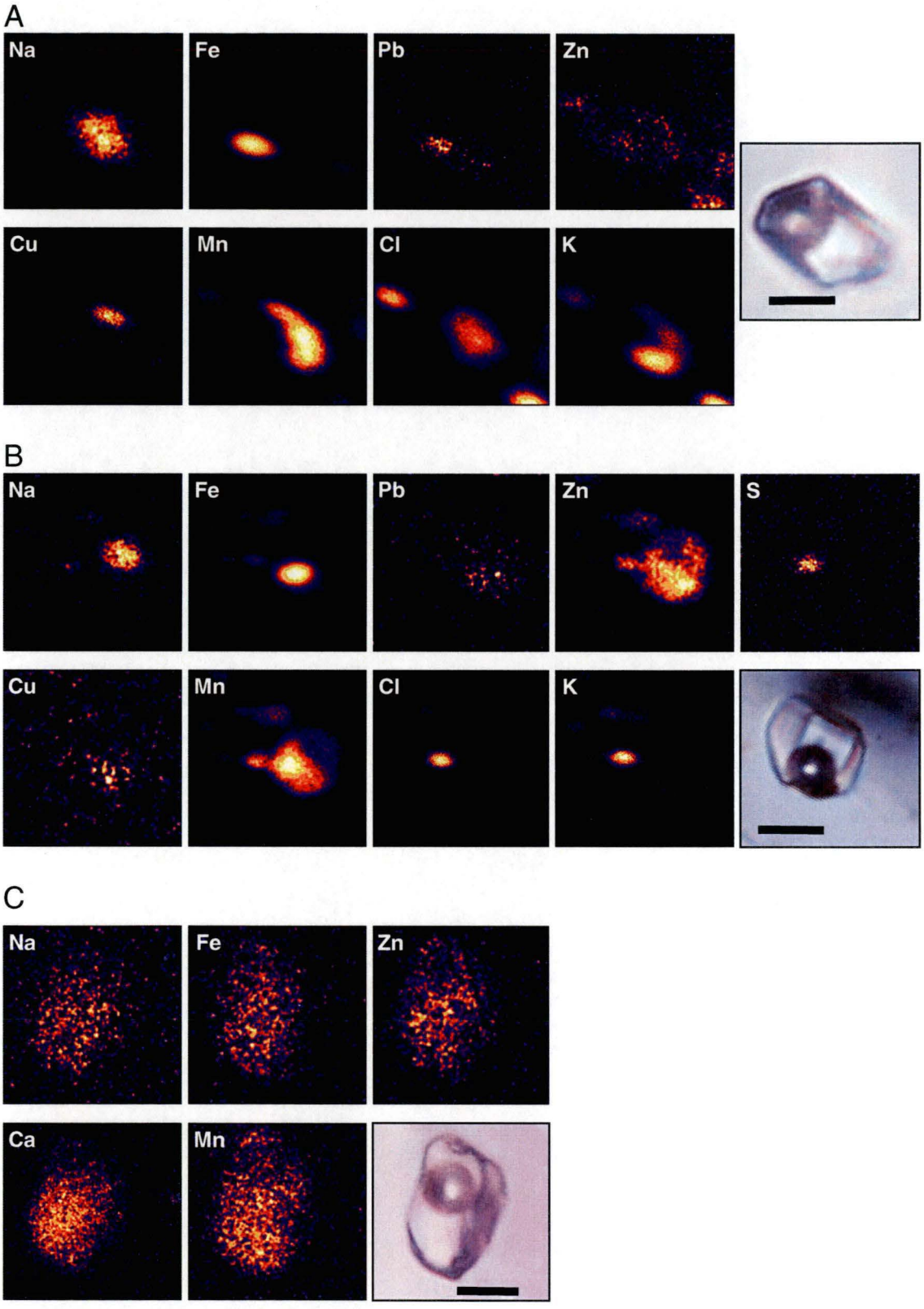

Figure 3.22. PIXE element distribution images. A. NJ3D/3 iv. B. NJ3D/3 ii. C. OK7/7 i. Scale bar is 5 μm. See text for discussion.

3.6.7. Discussion

Fluid inclusion microthermometry experiments have revealed that the three fluid inclusion populations can be categorised into high salinity (> 34 eq.wt.% NaCl population A) and low salinity (i.e., < 11 eq.wt.% NaCl; populations B and C) inclusions. The high salinity inclusions also tend to have higher homogenisation temperatures than the low salinity inclusions (Figures 3.20a and b).

High Salinity Fluid Inclusions : Population A

The coexistence of hypersaline liquid- and vapour-rich fluids trapped in primary quartz crystals in the Nasuji Pluton implies that both fluid types were present as separate phases within a silicate melt at the time of quartz crystallisation. Such inclusions have been reported in intrusions associated with porphyry copper deposits, for example at Panguna (Eastoe, 1978), Santa Rita (Reynolds and Beane, 1985), Acupan South (Cooke and Bloom, 1990) and Far Southeast (Hedenquist et al., 1998). Coexisting high and low density fluids in the magmatic-hydrothermal environment have been commonly interpreted to be the product of liquid-vapour phase separation from a magmatic-derived fluid (Henley and McNabb, 1978). However, depending on the prevailing conditions of temperature, pressure and dissolved Cl/H, it could also be possible for separate liquid and vapour phases to exsolve directly from the source magma (Bodnar et al., 1985; Bodnar, 1995).

There is no clear distinction between the secondary population A fluid inclusions in quartz crystals from the Nasuji Pluton and the primary fluid inclusions in quartz associated with the Nasuji-Sogongon biotite alteration assemblage (Figure 3.23). This is considered evidence for a genetic link between the late stage aqueous magmatic fluids of the Nasuji Pluton and those fluids responsible for the spatially associated biotite alteration assemblage. The magmatic-hydrothermal fluids from the Nasuji Pluton are interpreted to have escaped the confines of the intrusion, passing into the surrounding host rock and causing high temperature K-Fe metasomatism.

The population A fluid inclusions associated with the Puhagan biotite and propylitic (tremolite-actinolite) alteration assemblages appear to have lower salinities and homogenisation temperatures than those associated with the Nasuji-Sogongon biotite alteration assemblage (Figure 3.23). Nevertheless, the occurrence of these high salinity fluid inclusions in the Puhagan area is evidence for the existence of a 'blind' intrusive body beneath drilled depths, and for the involvement of magmatically-derived hydrothermal fluids in the formation of the Puhagan biotite and propylitic (tremolite-actinolite) alteration assemblages.

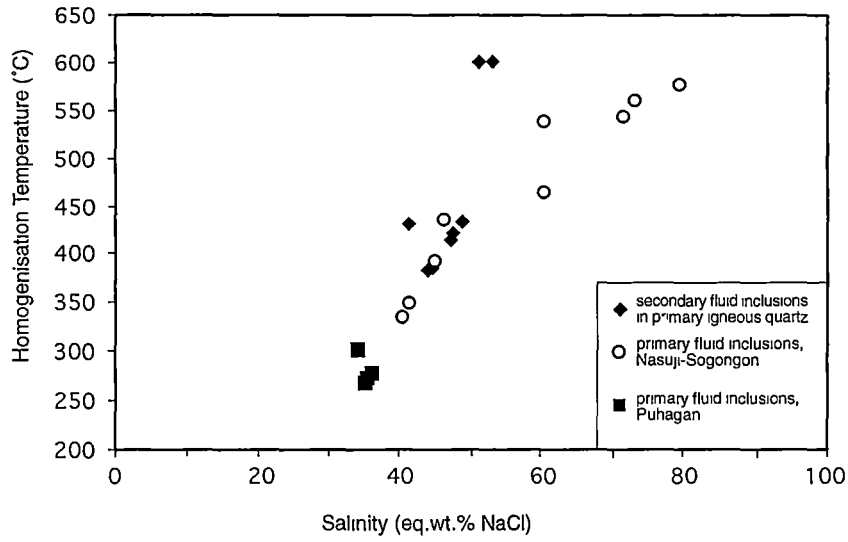

Figure 3.23. Homogenisation temperature versus salinity for population A fluid inclusions. Temperatures above 600°C (upper limit of heating stage) are recorded as 600°C. Salinities are recorded as eq.wt.% NaCl, except for type 4 fluid inclusions which are plotted as total eq.wt.% NaCl + KCl.

Pressure – Depth Estimates

Estimation of the depths of formation for the population A fluid inclusions can be gained by using phase relations in the NaCl-H_2O system (Bodnar et al., 1985; Fournier, 1987; 1999). In the pressure versus temperature diagram (Figure 3.24), modified from Muntean and Einaudi (2001), depths are shown assuming densities of 1 g/cm^3 hydrostatic pressures and 2.5 g/cm^3 for lithostatic pressures. The brittle-ductile transition is at about 400°C (Figure 3.24) with a strain rate assumed to be 10^{-14} sec^{-1} (Fournier, 1987). Within the two phase gas + liquid (G + L) field, contours of constant weight % NaCl dissolved in the liquid and gas are represented. To obtain an estimate of the pressures, and hence depths, of formation, population A fluid inclusions have been plotted in terms of their homogenisation temperatures and salinities (Figure 3.24). Uncertainties of approximately 100-200 bars are to be expected (Muntean and Einaudi, 2001).

The secondary fluid inclusions contained in primary quartz from the equigranular quartz diorite of the Nasuji Pluton are estimated to have formed at temperatures in excess of 600°C at minimum depths of 2 to 2.5 km under lithostatic pressures and ductile deformation (field 1; Figure 3.24; Table 3.7). The trapped aqueous fluid that originally exsolved from the partly crystallised magma plots in the two phase field (Figure 3.24, Bodnar et al., 1985), consistent with the trapping of fluids of high density liquid and a low density vapour. These fluids escaped from the magma chamber, via ductile deformation fractures to shallower levels, to form quartz veins associated with the biotite alteration assemblages. Some of these veins formed at approximately 550°C and 1.5 km beneath the palaeo-water table (field 2; Figure 3.24; Table 3.7). Their position close to the gas + liquid + salt field (G + L + S; Figure 3.24) indicates that at these temperatures and pressures, the fluids became supersaturated (~60 wt.% NaCl) with respect to NaCl and halite precipitated. Evidence for the fluid entering the G + L + S field from the G + L field comes from type 3 fluid inclusions that show vapour bubble disappearance prior to dissolution of the salt daughter minerals (i.e., types 3ad and 3bd fluid inclusions; Fournier, 1999).

As this highly saline fluid cooled from approximately 550° to <400°C, decompression from lithostatic to hydrostatic pressure conditions occurred, possibly as a result of overpressuring and breaching of the self-sealed brittle-ductile transition zone, in a manner described by Fournier (1999). Reasons for such a breach have been reviewed by Fournier (1999) and include accumulation of the exsolved magmatic fluids beneath an impermeable carapace (Norton and Cathles, 1973; Burnham, 1979); exsolution of magmatic gases at depth and transport to shallow levels of the pluton by magmatic convection (Shinohara et al., 1995); the injection of a new pulse of magma from depth (Fournier, 1999); or seismic failure that causes fracturing of the self-sealed zone (Lister, 1974).

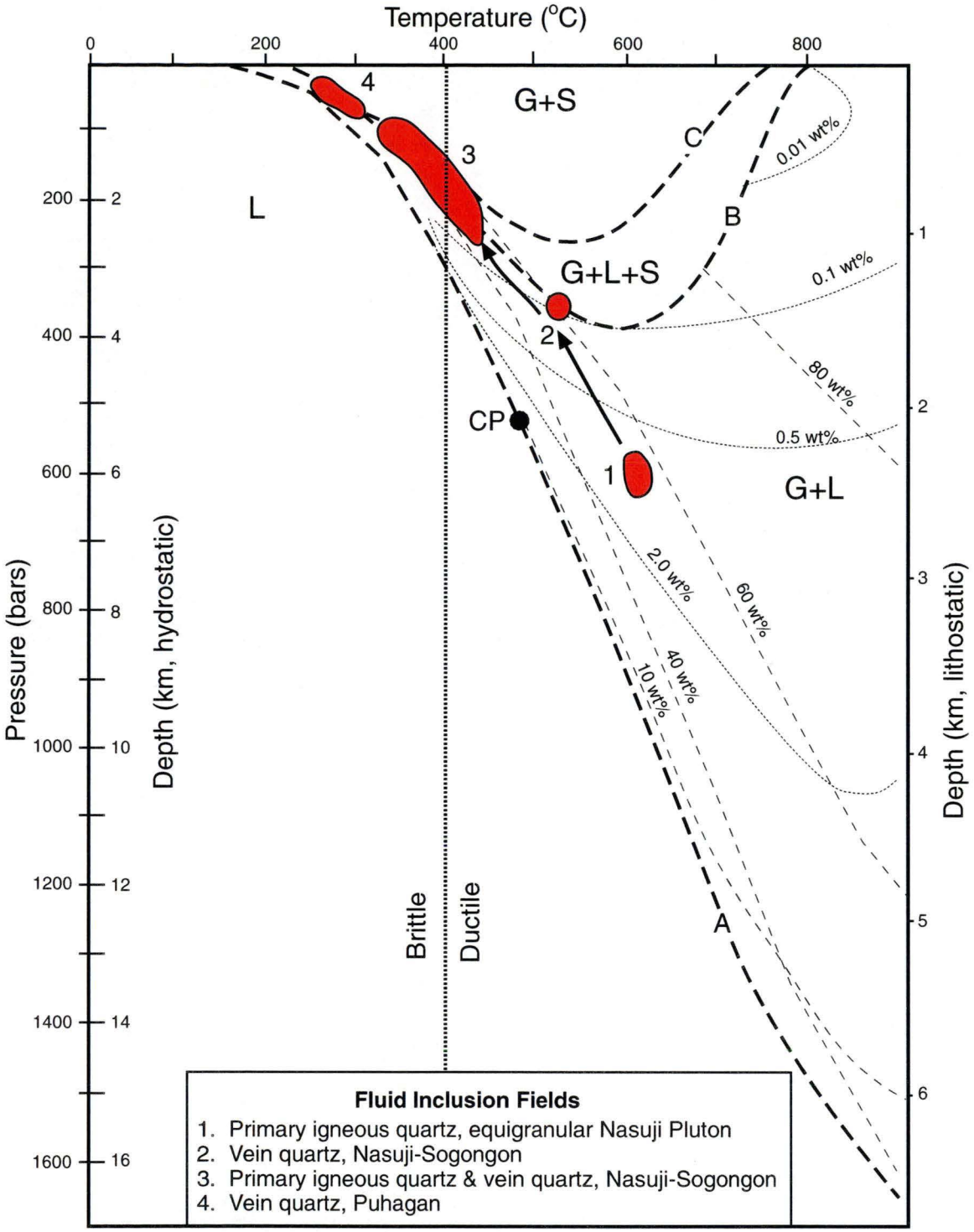

Figure 3.24. Temperature vs depth diagram in the NaCl-H_2O system. Based on Bodnar et al. (1985), Fournier (1999) and modified from Muntean and Einaudi (2001). The diagram shows the predominance fields for liquid (L), gas + liquid (G + L) and gas + halite (G + S). Curve A is the boiling point curve for a 10 wt.% NaCl solution, with point CP as its critical point. Curve B separates the G + L field from a three phase field (G + L + S) for the system NaCl-H_2O. Curve C is the liquid saturation curve for the NaCl-KCl-H_2O system, where Na/K ratios are in equilibrium with albite and K–feldspar. Contours of constant NaCl (wt.%) in the G + L field are shown for liquid (thin dash lines) and gas (thin dotted lines). The thick vertical dotted line is the approximate temperature of the brittle-ductile boundary. The diagram illustrates the proposed paths (fields 1 to 3) for fluids in the Nasuji-Sogongon area. Field 4 represents fluid inclusions associated with biotite and propylitic (tremolite-actinolite) alteration assemblages in the Puhagan area. See Table 3.7 for a summary of the samples characterising each field.

Table 3.7. Summary of the samples comprising fields 1 to 4 in Figure 3.24.

Field	Sample	Depth (m)	Area	Class	Host Rock	Host Quartz	Alter.	Tv (°C)	Ts (°C)	Salinity (wt.% NaCl)
1	NJ2D/1	2,910	N-S	S	NP-e	Igneous	-	>600	471	53.2
1	NJ2D/1	2,910	N-S	S	NP-e	Igneous	-	>600	454	51.3
2	OK6/2	1,340	N-S	P	SNF	vein	bio	368	537	60.7
3	OK6/2	1,340	N-S	P	SNF	vein	bio	269	386	44.8
3	OK6/2	1,340	N-S	P	SNF	vein	bio	435	404	46.4
3	OK8/5	2,310	N-S	P	LPVF	vein	bio	220	392	45.3
3	OK8/5	2,310	N-S	P	LPVF	vein	bio	218	334	40.4
3	OK8/5	2,310	N-S	P	LPVF	vein	bio	201	350	41.7
3	NJ2D/1	2,910	N-S	S	NP-e	Igneous	-	396	432	49 1
3	NJ2D/1	2,910	N-S	S	NP-e	Igneous	-	305	414	47.4
3	NJ2D/1	2,910	N-S	S	NP-e	Igneous	-	421	419	47.8
3	NJ3D/3	2,170	N-S	S	NP-p	Igneous	-	430	348	41.5
3	NJ3D/3	2,170	N-S	S	NP-p	Igneous	-	293	417	47.6
3	NJ3D/3	2,170	N-S	S	NP-p	Igneous	-	327	385	44.7
3	NJ3D/3	2,170	N-S	S	NP-p	Igneous	-	279	381	44.3
4	PN25D/2	3,270	Puh	P	LPVF	vein	bio	300	244	34.3
4	PN20D/2	3,100	Puh	P	PD	vein	prop-ta	267	263	35.4
4	PN20D/2	3,100	Puh	P	PD	vein	prop-ta	271	267	35 7
4	PN20D/2	3,100	Puh	P	PD	vein	prop-ta	271	269	35.8
4	PN20D/2	3,100	Puh	P	PD	vein	prop-ta	263	277	36.3

Key:
Depth = sample depth; **Class** = primary (P) or secondary (S) fluid inclusion; **Alter.** = Associated alteration assemblage; **Tv** = Temperature of vapour bubble disappearance; **Ts** = Temperature of salt dissolution; N-S = Nasuji-Sogongon area; Puh = Puhagan area; NP-e = equigranular Nasuji Pluton; NP-p = porphyritic Nasuji Pluton, SNF = Southern Negros Formation; LPVF = Lower Puhagan Volcanic Formation; PD = Puhagan Dikes; bio = biotite alteration assemblage; prop-ta = propylitic (tremolite-actinolite) alteration assemblage

Most of the population A fluid inclusions plot in a zone that transgresses the hydrostatic-lithostatic brittle-ductile transition at approximately 400°C. The depth is either between 1-2 km beneath the palaeo-water table, under hydrostatic pressure conditions, or approximately 1 km under lithostatic pressure (field 3; Figure 3.24). The fluid inclusions in this field include those in primary quartz from equigranular and porphyritic quartz diorites and those associated with the Nasuji-Sogongon biotite alteration assemblages (Table 3.7). Any of the mechanisms presented above could explain the reason for a transition between hydrostatic to lithostatic pressures.

The population A fluid inclusions associated with the Puhagan biotite and propylitic (tremolite-actinolite) alteration assemblages plot within the hydrostatic brittle field at depths less than 1 km below the palaeo-water table (field 4; Figure 3.24; Table 3.7), even though these inclusions come from a present-day sample depths of 3.1 to 3.3 km below the surface.

The estimated formation depth of fluid inclusions plotting in field 3 (Figure 3.24), is approximately 1-2 km beneath the palaeo-water table. In the Nasuji-Sogongon area, the present-day water table is up to 1000 m below surface. Therefore, their estimated depth of formation could be as much as 3 km below the surface. The drillcore samples containing these fluid inclusions are from near the top of the Nasuji Pluton, at depths ranging from 1-1.5 km

below the present-day surface (Figure 3.5). High temperature (i.e., > 250°C) propylitic and hypogene advanced argillic alteration mineral assemblages (i.e., epidote and zunyite, respectively) occur in rocks cropping out at the surface above the pluton. This provides convincing evidence for the erosion of at least 450 m of overlying rock (Reyes, 1990), assuming the palaeo-water table reached the surface, and closer to 1500 m if the palaeo-water table was as deep as the present-day water table. This implies the formation of the Nasuji-Sogongon biotite alteration assemblage and the emplacement of the porphyritic quartz diorite could have been as deep as 2.5-3 km below the surface. This depth is consistent with the depth estimates from Figure 3.24, for a hydrostatic pressure regime.

There is an inconsistency between the estimated and present-day depths of formation for the population A fluid inclusions associated with the Puhagan biotite and propylitic (tremolite-actinolite) alteration assemblages. Their estimated depths of formation are less than 1 km beneath the palaeo-water table. However, these fluid inclusion samples are from drillcores collected from the bottom of wells PN20D and PN25D (Figures 3.6 and 3.7) at approximately 3 km below the present-day water table. It should be noted that uncertainties of approximately 100-200 bars are associated with the salinity contours in Figure 3.24 (Muntean and Einaudi, 2001). Such an error equates to approximately 1-2 km under hydrostatic pressure conditions and could account for the discrepant depths.

Low Salinity Fluid Inclusions : Population B and C

Apparent Salinities

It was established by Hedenquist and Henley (1985) that in shallow crustal environments, dissolved CO_2 will strongly influence the freezing point depression of a hydrothermal fluid. Even for a fluid that lacks clathrate behaviour during freezing measurements (i.e. < 3.5 wt.% or 0.81 molal CO_2), up to –1.5°C of the freezing point depression could be due to dissolved CO_2.

Salinities calculated from freezing measurements indicate that fluid inclusions belonging to populations B and C are relatively dilute (Figure 3.20b). Furthermore, since CO_2 clathrate was not observed during any of the freezing measurements, the gas concentrations in these fluid inclusions must be less than 3.5 wt.% CO_2 (Hedenquist and Henley, 1985). The majority of population C fluid inclusions have final ice melting temperatures greater than –1.5°C (Figure 3.25), hence, their apparent salinities are possibly due to the trapped fluid containing as much as 3.5 wt.% CO_2. Population B fluid inclusions however, tend to have higher apparent salinities that cannot be accounted for by dissolved CO_2 alone (Figure 3.25).

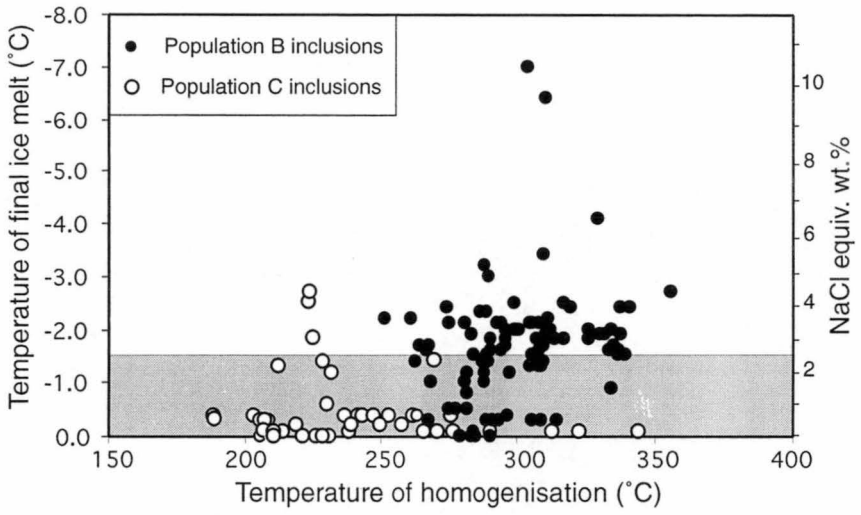

Figure 3.25. Homogenisation temperature vs. final ice melting temperature for population B and C fluid inclusions. The shaded area represents the final ice melting temperature (-1.5°C) for fluids containing up to 3.5 wt.% CO_2.

Average homogenisation and final ice melting temperatures for population B and C inclusions are presented Table 3.8. The effects of dissolved CO_2 on salinity are demonstrated by assuming maximum and minimum CO_2 concentrations and calculating the corresponding NaCl concentrations using equation 1 (Hedenquist and Henley, 1985) :

$$T_m = - K \Sigma m_I \quad (1)$$

where T_m is the final ice melting temperature; K is the molal freezing point depression constant (1.72 Kelvin/molal for electrolytes; 1.86 Kelvin/molal for nonelectrolytes); Σm_I is the sum of all dissolved solutes.

For the assumption that there is no dissolved CO_2 in the inclusion solution, the average salinities range between 0.2 and 1.5 eq.wt.% NaCl for population C inclusions and 0.5-5.9 eq.wt.% NaCl for population B inclusions (Table 3.8). Alternatively, by assuming a maximum dissolved CO_2 concentration (0.81 molal) in the inclusion solution, salinities for population C inclusions are 0.0 eq.wt.% NaCl and between 0.0 and 3.4 eq.wt.% NaCl for population B inclusions. No attempt was made to quantify the CO_2 concentrations further and the range of apparent salinities presented in Table 3.5 must be considered maximum values that could be lower by up to 2.5 eq.wt.% NaCl (Hedenquist and Henley, 1985).

The results from microthermometric and PIXE analyses show that some of the population B fluid inclusions (i.e., OK7/7; Table 3.6, Figure 3.22c) contain multicomponent solutions, including $CaCl_2$ and also $MnCl_2$, which can make salinity estimations difficult. This may account for sample OK7/7 containing the highest average apparent NaCl concentrations (5.9 wt.%) of all the population B fluid inclusions (Table 3.8). Reasons for the population B fluid inclusions having higher apparent salinities remain unclear. The location of the population B fluid inclusions are mostly in the Puhagan area close to, or peripheral to the upflow zone (Figure 3.19). It is possible that the higher salinities have formed due to input of either magmatic-brines from a 'blind' intrusion beneath the drilled depths, or connate-brines derived from the Okoy Formation. Alternatively, it is possible they have formed following localised open-system boiling (Simmons and Browne, 1997).

Table 3.8. Average homogenisation (T_H) and final melting (T_m) temperatures for Population B and C inclusions. Considering minimum and maximum CO_2 concentrations, apparent salinities have been recalculated using equation 4 of Hedenquist & Henley (1985).

Sample	T_H (°C) (mean)	T_m (°C) (mean)	No. of Inclusions	CO_2 (moles)	CO_2 (wt.%)	NaCl (moles)	NaCl (wt.%)
Pop. B							
N3/1	217.2	-0.6	5	0.00	0.0	0.17	1.0
				0.81	3.5	0.00	0.0
N3/4	246.5	-1.1	8	0.00	0.0	0.32	1.9
				0.81	3.5	0.00	0.0
NJ2D/2	288 2	-0.3	T_m=11; T_H=12	0.00	0.0	0.08	0.5
				0.81	3.5	0.00	0.0
OK7/7	297.4	-3.5	T_m=3; T_H=17	0.00	0.0	1.02	5.9
				0.81	3.5	0.58	3.4
OK7/9	303.2	-1.9	7	0.00	0.0	0.56	3.3
				0.81	3.5	0.13	0.7
OK12D/5	264.8	-2.0	2	0.00	0.0	0.57	3.3
				0.81	3.5	0.13	0.8
PN1RD/2	327.3	-1.7	T_m=5; T_H=6	0.00	0.0	0.48	2.8
				0.81	3.5	0.00	0.0
PN5RD/1	283.2	-2.1	T_m=9; T_H=10	0.00	0.0	0.60	3.5
				0.81	3.5	0.16	1.0
PN7RD/1	306.5	-1.6	T_m=8; T_H=9	0.00	0.0	0 45	2.7
				0.81	3.5	0.00	0.0
PN16D/2	297.3	-1.4	T_m=16; T_H=17	0.00	0.0	0.42	2.4
				0.81	3.5	0.00	0.0
PN20D/2	330.2	-2.0	T_m=4; T_H=11	0.00	0.0	0.58	3.4
				0.81	3.5	0.14	0.8
PN22D/1	293.9	-1.8	21	0.00	0.0	0.52	3.0
				0.81	3.5	0.00	0.0
PN30D/1	326.3	-2.0	T_m=10; T_H=11	0.00	0.0	0.59	3.4
				0.81	3.5	0.15	0.9
Pop. C							
N3/6	241.4	-0.4	14	0.00	0.0	0.12	0.7
				0.81	3.5	0.00	0.0
OK6/2	263.0	-0.1	4	0.00	0.0	0.03	0,2
				0.81	3.5	0.00	0.0
OK8/5	254.8	-0.9	T_m=12; T_H=15	0.00	0.0	0.26	1.5
				0.81	3.5	0.00	0.0
SG1RD/2	213.3	-0.3	T_m=28; T_H=25	0.00	0.0	0.09	0.5
				0.81	3.5	0.00	0.0

Homogenisation Temperatures

Population C inclusions tend to have lower homogenisation temperatures than population B inclusions (Figure 3.20a); however, there is a considerable temperature range for both populations. Explanations for a range of homogenisation temperatures within a fluid inclusion population (Ahmad and Rose, 1980) include :

- mixed trapping of both vapour- and liquid-rich phases after phase separation (i.e., boiling);
- the temperature variation is real and the inclusions have trapped fluids with different temperatures and salinities;
- leakage, either naturally since inclusion formation or during heating measurements;
- the inclusions may have necked into two or more inclusions since their original formation;
- observational difficulties during thermometric measurements;
- mistaken identity of inclusion types (i.e., primary, secondary, or pseudosecondary).

With regard to population C inclusions, there is no consistent evidence for the mixed trapping of vapour and liquid. Platey calcite is not observed in any of the samples and there are no type 2 inclusions coexisting with the ubiquitous type 1a fluid inclusions. It is likely that any of the other explanations listed above can account for the variations in homogenisation temperatures for population C inclusions.

Boiling and/or necking may explain the wide variation of homogenisation temperatures for the population B fluid inclusions. Trapping of mixed liquid and vapour phases within a single fluid inclusion will tend to result in anomalously high temperature measurements (Cooke and Bloom, 1990), whereas necking can produce both anomalously low and high homogenisation temperature values. Because only fluid inclusions that showed no evidence for necking were chosen for analysis, the minimum homogenisation temperature for each population B fluid inclusion is regarded to being closer to the temperature of formation, with mixed entrapment causing the scatter in the data.

Pressure – Depth Estimates

Samples which contain textural evidence for boiling, such as coexisting type 1a and 2 inclusions and platey calcite (i.e., population B fluid inclusions) are assumed to have been trapped under hydrostatic pressures on the two-phase (liquid-vapour) saturation curve. Thus, these inclusions can be used to determine pressures at the time of fluid trapping, and hence depths of deposition (Roedder and Bodnar, 1980).

For each well, population B fluid inclusion homogenisation temperature data are plotted at the sample depths, along with the average temperature at each depth, and the stable post-drilling measured temperatures (Figure 3.26). Also shown are the pure H_2O hydrodynamic boiling

point for depth curve and a hydrostatic boiling curve for a H_2O-CO_2 solution (Hedenquist and Henley, 1985). The H_2O-CO_2 curve was calculated assuming an initial CO_2 content of 3.5 wt.% (0.81 mol.) with the ascending fluid initially boiling at 320°C, which is approximately the maximum temperature of the present-day geothermal system. Both curves have been plotted assuming a relatively constant water table position across the geothermal field, at approximately 200 m above sea level (Batayola, 1983). For comparison, the plot for well N3 also shows the pure H_2O hydrostatic and H_2O-CO_2 (0.81 mol.) hydrodynamic curves. These are shown plotting between the hydrodynamic (H_2O) and hydrostatic (H_2O-CO_2) boiling curves, but for simplicity have been left off the other plots in Figure 3.26.

All fluid inclusion samples have homogenisation temperatures greater than, or close to, the present measured temperatures (Figure 3.26). This is consistent with the previous fluid inclusion studies by PNOC-EDC geologists, and implies that the modern geothermal system is thermally waning.

Four samples from wells N3 (sample N3/1), PN1RD, PN20D and PN30D have average homogenisation temperatures that plot between the hydrodynamic and hydrostatic (H_2O-CO_2) boiling curves, implying that quartz deposition occurred close to the present-day sample depths, and that there has been no burial, uplift or erosion since quartz deposition. These four wells are located in the upflow and eastern outflow zones (Figure 3.19).

Considering the minimum temperature within each sample data set is regarded to be closest to the temperature of formation, then all the remaining samples plot beneath the boiling curves. Similar trends have been reported from the Tiwi geothermal field, Philippines (Moore et al., 2000). At Palinpinon, fluid inclusions that are interpreted to have trapped boiling fluids have maximum homogenisation temperatures close to the boiling point curve, but minimum temperatures that are well below the boiling curve. This implies that either, since formation there has been burial and/or water table fluctuations, or that the trapped fluids contain greater than 3.5 wt.% CO_2. Both burial and water table fluctuations are possible given the active volcanic setting and tropical climate (Cooke and Bloom, 1990). Hydrostatic (CO_2-H_2O) boiling curves have been positioned to intersect the average homogenisation temperatures for each sample that plots beneath the present-day boiling curves (Figure 3.26). The average temperatures were chosen because anomalously high and low temperature measurements can result respectively, from fluid inclusions formed from a boiling fluid, and those that have necked since formation.

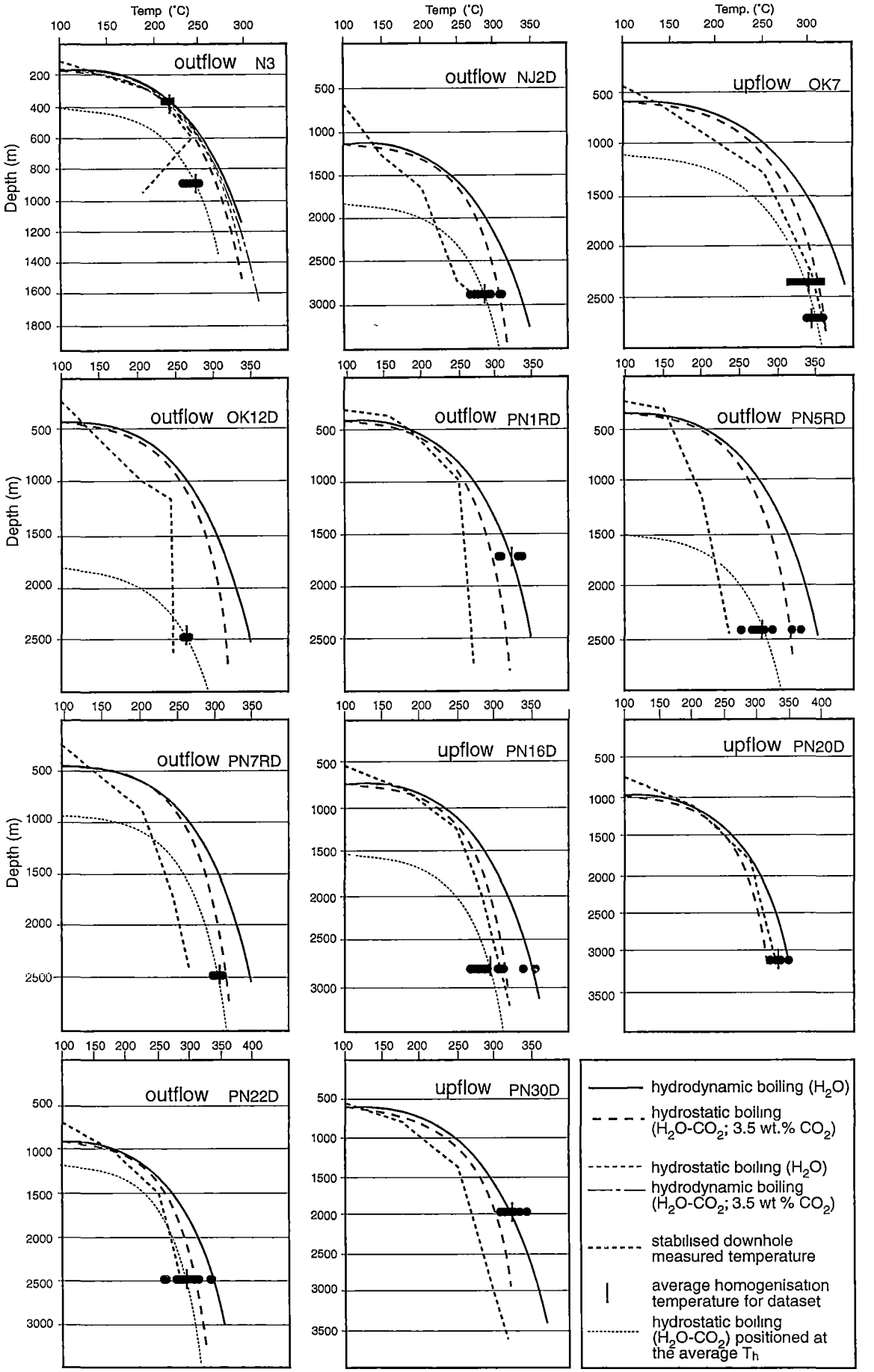

Figure 3.26. Boiling point for depth curves for population B fluid inclusions. Various hydrodynamic and hydrostatic boiling curves (see legend) are shown, as well as the stabilised downhole measured temperatures. Only well N3 shows all four boiling curves. For simplicity, only those boiling curves with the maximum and minimum temperatures, at a given depth, are shown on the other well plots. A hydrostatic boiling curve has been positioned to intersect the average homogenisation temperature (T_h). See text for discussion.

The results show that significant shifts in the boiling curve are necessary to explain the present-day sample depths by either burial or water table depth variation. Most samples require more than 500 m displacement, and a few more than 1000 m (OK12D, PN5RD), to explain their present locations (Figure 3.26). The Okoy Valley is a deeply dissected drainage area (Figure 3.7) so it seems unlikely that burial can solely account for the present fluid inclusion sample depths. Seasonal variation of the water table by as much as these depths also seems unlikely, given that the present-day seasonal water table fluctuations are never more than a few metres (H.P. Ferrer, pers. comm., 2001).

Another possibility is that the trapped solutions contain greater than 3.5 wt.% dissolved CO_2. With the exception of the samples from wells N3 and NJ2D, all those that contain population B fluid inclusions are from wells that have intersected the Okoy Formation. It is possible the calcareous sedimentary rocks are a source for high dissolved CO_2 in the upflow waters. However, CO_2-clathrates, should form at such high dissolved CO_2 concentrations, and these were not observed in any of the population B fluid inclusions.

It remains unresolved as to why the present estimates imply that the fluid inclusions formed at shallower depths than they were collected from. It could be due to the combination of uncertainties involving the estimation of the temperature of initial boiling, the amount of burial and erosion since fluid inclusion formation, variability of the present-day and palaeo-water table depths, and formation in a steep terrain that has relief differences of 1000 m across the field area

3.7. DISCUSSION AND CONCLUSIONS

3.7.1. Evolution of the Palinpinon Hydrothermal System

The evolution of hydrothermal activity at Palinpinon, conspicuous by the variety of alteration types occurring in the area, is interpreted to have been driven by two, and possibly three, intrusive events (Figure 3.27): the Puhagan dikes, the Nasuji Pluton, and an inferred 'blind' intrusion below drilled depths in the Puhagan area.

Possibly the earliest recognised alteration zones are those that are incipiently developed proximal to the Puhagan dikes. These relatively small and localised intrusions were emplaced into the lower Okoy Formation and Lower Puhagan Volcanic Formation approximately 4.2 Ma ago. It is unlikely intrusions of such small size were capable of causing extensive zones of hydrothermal alteration, and overprinting by later hydrothermal alteration events precludes their recognition. However, a few areas of incipient calc-silicate alteration (Figures 3.27and 3.28a), close to the intrusive contacts are interpreted to be genetically associated with dike intrusion.

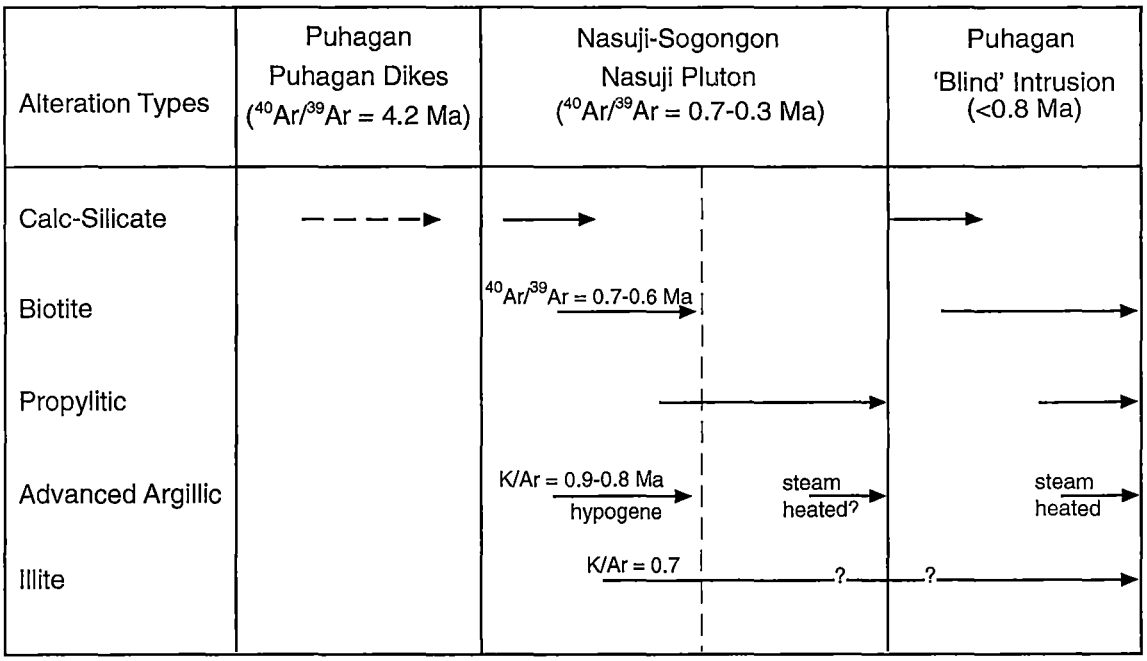

Figure 3.27. A summary of the evolution of the Palinpinon hydrothermal system showing the alteration timing relationships associated with each intrusive event.

The most extensive areas of biotite and hypogene advanced argillic alteration are in the Nasuji-Sogongon region, associated with the intrusion of the Nasuji Pluton. Also present in this region are calc-silicate, propylitic, illite and steam-heated advanced argillic alteration assemblages. The petrographic and geochronologic results from Palinpinon have defined relative and absolute temporal relationships (Figure 3.27). Geochronological ($^{40}Ar/^{39}Ar$) dating of primary hornblende from the Nasuji Pluton has established the time of emplacement to be between 0.7-0.3 Ma. This age is close to the formation of hydrothermal biotite (0.7-0.6 Ma), alunite (0.9-0.8 Ma) and illite (0.7 Ma) from spatially associated zones of biotite, hypogene advanced argillic and possibly illite alteration assemblages. Thus, a hydrothermal alteration system was established during intrusion of the Nasuji Pluton (Figures 3.27 and 3.28a). The older age of the advanced argillic alteration assemblage, compared to that of the intrusion and the biotite alteration assemblage, is interpreted to relate to closure temperatures and depths of formation, with the deeper samples taking longer to cool below the respective argon closure temperatures for hornblende and biotite. On the basis of these relationships, the age of the advanced argillic alteration (0.9-0.8 Ma) is probably the better estimate for the timing of the Nasuji Pluton emplacement and the establishment of the associated magmatic-hydrothermal system.

Therefore, the emplacement of the Nasuji Pluton at 0.9 to 0.8 Ma is interpreted to be associated with the formation of proximal skarn (calc-silicate) and porphyry (biotite) style alteration zones in the country rock close to the intrusive contact (Figure 3.28a). During the latter stages of magma crystallisation, a two phase, aqueous saline magmatic fluid became supersaturated and exsolved from the siliceous melt under lithostatic pressures at temperatures in excess of 600°C and minimum depths of 2-2.5 km. This two phase fluid consisted of a low density vapour and a high density saline (60-80 wt.% NaCl) liquid. Under lithostatic pressure conditions and ductile deformation, these supersaturated aqueous fluids escaped into the surrounding country rock to form high temperature (~550°C) biotite alteration assemblages and associated quartz + biotite + anhydrite + magnetite veins at approximately 1.5 km depth. In thin section, quartz in these veins have anhedral, mosaic textures (Figure 3.8d) typical of the "A" quartz veins described by Gustafson and Hunt (1975) that form in porphyry systems under ductile conditions.

With further cooling to approximately 400°C, there was a transition to hydrostatic pressures. This caused the last remaining vestiges of liquid magma to be quenched and form the porphyritic quartz diorite of the Nasuji Pluton. When hydrostatic pressures exceeded the lithostatic load plus the tensile strength of the surrounding rocks, hydrofracturing and brecciation of the solidified parts of the host intrusion and volcanic host rocks adjacent to the intrusion. This created enough permeability for the development of biotite breccia zones and quartz (+ biotite + anhydrite) veins, both associated with the biotite alteration assemblages (Figure 3.28a). PIXE analyses have shown that these magmatic-hydrothermal fluids were endowed with base metals (e.g., < 0.2 wt. % Cu), but the lack of any significant sulphide

accumulation implies either low fluid volumes and/or lack of an effective trap for base and precious metal mineral deposition.

Coeval with the biotite alteration assemblage, a zone of hypogene advanced argillic alteration formed at shallow levels above the Nasuji Pluton (Figures 3.27 and 3.28a). Magmatic volatiles (e.g., SO_2, HCl) escaped from the crystallising magma, ascending to shallower levels along near-vertical faults and/or joints (Figure 3.28a). The gases condensed in the near-surface environment and mixed with meteoric-derived groundwaters to form acidic aquifers (i.e., pH < 2, Hedenquist, 1986). These highly corrosive fluids caused intense leaching of the host rock and the development of hypogene advanced argillic alteration mineral assemblages. It is possible that acidic aquifers flowed eastwards due to the elevated topography to the west, forming an easterly directed outflow zone which altered the country rock to advanced argillic mineral assemblages (i.e., alunite ± silica; Figure 3.28a). The depth of formation of this alteration zone remains unknown. However, as discussed in the previous section, the occurrence of high temperature (> 250°C) minerals associated with propylitic (epidote) and advanced argillic (zunyite) alteration assemblages in surface outcrops implies at least 450 m of erosion (Reyes, 1990) over the past 0.9-0.8 Ma.

At Palinpinon, as the Nasuji Pluton cooled, the fluid inclusion data suggest a significant reduction of fluid sourced from the intrusion occurred, and the hydrothermal fluids became dominated by dilute, meteoric-derived groundwaters (Figure 3.28b). These moved into the pluton where they were heated and caused propylitic (epidote + tremolite-actinolite) alteration assemblages of the intrusive rocks, overprinting earlier-formed biotite alteration assemblages (Figures 3.27 and 3.28b). A similar scenario for the ingress of groundwaters and the formation of propylitic and calc-sodic mineral assemblages has been documented from Yerington, Nevada (Dilles et al., 2000). At shallower depths, hydrothermal circulation of meteoric groundwaters probably would have resulted in the formation of illite alteration mineral assemblages in Nasuji-Sogongon and the Puhagan area (Figures 3.27 and 3.28b). In regions above the palaeo-water table, gas condensation into perched aquifers may have caused the formation of steam-heated advanced argillic alteration assemblages (Figures 3.27 and 3.28b).

The erosion of at least 450 m of rock in the Nasuji-Sogongon area during the last 0.8 Ma (Figure 3.28c) suggests a minimum erosion rate for the area of 0.56 mm/yr. This exposed the Nasuji-Sogongon zone of 'high sulphidation-style' advanced argillic alteration assemblages as a series of northeasterly striking alunite ridges along the Okoy Valley (Figures 3.7 and 3.28c). During this period an intrusion was emplaced beneath the Puhagan dikes (i.e., > 2.5 km depth) at the intersection of the Ticala and Lagunao Faults. This shifted the focus of hypogene alteration eastwards and caused the development of the hydrothermal convection cell that defines the present-day geothermal system. It is difficult to know how long the current hydrothermal system has been maintained. Well constrained geochronological data from the Tiwi geothermal system, Luzon, implies that the hydrothermal system has developed over past

0.3 Ma, and possibly as long as 0.5 Ma (Moore et al., 2000). It is possible the Palinpinon hydrothermal system has had similar, and perhaps even longer, periods of development.

The magmatic-hydrothermal alteration that developed above the blind intrusion in the Puhagan area consist of calc-silicate and biotite assemblages (Figures 3.27 and 3.28c). Since the period of the calc-silicate assemblage development, based on the occurrence of clinopyroxene and garnet, this region of the hydrothermal system has cooled by at least 70°-100°C, while parts of the biotite alteration assemblage have remained in thermal equilibrium with present-day temperatures.

With ongoing hydrothermal convection, zones of propylitic alteration have developed as halos around the Puhagan calc-silicate and biotite alteration assemblages (Figures 3.27 and 3.28c). These propylitic zones are in thermal equilibrium with the present hydrothermal system. There is a systematic distribution of the propylitic subzones with distance from the biotite alteration assemblage and the upflow zone (Figure 3.28c). The tremolite-actinolite assemblage is restricted to the upflow zone, proximal to the zone of biotite alteration. With distance from this centre, the subzones vary from epidote to chlorite assemblages (Figure 3.28c). Such a systematic variation of propylitic subzones, away from a core of biotite alteration, has been recognised in alteration zones surrounding the Tintic porphyry Cu system (Norman et al., 1991). Based on their evidence from fluid inclusion and stable isotope ($\delta^{18}O$ and δ H) studies, the zoning of the subzones away from the core of the alteration system is thought to represent the progressive mixing of low-salinity, locally derived meteoric waters with an isotopically heavier saline fluid (Norman et al., 1991). This saline end-member represents either an evolved meteoric water or a fluid with magmatic origins. The results of the current fluid inclusion studies at Palinpinon suggest the involvement of high salinity (~35 eq.wt.% NaCl), possibly magmatic fluids in the formation of biotite and propylitic (tremolite-actinolite) alteration assemblages in the Puhagan area. However, the involvement of connate brines, derived from the Okoy Formation, cannot be completely ruled out as a source for dissolved constituents, in the high and moderate (i.e., 7-11 eq.wt.% NaCl) salinity fluids trapped in fluid inclusions in the Puhagan area.

Above the zones of propylitic alteration, illite alteration assemblages have developed which overprint biotite, propylitic and advanced argillic alteration zones associated with the Nasuji-Sogongon hydrothermal system (Figure 3.28c). Fluid inclusion evidence suggests that boiling zones have been mainly restricted to dilational structures adjacent to the hydrothermal upflow zone. Dissolved gases (CO_2, H_2S) separated from these boiling fluids have condensed above the water table and forming perched steam-heated acid sulphate aquifers associated advanced argillic alteration assemblages. The percolation of acid sulphate waters to greater depths along near-vertical permeable structures (i.e., faults and joints), results in steeply dipping zones of steam-heated advanced argillic alteration (e.g., in the Puhagan area; Figure 3.28c).

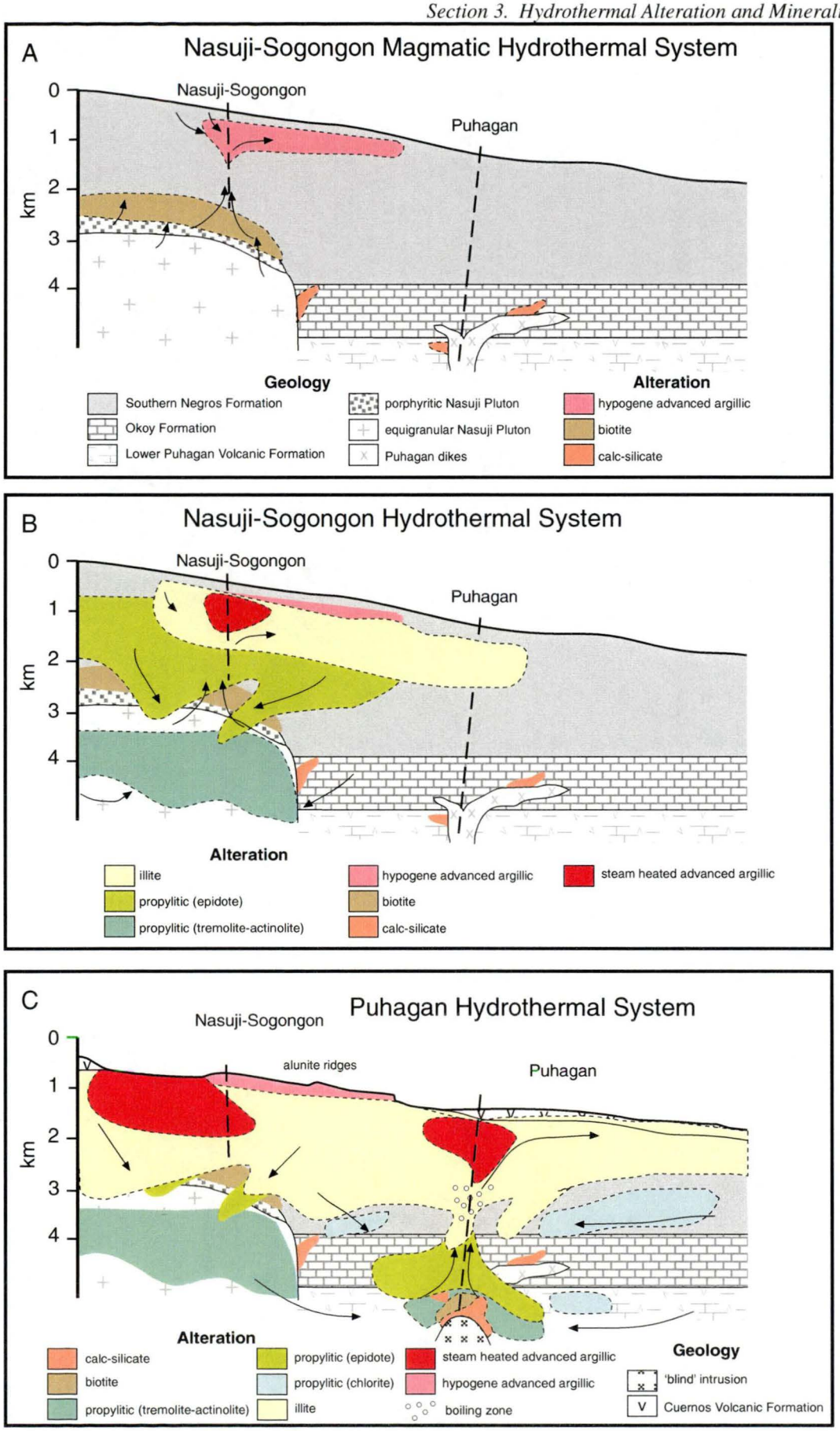

Figure 3.28. A schematic cartoon showing the evolution of the Palinpinon hydrothermal system along Section A-A' (Figure 3.5). Hydrothermal alteration occurred in three stages. In the Nasuji-Sogongon area, an early magmatic-hydrothermal system (A) followed by a hydrothermal system (B). A shift of intrusive activity to the east resulted in hypogene alteration zones in the Puhagan area (C).

An important difference between the Nasuji-Sogongon and Puhagan magmatic-hydrothermal alteration systems is the apparent lack of hypogene advanced argillic alteration in Puhagan. This is probably because degassing of the blind intrusion has been hindered or prevented, thus limiting the development of the hypogene advanced argillic assemblages. It may be that insufficient volumes of volatiles have been degassed from the intrusion, either because lithostatic confining pressures have been too great for exsolution to occur, or that there has been a dearth of major seismic ruptures to breach any sealed carapace above the intrusion. Without knowing the size or depth of the intrusion, it is difficult to suggest anything more conclusive.

3.7.2. Summary

Results of the alteration studies undertaken during this research and reported in this section of the thesis, shows that the hydrothermal alteration systematics at Palinpinon shares common characteristics to those associated with many magmatic-hydrothermal base and precious metal ore deposits (e.g., porphyry, high and low sulphidation epithermal systems; Gustafson and Hunt, 1975; White and Hedenquist, 1990). A summary of these similarities, along with a discussion on the potential for base and precious metal ore deposition at Palinpinon are presented in Section 5. Section 4 investigates the mineralising potential of the modern geothermal waters.

The main points of this section of the thesis are as follows:

- Hydrothermal alteration at Palinpinon is associated with three intrusions : the Puhagan dikes, the Nasuji Pluton and a 'blind' intrusion in the Puhagan area. Only incipient calc-silicate alteration is spatially associated with the Puhagan dikes.

- In the Nasuji-Sogongon region, hydrothermal alteration assemblages spatially associated with the Nasuji Pluton, are characterised by biotite, calc-silicate (garnet, clinopyroxene), hypogene advanced argillic (zunyite, andalusite, alunite), propylitic (tremolite-actinolite, epidote, chlorite), illite and steam-heated advanced argillic (alunite).

- Fluid inclusion evidence indicates that magmatic-hydrothermal fluids associated with the final stages of magma crystallization, and the formation of quartz + biotite + anhydrite + magnetite veins associated with the biotite alteration assemblage, were thermally and compositionally equivalent (T_H = 267° to > 600°C; salinities = 40 to 79 eq.wt.% NaCl). These fluids were also endowed with base metals (e.g., up to 0.2 wt. % Cu).

- The ages of hydrothermal biotite ($^{40}Ar/^{39}Ar$ = 0.7-0.6 Ma), hypogene alunite (K/Ar = 0.9-0.8 Ma) and illite (K/Ar = 0.7 Ma) demonstrate that these minerals all formed close to the time of the Nasuji Pluton (0.7-0.3 Ma), implying a genetic link between intrusion

emplacement and the formation of biotite, hypogene advanced argillic and illite alteration assemblages.

- The age of the advanced argillic alteration (0.9-0.8 Ma) yields the best estimate for the emplacement of the Nasuji Pluton and the establishment of the associated magmatic-hydrothermal system. The younger ages of the intrusion and biotite alteration assemblage may reflect longer cooling times to below the respective argon closure temperatures for hornblende and biotite .

- Emplacement of an intrusion beneath the drilled depths (i.e., > 2.5 km depth) within the last 0.8 Ma has shifted the focus of hypogene alteration to the Puhagan area. This intrusion provides the heat for present geothermal system. Hypogene hydrothermal alteration types in this area are deep level calc-silicate (garnet, clinopyroxene, scapolite), biotite and propylitic (tremolite-actinolite, epidote) alteration and shallow illite alteration.

- The present day geothermal system may be in thermal equilibrium with low sulphidation alteration assemblages and, in the Puhagan area, biotite alteration. This implies that these alteration types either have a protracted history of formation, or that they have formed during at least two discrete time periods in the past 0.8 Ma.

- With ongoing hydrothermal convection, areas of propylitic alteration have developed as halos surrounding the Puhagan magmatic-hydrothermal alteration zones. At shallower levels, illite alteration assemblages overprint the biotite, propylitic and hypogene advanced argillic alteration types associated with the Nasuji Pluton. Perched aquifers of steam-heated acid sulphate water have altered regions above the water table to an advanced argillic (steam-heated) alteration assemblage. The percolation of these waters down near-vertical permeable structures (i.e., faults and joints), results in steeply dipping zones of steam-heated advanced argillic alteration.

- A lack of significant base and precious metal mineral occurrences at Palinpinon is possibly due to a combination of a lack of sufficient permeability necessary to create a focus for fluid flow and ore deposition and/or a lack of significant metalliferous fluid flux from the intrusion into surrounding country rock.

4. POTENTIAL FOR BASE AND PRECIOUS METAL DEPOSITION FROM PALINPINON GEOTHERMAL FLUIDS

4.1. INTRODUCTION

This section investigates the mineralising potential of the Palinpinon deep geothermal fluids. To achieve this, the deep geothermal water has been analysed for trace metal concentrations and a suite of mineral precipitates (scale deposits) collected from the inside walls of six geothermal wells has been examined petrographically. Calculation of aqueous and mineral equilibria for the reservoir, along with computer modelling of reservoir hydrothermal processes (i.e., boiling, mixing, cooling, heating), are used to investigate processes that may have been important for precious and base metal deposition.

4.2. PREVIOUS WORK

Previous investigations into the mineralising potential of geothermal fluids have included studies of dissolved metal concentrations and the examination of mineral precipitates, both around natural surface discharges and scale deposits from geothermal wells and surface pipework. These have included the Taupo Volcanic Zone geothermal systems in New Zealand, Waiotapu, Rotokawa, Ohaaki-Broadlands, Kawerau (Weissberg, 1969; Brown, 1986; Simmons and Browne, 2000). Other areas studied include Oku-Aizu, Japan (Imai et al., 1988); Cerro Prieto, Mexico (Clark and Williams-Jones, 1990); Salton Sea, USA (McKibben et al., 1989; 1990); Tongonan, Philippines (Arevalo, 1987); and Momotombo, Nicaragua (Archibald and Williams-Jones, 1999).

Weissberg (1969) described gold- and silver-rich sinters and precipitates that occur in hot spring and well discharges at various New Zealand geothermal fields, in particular Waiotapu, Rotokawa and Ohaaki-Broadlands. These geothermal systems are typical of the Taupo Volcanic Zone in that they are characterised by one principal fluid type, a near neutral chloride water with a variable CO_2 content (Hedenquist, 1986). They have low precious metal concentrations. Water discharged from Ohaaki-Broadlands drillhole 2 contained 4×10^{-2} µg/kg Au and 0.6 µg/kg Ag (i.e., only 10 and 2 times greater than seawater, respectively). However, the discharge precipitates from this drillhole were enriched in precious metals with 55 mg/kg Au and 200 mg/kg Ag (i.e., ore grade concentrations). Hence, it appears that high concentrations of gold and silver are not essential in ore-forming solutions and that effective concentrating mechanisms are more important for precious metal deposition (Weissberg, 1969). It was suspected that gold and silver were co-precipitated with antimony sulphide which became saturated when chloride water cooled from 250°C, at depth, to 100°C at the surface. The conclusion was made that both high natural discharge rates (e.g. Wairakei: 1 6 x 10^6 kg/hr) and long lifetimes (e.g. Wairakei: 500,000 yr.) are adequate to form economic

quantities of precious metals similar to epithermal-type gold deposits (Weissberg, 1969).

A problem with Weissberg's (1969) study is that the concentration of metals in the deep aquifer was inferred from the concentration of metals in the water discharged at surface. It was assumed that no significant metal deposition occurs during discharge. However, the discovery of copper, silver, and gold precipitates inside the pipelines at Ohaaki-Broadlands and Kawerau, New Zealand (Brown, 1986) invalidates this assumption, and intimates that either base and precious metal concentrations in the deep aquifer are closer to saturation, or they require efficient trapping mechanisms in order to precipitate. Based on these precipitates, the gold concentration of the aquifer fluid was calculated to be approximately 1.5 µg/kg (Brown, 1986). The solubility of gold under Ohaaki-Broadlands reservoir conditions was thermodynamically estimated to be 10.5 µg/kg (Brown, 1986), an order of magnitude higher than the predicted gold content of this fluid. This differs from earlier work that suggested the aquifer was highly undersaturated with respect to gold (Weissberg, 1969; Weissberg et al., 1979). The consequence of this result is that it greatly reduces the time and fluid flux required to form an epithermal-type Au deposit.

An important question relating to the metal content of geothermal fluids is the amount of precipitation that occurs in the well during flow to the surface. Brown (1986) estimated that only 14% of the total dissolved gold in the reservoir fluid at Ohaaki-Broadlands is deposited at the surface. Mass balance calculations by McKibben et al. (1990) using data from the Salton Sea geothermal field, USA, indicate that the measured gold contents of water collected at the surface closely represent that of the deep reservoir fluid, and that only 4% of the total gold that passes through the well precipitates as scale. This implies that either deposition in the turbulent high flow rate environment of a geothermal well is inefficient, or that the waters are initially undersaturated with respect to gold.

Despite these apparent inefficiencies, precious and base metal well scales were found in wells at the Cerro Prieto geothermal field, Mexico (Clark and Williams-Jones, 1990). Precious and base metal concentrations were found to be highest at, or near the aquifer feed zones where boiling and phase separation occurs. This led Clark and Williams-Jones (1990) to conclude that boiling of neutral chloride hydrothermal solutions may be responsible for the deposition and zonation of precious and base metals in epithermal vein deposits.

Hydrothermal fluids at the Salton Sea geothermal field are highly saline and metalliferous (Skinner et al., 1967). The geothermal water contains 0.02 to 0.6 µg/kg Au, whereas gold concentrations of the well scales ranged from 45 to 15,728 µg/kg, with one sample exceeding the upper detection limit of 1 wt.% Au (McKibben et al., 1990). The highest concentrations corresponded to depths close to regions of phase separation. The gold concentration of galena-bearing scales from the wellhead assembly, where additional boiling occurs, were 267 to 5,644 µg/kg Au (McKibben et al., 1990).

The measured gold solubilities in the Salton Sea geothermal waters (McKibben et al., 1989; 1990) are consistent with gold transportation as either bisulphide or chloride complexes, but the solubility for a bisulphide complex is an order of magnitude greater than that for a chloride complex (McKibben, et al., 1990). The enrichment of gold close to boiling zones therefore results from destabilisation of the bisulphide complex due to phase separation. However, the role of chloride as a complexing agent could not be ruled out completely, and the possibility exists that some of the gold at the wellhead being deposited by cooling rather than gas partitioning (McKibben, et al., 1990). The association of gold with magnetite in the well casing, and the presence of galena in the wellhead assembly led McKibben et al. (1989; 1990) to propose that gold may have precipitated due to reduction with the steel casing and the sulphide. This was also proposed by Archibald and Williams-Jones (1999) for wellhead scales at the Momotombo geothermal field, Nicaragua. However, McKibben et al. (1989) concluded that reduction is inefficient at removing gold from solution because it may be kinetically inhibited due to the involvement of adsorption processes.

To fully understand the metal content of the deep reservoir fluid, Brown et al. (1996) attempted down-hole water sampling at the Ohaaki-Broadlands geothermal field, New Zealand. Accurate down-hole sampling is difficult, due to the potential for contamination from the sampling equipment and the need to capture any metals that precipitate on the walls of the sampling chamber during transport to the surface. The exercise involved analysing water samples for gold, silver, copper and platinum group elements. The results show gold concentrations in the down-hole water to be about 1 μg/kg and silver concentrations of 6 to 18 μg/kg. Thus, the measured gold concentration is approximately the same as that calculated from surface precipitates (1.5 μg/kg; Brown, 1986) and goes further to substantiating that aquifer gold contents are an order of magnitude lower than the gold solubility (10.5 μg/kg; Brown, 1986). These results reaffirm the early results by Weissberg (1969) that dilute, neutral chloride waters are not particularly enriched with respect to precious metals, and that efficient trapping mechanisms are the most important criteria for the formation of a low sulphidation epithermal-type Au-Ag deposit.

4.3. HYDROLOGY AND RESERVOIR CHEMISTRY OF PALINPINON GEOTHERMAL FIELD

4.3.1. Effects of Steam Production on the Reservoir

To provide the framework for a discussion on the hydrology and chemistry of the reservoir at Palinpinon, it is important to be aware of the effects of exploitation. Utilisation of geothermal steam for power production can impose major changes on the subsurface hydrology. Fluid withdrawal from the geothermal wells commonly results in pressure drawdown and dilution of the deep fluid due to encroachment of shallow-derived, often acidic, waters into deeper parts of the reservoir (Ellis and Mahon, 1977). The pressure decrease imposed by the discharging wells

can also lead to increased boiling in the feed zones. Initially, such wells can discharge fluid with an enthalpy equal to the measured temperatures. However, with continued production, the enthalpy can increase to become greater than the equivalent enthalpy for the measured temperature at a given saturated liquid phase. In such cases, the well the well is said to have "excess enthalpy" (Henley et al., 1984). There are two processes that can lead to an enthalpy increases. Due to density and viscosity differences, phase separation will result in vapour reaching the well prior to the liquid, and hence provide additional heat to the discharging fluid. The other process involves evaporation of the flowing liquid due to conductive heat gain from the country rock (Henley et al., 1984).

Other effects of power production on the hydrology occur when waste water is reinjected back into the reservoir. The reinjected water is more saline and cooler than the reservoir fluid. At Palinpinon, reinjected brine has up to 11 000 mg/kg Cl^- and a temperature of approximately 165-170°C (D'Amore et al., 1993). Thus, a decrease in measured temperature and/or an increase in salinity of the discharging geothermal water can be indicative of encroachment of reinjected water into the deep reservoir.

By 1982, a total of 26 vertical and directionally drilled geothermal wells had been drilled in the upper Okoy Valley (Figure 1.5). Immediately after the commissioning of the Palinpinon I (Puhagan) power plant in 1983, a programme of waste water reinjection using wells close to the Puhagan production sector was commenced. By 1985, 17 of the 21 production wells had shown an increase in chloride contents (Harper and Jordan, 1985). In an attempt to reduce the effects of reinjection, ten wells were drilled to the northeast in the main outflow zone and at lower elevation to the production sector. From 1989, waste water was reinjected in this area, the Ticala-Malaunay sector (Figure 1.5) and the return of injected waste water declined substantially (Figure 1.5, Amistoso et al., 1993; D'Amore et al., 1993).

In summary, wells affected by steam production are recognised by sudden changes in specific physical and chemical conditions. These include a decrease in wellhead pressure, measured downhole temperature and reservoir pH, an increase in discharge enthalpy and the discharge chemistry becoming more saline or dilute. To provide an understanding of the geochemistry of the hydrothermal reservoir in its least disturbed (pre-exploitation) state, the following sections focus largely on chemical data obtained prior to 1983.

4.3.2. Hydrology and Reservoir Chemistry

The hydrology and reservoir chemistry of the Palinpinon geothermal field is based on pre-existing water chemistry data from a variety of unpublished sources (Glover, 1975; KRTA, 1977; Clemente, 1981; Jordan, 1983; Seastres, 1985). Most of the information comes from Jordan (1983), but data from an additional 13 wells has been included here to extend the data set to 31 wells. The sources for this data are presented in Table 4.1. These data have been

reinterpreted using the geochemical discrimination diagrams of Giggenbach (1988) and Giggenbach and Corrales (1992) in order to provide a better understanding of the ongoing hydrological processes in the deep reservoir.

The locations of the 31 wells listed in Table 4.1 are shown in Figure 4.1. The waters were collected mostly from the surface at atmospheric pressure, but some were collected at higher pressures using a Webre separator. Downhole water samples, and their collection depths, from wells N1, N2 and OK11D are also represented in Table 4.1. The enthalpies presented in Table 4.1 are mostly derived from surface measurements. Those for downhole samples N1 and N2 are based on temperatures measured at the collection depths.

The isothermal structure of the reservoir hydrology, as reflected in the distribution of the 200°, 250° and 300°C isotherms at 1500 m bsl, is illustrated in Figure 4.1 (see Appendix 4). The region of highest temperature (> 300°C), or upflow zone, occurs close to the intersection of the northwest trending Lagunao Fault and the northeast trending Ticala Fault (Figure 4.1). Outflow zones are recognised by the southwest elongation of the 250°C isotherm along the Ticala Fault and the northeast elongation of the 200°C isotherm along the Puhagan and Nasuwa Faults (Figure 4.1).

Geothermal waters from most Palinpinon wells are characteristically neutral to slightly alkaline, chloride (< 7200 mg/kg) waters with significant amounts of alkali metals, boron and silica (Table 4.1). There is a marked difference in water chemistry in the three Nasuji wells NJ1D, NJ2D and OK11D drilled to the south (Figure 4.1). Waters from these wells have the highest SO_4 and Mg concentrations, are acidic at 20°C (Table 4.1) and are classified as mixed sulphate-chloride waters (Seastres, 1985).

The calculated reservoir conditions, in terms of chloride and silica concentrations and enthalpy are presented in Table 4.2. Reservoir enthalpies have been estimated using silica solute geothermometry, as not all samples have representative measured enthalpies (Table 4.2). For discharge waters, which have boiled in response to pressure decreases, the quartz adiabatic geothermometer was used because it is believed to provide a better estimate of the reservoir temperature (Fournier, 1981). The chalcedony geothermometer was used for cooler waters where chalcedony is more likely to be the stable silica polymorph (i.e., T < ~180°C, Fournier, 1981; 1985). Reservoir chloride and silica concentrations (Table 4.2) have been calculated using the estimated reservoir enthalpies and their respective initial discharge concentrations (Table 4.1). As there was no steam loss during collection of the downhole samples, a correction to reservoir concentrations is not required.

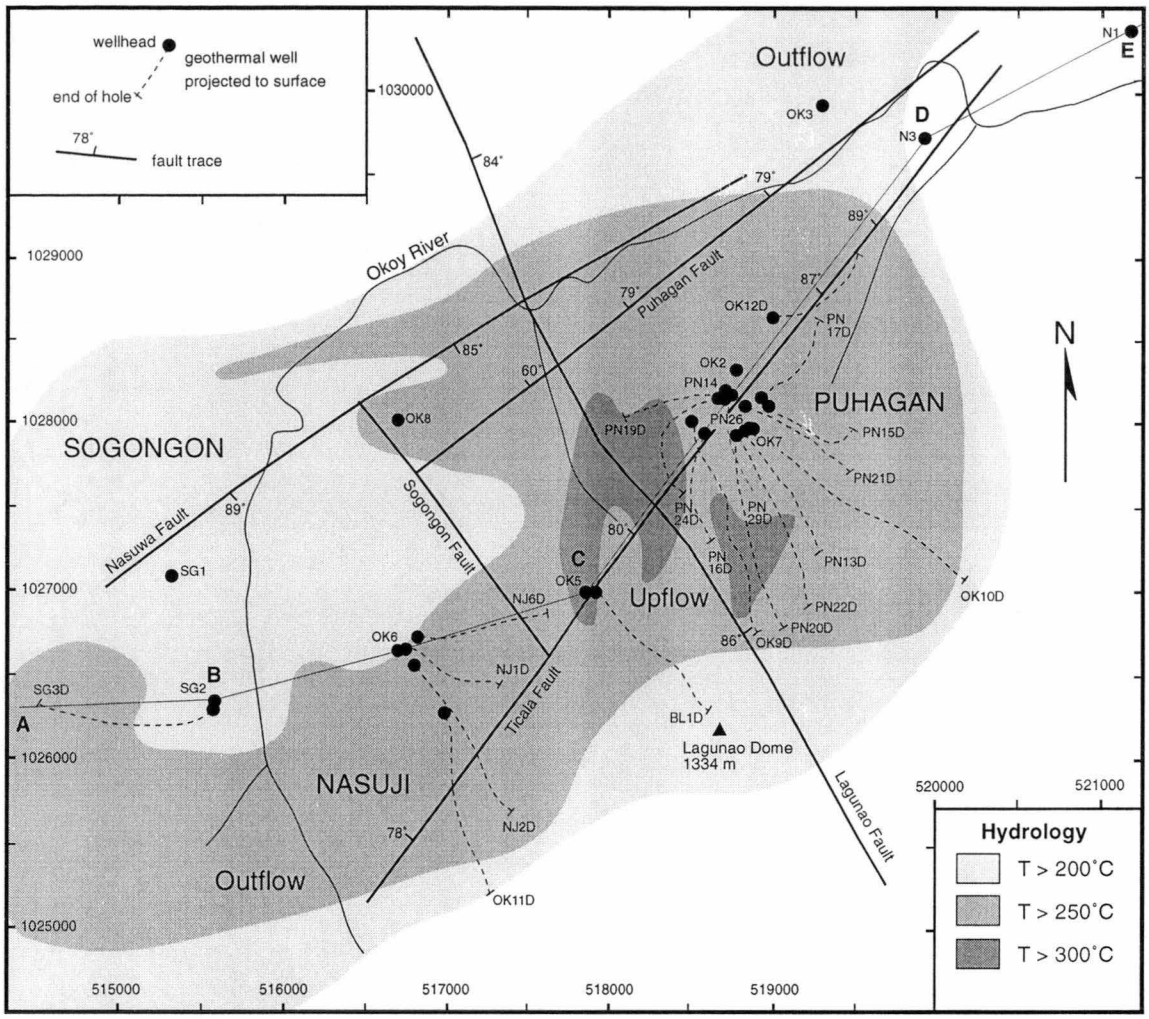

Figure 4.1. Geothermal well location map showing the 1500 m b.s.l. isotherms and several faults. Zones of upflow and outflow are highlighted. The cross-section shown in Figure 4.6 is along the line A-B-C-D.

Table 4.1. Chemistry of initial discharge and downhole (d/h) water samples from selected geothermal wells (data sources listed below table)
When given, enthalpy for d/h samples is from measured downhole temperature W H P. and Sample P refer to wellhead pressure and sample pressure, respectively
The collection depth from well OK11D is given as vertical depth.

Well	Wellhead Grid Reference	Date	Enthalpy (kJ/kg)	W H P (bars atmos)	Sample P. (bars atmos)	pH (T=20°C)	Li	Na	K	Rb	Cs	Ca	Mg	Cl	SO_4	HCO_3	B	SiO_2	CO_2T	H_2S	NH_3
															(mg/kg)						
BL1D[1]	517909, 1026486	5-Feb-91	1117	8.7	7 0	7 16	6.40	1400.00	330.00	1 86	1 31	46.00	0.09	2535 00	37.00	19 52	30 70	670 00	19.54	2.38	30.70
N1[2]	521043, 1029769	14-Dec-76	-	-	1.0	8 23	10 57	2529 00	350 00	-	-	144 00	2 17	4397 00	135 00	36 00	-	345 00	0 10	-	-
N1d/h[2], 457m		16-Dec-76	798.7	-	1 0	7.5	9 70	2230 00	308.00	-	-	186 00	0 68	4044.00	100.00	41.00	44 40	295.00	4 00	-	-
N2[2]	525564, 1029862	13-Dec-76	-	-	1 0	8 14	10.00	2588.00	194 00	-	-	210 00	2.55	4414.00	92.00	86 00	-	155.00	1 20	-	-
N2d/h[2], 392m		27-Nov-76	684 3	-	1.0	7 4	9.00	2300 00	174 00	-	-	195 00	2.60	3955.00	18 00	144.00	43 50	204 00	11 00	-	-
N3[3]	519939, 1029248	6-May-80	-	-	1.0	8 04	14.60	3205.00	444.00	4.14	3.00	81 40	0.09	5961.00	60.00	-	-	880.00	25.20	-	3.60
NJ1D[4]	516790, 1026135	24-Apr-82	1195	3 1	1.0	5 60	8.29	1885 00	392.00	2 29	1.67	15.50	5 38	3369.00	379.00	-	40.50	783.00	10 60	7.87	8 79
NJ2D[4]	516844, 1026012	2-Dec-82	1248	4.3	1 0	3 62	9.28	2304 00	408 00	2.46	1.81	36 30	12 00	4098 00	954.00	-	51 30	1003 00	224 00	0.75	-
NJ6D[1]	516840, 1026175	28-May-84	1216	9.7	7.7	7.61	10.30	1922 00	463.00	2 17	1.44	35 00	0 85	3405 00	46 50	43 90	39 30	745 00	36 53	10.20	2.32
OK2[3]	518743, 1027788	21-Jul-79	-	-	1.0	7 29	10.60	2853.00	641.00	3.19	2 63	38 30	2.52	4609.00	175.00	33.70	-	790.00	-	-	-
OK3[1]	519221, 1029368	27-Aug-84	789	1 3	1.0	7.94	10 44	2748 78	421.93	1.79	1.53	213 89	3.59	4358 78	292 42	57 90	48 12	371.80	21 39	1.92	0.92
OK5[1]	517887, 1026480	16-Apr-80	1332	26 1	1 0	7.38	15.00	3134.00	495.00	4.75	3.23	29 50	0 04	5829 00	36 60	-	71.60	1070 00	12 80	4.61	2.40
OK6[5]	516788, 1026105	8-Jan-82	1129	24.9	1 0	7.76	13.80	2839 00	576 00	3 62	2.63	29.80	0 07	5057 00	32.70	-	50 80	850 00	32 40	0 89	3 82
OK7[1]	518863, 1027477	13-Aug-80	1360	11 8	1 0	7.68	17 50	3977 00	884.00	4 84	3.40	145 00	0.16	7205 00	39.60	52 00	83.40	1097.00	-	-	-
OK8[5]	516728, 1027405	28-Apr-82	1285	8 2	1 0	8 00	14 40	2764 00	646 00	4 24	2 87	34 50	0.05	5319 00	48 80	-	68 60	974 00	8 80	2.56	-
OK9D[5]	518539, 1027486	21-Feb-81	1223	13 9	1 0	7 90	17 50	3532.00	767.00	4 27	3 56	100 00	0 26	6364 00	44.20	-	76 80	975 00	7 48	-	-
OK10D[5]	518839, 1027465	20-May-81	1207	15.4	1.0	7 42	15 10	3342 00	687 00	4 08	3 49	129.00	0 94	6311.00	-	-	75.10	829 00	11.10	-	-
OK11Dd/h[4], 2300m	517011, 1025674	18-Jun-81	-	-	-	3 12	-	-	151 00	-	-	34.50	21.10	1062 00	1032.00	-	15.10	256 00	226 00	-	-
OK12D[5]	518970, 1028087	12-Sep-81	1089	15 5	10.9	6 70	10 70	2352 00	527 00	2.53	2.10	76 00	0 36	4361.00	32.00	-	49 20	532 00	59.80	62.60	-
PN13D[5]	518822, 1027450	20-Jan-82	1179	7 7	1 0	7 75	18 10	3578 00	707 00	3 87	3 04	81 90	0 53	6418.00	53.80	-	81.70	852 00	22 40	19.10	-
PN14[5]	518682, 1027656	24-Sep-82	1341	24 3	5 6	6 85	14.70	3160.00	858 00	4 41	2 80	59 20	0.06	6009 00	10.60	-	69 10	909 00	22 00	1.97	9.12
PN15D[1]	518852, 1027624	5-Oct-81	1068	6 9	1 0	7.89	9.16	2518 00	418.00	2 31	1 67	42 90	0 31	4457.00	48.00	-	55 40	767 00	74 00	2 39	5.40
PN16D[5]	518713, 1027433	22-Oct-82	1309	28 4	1 0	7 60	15 40	3557.00	739 00	4 08	3 03	52 50	0.36	6035.00	18 00	-	74 50	1120 00	19 30	2 04	5.00
PN17D[5]	518872, 1027634	16-Feb-82	1078	6.1	3.9	5 75	8 95	2671 00	453 00	2 65	2 30	73.30	0 41	4731.00	31.90	-	57 30	547 00	58 70	9 46	9.17
PN19D[5]	518669, 1027639	21-Oct-82	1196	8 7	7 3	7.00	12.10	3102.00	682 00	3.88	2.93	69 70	0 21	5495.00	26 90	-	65 90	693.00	11 90	2 70	7.10
PN20D[5]	518779, 1027444	16-Dec-82	1375	32 5	32 3	5 68	11 20	2267.00	567 00	3.47	2.39	43.20	0.14	4246.00	25.70	-	52 70	710.00	132 00	13.60	7.90
PN21D[5]	518830, 1027618	5-Oct-82	1016	8.5	0 9	7 87	12 70	3427 00	514 00	2 91	2 92	117.00	0.84	5807 00	60.70	-	66 10	639 00	7.92	3 03	36 00
PN22D[5]	518802, 1027448	12-Nov-82	1178	21.7	2.8	5 85	13.80	3000.00	676 00	3.80	2.75	74 40	0 22	5727 00	26.20	-	67 80	767 00	109 00	4 09	5.85
PN24D[5]	518656, 1027621	21-Dec-82	1322	18 5	17 9	5 00	11 80	2370 00	637 00	3 80	2 51	30 60	0 08	4668.00	27 00	-	57.10	822 00	94.20	12 90	6 00
PN26[5]	518809, 1027612	28-Dec-82	1167	27 5	5 8	6 95	15 40	3513.00	794 00	4 52	3.40	116 00	0 12	6704 00	28 70	-	78 50	743.00	38 30	4.77	6 10
SG1[4]	515422, 1026635	19-Nov-81	1126	10.8	1.0	7.74	12.20	2696.00	523.00	3 49	2.50	40.00	0 08	4765.00	30 80	-	59.30	737 00	40 90	0.94	-
SG2[4]	515625, 1025823	6-Jan-82	1197	26 5	1 0	7.71	12 30	2643 00	576 00	3 52	2 46	34.70	0 07	4893.00	38 40	-	60 30	807 00	9 50	4.94	-
SG3D[1]	515630, 1025802	26-Jan-83	1171	10 9	9 5	6 21	5 60	1380 00	300 00	1 49	0 92	0 20	0 18	2422 00	80.40	-	29 20	595.00	149.00	3.41	1 28
Okoy River[6]	518104, 1028559	1975	100 7	-	1 0	7 6	0 01	7 60	2 00	-	-	45.00	4.50	1.20	103 00	39.00	-	47 00	1.00	-	0 06

Sources. [1]Unpublished PNOC-EDC company reports and files, [2]KRTA (1977), [3]Clemente (1981), [4]Seastres (1985), [5]Jordan (1983), [6] Glover (1975)

Table 4.2. Calculated Palinpinon reservoir data.

Well	Date	Hmeas	Tcha	Tq-adi	Hqtz/cha	Hxs	Hres	Cl⁻res	SiO_2res
		(kJ/kg)	(°C)			(kJ/kg)		(mg/kg)	
BL1D	5-Feb-91	1117	-	247	1071	46	1071	2077	549
N1d/h	16-Dec-76	799	192	-	817	-18	799	4044	295
N1	14-Dec-76	-	-	201	857	-	857	3541	278
N2d/h	27-Nov-76	684	160	-	676	8.3	684	3955	204
N2	13-Dec-76	-	140	-	589	-	589	4079	143
N3	6-May-80	-	-	269	1179	-	1179	3951	583
NJ1D	24-Apr-82	1195	-	260	1134	61	1134	2300	535
NJ2D	2-Dec-82	1248	-	281	1241	7	1241	2603	637
NJ6D	28-May-84	1216	-	256	1115	101	1115	2740	600
OK2	21-Jul-79	-	-	260	1134	-	1134	3146	539
OK3	27-Aug-84	789	-	206	880	-91	880	3467	296
OK5	16-Apr-80	1332	-	286	1268	64	1268	3633	667
OK6	8-Jan-82	1129	-	266	1164	-35	1164	3385	569
OK7	13-Aug-80	1360	-	289	1284	76	1284	4440	676
OK8	28-Apr-82	1285	-	278	1226	59	1226	3414	625
OK9D	21-Feb-81	1223	-	278	1226	-3	1226	4085	626
OK10D	20-May-81	1207	-	264	1154	53	1154	4253	559
OK11Dd/h	18-Jun-81	-	179	-	759	-	759	1062	256
OK12D	12-Sep-81	1089	-	230	990	99	990	3903	476
PN13D	20-Jan-82	1179	-	267	1169	10	1169	4282	568
PN14	24-Sep-82	1341	-	272	1195	146	1195	4470	676
PN15D	5-Oct-81	1068	-	258	1124	-56	1124	3062	527
PN16D	22-Oct-82	1309	-	290	1289	20	1289	3706	688
PN17D	16-Feb-82	1078	-	232	1000	78	1000	3849	445
PN19D	21-Oct-82	1196	-	250	1085	111	1085	4479	565
PN20D	16-Dec-82	1375	-	252	1095	280	1095	4086	683
PN21D	5-Oct-82	1016	-	244	1056	-40	1056	4150	457
PN22D	12-Nov-82	1178	-	258	1124	54	1124	4215	564
PN24D	21-Dec-82	1322	-	264	1154	168	1154	4007	706
PN26	28-Dec-82	1167	-	256	1115	52	1115	5260	583
SG1	19-Nov-81	1126	-	255	1110	16	1110	3304	511
SG2	6-Jan-82	1197	-	262	1144	53	1144	3319	547
SG3D	26-Jan-83	1171	-	238	1028	143	1028	2092	514

Hmeas : measured enthalpy
Tcha : chalcedony geothermometer (Fournier, 1981)
Tq-adi : quartz (adiabatic) geothermometer (Fournier, 1981)
Hqtz/cha : enthalpy, based on quartz or chalcedony geothermometer
Hxs : excess enthalpy (Hmeas. - Hqtz/cha)
Hres : reservoir enthalpy used in calculation of Cl⁻res.
Cl⁻res : reservoir Cl⁻ or total discharge Cl⁻
SiO_2res : reservoir SiO_2 or total discharge SiO_2

Relationships between reservoir chloride concentrations and enthalpy are illustrated in Figure 4.2. Also included are the Okoy Valley spring data (Figure 1.11; Table 1.1; Glover, 1975). Despite a more extensive data suite, Figure 4.2 does not vary significantly from the diagram as presented by Jordan (1983; see Figure 1.18). Figure 4.2 illustrates that the Nasuji-Sogongon wells are generally less saline than the Puhagan wells. The most saline water is from well PN26, which is interpreted to indicate that this water has undergone the greatest amount of boiling. The boiling trend is defined by the line connecting the position of PN26 with that of the enthalpy for pure steam (i.e., 2694 kJ/kg, 0 mg/kg Cl^-; Figure 4.2).

A possible mixing, or dilution, trend is defined by the line of best fit through the most dilute waters with the highest enthalpies (i.e., BL1D, NJ1D, NJ2D, OK11D, SG3D and NJ6D; line A on Figure 4.2). The predicted end-member dilutant has zero chloride and an enthalpy of approximately 680 kJ/kg, i.e., a steam-heated condensate with a temperature of about 160°C (Figure 4.2). The six wells defining this steam-heated condensate mixing trend are located in the upper reaches of the Okoy Valley, in the Nasuji-Sogongon and southern Puhagan areas (Figure 4.1) and were directionally drilled beneath areas of higher elevation. They include the three wells that discharge mixed sulphate-chloride waters (NJ1D, NJ2D and OK11D). The intersection of this mixing trend with the boiling trend gives an indication of the nature of the reservoir parent liquid. This is estimated to have 4050 mg/kg Cl^- and a temperature of 322°C (Figure 4.2). This compares favourably with 4150 mg/kg Cl^- and 328°C, estimated by Jordan (1983), and the maximum measured temperature of 330°C in well PN20D.

Another possible dilution trend (line B on Figure 4.2) is represented by a mixing line between the parent reservoir fluid and a surface derived, cold meteoric water (Okoy River; Table 4.1). Chemistry of water from wells OK2, OK5, OK6, OK8, PN15D, PN16D, SG2 and SG1 have possibly influenced the mixing process (Figure 4.2). These eight wells are mostly from Nasuji Sogongon, but also includes several from Puhagan (OK2, PN15D and PN16D). Of the Puhagan wells, PN16D and OK5 are located closest to the upflow zone (Figure 4.1) and their discharge water chemistries are most similar to that of the parent liquid (Figure 4.2). The remaining six waters that plot along the line B trend are from wells peripheral to the upflow zone (Figure 4.1).

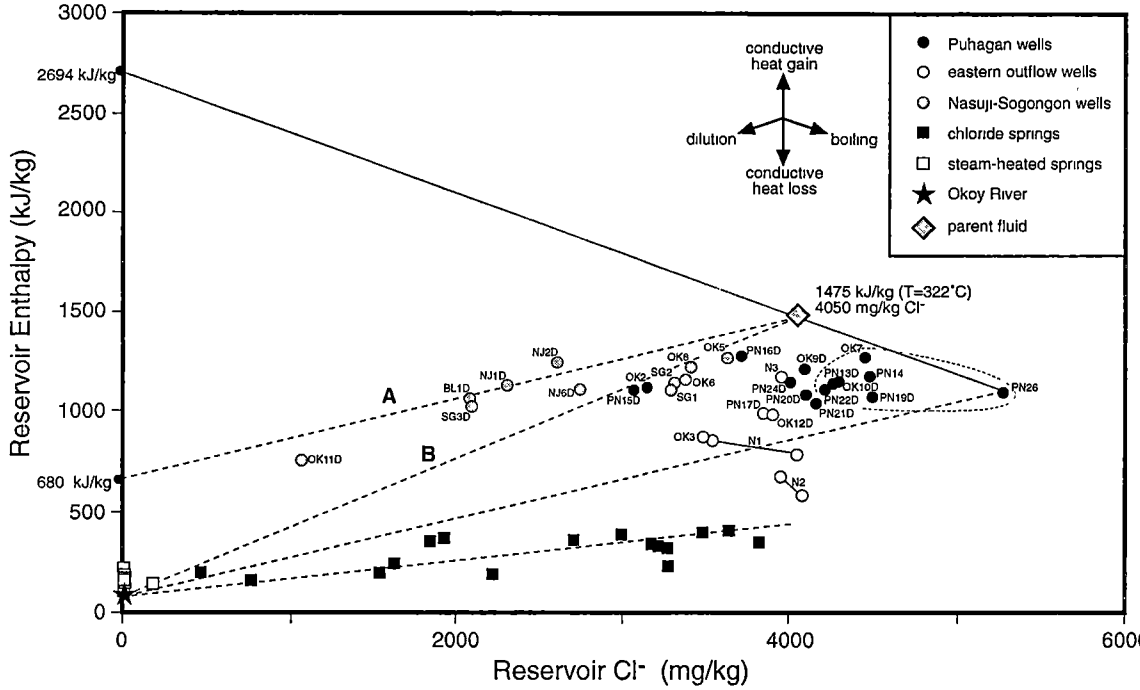

Figure 4.2. Reservoir chloride versus enthalpy plot for Palinpinon geothermal well and Okoy Valley spring waters. See Table 4.1 for well data sources; spring chemistry is presented in Table 1.1 and Figure 1.10 (Glover, 1975). The boiling trend is defined by a line connecting the most saline water (PN26) with the enthalpy for steam (2694 kJ/kg). Line A is a mixing trend, defined by wells OK11D, SG3D, BL1D, NJ1D, NJ2D and NJ6D, with a steam-heated end-member dilutant (0 mg/kg Cl^-, 680 kJ/kg). Line B is a mixing trend, defined by wells PN15D, OK2, SG1, SG2, OK6, OK8, OK5 and PN16D, with a meteoric (i.e., Okoy River water) end-member dilutant (0 mg/kg Cl^-, 100 kJ/kg). Two other dashed lines represent other possible mixing trends. Wells with water compositions more saline than the parent fluid (> 4050 mg/kg Cl^-) are most likely to have been influenced by boiling and are enclosed by the dotted line.

Water chemistries predominantly influenced by boiling are those with higher salinities than the parent liquid (i.e., OK7, OK10D, PN13D, PN14, PN19D, PN22D and PN26). Their positions below the boiling trend (Figure 4.2) can be explained by variable amounts of mixing and/or conductive cooling. The remaining wells represented in Figure 4.2 mostly plot below the parent liquid position, with similar salinities but lower enthalpies. These wells are located in the easterly outflow zone and also in the Puhagan area close to the upflow region. Conductive cooling of the parent liquid, or a combination of boiling and mixing, can account for the composition of these waters. However, the most saline Okoy Valley spring waters have similar salinities to many of the Puhagan wells (Figure 4.2). This is interpreted to indicate that conductive cooling affects the water chemistry in the outflow zone.

A better resolution between mixing, boiling and cooling processes is seen by comparing reservoir chloride and silica concentrations (Figure 4.3). The dilute Nasuji-Sogongon waters define a mixing trend towards low chloride and low silica end-members (i.e., steam-heated condensates and/or meteoric waters). Boiling imposes two processes on hydrothermal water: vapour loss and adiabatic cooling. With vapour loss, SiO_2 and Cl^- will be concentrated in the liquid. Upon adiabatic cooling of the residual liquid, the precipitation of silica will result in a decrease in the SiO_2 concentration. Thus, waters from the seven wells most affected by boiling (OK7, OK10D, PN13D, PN14, PN19D PN22D and PN26) have the highest Cl^- concentrations but lower silica concentrations than other Puhagan wells (Figure 4.3). The six wells located in the eastern outflow zone, N2 (Figure 1.5), N1, N3, OK3, OK12D and PN17D (Figure 4.1) define a vertical trend of decreasing silica with approximately constant chloride concentrations, consistent with conductive cooling (Figure 4.3). The most saline spring waters have silica and chloride concentrations similar to the outflow well waters. This suggests that there are areas in the outflow zone where, neutral chloride waters from the deep parts of the system remain unaffected by mixing with shallow-derived (i.e., steam-heated and meteoric) waters. However the trend of spring water compositions towards the Okoy River composition (Figure 4.3) implies that mixing of neutral chloride and meteoric waters does occur, and it probably does so in the shallowest parts of the outflow zone.

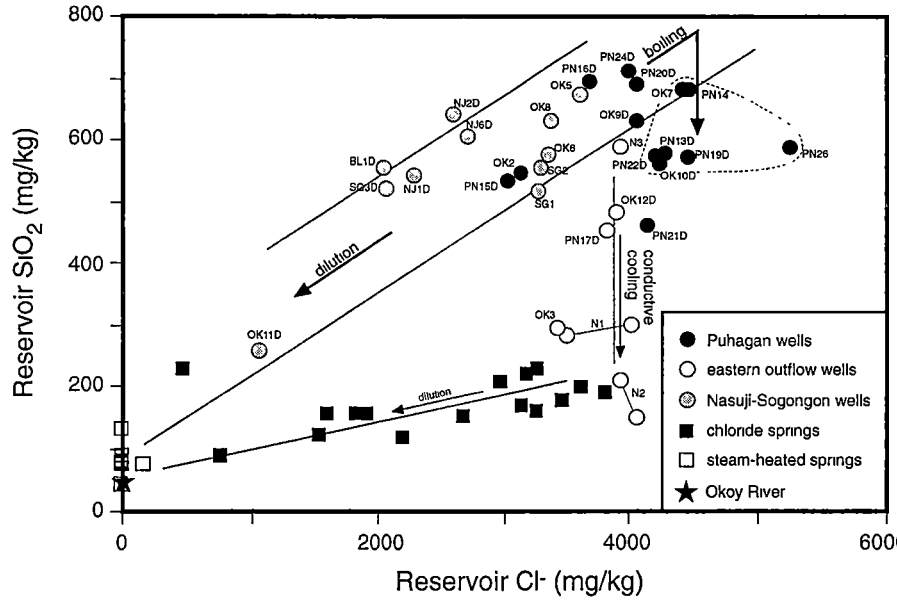

Figure 4.3. Reservoir chloride versus silica plot highlights the important hydrological processes that influence water chemistry (ie., solid lines : boiling, dilution and conductive cooling). Wells with water compositions mostly influenced by boiling are enclosed by the dashed line. Wells located in the eastern outflow have compositions influenced by conductive cooling. Nasuji-Sogongon wells have dilute water compositions and are influenced by mixing. The boiling trend is a combination of two processes: vapour loss concentrates SiO_2 and Cl^- in the residual liquid; adiabatic cooling promotes silica precipitation and hence decreases SiO_2 in the liquid. The maximum concentration of SiO_2 achieved before quartz saturation is not known.

Combining the K-Mg and K-Na solute geothermometers and plotting water compositions in terms of Na, K and Mg concentrations can be used to assess whether geothermal waters have attained full water-rock equilibrium (Figure 4.4, Giggenbach, 1988). The K-Na geothermometer is slower to respond to changes in the physicochemical environment than the K-Mg geothermometer (Giggenbach, 1988). Waters not in chemical equilibrium with the host rocks will have different temperatures calculated by each geothermometer and will plot towards the Mg apex, in areas labelled "partial equilibrium" and "immature waters" (Figure 4.4). Their positions indicate differences between calculated K-Mg and K-Na temperatures. Waters that have equilibrated with the chemistry of the surrounding rock will have approximately equal Na-K and K-Mg temperatures and plot on, or close to, the line labelled "full equilibrium" (Figure 4.4).

The Puhagan and Nasuji-Sogongon waters from wells located close to the upflow zone have compositions influenced by mixing with meteoric water and plot close to the full equilibrium line, implying they are in approximate chemical equilibrium with the host rock (Figure 4.4). The indicated 300-330°C temperature range is in close agreement with the 330°C maximum temperature measured in well PN20D, and the parent liquid temperature estimated from reservoir enthalpy estimations (Figure 4.2). Most of the wells that have discharge chemistries influenced by mixing with a meteoric end-member plot close to, or on the full equilibrium line. Well waters influenced by steam-heated mixing define a mixing trend away from full equilibrium, towards the Mg apex and the area labelled "immature waters" (Figure 4.4). Wells that plot furthest from the full equilibrium line (NJ1D, NJ2D), have K-Mg temperatures (189° and 174°C, respectively) approximately 110°C lower than K-Na temperatures (299° and 283°C, respectively). This difference indicates that water chemistries have not had time to re-equilibrate since mixing with a relatively Mg-rich dilutant (i.e., a steam-heated condensate).

The six wells located in the eastern outflow, with waters influenced by conductive cooling, also define a trend away from the full equilibrium line (Figure 4.4). However, differences between the K-Mg and K-Na temperatures for these waters are less than those defining the steam-heated mixing trend. For example, well N2 has K-Mg temperatures (171-176°C) only 34-40°C lower than the K-Na temperatures (210-211°C). This implies that the residence time in the eastern outflow is long enough for water chemistries to at least partially re-equilibrate at lower temperatures during conductive cooling.

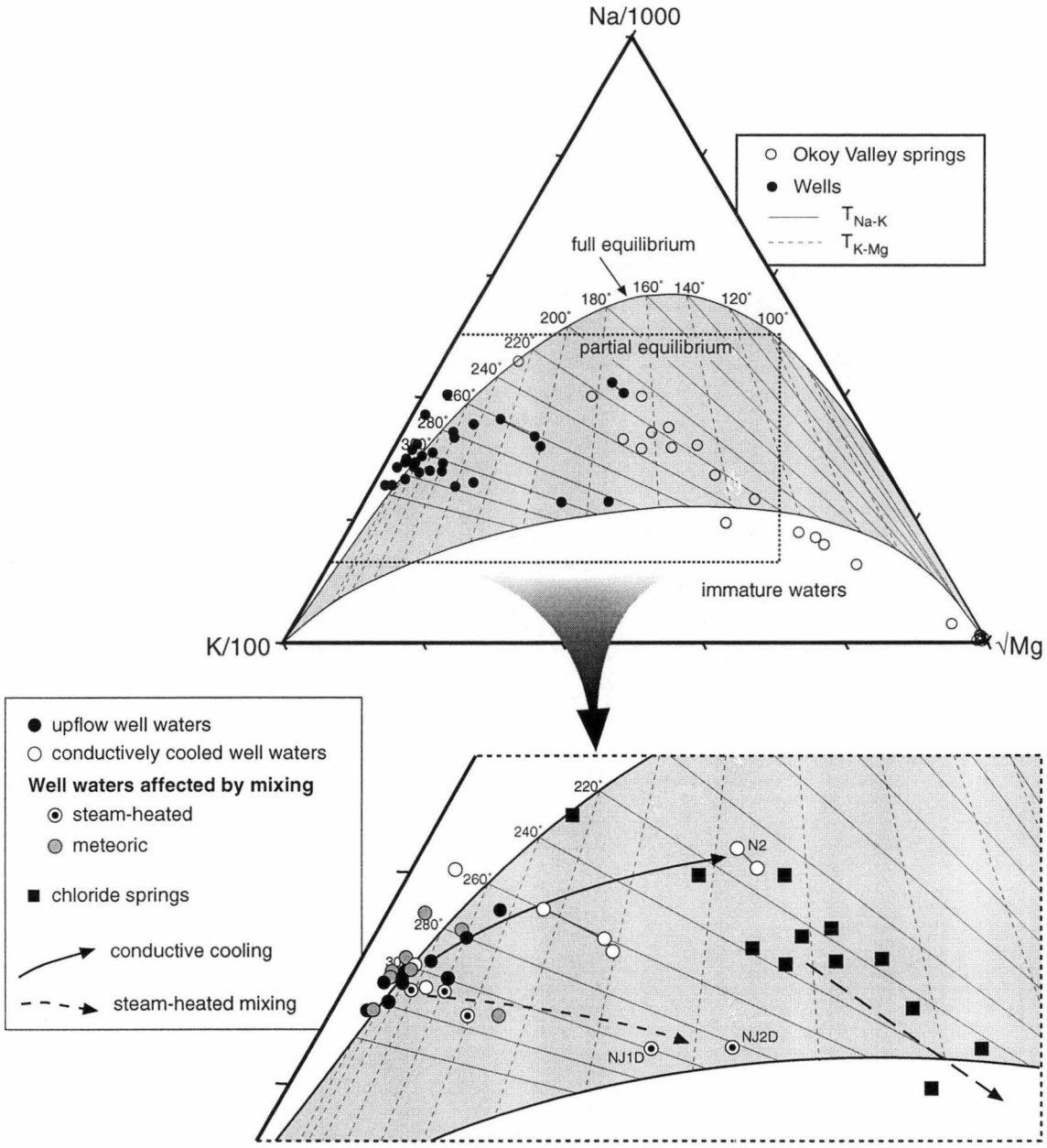

Figure 4.4. Relative concentrations of K, Mg and Na for Palinpinon well discharges and Okoy Valley spring waters (Figure 1.15). The diagram enables evaluation of the Na-K and K-Mg geothermometers (Giggenbach, 1988; see Figure 1.16 for an explanation). Most of the waters from wells located close to the upflow zone, or with compositions influenced by meteoric mixing, plot close to the full equilibrium line between 300-330°C. Waters influenced by mixing with steam-heated waters define a trend towards the Mg apex, whereas waters influenced by conductive cooling define a trend subparallel to the full equilibrium line. See text for a detailed discussion.

Ionic solute concentrations of K, Mg and Ca in the discharge waters can be used to evaluate the CO_2 contents of the deep reservoir (Giggenbach, 1988). This is done by correlating the processes that simultaneously affect liquid and vapour phases and plotting the data in terms of $L_{kc}=\log(c^2_K/c_{Ca})$ and $L_{km}=\log(c^2_K/c_{Mg})$, where c is the respective ionic concentrations of K, Mg and Ca, in mg/kg, of the liquid phase (Figure 4.5; Giggenbach, 1988). The carbon dioxide fugacity of the vapour phase (f_{CO_2}) can be correlated with the ionic solutes to define the stability field of calcite (Figure 4.5). Above this field, and the line labelled "full equilibrium", f_{CO_2} is too low for the formation of calcite. Below the calcite stability, and the line labelled "immature waters", f_{CO_2} is too high for calcite formation (Giggenbach, 1988). Lastly, the K-Mg solute geothermometer (Giggenbach, 1988) temperature scale is represented on the top axis (Figure 4.5).

Most of the upflow waters, and those affected by mixing with meteoric water plot in the "rock dominated" region (Figure 4.5), indicating that these waters have low CO_2 contents and are undersaturated with respect to calcite. The most likely reason for low CO_2 is the previous loss of CO_2 vapour to fumaroles and gas vents, such as in the kaipohan areas. Waters at slightly lower K-Mg temperatures (i.e., < 300°C; Figure 4.5) mostly plot close to the full equilibrium line and indicate attainment of CO_2 fugacities that are conducive for calcite formation. A trend defined by the conductively cooled eastern outflow waters falls along the full equilibrium line towards the chloride spring data (Figure 4.5). It is apparent that CO_2 fugacities in the chloride spring waters are high enough for calcite formation. Waters affected by mixing with steam-heated condensate define a trend across the calcite stable field, into the "fluid dominated" area (Figure 4.5) . The position of the rock dissolution lines, for solutions of average rock compositions (Nasuji Pluton, Cuernos Volcanic Formation and Southern Negros Formation), demonstrates that the composition of the steam-heated waters are largely influenced by the chemical dissolution of host rocks (Figure 4.5).

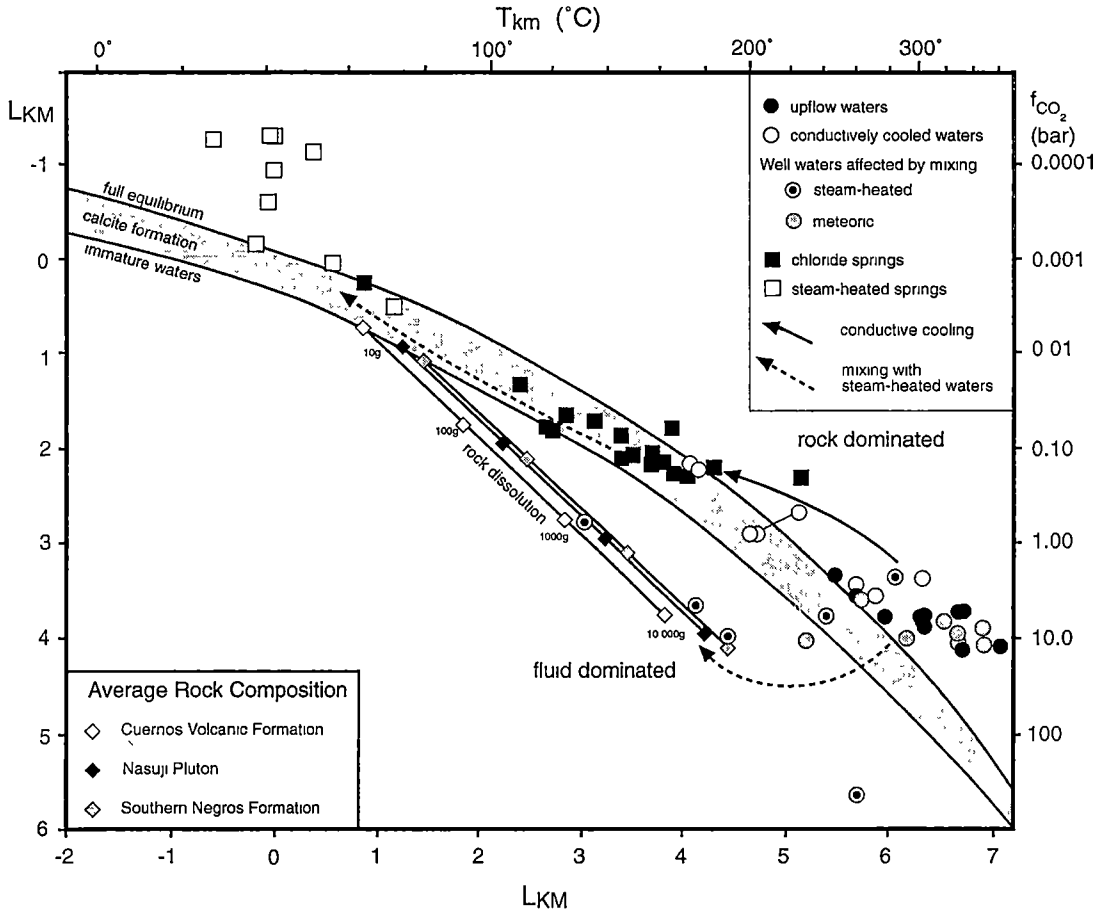

Figure 4.5. A diagram from Giggenbach (1998) showing the relative concentrations of K, Mg and Ca in geothermal waters plotted in terms of L_{KC} and L_{KM} (see text for definition of terms). Correlation with the CO_2 fugacity (f_{CO_2}; right axis) of the vapour phase defines the calcite stability field (shaded area labelled "calcite formation"). A K-Mg solute geothermometer temperature scale (T_{km}; Giggenbach, 1998) is labelled on the top axis. Also plotted are rock dissolution lines for the average compositions of the Nasuji Pluton, Cuernos Volcanic and Southern Negros Formation rocks. These lines connect points of solutions containing 10 g, 100 g, 1000 g and 10 000 g of average composition of each rock type in 1 kg of water. The diagram plots well discharge waters along with neutral chloride and steam-heated spring waters (Glover, 1975). See text for more explanation and discussion.

4.3.3. Summary

The preceding discussion on the hydrology and reservoir chemistry, using recently developed geochemical discrimination diagrams, has provided important, and previously unrecognised, insights into ongoing hydrological processes in the Palinpinon geothermal reservoir (Figure 4.6). A single upflow zone of neutral to slightly alkaline chloride water exists beneath the Puhagan area, where the parent reservoir has a temperature of 320°-330°C and a salinity of approximately 4100 mg/kg Cl^-. The Puhagan wells discharge water with the highest salinities, implying that these waters have undergone the greatest amount of boiling (Jordan, 1983). The subsequent loss of CO_2 from these waters results in them being undersaturated with respect to calcite. This implies that Ca-Al-silicates (e.g., epidote, wairakite), rather than calcite, are more likely to be products of hydrothermal alteration. This is consistent with drillcore observations and the occurrence of epidote, wairakite and prehnite in the calc-silicate alteration assemblage (see Section 3.4.1).

Wells in the Nasuji-Sogongon region discharge more dilute waters (Jordan, 1983) and have undergone mixing with two end-member dilutants: steam-heated sulphate and meteoric waters. Steam-heated sulphate waters are sourced from perched aquifers beneath areas of high elevation (Figure 4.6). Discharge waters that have mixed with these aquifers have a chemistry that is influenced by host rock dissolution and have not attained chemical equilibrium. This is in contrast to the discharge waters that have mixed with a meteoric water. Their apparent chemical equilibrium implies mixing has occurred over longer periods allowing the water chemistry to adjust to the change in physicochemical conditions.

Adjacent wells that discharge water with contrasting chemistries imply that zones of boiling and mixing are largely restricted to narrow areas, such as fault zones and lithologic boundaries (Jordan, 1983). Fault related permeability appears to dominate the overall hydrologic structure of the reservoir (Urbino et al., 1986; Amistoso et al., 1993). The upflow region is located at the intersection of the Lagunao and Ticala Faults, and the major easterly outflow is controlled by the northeasterly striking Puhagan and Ticala Faults. However, lithological boundaries may also impose hydrological controls with the boundary between the Okoy Formation and the overlying Southern Negros Formation providing one possible permeable horizon for the inflow of cooler meteoric waters (Figure 4.6).

Wells located in the easterly outflow region currently discharge water that have compositions consistent with conductive cooling. The long residence times of the water in this zone enables the chemistry to maintain equilibrium with the surrounding host rock and adjust to changing conditions as it moves towards areas of lower elevation beneath the Okoy River. Boiling is not a major influence on the outflow water chemistry, possibly because restricted permeability within the outflow zone results in fluid pressures high enough to hinder gas separation, via boiling.

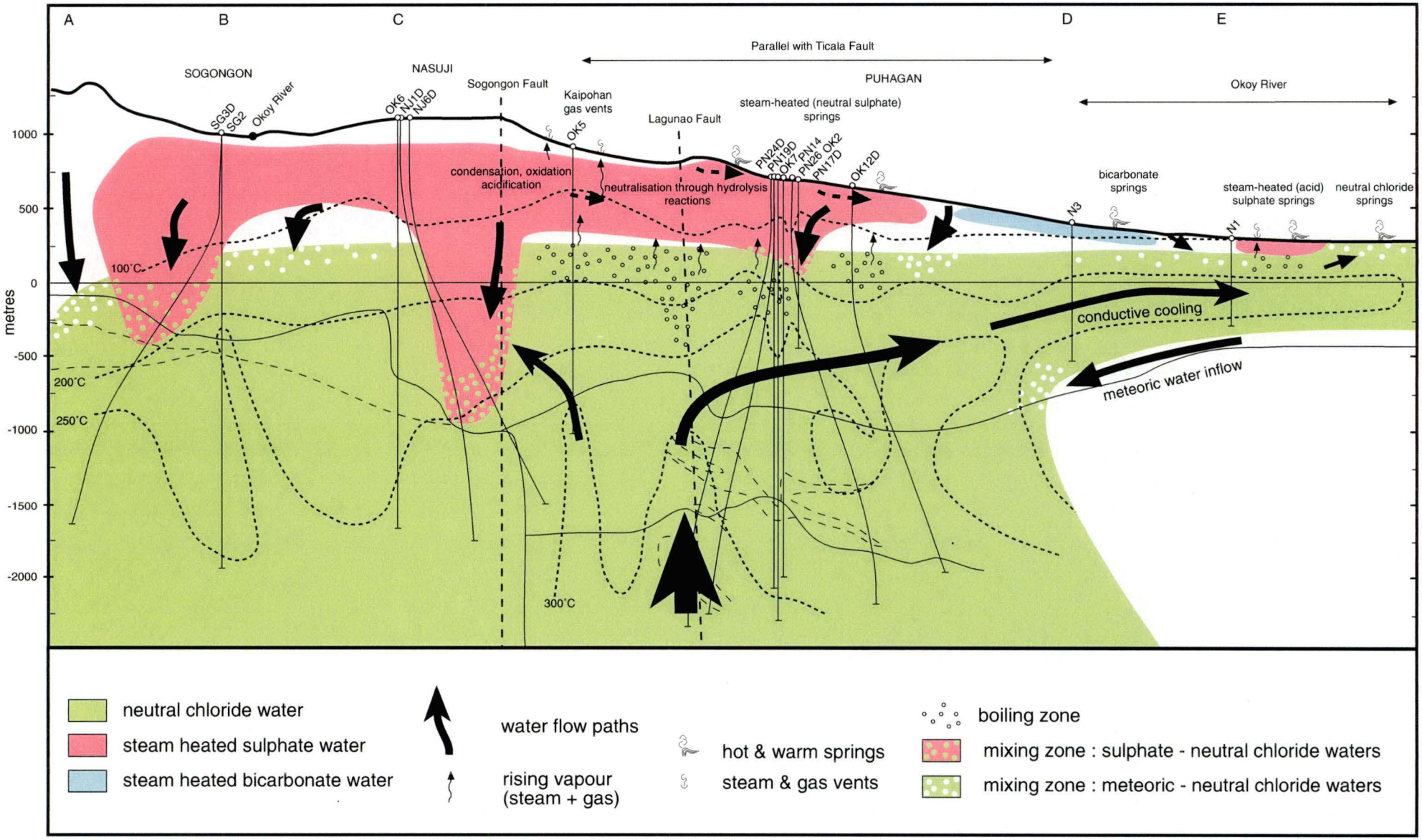

Figure 4.6. Hypothetical hydrologic cross-section through the Palinpinon geothermal field, with present-day fluid flow paths for neutral chloride, meteoric and steam heated condensate waters. The diagram shows the relationship between the deep hydrology and surface discharges. Downflowing meteoric and shallow, steam heated aquifers mix with the deeper chloride waters. Boiling and mixing zones are probably restricted to localised permeable zones (e.g., faults, lithologic contacts). The cross-section line (A-B-C-D-E) is shown in Figure 4.1.

4.4. SCALE DEPOSITS

4.4.1. Introduction

During routine well maintenance, geothermal well liners are reamed to clear mineral deposit build-up. As part of the current study, a selection of mineral deposit (scale) scrapings, or chips, have been examined using polished thin section microscopy. The purpose of this work was to evaluate the capability of the Palinpinon geothermal waters to deposit base and/or precious metals.

Previous published work on scale deposit mineralogy from Palinpinon (Reyes and Cardile, 1989) focussed on the types of clay minerals occurring as scales in Philippine geothermal wells at Tongonan, Palinpinon and Bacon-Manito geothermal fields. Clay scales from Palinpinon are predominantly vermiculite, with mixtures of montmorillonite and saponite. These scales were thought to have formed by either conversion of bentonitic drilling muds that remained in the well as substrate or by precipitation from hydrothermal fluids (Reyes and Cardile, 1989).

The scale samples analysed in the current study represent either deposit build-up from spot depths or from a depth interval. Descriptions of each sample, along with a tabulation of collection depths and aquifer zones for each well are presented in Appendix 3. The scale deposit samples are from eleven wells (BL1D, NJ6D, OK3, OK10D, PN13D, PN15D, PN17D, PN21D, PN22D, PN29D and SG3D), the location of which are shown in Figure 4.1. Wells OK3 and PN17D are situated in the eastern outflow region. Wells PN15D, PN21D and OK10D are located in the Puhagan area, on the eastern margin of the upflow zone. Wells PN29D, PN13D and PN22D are located in the upflow zone. BL1D and NJ6D are Nasuji wells located south and west of the upflow zone, respectively. Sogongon well SG3D is located in the western outflow zone (Figure 4.1).

A schematic diagram of the eleven wells (Figure 4.7) summarises the mineralogy of each scale sample and the scale deposit location from each well, with respect to elevation, aquifers, lithologic boundaries and sections of slotted well (or production) casing. Most of the scale samples examined are from areas of slotted casing close to aquifers. Only those from well PN17D and most from OK3 are from unslotted well casings (Figure 4.7). It is apparent from Figure 4.7 that there is a close spatial association of aquifers with lithological contacts. This implies that permeability at Palinpinon is not only related to faults but also lithologic boundaries, especially the contact between the Okoy Formation and the overlying Southern Negros Formation in the eastern outflow zone.

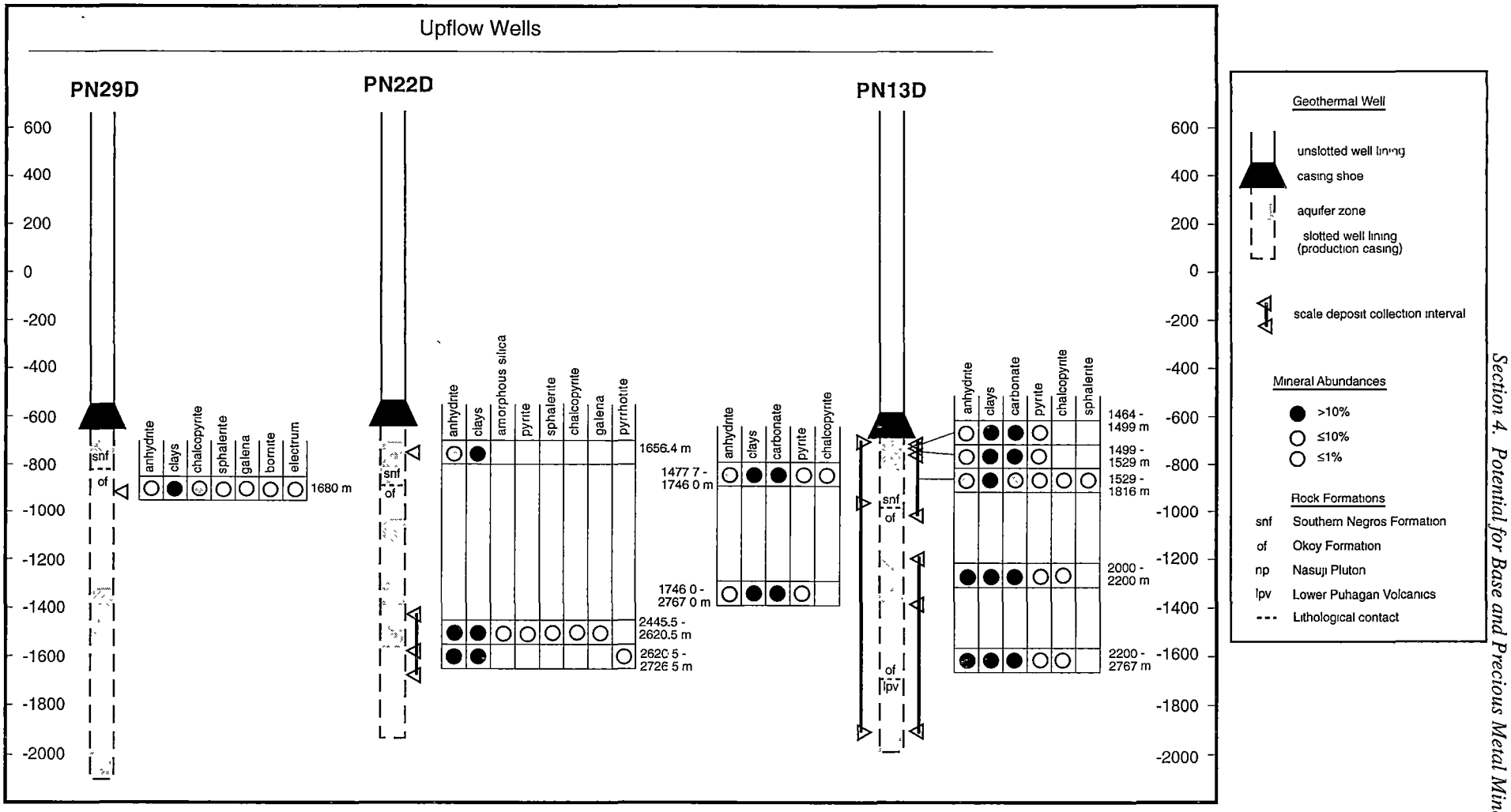

Figure 4.7a. Schematic representation of scale samples from three wells in the upflow zone (Puhagan). The diagram graphically summarises the scale mineralogy of each sample and its location relative to the aquifers, elevation, lithologic boundaries and sections of slotted (production) well casing. Measured depths are listed beside each sample.

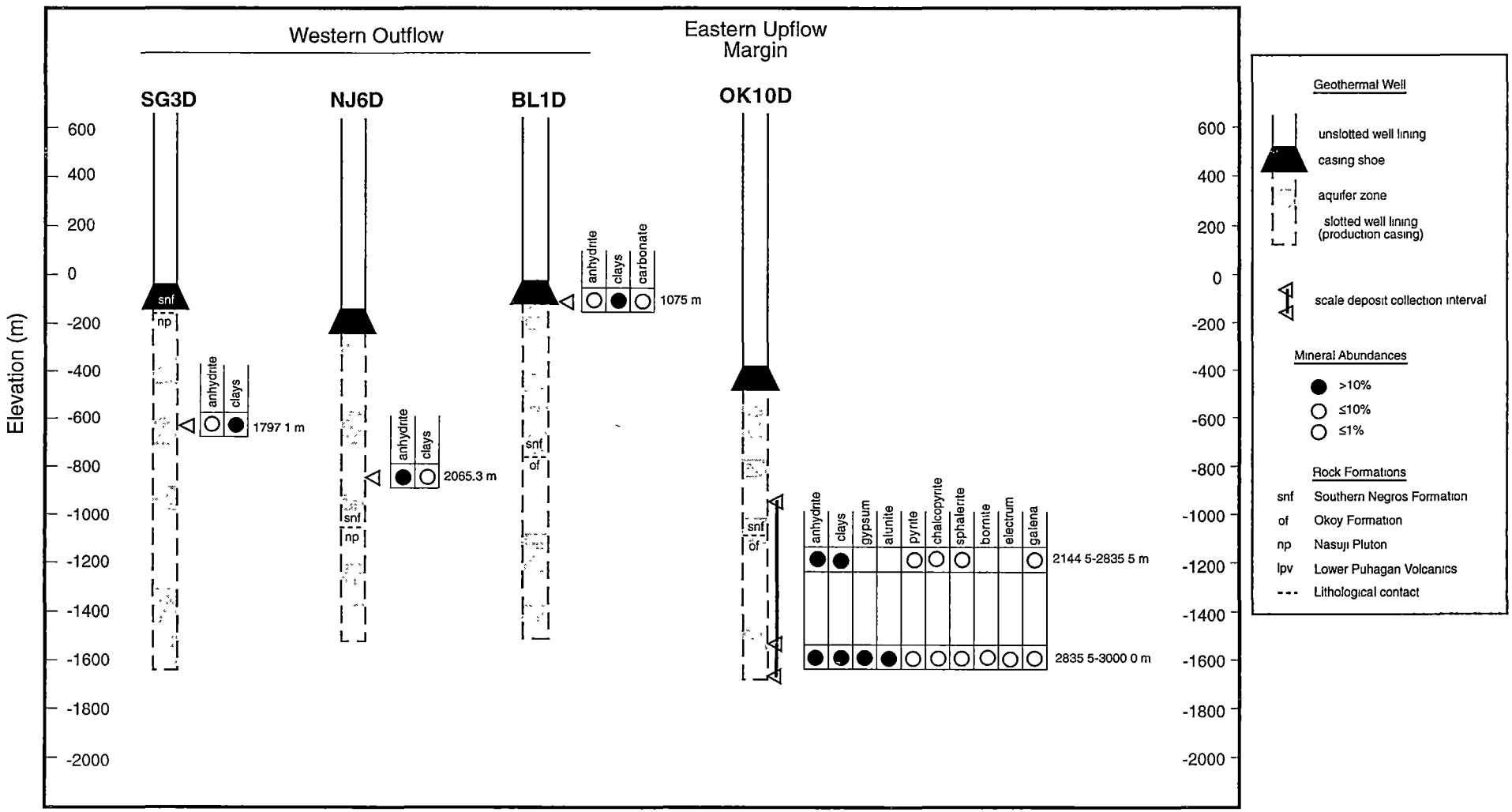

Figure 4.7b. Schematic representation of scale samples from three wells in the western outflow (Nasuji-Sogongon) zone and one from the eastern margin of the upflow zone. The diagram graphically summarises the scale mineralogy of each sample and its location relative to the aquifers, elevation, lithologic boundaries and sections of slotted (production) well casing. Measured depths are listed beside each sample.

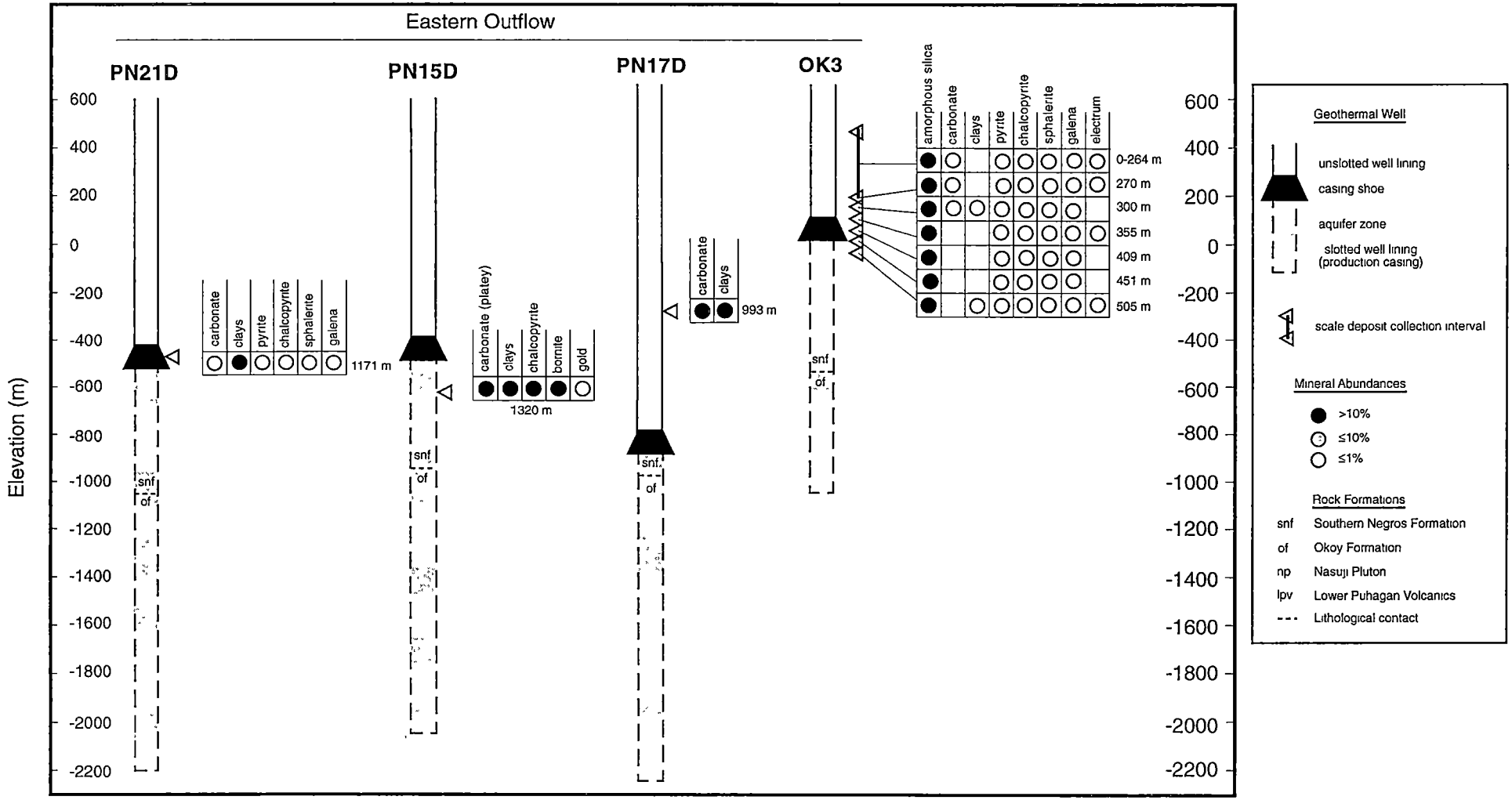

Figure 4.7c. Schematic representation of scale samples from four wells in the eastern outflow zone. The diagram graphically summarises the scale mineralogy of each sample and its location relative to aquifers, elevation, lithologic boundaries and sections of slotted (production) well casing. Measured depths are listed beside, or below, each sample.

4.4.2. Scale Mineralogy

Based on the presence of the dominant non-sulphide mineral, scale chips from the eleven geothermal wells can be classified as being either anhydrite-, carbonate- or amorphous silica-types. Each scale type also contains clay minerals, sulphide minerals (chalcopyrite, pyrite, sphalerite, galena and bornite), gold and Ag-rich electrum (Figure 4.7). Specific clay and carbonate mineralogies were not determined in this study. The clay mineral, a fine grained (< 40 μm) white mica, is assumed to be the same as that identified as smectite by Reyes and Cardile (1989). Carbonate in Palinpinon scales has previously been identified as calcite (Reyes and Cardile, 1989). In the current study, gold was identified petrographically, whereas the composition of Ag-rich electrum was determined using the electron microprobe (Table 4.3)

Most of the anhydrite scales have a tabular, bladed habit, but acicular crystal forms are also present (Figure 4.8a). Carbonate scales occur mostly as monomineralic aggregates of fine grained anhedral crystals (< 0.1 mm; Figure 4.8a). However, a few bladed crystal aggregates are also present (Figure 4.8b). Amorphous silica scales are present in wells OK3 and PN22D (Figure 4.8c). Clay minerals either occur as discrete chips or as aggregates intergrown with anhydrite and carbonate scales.

Sulphide minerals are fine grained (< 25 μm) and occur either as discrete aggregates, or as dendritic inclusions in anhydrite, carbonate or clay scales (Figure 4.8d). In both occurrences they typically consist of intergrowths of chalcopyrite, sphalerite and galena (Figure 4.8e; Table 4.3). Minute (< 5 μm) Ag-rich electrum grains (Table 4.3) are present in some intergrowths (Figure 4.8e). One sample (PN15D, 1320 m) contains bornite as the dominant sulphide mineral, with inclusions of chalcopyrite and gold and rectangular voids (Figure 4.8f). The voids are interpreted to have formed via the dissolution of a tabular mineral (anhydrite or platey carbonate).

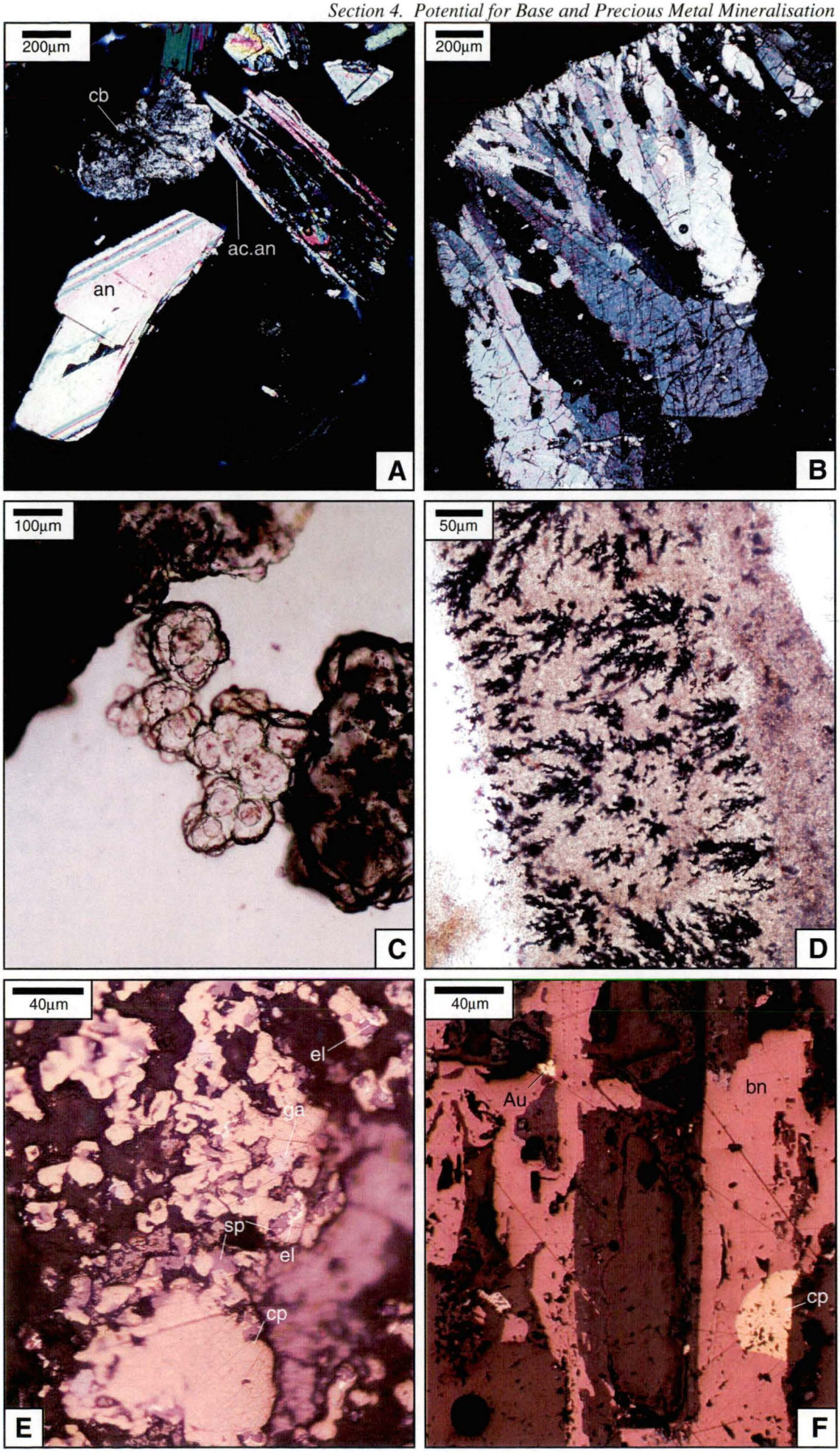
200µm
cb
ac.an
an
A
200µm
B
100µm
C
50µm
D
40µm
el
ga
sp
el
cp
E
40µm
Au
bn
cp
F

Table 4.3. Electron microprobe analyses of sulphide minerals and precious metal scale deposits from geothermal well PN29D, 1680 m depth.

	Scale Minerals				
	chalcopyrite	**chalcopyrite**	**sphalerite**	**galena**	**Ag-rich electrum**
S	33.02	34.46	30.20	13.62	-
Fe	30.40	30.73	3.87	-	-
Cu	33.88	33.56	1.72	-	-
Zn	0.40	0.30	55.21	-	-
Pb	-	-	-	85.84	-
As	0.17	1.00	0.19	-	-
Ag	0.27	0.13	4.09	0.14	65.06
Sb	0.00	0.00	0 00	-	-
Bi	0.00	0.00	0.00	-	-
Se	-	-	-	0 1	-
Au	-	-	-	-	20 07
Hg	-	-	-	-	-
Total	98.15	100.17	95.28	99.69	85.13
	Atomic Proportions				
S	0.49	0.49	0.49	0.50	-
Fe	0.26	0.25	0.04	-	-
Cu	0.25	0.24	0.01	-	-
Zn	0.00	0.00	0.44	-	-
Pb	-	-	-	0.49	-
As	0.00	0.01	0.00	-	-
Ag	0.00	0.00	0.02	0.00	0.86
Sb	0.00	0.00	0.00	-	-
Bi	0.00	0.00	0.00	-	-
Se	-	-	-	0.00	-
Au	-	-	-	-	0.14
Hg	-	-	-	-	-

- = below detection limit

4.4.3. Discussion and Summary of Scale Deposits

Each of the three scale types identified come from a distinct part of the reservoir. The five wells with anhydrite scales (NJ6D, OK10D, PN22D, PN29D, SG3D) were directionally drilled towards the south, beneath areas of elevated topography. They include two Nasuji-Sogongon wells and three Puhagan wells, located close to the upflow zone (Figure 4.1). Wells with carbonate scales (PN15D, PN17D, PN21D) were drilled towards the east or north-east in the eastern outflow zone, (Figure 4.1). Only one well has amorphous silica scales (OK3). It is located at the lowest elevation in the eastern outflow zone (Figure 4.1).

Four wells contain two scale types (BL1D, OK3, PN13D, PN22D). Wells BL1D and PN13D contain both anhydrite and carbonate scales. Sample PN22D (2445.5-2620.5 m) contains scale chips of anhydrite and minor amorphous silica, and the three shallowest samples from well OK3 (0-264 m, 270 m, 300 m) contain amorphous silica with minor amounts of carbonate (Figure 4.7). Even though these wells have more than one type of scale deposit, the

characteristic minerals of each type (anhydrite, carbonate, amorphous silica) are never seen together as intergrowths in the same chip. They always occur in separate chips, implying that they were deposited either in different parts of the well or at different times.

Base metal sulphide minerals (i.e., chalcopyrite, bornite, sphalerite and/or galena) occur in scales from seven wells (OK3, OK10D, PN13D, PN15D, PN21D, PN22D and PN29D; Figure 4.7). Electrum- or gold-bearing scales have been identified from four of these wells (OK3, OK10D, PN15D and PN29D). Base metal sulphide and precious metal-bearing scales occur in each of the three scale types, but in wells located either close to the upflow zone or in the eastern outflow region (Figures 4.1 and 4.7). The three wells located in the western part of the reservoir (BL1D, NJ6D, SG3D; Figures 4.1 and 4.7) have anhydrite scales without base metal sulphides or precious metal minerals.

To ascertain the processes of base and precious metal deposition based solely on the examination of scale mineralogy requires a sampling program that incorporates geothermal wells from different parts of the geothermal field, and a complete knowledge of the well history. Unfortunately, the scale samples examined here were only collected as part of a routine geothermal well maintenance program, and well conditions at the time were not recorded. Nevertheless, the examination of these scales demonstrates that Palinpinon geothermal waters are capable of transporting and depositing base and precious metals. The occurrence of base metal sulphide and precious metal-bearing scales from distinct regions of the geothermal reservoir probably reflects the dominant ongoing hydrological process occurring in each area, specifically : (1) boiling in the upflow zone; (2) mixing beneath regions of high elevation; and (3) conductive cooling in the outflow zone. Each of these processes will be modelled chemically in Section 4.6, to ascertain their ability and efficiency for precipitating base and precious metals. However, it must be noted that conditions in the geothermal well, such as high flow-rates and mass fluxes may be equally significant for mineral deposition.

4.5. TRACE METAL FLUID CHEMISTRY

4.5.1. Introduction

In a previous study by Brown et al. (1996), downhole water samples from two wells at Ohaaki-Broadlands geothermal field, N.Z. (BR9, BR20) were analysed for Au, Ag, Cu and PGE contents. The downhole water sampler used in that study was specifically designed for collecting water samples for trace metal analysis. The same sampler has been used in the current study in an attempt to determine the trace metal composition of the downhole fluids at Palinpinon.

Sampling downhole water from geothermal wells for trace metal analysis is difficult. After sample collection, while the tool is returning to the surface, the reduction in temperature and

associated gas loss can cause some elements (e.g., Au and Ag) to precipitate on the inside walls of the sample chamber. To capture these elements it is necessary to rinse out the chamber with aqua regia (AR) after each sampling run; AR is a solution reactive enough to dissolve any precipitates coating the interior walls. The sampler has been designed to withstand the reactive qualities of AR (Brown et al., 1996). After sampling, the trace metal concentrations of the geothermal water and the AR rinse are analysed by ICP-MS. Provided that no contamination occurs from the sampling tool, the total metal content of the deep geothermal water can be determined from the sum of the trace metals in the water and the AR rinse.

4.5.2. Well Selection

Ideally, geothermal wells used for deep water sampling should have a wide geographical distribution across the hydrothermal system. So that a range of hydrologic environments can be sampled. However, the realities of an active geothermal field utilised for power production place severe constraints on well selection. These are as follows:

- A deviated well cannot be used. Jerking on the suspension wire, which activates the inertia mechanism to open the valve and allow fluid to enter the chamber is more effective if the well is vertical. This also minimises the danger of losing the sampler down the well if the suspension wire gets caught on the well lining and breaks. Unfortunately most geothermal wells collared in steep terrains, such as at Palinpinon, are deviated.
- The well has to be off-line, i.e. not supplying steam to a power station. If this is not the case, an alternative well that could maintain an equivalent energy output needs to be brought on-line whilst the selected well is sampled.
- The well has to have a water-dominant fluid. Otherwise, high vapour pressures will allow steam to pass preferentially into the sampling chamber and the water returned to the surface will consist mostly of steam condensate.
- The well cannot have any blockages, such as scale deposits or damaged well lining, that hinder passage of the sampling tool.
- The effects of waste water reinjection return or inflow of cooler fluids due to pressure drawdown should be minimal.
- The well water chemistry cannot be too severe on sampling equipment. Highly acidic waters can damage the sampler and the suspension wire.
- The well must be able to be opened. Many of the earliest drilled wells at Palinpinon are abandoned and plugged with cement.

Considering these criteria, two wells were selected for downhole water sampling for trace metal analysis. The key characteristics for each are summarised in Table 4.4.

Well N1 is located in the outflow zone at a low elevation (300.7 m) in the Okoy Valley

(Figures 4.1 and 4.6). The well is shut-in, and does not supply steam for electricity production. The well has a total depth of 603.3 m with a water level located at approximately 300 m depth. The main hydrological feed zone occurs at 450 m depth. The maximum down-hole temperature measured in September 1997 was 206°C at 300 m depth. A well blockage, either due to damaged well casing or scale deposit build-up, is located at a depth of 500 m.

Well PN14 is located in the central Puhagan area, close to the hydrologic upflow zone at an elevation of 710.5 m (Figures 4.1 and 4.6). It is currently shut-in, and does not supply steam to the power station. PN14 has a depth of 3,077.7 m with the water level at approximately 500 m below the surface. The main feed zone is situated between 2,600 and 2,800 m. A maximum temperature of 261°C was measured in September 1997 at 2,900 m. A well blockage occurs at this depth.

Table 4.4. Characteristics of sampled wells.

Well	N1	PN14
Hydrologic location	outflow	upflow
Status (as of 12/97)	shut	shut
Total depth	603.3 m	3,077.7 m
Water level	~100 m	~500 m
Wellhead pressure	2.2 MPag	0.9 MPag
Main feed zone	450 m	2,600-2,800 m
Blockage depth	500 m	2 900 m
Max. temp (as of 09/97)	206° C	261° C
Max. temp. depth	300 m	2 900 m

4.5.3. Sample Preparation

Prior to sampling, washing and weighing of the sample bottles and the preparation of fresh AR and analytical blanks were carried out in the PNOC-EDC geochemistry laboratory at Palinpinon. Acids used for the AR were Merck suprapur grade HCl and HNO_3.

New Nalgene sample bottles were washed in concentrated HNO_3 ('analaR', BDH) and then left to soak overnight in 5N HNO_3 ('analaR', BDH). They were then rinsed with distilled and deionised water and allowed to air dry. To preserve the water sample chemistry, 20 ml of concentrated HNO_3 (suprapur, Merck) was added to the water sample bottles.

Analytical blanks were prepared as follows:

- **DDI** : distilled and deionised (DDI) water from the Palinpinon geochemistry laboratory.
- **d/hDDI acid** : a down-hole DDI blank consisting of 500 ml of DDI water placed in the sampling chamber and lowered down well PN14 to the sampling depth (2,299 m). The sampler was left unopened for 2 minutes before returning to the surface. The water was collected and acidified with 20 ml conc. HNO_3 (suprapur, Merck).

- **AR** : a 100 ml AR blank consisting of 50% AR and 50% DDI.
- **AR wash** : the pre-cleaned sampling chamber was rinsed with 80 ml AR followed by 80 ml DDI. These were combined and kept as a wash blank (**AR wash 1**). This procedure was repeated and a second wash blank was collected (**AR wash 2**).

4.5.4. Results

Two water samples were collected from each well. Table 4.5 summarises their volumes and sample depths. Three sampling runs to a target depth of 500 m were attempted in N1. The sampling tool was left at these depths for 15 minutes. The first run provided only 150 ml of water. The steel shim above the non-return valve had not been pierced, suggesting that the water contents represented steam condensate that had leaked into the sampling chamber. A second run to 501 m depth yielded 600 ml of water; the third to 500 m yielded 410 ml. Only results from the second and third sampling runs are reported here. Two sampling runs were made in PN14. The first, to 2,300 m depth, returned 525 ml of water. The second, at 2,306 m, yielded 550 ml of water. A third run was made to obtain a down-hole DDI blank (d/hDDI acid).

The water samples, AR washes and blanks were quantitatively analysed for 15 trace elements using the inductively coupled plasma mass spectrometer (ICP-MS) facility at the University of Tasmania. The elements analysed were Co, Cu, Zn, Mo, Ag, Cd, Sn, Sb, Te, W, Au, Hg, Tl, Pb and Bi. The analytical results for the blanks are presented in Table 4.6a, while the sampled waters and respective AR washes are presented in Table 4.6b.

Table 4.5. Volumes of sampled water and their sample depths.

Well & Sample No.	Sample Volume (ml)	Sample Depth (m)
N1 #2	600	501
N1 #3	410	500
PN14 #1	525	2,300
PN14 #2	550	2,306

Table 4.6a. Results of trace metal analyses of blanks (µg/kg).

	Blank DDI	Blank d/hDDI acid	Blank AR	Blank AR wash 1	Blank AR wash 2
Co	0.07	18.04	0.32	5,484.21	4,653.64
Cu	0.48	82.24	8.83	15,046.88	4,944.75
Zn	1.52	74.75	9.76	3,984.83	3,500.06
Mo	0.07	54.81	0.29	415.89	355.04
Ag	0.01	0.03	0.27	48.25	7.29
Cd	0.01	0.20	0.08	4.23	2.32
Sn	0.09	1.01	1.50	147.74	109.57
Sb	0.02	20.99	0.78	47.38	28.30
Te	0.02	0.09	0.08	0.93	0.81
W	0.20	11.72	0.82	22.13	16.22
Au	0.01	0.02	0.04	0.63	0.16
Hg	0.24	0.50	1.12	53.72	2.60
Tl	0.00	1.42	0.73	1.00	0.68
Pb	0.11	1.65	1.58	105.99	94.81
Bi	0.02	0.08	0.10	1.58	1.15

Table 4.6b. Results of trace metal analyses of waters and Ar washes (µg/kg).

	N1 #2 water	N1 #2 AR	N1 #3 water	N1 #3 AR	PN14 #1 water	PN14 #1 AR	PN14 #2 water	PN14 #2 AR
Co	2.44	6,680.01	63.74	4,450.48	9.14	2,382.30	3.80	2,151.73
Cu	100 38	14,057.08	1,229.21	9,246 26	694.32	5,384.00	121.87	3,865.89
Zn	237.36	6,140.47	960.49	4,698.66	116.85	2,333.16	85.93	1,683.46
Mo	32 91	515.74	89.60	985.86	241.40	615.25	235.60	1,105.29
Ag	0.56	17.33	3.51	8.90	6.87	52.06	0.75	8.03
Cd	0.36	6.31	0.81	3.89	0.98	3.13	0.56	2.43
Sn	0.71	154.61	2.53	303.98	1.93	271.41	0.59	324.50
Sb	114 85	2,473.34	514.18	1,420.74	171.49	315.43	119.92	211.42
Te	0.62	1.82	0.51	1.26	0.26	0.68	0.62	0 56
W	4.39	48.10	10.18	34 08	23.72	14.83	16.13	30.77
Au	0.13	3.18	0.94	1 95	0.74	4.49	0.10	0.67
Hg	1.39	23.64	7.92	12 02	0.62	0.98	0.45	0 59
Tl	25.88	596.17	133.81	308.57	22.72	69.12	27.09	63.27
Pb	3 31	171.81	21.35	113.90	17.15	139.43	4.20	49.72
Bi	0.08	2.10	0.09	1.39	0.08	0.84	0.08	0.50

Analyses of blanks are used to negate the effects of contamination. The most likely source for contamination is the sampler because the AR rinse can potentially leach metals from the sample chamber walls. The concentration of trace metals in the blanks are assumed to be background levels. Thus, the metal concentrations in the DDI and d/hDDI acid blanks are subtracted from the water analyses and the metal concentrations in AR wash 2 are subtracted from the AR wash analyses. Comparing analyses of the AR blank with the AR washes (Table 4.6a) reveals that most elements are significantly higher in the AR washes, especially Co, Cu, Zn and Mo. This implies that the AR was leached metals from the ceramic surface coating of the sample chamber. Elements least affected by contamination are Au, Tl and Te (Table 4.6a).

The total trace metal concentrations of the downhole water have been calculated by combining analyses of the waters with their respective AR washes (Table 4.6b) and taking into account blank analyses and the volumes of water collected. The recalculated metal concentrations for the deep water from both wells are presented in Table 4.7. Some metals are present in high concentrations, for example the outflow water (N1) contains 5-6 mg/kg Cu and 2 mg/kg Zn and Sb. However, generally the trace metal concentrations are variable, not only between waters from different wells but also between waters from the same well (e.g. PN14: 40-950 µg/kg Cu, 1-41 µg/kg Ag, 3-50 µg/kg Pb; N1: 50-1350 µg/kg Co, 110-650 µg/kg Mo, 30-190 µg/kg Sn). Despite the variability, the outflow water (N1) appear to have higher concentrations of Co, Cu, Zn, Sb, Hg and Tl than the upflow water (PN14; Table 4.7).

Table 4.7. Recalculated trace metal content of downhole waters (µg/kg).

	Outflow Zone		Upflow Zone	
	N1 #2	N1 #3	PN14 #1	PN14 #2
Co	1,350.91	45.71	0.00	0.00
Cu	6,093.02	5,344.56	946.74	39.63
Zn	1,923.89	2,055 11	42.10	11.18
Mo	107.14	650.22	385.84	726.43
Ag	7.22	5.05	40.96	1.27
Cd	2.83	2.16	1.40	0.44
Sn	30.03	191.19	124.23	156.31
Sb	1,723.88	1,851.66	369.27	232.10
Te	1.20	0.86	0.16	0.53
W	21.25	17.42	12.00	14.99
Au	2.12	2.67	4.02	0.45
Hg	14.91	16.62	0.13	0.00
Tl	421.45	432.78	73.45	71.19
Pb	52.99	38 33	49.49	2.54
Bi	0.63	0 24	0.00	0.00

It is useful to compare these results with the trace metal contents of waters from other geothermal areas. Precious and base metal concentrations in waters from Ohaaki-Broadlands, N.Z., Cerro Prieto, Mexico and the Salton Sea, U.S.A. are presented in Table 4.8 and illustrated in Figures 4.9. To provide a comparison of salinities, the Cl^- concentrations from each area are also presented. With a salinity range of 6 800-8 600 mg/kg Cl^-, the Palinpinon waters are more saline than Ohaaki-Broadlands, but less than the Cerro Prieto waters and more than one order of magnitude less than the brines from the Salton Sea geothermal field.

Table 4.8. Trace metal contents in geothermal waters (µg/kg, unless specified otherwise)

	Au	Ag	Cu	Pb	Zn	Cl^- (mg/kg)
Palinpinon						
N1	2-3	5-7	5,350-6,100	38-53	1,900-2 060	6,800-7,050
PN14	1-4	1-41	40-950	3-50	11-42	8,500-8,600
Ohaaki, N.Z.						
BR9[1,2]	0.9-1.0	13-19	5,000-29,700	-	-	1,766
BR20[1,2]	0.5-1.2	6-12	11,300-15,200	-	-	1,712
BR22[3]	1 5	8	9	2.3	1	1,188
Cerro Prieto, Mexico[4,5]	4	4	5	4.6	6	13,800
Salton Sea, USA[6,7]	0.02-80	45-1,400	4,000-8,000	$7x10^4$-$9x10^4$	$28x10^4$-$79x10^4$	$15.1x10^4$

[1] Brown et al. (1996); [2] Hedenquist (1990); [3] Brown (1986); [4] Weissberg et al. (1979); [5] Henley et al (1984); [6] McKibben et al. (1990), [7] Gallup (1998)

The Au concentrations of the Palinpinon waters (1-4 µg/kg) are comparable to the Au contents at Ohaaki-Broadlands, N.Z. (< 2 µg/kg) and Cerro Prieto, Mexico (4 µg/kg; Table 4.8; Figure 4.9a). In contrast, Au concentrations in the Salton Sea brines range from < 0.1 µg/kg to as high as 80 µg/kg (McKibben et al., 1990; Gallup, 1998). The Ag contents of the Palinpinon waters (1-41 µg/kg) are also comparable to Ohaaki-Broadlands and Cerro Prieto geothermal areas. However, 41 µg/kg in Palinpinon sample PN14#1 (Table 4.8) is very high for a low salinity geothermal waters and is more comparable to the Salton Sea brines (Figure 4.9b).

The Cu values in Palinpinon and Ohaaki-Broadlands (BR9, BR20) waters (Table 4.8) are very high. They are analogous to, but still well above that of the Salton Sea (Figure 4.9c). These results possibly reflect contamination from the sampling tool. The Pb and Zn contents at Palinpinon are higher than those at Ohaaki-Broadlands (BR22) and Cerro Prieto but considerably less than the Salton Sea Pb and Zn concentrations (Figures 4.9d and 4.9e).

Without a large source of published data to draw on, it is difficult to ascertain the degree of contamination and the sampling errors affecting the base and precious metal contents of the Palinpinon geothermal waters. Results from the trace metal analyses of the blanks (Table 4.6a) shows that copper, lead, zinc and silver are apparently affected by contamination from the sampling equipment. However, gold, tellurium and thallium appear to be the metals least affected by contamination, with gold present in concentrations comparable to other relatively dilute, chloride waters (i.e. Ohaaki-Broadlands, Cerro Prieto; Table 4.8; Figure 4.9a).

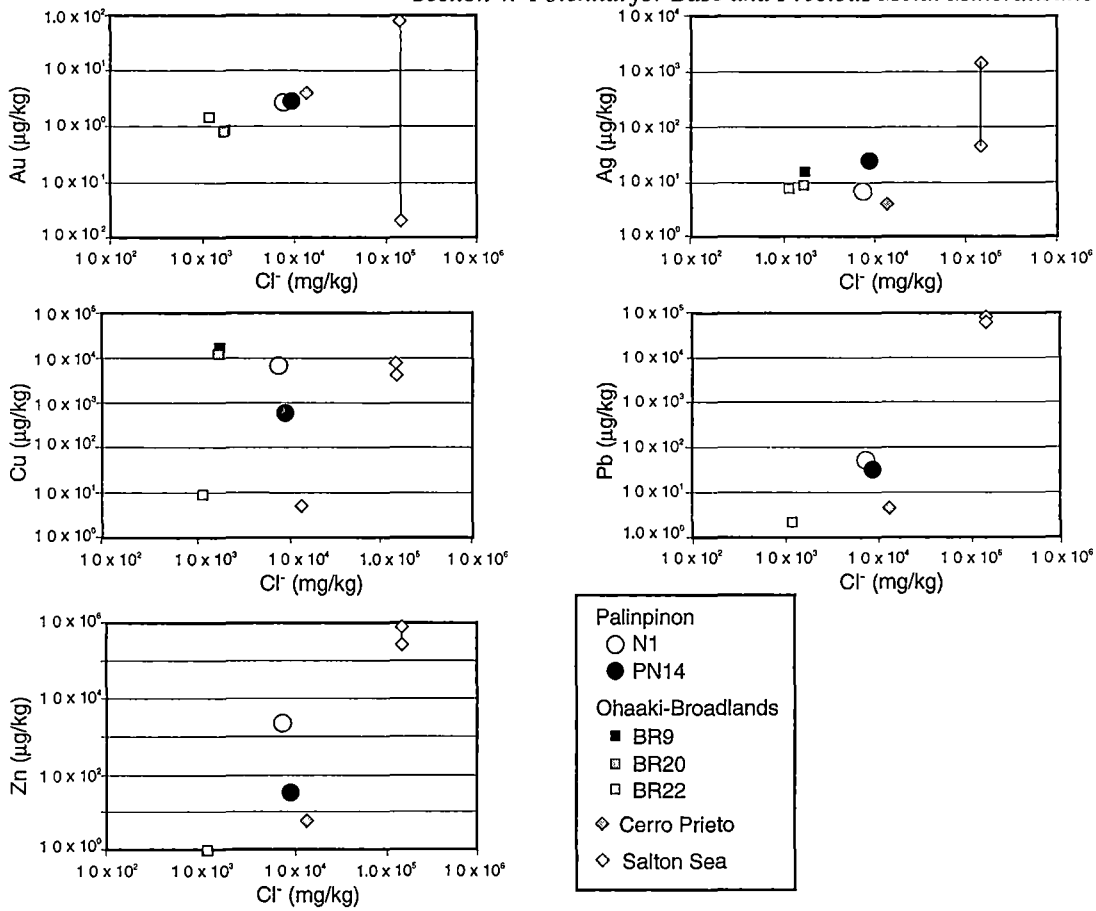

Figure 4.9. Base and precious metals relative to the Cl^- concentrations of geothermal fluids from Palinpinon, Ohaaki-Broadlands, Cerro Prieto and Salton Sea geothermal fields (Table 4.8). The Palinpinon samples and those from BR9 and BR20 represent the average of 2 samples, whereas the Salton Sea data is represented as a range of values. See Table 4.8 for the source of the data.

4.6. CHEMICAL MODELLING

4.6.1. Gold Transport and Deposition in the Epithermal Environment

Table 4.8 illustrates that relatively dilute chloride waters, such those from the Palinpinon, Ohaaki-Broadlands and Cerro Prieto geothermal fields, are not especially enriched with respect to gold (1-4 μg/kg Au). Concentrations of this magnitude are the expected average background levels for volcanic and plutonic rocks in areas of plate convergence (Crocket, 1993), but are 3-4 orders of magnitude lower than ore grade gold in epithermal and porphyry deposits in volcanic terranes. Therefore, an important point to be addressed is whether such concentrations are to be expected for epithermal ore-forming solutions. Crucial to this is the estimation of the dominant Au-bearing complexes and gold solubilities at Palinpinon reservoir conditions.

Using water and gas analyses from PN14 collected a month prior to the trace metal sampling exercise, along with the measured wellhead enthalpy and the sampling pressure, the chemistry of the deep reservoir fluid has been calculated (Table 4.9). Based on the wellhead enthalpy, the deep reservoir temperature is estimated to be 240°C. Comparing this temperature with those calculated using the silica geothermometers (Table 4.9, Fournier 1981) shows that no excess enthalpy is present. The reservoir fluid has a total sulphur concentration ($\sum S$) of 0.003 m and a pH of 5.5, calculated using the dissociation of H_2CO_3 (Henley et al., 1984) according to the reaction :

$$H_2CO_3 = HCO_3^- + H^+$$

These conditions are presented as functions of redox potential ($-R_H$), pH and temperature in Figures 4.10 and 4.11. The redox potential is defined as :

$$-R_H = -\log(f_{H_2}/f_{H_2O}) \qquad \text{(Giggenbach, 1997)}$$

where $f_{H_{2(g)}}$ and $f_{H_2O_{(g)}}$ represent the fugacities for $H_{2(g)}$ and $H_2O_{(g)}$ respectively, and increasing $-R_H$ values correspond to increasing potential for oxidation. Assuming the geothermal gases (Table 4.9) were dissolved in a single liquid phase and the existence of equilibrium conditions between water and rock, the redox potential of the deep reservoir can be calculated using the relation :

$$-R_H = -\log(X_{H_{2(aq)}} \cdot B_{H_2}) \qquad \text{(Giggenbach, 1997)}$$

where $X_{H_{2(aq)}}$ is the mole fraction of $H_{2(aq)}$ in the reservoir and B_{H_2} is the liquid-vapour distribution coefficient of $H_{2(g)}$ at the water-rock equilibration temperature (Giggenbach, 1980). The calculated $-R_H$ for the PN14 fluid is 3.42.

Table 4.9. The initial discharge composition of water and gas from well PN14 collected in Nov. 1997. Enthalpy is the measured enthalpy at the wellhead on the date of collection. Sampling P. is the sampling pressure in bars atmosphere (b.a.). The discharge water and gas chemistry, enthalpy and S.P. are used to derive the reservoir chemistry used in the thermodynamic calculations. The reservoir pH (pH_{res}) has been calculated for reservoir conditions using the dissociation of dissolved CO_2 (Henley et al., 1984). The reservoir temperature (T_{res}) is based on the measured wellhead enthalpy. The quartz adiabatic ($T_{qtz\text{-}adiab}$) and quartz conductive ($T_{qtz\text{-}cond}$) geothermometers (Fournier, 1981) were used to ascertain the degree, if any, of excess enthalpy. The redox potential ($-R_H$) has been calculated using the method described by Giggenbach (1997). See text for discussion.

Well : PN14		
Collection Date :	11/97	
Enthalpy :	1039 kJ/kg	
Sampling P .	7 b.a.	
	Water Discharge Chemistry (mg/kg)	**Derived Reservoir Chemistry**
Na	4917	4104.04
K	804	671.07
Ca	250	208.67
Mg	0.19	0.16
Cl	8581	7162.25
B	94	78.46
SO_4	16.0	13.35
HCO_3	14.56	792.19
SiO_2	700	584.26
H_2S	1.5	86.12
	Gas Discharge Chemistry (mmol/100mol)	
CO_2	193.00	
H_2S	15.07	
NH_3	2.66	
He	0 03	
H_2	0.31	
N_2	1.52	
CH_4	1.86	
pH (T=20°C)	7.1	-
pH_{res}	-	5 5
T_{res} (°C)	-	240
$T_{qtz\text{-}adiab}$ (°C)	-	250.8
$T_{qtz\text{-}cond}$ (°C)	-	267.0
$-R_H$	-	3.42
$\sum S$ (m)	-	0.003

The estimated composition of the deep PN14 reservoir fluid (Figures 4.10 and 4.11) falls within the stability fields of pyrite and K-feldspar stable with aqueous sulphur present as $H_2S_{(aq)}$. Neither anhydrite or calcite are stable under these conditions. The predominant gold-bearing complex is $Au(HS)_2^-$ with an estimated solubility of approximately 100 µg/kg Au (Figures 4.10 and 4.11). Under these conditions the reservoir fluid discharged at well PN14 (1-4 µg/kg Au) is undersaturated with respect to gold by two orders of magnitude. Effective processes for lowering gold solubility and promoting deposition may include boiling, fluid mixing, water-rock interactions and conductive cooling (Cooke et al., 1996; Cooke and Simmons, 2000; Cooke and McPhail, 2001).

Boiling has been shown to be an effective mechanism for gold deposition in hydrothermal systems (Drummond and Ohmoto, 1985; Spycher and Reed, 1989). It can be represented by the reaction :

$$Au(HS)_2^-{}_{(aq)} + H^+_{(aq)} + 0.5H_{2(aq)} = Au_{(s)} + 2H_2S_{(aq)} \quad (1)$$

where loss of $H_2S_{(aq)}$ to the vapour phase will cause gold precipitation. This reaction shows that increasing $Au(HS)_2^-$ and H_2 or decreasing pH and total sulphur concentrations will also result in gold precipitation.

Fluid mixing in the epithermal environment is another mechanism proposed for gold deposition (Hayba et al., 1985; Plumlee, 1994; Corbett and Leach, 1998). The shape of the gold solubility contours in Figures 4.10 and 4.11 illustrates that an increase of the oxidation potential can lower the gold solubility dramatically and promote gold deposition from a near-neutral low salinity water. Mixing with an oxygenated and/or sulphate predominant water will increase the oxidation potential and cause the chemical breakdown of the gold-bisulphide complex, represented by a shift to the right side of the following reaction :

$$Au(HS)_2^-{}_{(aq)} + 8H_2O_{(aq)} = Au_{(s)} + 2SO_4^{2-}{}_{(aq)} + 7.5H_{2(g)} + 3H^+_{(aq)} \quad (2)$$

Gold deposition through water-rock interactions can occur by the reaction of the gold-bisulphide complex with iron from the host rock (Hofstra et al., 1991; Cooke and McPhail, 2001) causing the deposition of gold and pyrite, according to the reaction :

$$Au(HS)_2^-{}_{(aq)} + (FeO)_{(s)} + H^+_{(aq)} = Au_{(s)} + FeS_{2(s)} + H_2O_{(aq)} + 0.5H_{2(aq)} \quad (3)$$

Conductive cooling of a hydrothermal solution results in a pH decrease due to acid dissociation (e.g. $H_2S_{(aq)}$, $H_2CO_{3(aq)}$, $HSO_4^-{}_{(aq)}$, $HCl_{(aq)}$) with falling temperature (Spycher and Reed, 1989). According to reaction 1, for a sulphide-rich hydrothermal fluid, a pH decrease may cause gold precipitation. A progressive increase in acidity will ultimately cause a switch over to $AuHS_{(aq)}$ predominance, which would result in the cessation of Au deposition (Figure 4.10).

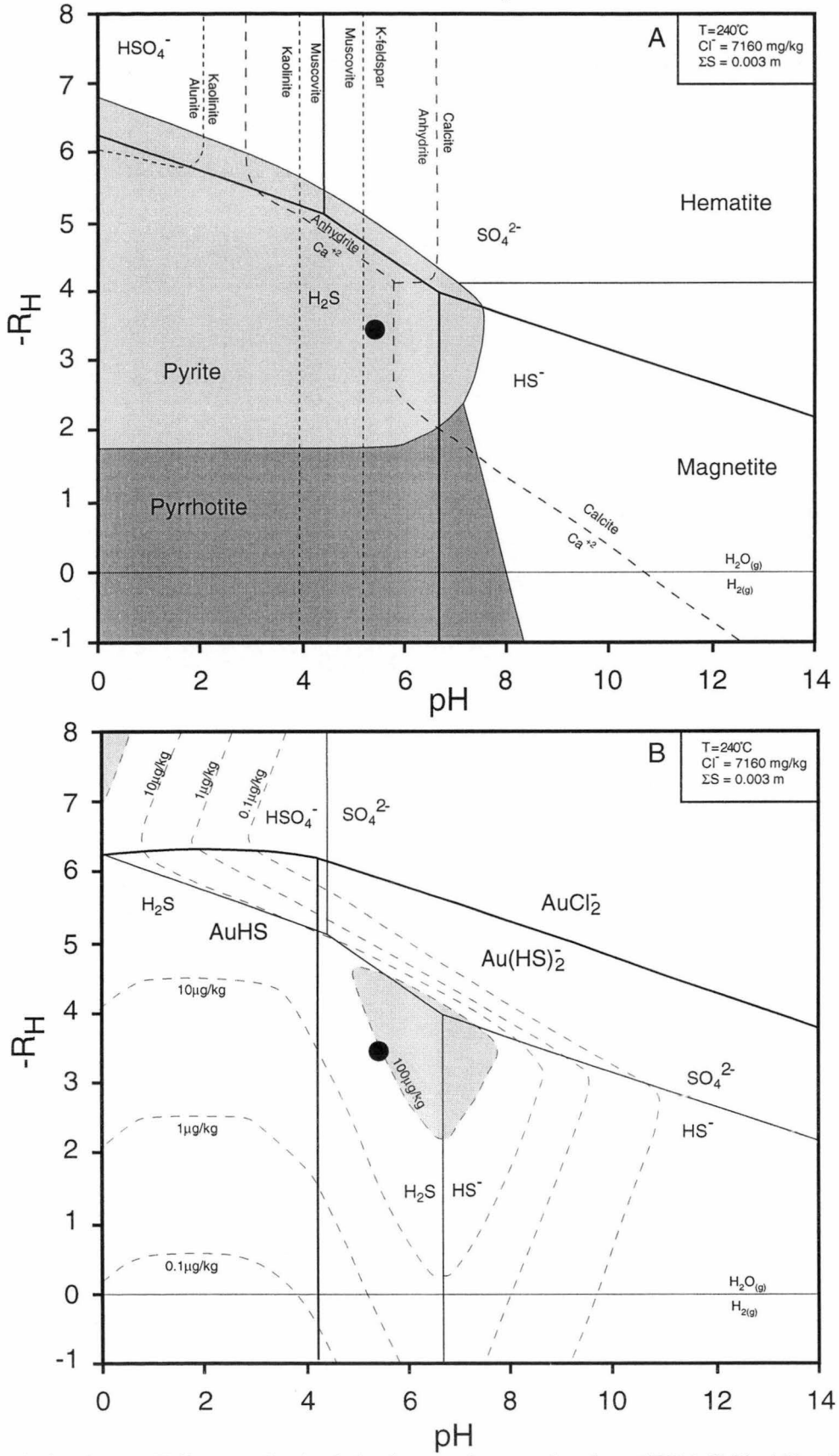

Figure 4.10. $-R_H$ vs pH diagrams for the derived reservoir water chemistry (PN14; Table 4.9), which has 7160 mg/kg Cl^- and a total sulphur (ΣS) concentration of 0.003 *m* at 240°C. A. The stability fields of Fe-oxides, sulphides, K-feldspar, muscovite, kaolinite, alunite, anhydrite and calcite, and aqueous sulphur-bearing species. B. Gold solubility contours and fields of aqueous gold and sulphur-bearing species. The shaded area in B highlights conditions of gold solubility greater than 100 µg/kg. The estimated composition of the Palinpinon reservoir water is marked by the black circle in both diagrams. Species distributions havve been calculated using a Newton-Raphson iteration. $\Sigma C = 0.0132$ *m*; $a_{K+} = 0.0092$; $a_{Ca2+} = 0.0008$.

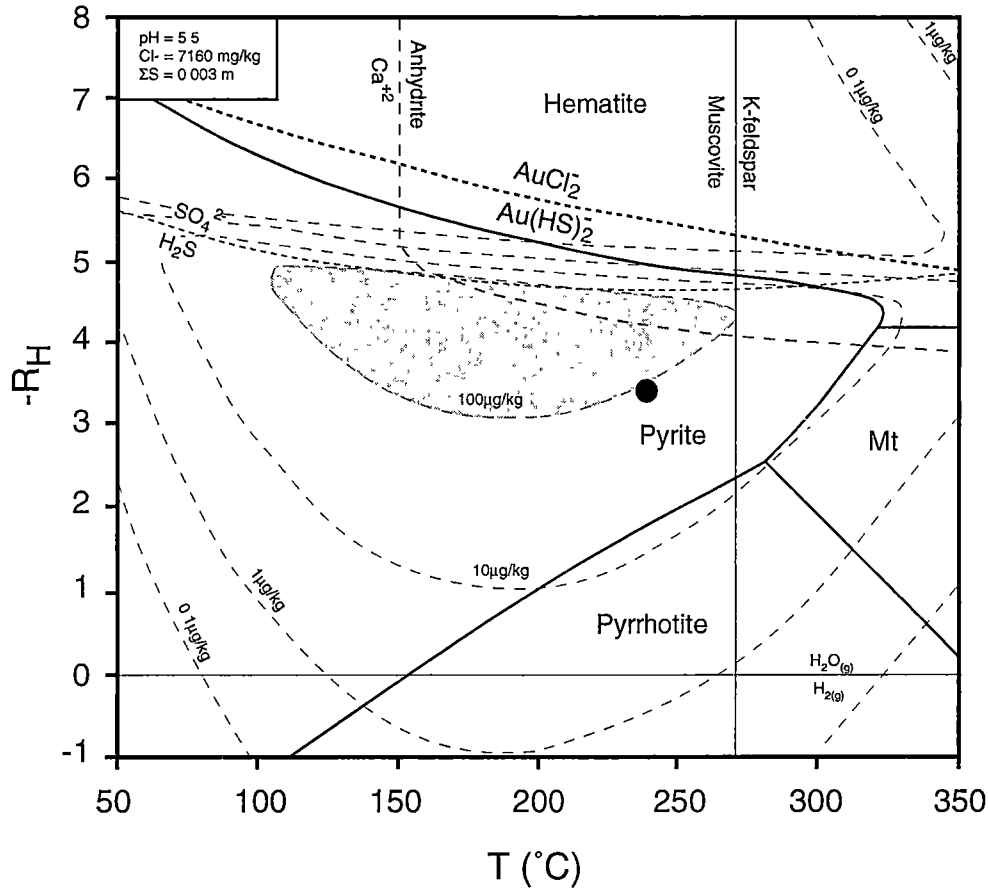

Figure 4.11. $-R_H$ vs temperature diagram for the derived reservoir water chemistry (PN14; Table 4.9), which has 7160 mg/kg Cl^- and a total sulphur (ΣS) concentration of 0.003 *m* at 240°C. Gold solubility contours, stability fields of Fe-oxides, sulphides, K-feldspar, muscovite and anhydrite, and the fields of aqueous gold and sulphur-bearing species. The shaded area highlights conditions of gold solubility greater than 100 µg/kg. The estimated composition of the Palinpinon reservoir water is marked by the back circle. Species distributions have been calculated using a Newton-Raphson iteration. ΣC = 0.0132 *m*; $a_{K+} = 0.0092$; $a_{Ca2+} = 0.0008$.

4.6.2. Reaction Path Simulations

Numerical reaction path modelling of the Palinpinon geothermal water has been attempted to simulate mineral deposition in the geothermal wells. Depositional processes that have been modelled are boiling, conductive cooling, heating and mixing. Modelling of water-rock interactions has not been attempted. The computer program SOLVEQ (Reed, 1982) has been used to calculate the distribution and concentration of mineral, aqueous and gaseous species. Thermodynamic data are from the SOLTHERM database (Spycher and Reed, 1989) with additional and more recent data from SUPCRT92 (Johnson et al., 1992). The program CHILLER (Reed, 1982), models the depositional mechanisms by calculating the variation in species concentrations during changes to the physicochemical environment. Methods used are similar to those described by Reed and Spycher (1985), Spycher and Reed (1989), Simmons and Browne (2000) and Cooke and McPhail (2001)

The initial fluid composition used in the modelling is based on the derived PN14 reservoir chemistry (Table 4.9) at a temperature of 240°C. However, the chemistry has been modified (Table 4.10) by assuming saturation with respect to quartz, muscovite and anhydrite. These are three common hydrothermal minerals occurring in the altered reservoir host-rocks. Based on this modified chemistry, the estimated reservoir pH of 5.2 (Table 4.10) is slightly lower than the previous estimate (pHres=5.5; Table 4.9).

During the reactions, the minerals were assumed to behave under open system conditions. That is, after they have deposited there is no back reaction with, and dissolution into, the aqueous solution. As part of this study, 38 reaction path simulations were used to test the sensitivity to initial fluid composition. Amongst these, the only variability in predicted mineralogies was the sequence and the amounts of minerals precipitated.

Boiling

The results of two boiling simulations are described here. In both, the initial fluid (Table 4.10) is boiled continuously from 240° to 100°C in 5°C increments, and the minerals removed (or fractionated) from solution as they precipitate. Under the conditions of the first simulation (closed system boiling), the gases are kept in contact and in equilibrium with the aqueous solution. This reaction path is the closest simulation to conditions of fluid (i.e., liquid and gas) ascent in a geothermal well (Simmons and Browne, 2000). The second calculation simulates open system boiling conditions, where the gases are fractionated from the aqueous solution at each reaction increment. The removal of gases from a boiling solution may play an important role in the formation of high-grade ore zones in near vertical conduits, such as faults and zones of dilation (Spycher and Reed, 1989; Cooke and McPhail, 2001).

Table 4.10. Fluid compositions used in reaction path modelling simulations.

		Mixing Waters			
	[1]Initial reservoir fluid	[2]Mixed acid sulphate chloride	[3]Acid sulphate (mg/kg)	[4]Neutral bicarbonate	[5]Neutral meteoric
pH (T=20°C)	5.19*	3.62	3.62	6.76	7.6
H^+	23.68	2.83	3.08	0.91	0.15
Cl^-	7,161.51	2,605 80	8.36	234 27	1.20
SO_4^{2-}	98.46	606.41	1,204.56	89.10	115.23
HCO_3^-	1,332.61	142.84	142.54	304.35	39 01
HS^-	63.49	0.47	0.47	0.68	-4.19†
SiO_2	33,557.08	637.49	636.29	141.20	47.01
Al^{3+}	0.0340	0.0	0.0	0.0	0.0
Ca^{2+}	208.66	23.03	22.99	60.08	45.01
Mg^{2+}	0.1600	7.63	7.62	5.96	4.50
Fe^{2+}	0.0012	0.0	0.0	0.0	0.0
K^+	670.93	259.46	258.95	40.74	2.00
Na^+	4,056.26	1,776.19	372.66	184.77	3.08
Zn^{2+}	0.0912	0.0	0.0	0.0	0.0
Cu^+	0.0092	0.0	0.0	0.0	0.0
Pb^{2+}	0.0142	0.0	0.0	0.0	0.0
Ag^+	0.0261	0.0	0.0	0.0	0.0
$AuCl_2^-$	0.0054	0.0	0.0	0.0	0.0
NH_4^+	4.69	0.0	0.0	0.0	0.0
H_3BO_3	448.78	0.0	0.0	0.0	0.0

* The pH for the initial reservoir fluid is at the estimated reservoir temperature of 240°C.

† A negative value for the sulphide component is the result of the choice of component species (SO_4^{2-} and HS^-) and relates to the abundance of sulphate relative to sulphide species in this oxidised water. See comment 5 below.

Comments :

1 The initial reservoir fluid is the same as the derived reservoir fluid presented in Table 4.9 However, the chemistry has been modified by assuming saturation with respect to quartz, muscovite and anhydrite. This results in the slightly lower estimated reservoir pH. The initial reservoir temperature used in all simulations is 240°C (see Table 4.9).

2 An acidic, mixed sulphate-chloride water collected from well NJ2D (sampling date 2/12/82; Seastres, 1985). The initial discharge analysis of this sample is presented in Table 4.1. For the fluid modelling simulations, the chemistry has been recalculated to reservoir conditions.

3 To simulate a hypothetical acid sulphate water, the mixed sulphate-chloride water has been modified by increasing the sulphate and decreasing the chloride components.

4 An analysis of a neutral bicarbonate spring water from an unpublished PNOC-EDC data file. Collected 30/04/96 from spring "Palinpinon 2" in the Okoy Valley.

5 An analysis of meteoric water collected from the Okoy River, 1975 (Table 4.1; Glover, 1975). Sulphide was not originally analysed for (Table 4.1), so to determine the SO42- : HS- ratio the water composition has been modified by assuming saturation with respect to atmospheric oxygen.

Closed System Boiling (Mineral Fractionation)

In this simulation, the predicted gangue mineralogy consists of quartz, K-feldspar and muscovite. Upon cooling from 240° to 195°C and reaching a pH of 5.9, K-feldspar is predicted to precipitate in place of muscovite deposition (Figure 4.12a).

The base metal sulphide mineralogy consists of sphalerite, galena and the copper minerals bornite, chalcocite, ± chalcopyrite (Figure 4.12b). Acanthite precipitates throughout the simulation, whereas gold and silver precipitate in equal amounts from 215° to 100°C. Closed system boiling predicts an efficient deposition of metallic minerals (Figure 4.12c). Adiabatic cooling from 240° to 220°C deposits over 70% of the available Zn and Pb as sphalerite and galena, respectively, and up to 60% of the total Cu and Ag in solution as bornite and acanthite, respectively (Figure 4.12c). Also, once gold precipitation is predicted to commence at 215°C, up to 80% of the available gold in solution is deposited within 20°C of boiling-induced cooling (Figure 4.12c).

The pH is predicted to increase from 5.2 to 6.6 (Figure 4.12d). Any pH increase due to boiling is caused by loss of $H^+_{(aq)}$ from solution during gas separation, of $H_2S_{(aq)}$ and $CO_{2(aq)}$.

Open System Boiling (Mineral and Gas Fractionation)

The gangue mineralogy predicted during open system boiling has a similar deposition sequence to the closed system simulation, with the addition of chlorite (clinochlore-chamosite), tremolite-actinolite and hematite precipitation (Figure 4.13a).

The base and precious metal mineralogy is the same as the closed boiling simulation (Figure 4.13b). However, all of the metallic minerals are predicted to deposit above 185°C and do so more efficiently than the closed system boiling simulation. Up to 70% of all the base and precious metals in solution are predicted to have deposited as sphalerite, galena, bornite, acanthite and gold, before cooling to 220°C occurs (Figure 4.13c).

The pH increase in this simulation (5.2 to 6.8) is greater than in the previous simulation and increases from 5.2 to 6.3 within the first 25°C of adiabatic cooling (Figure 4.13d). This difference is attributed to a rapid loss of gas under open boiling conditions (Spycher and Reed, 1989).

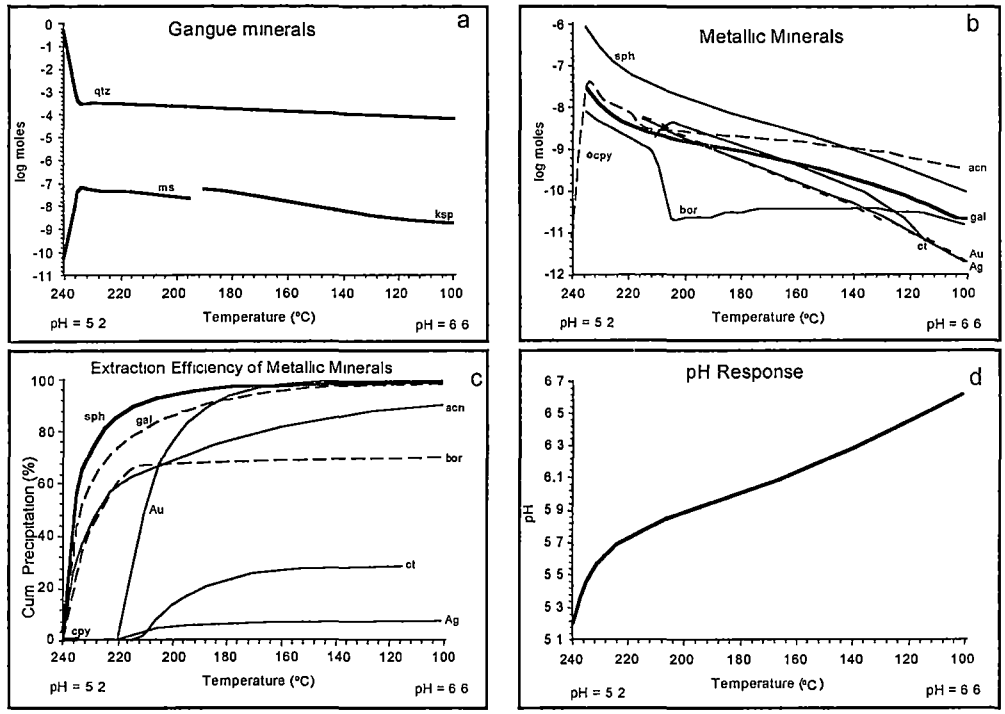

Figure 4.12. Results of the numerical simulation of closed system boiling of Palinpinon reservoir water (Table 4.10) from 240° to 100°C, in 5°C increments. A. Predicted sequence of gangue mineral precipitation. B. Predicted sequence of metallic mineral precipitation. C. Cumulative precipitation (%) of total aqueous Zn (as sphalerite), Pb (as galena), Ag (as acanthite and silver), Au (as gold) and Cu (as bornite, chalcopyrite and chalcocite). D. The predicted pH response during the simulation. Mineral abbreviations used in this and subsequent figure captions: acn = acanthite, act = actinolite, Ag = silver, anh = anhydrite, Au = gold, bor = bornite, cc = calcite, chm = Fe-rich chlorite (chamosite), clc = Mg-rich chlorite (clinochlore), cov = covellite, cpy = chalcopyrite, ct = chalcocite, dol = dolomite, gal = galena, hem = hematite, kao = kaolinite, ksp = K-feldspar, ms = muscovite, py = pyrite, qtz = quartz, sph = sphalerite, tlc = talc, trm = tremolite.

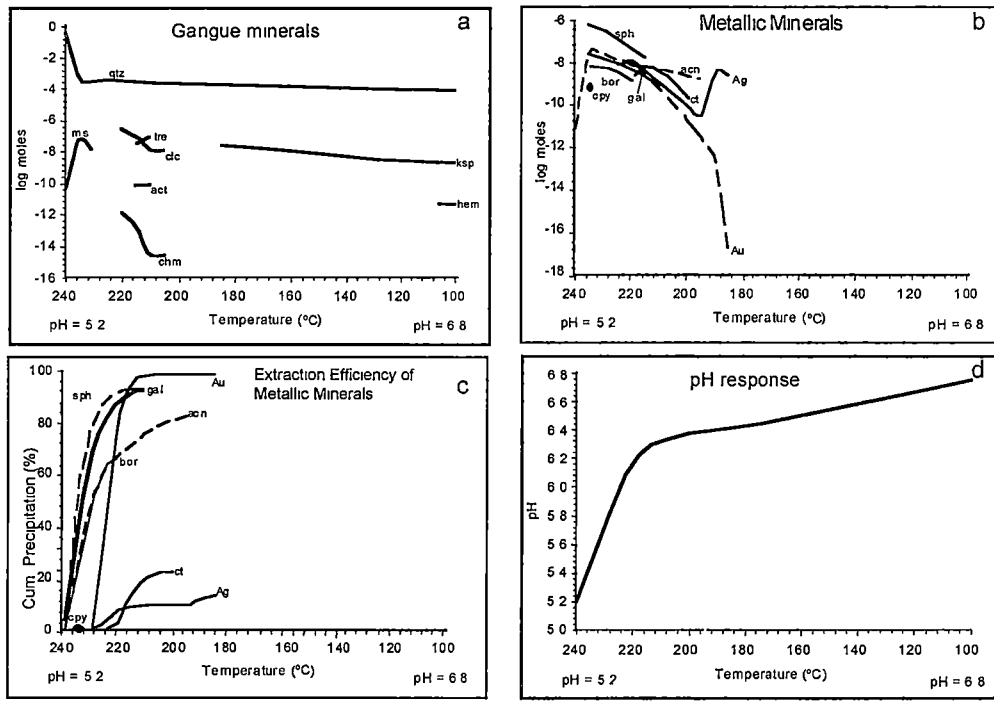

Figure 4.13. Results of the numerical simulation of open system boiling of Palinpinon initial reservoir water (Table 4.10) from 240° to 100°C, in 5°C increments. Gases were fractionated out of the system in 0.001°C boiling increments. A. Predicted sequence of gangue mineral precipitation. B. Predicted sequence of metallic mineral precipitation. C. Cumulative precipitation (%) of total aqueous Zn (as sphalerite), Pb (as galena), Ag (as acanthite and silver), Au (as gold) and Cu (as bornite, chalcopyrite and chalcocite). D. The predicted pH response during the simulation.

Conductive Cooling

During the conductive cooling simulation, the initial fluid (Table 4.10) was cooled from 240° to 100°C in 5°C increments. To prevent boiling, a constant pressure of 250°bars is maintained. Quartz and muscovite precipitate from 240° to 140°C, with kaolinite replacing muscovite at temperatures below 135°C and a pH of less than 4.4 (Figure 4.14a).

Sulphide minerals predicted to precipitate during this simulation are pyrite, sphalerite, bornite, acanthite, covellite and galena (Figure 4.14b). When compared to the boiling simulations, the metals are extracted less efficiently from solution (Figure 4.14c). Sphalerite is predicted to precipitate most efficiently, but it takes 70°C of cooling for deposition of approximately 80% of the available Zn.

In contrast to the boiling simulations, conductive cooling causes the pH to decrease from 5.2 to 4.3 (Figure 4.14d). This is because decreasing temperatures without associated gas loss causes acids to dissociate (e.g. $HCl_{(aq)}$, $H_2S_{(aq)}$; Reed and Spycher, 1985; Spycher and Reed, 1989; Cooke and McPhail, 2001).

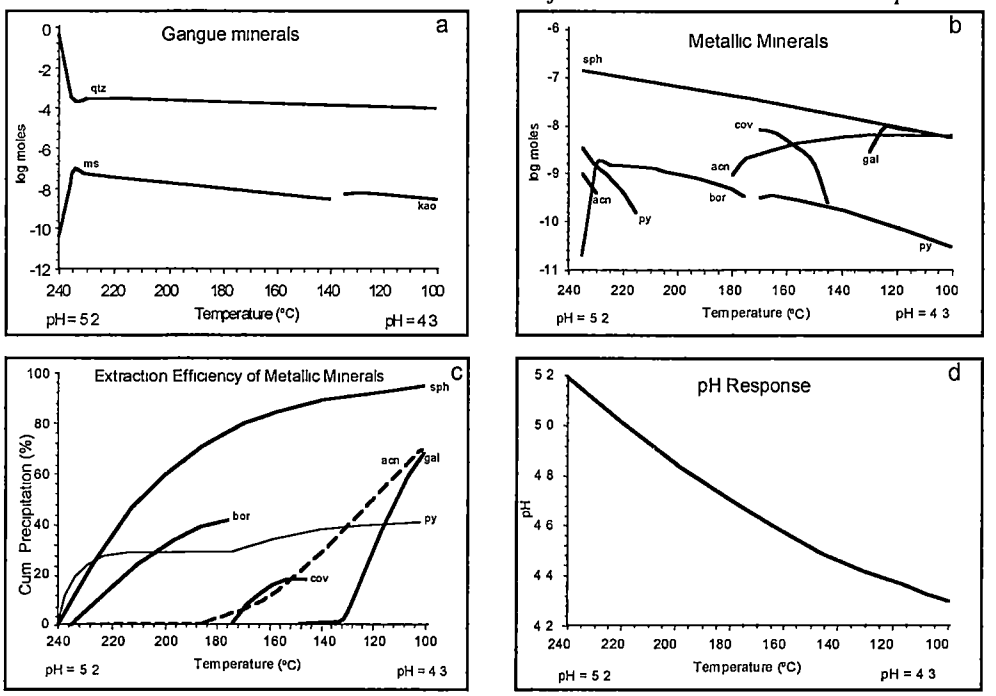

Figure 4.14. Results of the conductive cooling simulation of the Palinpinon reservoir water (Table 4.10). The water was cooled from 240° to 100°C in 5°C increments. To prevent boiling, a constant pressure of 250 bars was maintained. A. Predicted sequence of gangue mineral precipitation. B. Predicted sequence of metallic mineral precipitation. C. Cumulative precipitation (%) of total aqueous Zn (as sphalerite), Pb (as galena), Ag (as acanthite), Fe (as pyrite) and Cu (as bornite and covellite). D. The predicted pH response during the simulation.

Fluid Mixing

To test the effectiveness of fluid mixing as a mechanism for mineral deposition, four fluid mixing reaction paths have been modelled. The composition of the four mixing waters are presented in Table 4.10. With each simulation, 50 g increments of mixing water are titrated into 1 kg of non-boiling 240°C initial reservoir fluid (Table 4.10).

Mixed Acid Sulphate-Chloride and Acid Sulphate Waters

Mixing 60°C acidic, sulphate-chloride water with a 240°C reservoir fluid is predicted to produce quartz and muscovite, with minor anhydrite at 230°C (Figure 4.15a). The main sulphide minerals are sphalerite, bornite and covellite. Small amounts of pyrite are deposited early in the simulation. Acanthite, galena, silver and gold precipitate only at low temperatures (< 130°C; Figure 4.15b).

The mixing simulation involving a hypothetical acid sulphate water results in the same mineral deposition sequence (Figure 4.16). The major differences are, anhydrite precipitates over a larger temperature interval (230°-200°C), and pyrite over a smaller interval (230°C). This is attributed to the higher sulphate concentrations in the acid sulphate water.

Both these mixing simulations have similar efficiencies of metal extraction from solution (Figures 4.15c and 4.16c). However, by the time the mixed solutions have cooled to 100°C, none of the metals are predicted to have been completely extracted from solution. For both simulations, sphalerite is predicted to be the most efficiently precipitated metallic mineral, with over 75% of the available Zn taken out of solution upon cooling to 150°C (Figures 4.15c and 4.16c).

During both of these mixing simulations, the pH decreases from 5.2 to 4.0 and 3.9, respectively (Figures 4.15d and 4.16d).

Bicarbonate Water

Mixing a 60°C neutral bicarbonate water with the reservoir water results in the precipitation of quartz, muscovite and chlorite (Figure 4.17a). Muscovite deposition stops between 205° and 150°C, while chlorite precipitates between 175° and 150°C. Sphalerite and pyrite precipitate throughout the simulation, with galena and acanthite depositing at temperatures less than 145°C (Figure 4.17b).

Pyrite and sphalerite are the metallic minerals predicted to precipitate most efficiently. Over 70% of the available Zn has precipitated from the hybrid solution within the first 40°C of cooling (Figure 4.17c). Other metals, Pb and Ag are efficiently extracted from solution as galena and acanthite, respectively, but only do so once the solution has cooled to less than 150°C (Figure 4.17c). The pH increases from 5.2 to 6.0 (Figure 4.17d).

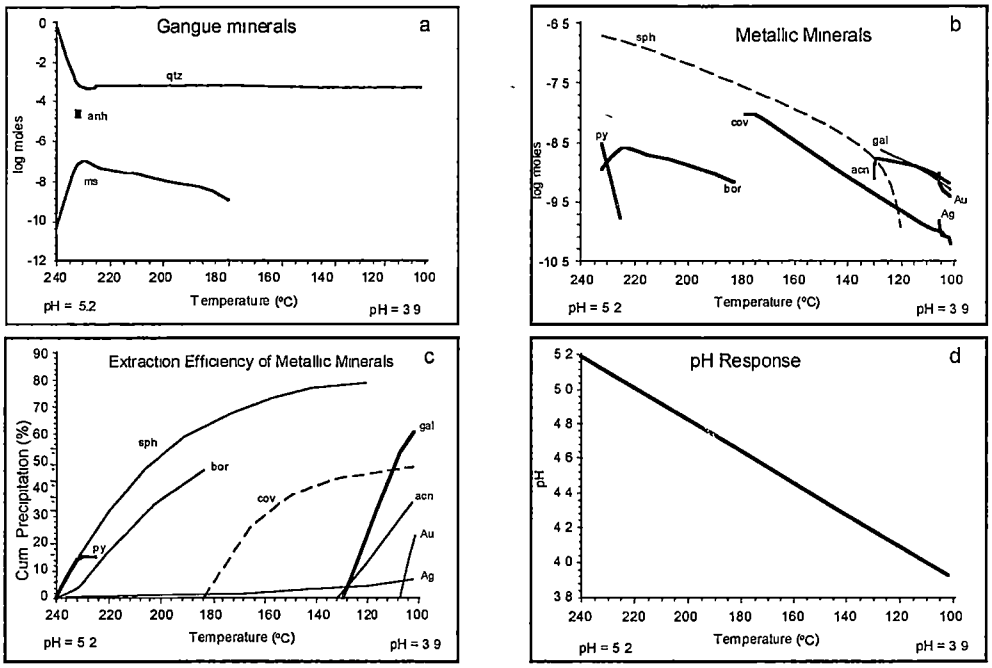

Figure 4.15. Results of the numerical simulation of mixing a non-boiling 240°C reservoir water (Table 4.10) with 60°C acid sulphate-chloride water (Table 4.10). During the simulation, 50 g increments of mixing water were titrated into 1 kg of reservoir water until the hybrid water had cooled to 100°C. A. Predicted sequence of gangue mineral precipitation. B. Predicted sequence of metallic mineral precipitation. C. Cumulative precipitation (%) of total aqueous Zn (as sphalerite), Pb (as galena), Ag (as acanthite and silver), Au (as gold), Fe (as pyrite) and Cu (as bornite and covellite). D. The predicted pH response during the simulation.

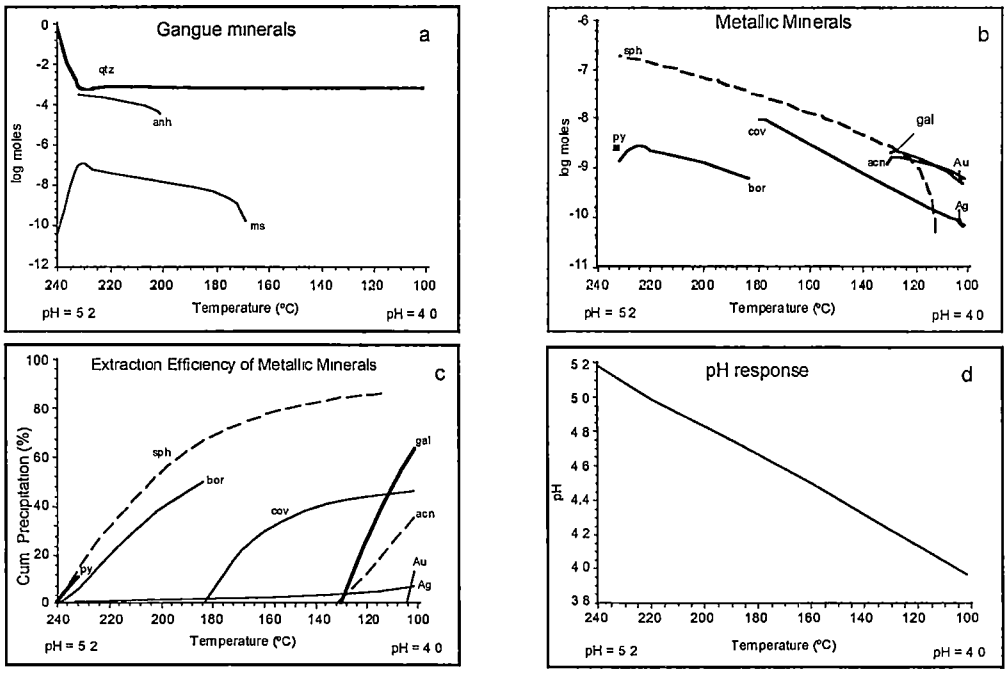

Figure 4.16. Results of the numerical simulation of mixing of non-boiling 240°C reservoir water (Table 4.10) with 60°C acid sulphate water (Table 4.10). During the simulation 50 g increments of mixing water were titrated into 1 kg of reservoir water until the hybrid water had cooled to 100°C. A. Predicted sequence of gangue mineral precipitation. B. Predicted sequence of metallic mineral precipitation. C. Cumulative precipitation (%) of total aqueous Zn (as sphalerite), Pb (as galena), Ag (as acanthite and silver), Au (as gold), Fe (as pyrite) and Cu (as bornite and covellite). D. The predicted pH response during the simulation.

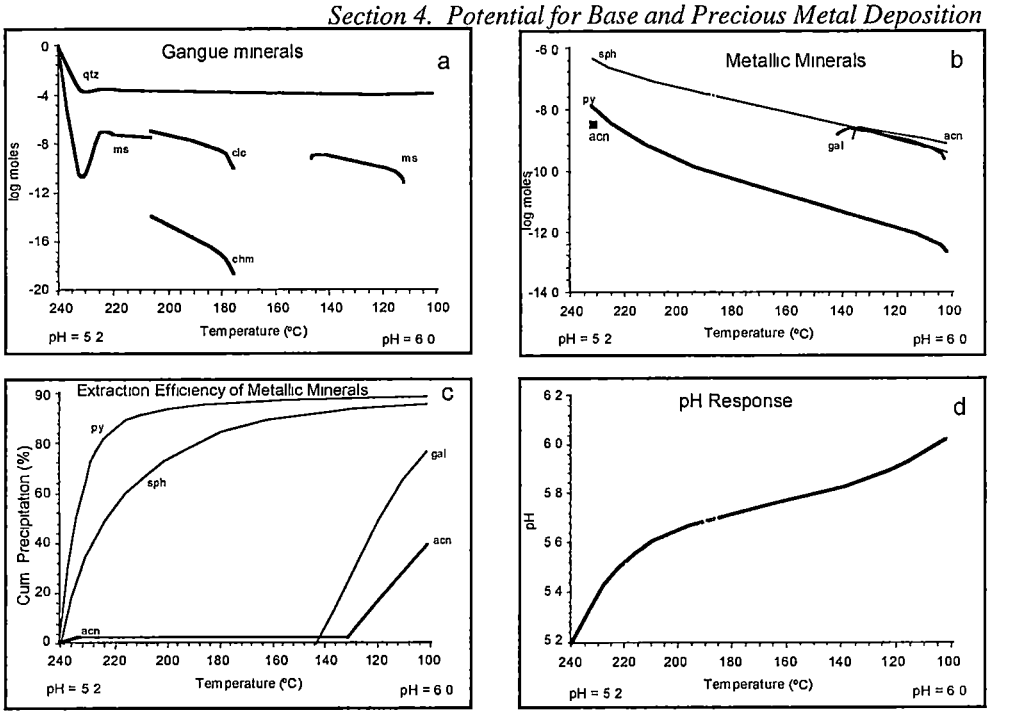

Figure 4.17. Results of mixing a non-boiling 240°C Palinpinon reservoir water (Table 4.10) with a 60°C neutral bicarbonate water (Table 4.10). During the simulation 50 g increments of mixing water were titrated into 1 kg of initial reservoir water until the hybrid water had cooled to 100°C. A. Predicted sequence of gangue mineral precipitation. B. Predicted sequence of metallic mineral precipitation. C. Cumulative precipitation (%) of total aqueous Zn (as sphalerite), Pb (as galena), Ag (as acanthite) and Fe (as pyrite) and Cu (as bornite and covellite). D. The predicted pH response during the simulation.

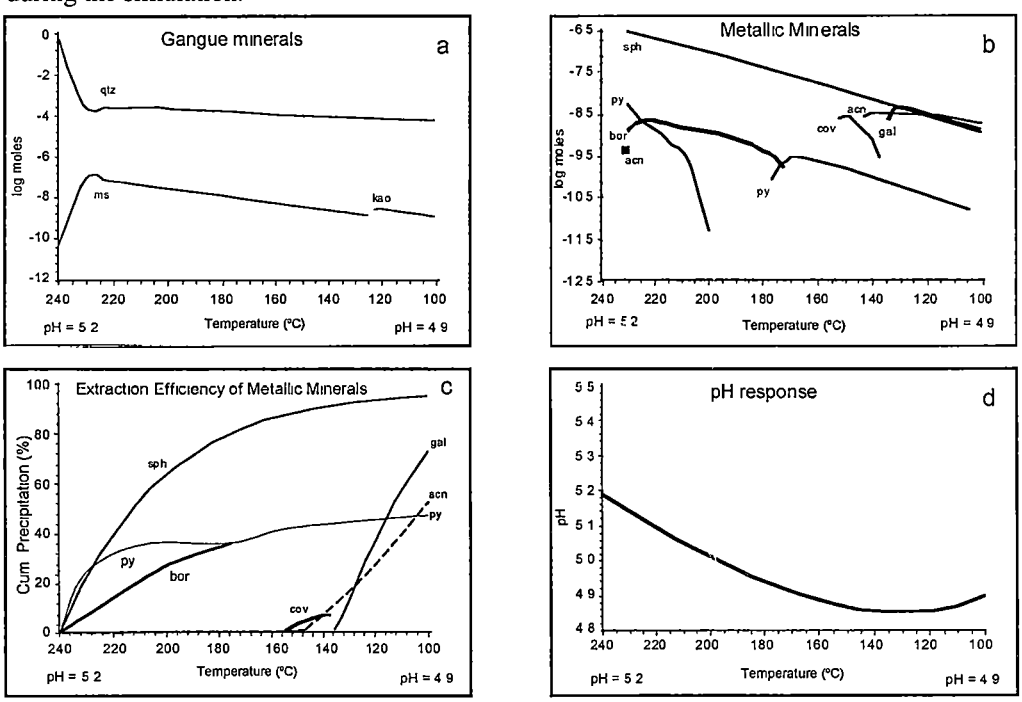

Figure 4.18. Results of mixing a non-boiling 240°C Palinpinon reservoir water (Table 4.10) with a 24°C neutral meteoric water (Table 4.10). During the simulation 50 g increments of mixing water were titrated into 1 kg of reservoir water until the hybrid water had cooled to 100°C. A. Predicted sequence of gangue mineral precipitation. B. Predicted sequence of metallic mineral precipitation. C. Cumulative precipitation (%) of total aqueous Zn (as sphalerite), Pb (as galena), Ag (as acanthite) and Fe (as pyrite) and Cu (as bornite and covellite). D. The predicted pH response during the simulation.

Meteoric Water

Mixing 24°C Okoy River water with the 240°C reservoir fluid results in the deposition of quartz, muscovite and kaolinite (Figure 4.18a). Kaolinite deposition only occurs at temperatures less than 125°C. Sulphide minerals deposited during this simulation are sphalerite, pyrite, bornite, acanthite, covellite and galena (Figure 4.18b). Sphalerite is most efficiently precipitated. Over 80% of the available Zn is predicted to precipitate once the hybrid solution has cooled to 170°C (Figure 4.18c). The pH is predicted to decrease only slightly, from 5.2 to 4.9, and increases at the end of the simulation (Figure 4.18d).

Closed and Open System Boiling, Followed by Fluid Mixing With Acid Sulphate Water

These simulations involve boiling the reservoir fluid continuously from 240° to 200°C, until all gases have separated into the vapour phase. The residual liquid is then mixed with acid sulphate water (Table 4.10). During the first simulation, boiling is under closed system conditions, whereas the second simulation assumes open system boiling. In both simulations, gases separate from the aqueous solution prior to the commencement of mixing.

In the closed system simulation of boiling followed by mixing, quartz and muscovite precipitate from the boiling liquid between 240° and 200°C. At the very last stages of boiling, at a temperature of 200°C, anhydrite precipitates with quartz (Figure 4.19a). During the mixing phase of the simulation, quartz is the only gangue mineral to deposit (Figure 4.19a). Gold, silver and most sulphide minerals (sphalerite, acanthite, chalcopyrite, bornite, galena, chalcocite) are predicted to precipitate during boiling. The most efficiently precipitated metallic minerals are sphalerite, galena, bornite, gold, and acanthite (Figure 4.19d). Covellite is the only sulphide mineral to precipitate during mixing, and does so at temperatures less than 155°C (Figure 4.19b).

In the open system boiling-mixing simulation, a more complex gangue mineralogy is predicted to precipitate. During the boiling phase (240°-200°C), quartz, muscovite, chlorite (clinochlore-chamosite), tremolite-actinolite ±K-feldspar are predicted to precipitate (Figure 4.20a). Quartz is the only mineral predicted to precipitate during the mixing simulation. The same metallic minerals that precipitated during the closed system simulation, are predicted to deposit during the open simulation. The difference between the two is that metallic minerals are predicted to precipitate more efficiently in the open simulation (Figure 4.20c). For example, over 80% of the available Zn, Pb and Au is predicted to deposit as sphalerite, galena and gold respectively within the first 20°C of adiabatic cooling (Figure 4.20c). Also, during the mixing phase, chalcocite precipitates before covellite (Figure 4.20b)

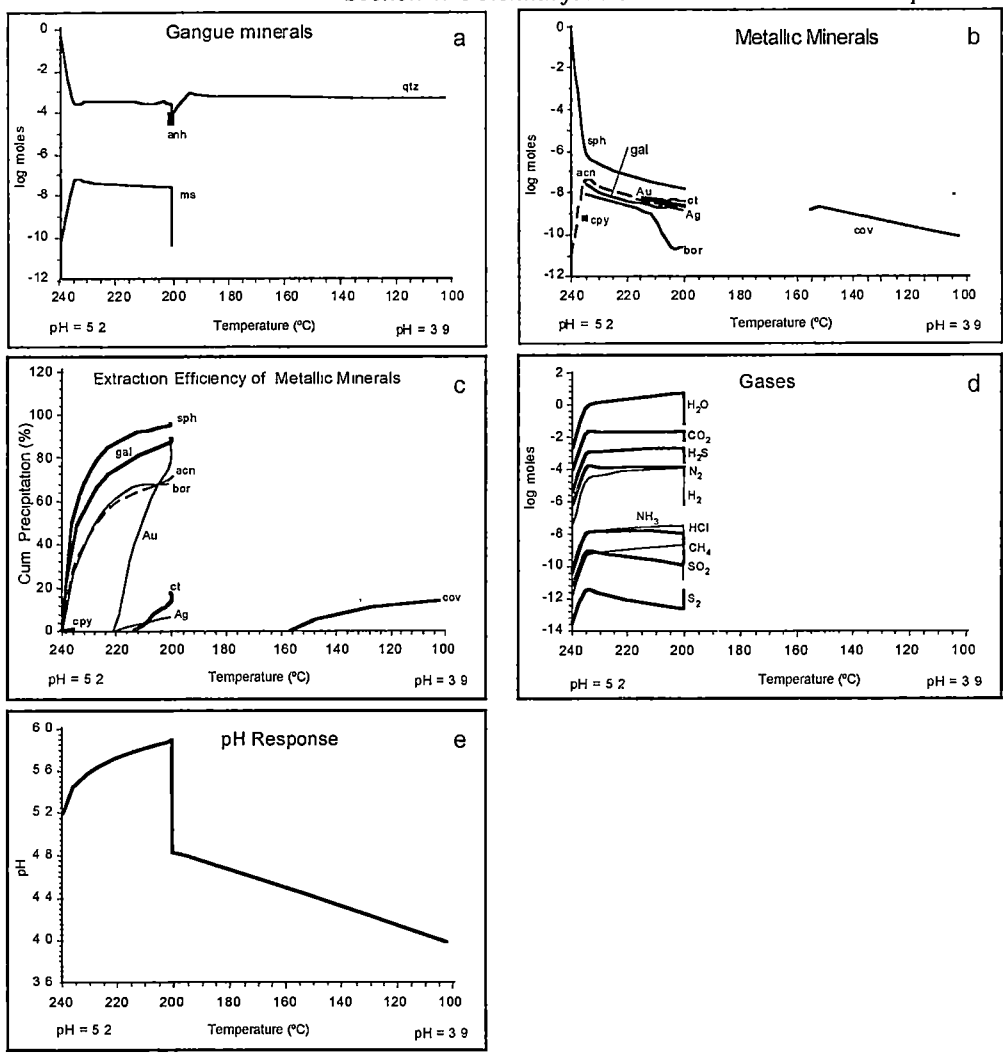

Figure 4.19. Simulation of closed system continuous boiling of the Palinpinon reservoir water (Table 4.10) from 240° to 200°C. This was followed by mixing with 60°C acid sulphate water (Table 4.10). During the mixing simulation, 50 g increments of mixing water were titrated into 1 kg of residual reservoir water until the hybrid water had cooled to 100°C. A. Predicted sequence of gangue mineral precipitation. B. Predicted sequence of metallic mineral precipitation. C. Cumulative precipitation (%) of total aqueous Zn (as sphalerite), Pb (as galena), Ag (as acanthite and silver), Au (as gold) and Cu (as bornite, chalcopyrite, chalcocite and covellite). D. Predicted sequence of gas fractionation during the boiling simulation. E. The predicted pH response during the simulation.

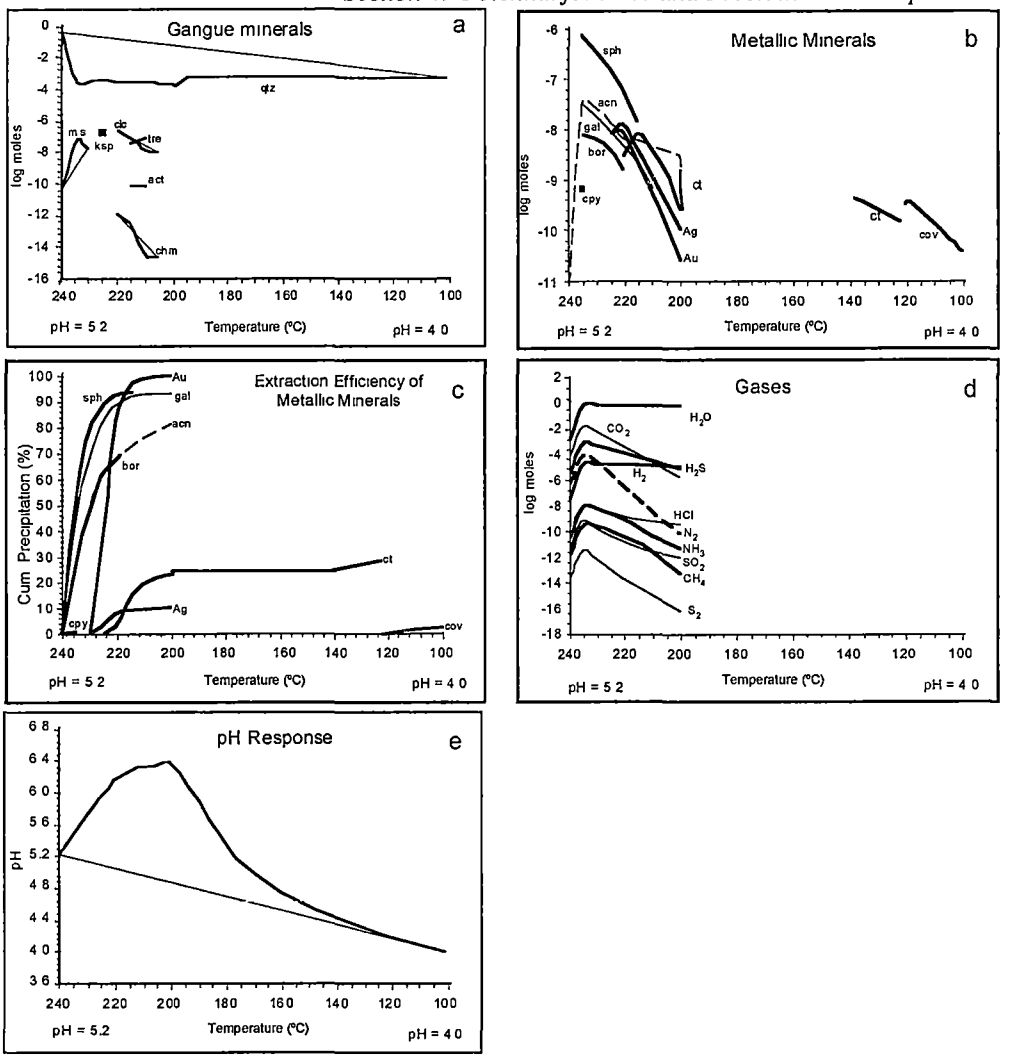

Figure 4.20. Results of the numerical simulation of open system continuous boiling of the Palinpinon reservoir water (Table 4.10) from 240° to 200°C. This was followed by mixing with 60°C acid sulphate water (Table 4.10). During the mixing simulation, 50 g increments of mixing water were titrated into 1 kg of residual reservoir water until the hybrid water had cooled to 100°C. A. Predicted sequence of gangue mineral precipitation. B. Predicted sequence of metallic mineral precipitation. C. Cumulative precipitation (%) of total aqueous Zn (as sphalerite), Pb (as galena), Ag (as acanthite and silver), Au (as gold) and Cu (as bornite, chalcopyrite, chalcocite and covellite). D. Predicted sequence of gas fractionation during the boiling simulation. E. The predicted pH response during the simulation.

Heating

As part of the reaction path modelling exercise, simulation of the peripheral water behaviour during heating was attempted. Waters chosen for this exercise were the acid sulphate water and the bicarbonate waters (Table 4.10). Both were heated from 60°C to 240°C, in 5°C increments, but only the results of the bicarbonate simulation are presented (Figures 4.21a and 4.21b). During the acid sulphate heating simulation, quartz was predicted to precipitate throughout the simulation (because quartz was supersaturated in the initial water) and anhydrite deposited between 220° and 240°C. The pH was predicted to increase from 3.6 to 5.2.

Heating of the bicarbonate water is predicted to cause precipitation of quartz (due to supersaturation), dolomite and calcite above 90°C (Figure 4.21a). At the final temperature of 240°C, the only minerals predicted to precipitate are calcite and tremolite. Talc deposited between 150° and 170°C prior to the initiation of tremolite precipitation. Metallic minerals did not deposit at any stage of the heating simulation. Upon heating there is a pH decrease (6.8 to 6.5) until the temperature reaches 150°C, then the pH increases to 6.9 at 240°C (Figure 4.21b).

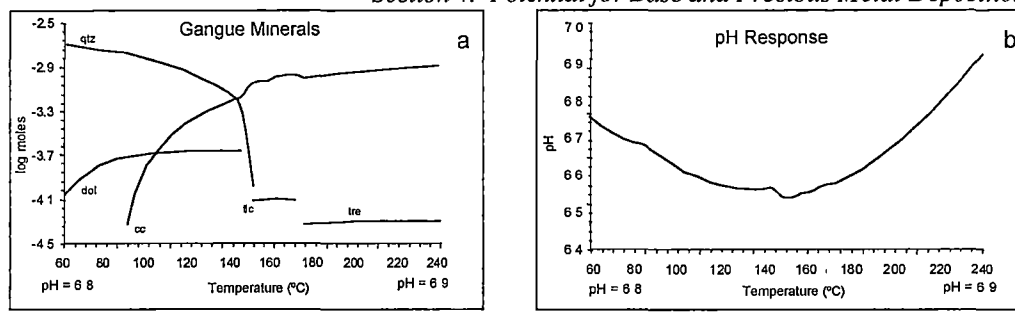

Figure 4.21. Results of heating the neutral bicarbonate water (Table 4.11) from 60° to 240°C in 5°C increments. To prevent boiling, a constant pressure of 250 bars was maintained. A. Predicted sequence of gangue mineral precipitation. B. The predicted pH response during the simulation. During this simulation, the tremolite-actinolite solid solution was turned off and hence, only tremolite is predicted to precipitate.

4.6.3. Discussion and Summary of Reaction Path Modelling

The results of the ten reaction path modelling simulations are summarised in Table 4.11 and also compared with the minerals seen in well scales. Seven involve boiling, mixing and cooling the initial reservoir fluid. Mixing end-members are acid sulphate-chloride, acid sulphate, neutral bicarbonate and neutral meteoric waters. In two simulations, the initial reservoir fluid was boiled under open and closed conditions, and then allowed to mix with an acid sulphate water. One simulation involved the heating of a steam heated neutral bicarbonate water.

The boiling simulations show gas separation to be the most effective depositional mechanism for sphalerite, chalcopyrite, bornite, galena and electrum. Both boiling simulations predict the same depositional sequence of base and precious metal minerals. However, under open system boiling these minerals precipitate with greater efficiency. Up to 70% of all the aqueous base and precious metals precipitate within the first 20°C of adiabatic cooling. This emphasises the efficiency of gas fractionation in base and precious metal deposition from low-salinity sulphide-rich water. In such waters, base and precious metals form bisulphide complexes (Spycher and Reed, 1989). Gas fractionation results in the rapid removal of $H_2S_{(g)}$ from solution, with consequential depletion of aqueous sulphide from solution and precipitation of ore minerals (Spycher and Reed, 1989). Under closed system boiling, gases maintain equilibrium with the aqueous species and back-react with the water. Hence, gas loss and mineral deposition is slower.

The two simulations involving mixing with an acidic sulphate-bearing water produce a variety of minerals similar to those predicted from the boiling simulations. However, these simulations are less efficient for metal deposition. None of the metals are predicted to be completely extracted from solution. Sphalerite was predicted to be the most efficiently precipitated with over 75% of the available Zn removed from solution. Chalcopyrite was not predicted to precipitate, and galena, acanthite and electrum did not precipitate until temperatures were below 140°C.

Other mixing simulations presented here failed to produce the ore minerals predicted from boiling and mixing with acid sulphate water. Mixing with meteoric water is predicted to result in the precipitation of sphalerite, bornite, galena, covellite and acanthite. These, along with the gangue phases (quartz, muscovite and kaolinite), are identical to the mineral sequence predicted from conductive cooling of the reservoir fluid. This implies that cooling, rather than dilution, is the predominant mechanism influencing deposition of these minerals in this simulation. Mixing with bicarbonate water is predicted to be the least efficient mixing process for sulphide deposition, with only sphalerite, galena and acanthite predicted to precipitate. In this simulation, Pb and Ag are only efficiently removed from solution when the temperature has cooled to less than 150°C.

Table 4.11. A summary and comparison of the predicted mineralogies from the ten simulations using the reservoir fluid presented in Table 4.10.

	Boiling (closed)	Boiling (open)	Cooling	Mixing acid SO_4^{2-}/Cl^-	Mixing acid SO_4^{2-}	Mixing HCO_3^-	Mixing meteoric	Boil-Mix (closed)	Boil-Mix (open)	[1]Heating HCO_3^-
pH	↗6.6	↗6.8	↘4.3	↘3 9	↘4.0	↗6.0	↘4.9	↗5.9 ↘3.9	↗6.4 ↘4.0	↘6.5 ↗6.9
muscovite[2]	●	●	●	●	●	● ○	●	●	●	
anhydrite				●	●			●		
sphalerite	●	●	●	●	●	●	●	●	●	
chalcopyrite	●	●						●	●	
bornite	●	●	●	●	●		●	●	●	
galena	●	●	○	○	○	○	○	●	●	
gold	●	●		○	○			●	●	
silver	●	●		○	○			●	●	
pyrite			● ○	●	●	●	● ○			
covellite			○	○	○		○	○	○	
carbonate (dm + cc)[3]										○
quartz[4]	●	●	●	●	●	●	●	●	●	○
K-feldspar	○	○							●	
talc										○
chlorite		●				●			●	
tremolite-actinolite		●							●	○[5]
hematite		○								
kaolinite			○				○			
acanthite	●	●	● ○	○	○	○	● ○	●	●	
chalcocite	●	●						●	● ○	

Key:
[1] heating of bicarbonate water (Table 4.10) from 60° to 240°C, initial pH = 6.8; [2] muscovite is used as a proxy for the clay scale mineral, and has not been italicised;
[3] dm = dolomite; cc = calcite; [4] minerals in italics indicate they have not been observed in well scales; [5] during heating only tremolite precipitated,
● = mineral deposition initiated at T ≥ 200°C; ○ = mineral deposition initiated between 140° and 200°C; ○ = mineral deposition initiated at T ≤ 140°C;
● ○ = two symbols together indicate two episodes of mineral deposition, each initiated within the indicated temperature ranges;
↗ = pH increase, to indicated pH value; ↘ = pH decrease, to indicated pH value.

The minerals predicted to deposit during the boiling followed by mixing simulations are simply combinations of the respective boiling and acid sulphate mixing simulations, with most ore minerals precipitating during the boiling stage. A significant difference is predicted under closed system boiling conditions where the precipitation of anhydrite occurs at the end of the boiling stage. This is the only occasion where anhydrite is predicted to deposit from a boiling fluid and also the only occasion where anhydrite is predicted to precipitate without the involvement of mixing with an acid sulphate water.

The results of this study have implications for the formation of minerals belonging to the illite alteration assemblage. Muscovite, or its proxy illite (Simmons and Browne, 2000), is a characteristic mineral of the illite alteration assemblage and can precipitate directly from boiling and cooling of the neutral chloride reservoir water, or by mixing with between reservoir water and acid sulphate, bicarbonate, or meteoric waters. Other minerals belonging to the illite alteration assemblage are anhydrite and calcite. Anhydrite will precipitate only by mixing with acid sulphate waters, which at Palinpinon are sourced from perched steam-heated aquifers beneath areas of high elevation (Figure 4.6). Calcite can precipitate only by heating of steam-heated bicarbonate waters, which occur in perched aquifers in the outflow zone (Figure 4.6).

4.7. DISCUSSION, SUMMARY AND CONCLUSIONS

The results of this study have shown that the water chemistry of the geothermal reservoir at Palinpinon is influenced by boiling, conductive cooling, mixing and water-rock interactions. Boiling is mostly restricted to the upflow zone. Conductive cooling occurs in the eastern outflow zone. Water chemistries influenced by this process are close to chemical equilibrium with the host rocks.

Mixing occurs peripheral to the upflow zone. There are two recognised end-member dilutants, steam-heated sulphate and meteoric waters. Mixing with steam-heated sulphate waters sourced from perched aquifers occurs beneath topographically high areas. The chemistry of these hybrid waters are strongly influenced by host rock dissolution, or water-rock interactions, but chemical equilibrium has not been attained. In contrast, reservoir waters that have mixed with meteoric waters have chemistries that are closer to chemical equilibrium with the host rocks.

Permeability in the reservoir is mostly provided by faults and lithologic contacts. These structures control regions of mixing and boiling. Permeability in the eastern outflow zone must be relatively restricted, as residence time in the outflow zone must be long enough for chemical equilibrium to be maintained with the surrounding host rocks, and also for high fluid pressures to limit gas separation, or boiling.

Examination of the scale deposits collected from eleven geothermal wells, has revealed that the

Palinpinon geothermal waters are capable of depositing precious and base metal minerals. Trace metal chemistry analyses show these waters to have gold concentrations (1-4 μg/kg Au) that are comparable to other relatively dilute geothermal waters (Ohaaki-Broadlands, Cerro Prieto). Such gold concentrations are two orders of magnitude lower than the estimated gold solubility of Palinpinon geothermal waters (100 μg/kg) and these waters are theoretically capable of transporting more gold in solution than is currently occurring.

Reaction path modelling of boiling, mixing, conductive cooling and heating processes has attempted to simulate base and precious metal mineral deposition in the geothermal wells at Palinpinon. The results show that the minerals predicted to deposit during boiling most closely match those seen in well scales. Mixing simulations involving acid sulphate water predicted similar mineral assemblages; however, boiling was found to be the more efficient process in terms of more metal being deposited over a shorter temperature interval. In terms of the type of minerals produced and their depositional sequence, mixing with meteoric water is effectively the same as conductive cooling. Based on fluid modelling results, neither can be considered an effective depositional mechanism for base or precious metals.

The gangue minerals (muscovite, quartz, anhydrite, calcite) predicted to precipitate during the reaction path simulations are part of the illite alteration assemblage. Muscovite, or its proxy illite, and quartz can precipitate during boiling, cooling or mixing with any of the modelled end-member dilutants. In these models, anhydrite precipitates only by mixing with the acid sulphate waters and calcite precipitates only by heating of steam-heated bicarbonate waters.

The implications from this study for low sulphidation style epithermal ore deposition at Palinpinon is that gas separation appears to be the most effective mechanism for the precipitation of base and precious metals from the dilute neutral chloride waters. However, significant metal deposition is only likely to occur in regions of high permeability where fluid pressures have decreased enough to promote high fluid flux and gas separation. At Palinpinon, such zones are predicted to be restricted mostly to fault zones close to the zone of hydrological upflow. Discussion of whether ore mineralisation has, or will, form at Palinpinon is provided in Section 5.

5. DISCUSSION AND CONCLUSIONS

5.1. PALINPINON : A COUPLED PORPHYRY-EPITHERMAL ALTERATION ENVIRONMENT?

In agreement with the work by Leach and Bogie (1982), many of the geological and chemical aspects of the Palinpinon geothermal system are similar to those that characterise porphyry and epithermal ore deposits (Gustafson and Hunt, 1975; White and Hedenquist, 1990). These include :

- Many porphyry deposits of the SW Pacific and most of those in the Philippines are genetically associated with mid- to late-Tertiary calc-alkaline intrusions (Titley, 1975; Sillitoe and Gappe, 1984). In the Philippines, many intrusions associated with porphyry Cu and epithermal Au are related to adakitic magmatism (Sajona and Maury, 1998). The geothermal system at Palinpinon is also associated with adakitic magmas.
- The Palinpinon geological setting, consisting of small intrusions emplaced close to a large pluton with extensive zones of hydrothermal alteration, is similar to many Philippine porphyry copper deposits. According to Sillitoe and Gappe (1984), approximately 75% of porphyry copper environments in the Philippines have porphyry stocks emplaced within 4 km of the margin of a large equigranular intrusion.
- The mineral assemblages associated with the biotite and calc-silicate alteration types at Palinpinon are distinctive of K-silicate (potassic) alteration and skarn assemblages associated with porphyry copper environments (Meyer and Hemley, 1967). Fluid inclusions associated with Palinpinon biotite alteration (300° to > 600°C; 34 to 79 eq.wt.% NaCl; < 0.2 wt.% Cu) have similar thermal and compositional characteristics to those associated with potassic alteration in other porphyry environments (Gustafson and Hunt, 1975; Hedenquist and Lowenstern, 1994; Heinrich et al., 1999). However, no high grade quartz vein stockwork has been identified at Palinpinon, in contrast to economic deposits such as Grasberg (Irian Jaya), which have up to 30% quartz veins (by volume) in their high grade core (Kavalieris, 1994).
- The hypogene advanced argillic assemblage at Palinpinon is comparable to that developed in high sulphidation epithermal deposits, although a core zone of residual (vuggy) quartz has not been identified. Such silicified zones are the host for high grade Au - (Ag - Cu) mineralisation in most high sulphidation epithermal deposits (Arribas, 1995).
- The minerals that define the illite alteration assemblage at Palinpinon are in equilibrium with parts of the present-day hydrothermal system (e.g., illite – K-feldspar – epidote – chlorite) and are typical of alteration assemblages associated with low sulphidation epithermal deposits (White et al., 1995).

- Radiometric dating of primary igneous and secondary alteration minerals at Palinpinon shows that porphyry- (0.7-0.6 Ma) and high sulphidation epithermal-style (0.9-0.8 Ma) alteration environments were synchronous with emplacement of at least part of the Nasuji Pluton (0.7-0.3 Ma). Similar temporal relationships are seen at the Lepanto high sulphidation Au-Cu and subjacent Far Southeast (FSE) porphyry Cu-Au deposits, Philippines, where a maximum time period of 0.3 Ma was determined for the formation of porphyry and advanced argillic alteration assemblages (Arribas et al., 1995). Palinpinon is anomalous in that the advanced argillic assemblage is older than the potassic assemblage and host intrusions. This is interpreted to relate to closure temperatures and depths of formation, with both the potassic and advanced argillic assemblages being synchronous with intrusion emplacement, but with the K-Ar geochronometer stopping first in the near-surface advanced argillic assemblage.

The hydrothermal alteration assemblages at Palinpinon are interpreted to record a long-lived (0.8 ± 0.1 Ma) hydrothermal system that evolved with respect to : temperature (600° to 300°C), fluid sources (dominantly magmatic to dominantly meteoric), acidity (acid to near neutral), and confining pressures (0.3-0.4 kb lithostatic to 0.1-0.2 kb hydrostatic). There is an intimate spatial and temporal relationship between the intrusion emplacement and the styles of alteration that are characteristic of deposit styles such as, porphyry, high sulphidation epithermal and low sulphidation epithermal.

The earliest formed hydrothermal alteration assemblages at Palinpinon can be categorised as porphyry- and high sulphidation epithermal-styles that formed at approximately 0.8-0.7 Ma. Close temporal relationships between these alteration styles have been documented at several mineral deposits/districts and a close genetic relationship has now been effectively demonstrated (Sillitoe, 1973; 1989; Asami and Britten, 1980; Rye, 1993; Arribas et al., 1995; Losada-Calderón and McPhail, 1996; Hedenquist et al., 1998; Rohrlach et al., 1999; Muntean and Einaudi, 2001). A comparison of the alteration mineral assemblages and radiogenic ages from Palinpinon and a few of these coupled porphyry- and high sulphidation epithermal alteration environments is presented in Table 5.1. The lack of any known ore grade mineralisation in the coeval biotite and advanced argillic alteration assemblages at Palinpinon indicate that coupled barren porphyry – high sulphidation environments can form, and that the presence of these alteration assemblages is no guarantee of the presence of ore.

The illite alteration assemblage (smectite – illite – chlorite) at Palinpinon appears to be in equilibrium with the present-day thermal conditions. Consequently, the present-day Palinpinon geothermal system can be regarded as a modern analogue for a low sulphidation epithermal environment (Henley and Ellis, 1983). Genetic relationships between low sulphidation epithermal and magmatic-hydrothermal systems (porphyry- and high sulphidation epithermal) have been discussed by several workers (e.g., Sillitoe, 1973; 1989; 1994; Heald et al., 1987;

Cooke and Bloom, 1990; White and Hedenquist, 1990; Hedenquist et al., 2000), although a direct genetic relationship has not yet been proven unequivocally.

Table 5.1. A comparison of a few well documented coupled porphyry-high sulphidation (HS) epithermal alteration systems, in terms of their potassic and hypogene advanced argillic alteration mineral assemblages and radiogenic ages. Geochronological methods used and minerals dated are shown with their ages.

	Alteration Assemblage		Age (Ma)			References
	Porphyry (potassic)	HS Epithermal (advanced argillic)	Intrusion	Porphyry	HS Epithermal	
Palinpinon	bio, mt, anh, ksp, qtz	qtz (±VS), al, dsp, zun, pyro, dic, APS	0.7-0.3 Ar/Ar: hnb	0.7-0.6 Ar/Ar: bio	0.9-0.8 K-Ar: al	This study
Lepanto - FSE	bio, mt, qtz, ksp	VS, al, kao, pyro, dsp	~1.5 – 1.2 relative	1.41 ± 0.05 K-Ar. bio	1.42 ± 0.08 K-Ar: al	Arribas et al., 1995 Hedenquist et al., 1998
La Mejicana - Nevados del Famatina	bio, mt, qtz, ksp	qtz, pyro, APS, zun, kao, al	5.0 ± 0.3 Ar/Ar. bio	4.0 ± 0.2 Ar/Ar: ms	3.6 ± 0.1 Ar/Ar: ms	Calderón & McPhail, 1996
Tampakan	bio, mt, anh, qtz, chl	VS, pyro, dic, dsp, al	Pliocene			Rohrlach et al., 1999 Sillitoe, 1999
Nena - Frieda River	bio, mt, ksp, qtz, chl	qtz, al, and, pyro, kao	13?	13?	13?	Asami & Britten, 1980 Sillitoe, 1999
La Pepa, Maricunga	bio, mt, qtz, ksp	VS, al	?	23.81 ± 0.08 Ar/Ar: bio	23.50 ± 0.06 Ar/Ar: al	Muntean & Einaudi, 2001

Abbreviations:
al = alunite; and = andalusite; anh = anhydrite; APS = aluminium-phosphate-sulphate minerals; bio = biotite; chl = chlorite; dic = dickite; dsp = diaspore; hnb = hornblende; kao = kaolinite; ksp = K-feldspar; ms = muscovite; mt = magnetite; pyro = pyrophyllite; qtz = quartz; VS = vuggy silica; zun = zunyite

In some cases low sulphidation environments are probably related to magmatic-hydrothermal systems indirectly, with the two hydrothermal systems forming from two discrete fluids separated either by time and/or distance (Sillitoe, 1989; 1999). Fluids in the magmatic-hydrothermal environment are magmatic-derived, oxidised (sulphate predominant) and acidic. Fluids associated with 'distal' low sulphidation environment are reduced (sulphide predominant), near-neutral, and in most cases derived from meteoric sources. Insights into the temporal relationships between the two settings are gained from deposits where the superposition, or telescoping (Sillitoe, 1994), of low sulphidation alteration assemblages onto magmatic-hydrothermal assemblages has occurred. At the Acupan Au-Ag deposit, Philippines (Cooke and Bloom, 1990), Ladolam Au deposit, Papua New Guinea (Moyle et al., 1990) and Porgera Au deposit, Papua New Guinea (Richards, 1992), low sulphidation epithermal assemblages have overprinted porphyry-type alteration assemblages. Whereas at both the Masupa Ria district, Indonesia and the Kelly deposit, Baguio district, Philippines, low sulphidation assemblages have overprinted high sulphidation-style alteration assemblages (Aoki et al., 1993; Thompson et al., 1994), with the age difference between the two styles in the Baguio district being 0.3 Ma (Aoki et al., 1993). These overprinting relationships imply the abatement of magmatic-derived fluids and the increasing input of meteoric-derived waters into

the hydrothermal system. It has been suggested that such a scenario can occur from either rapid erosion rates (i.e., 1.2 mm/yr at Acupan, Cooke and Bloom, 1990), magma withdrawal (e.g., Masupa Ria, Thompson et al., 1994) or instantaneous sector collapse (e.g. Ladolam, Moyle et al., 1990; Sillitoe, 1994).

The coupled low sulphidation and magmatic-hydrothermal alteration systems described above are examples where the magmatic-hydrothermal system predates the low sulphidation environment. Few of these coupled systems appear to have formed at the same time. A possible exception is the Victoria low sulphidation Au deposit, Philippines, which has been genetically associated with the high sulphidation Lepanto-FSE (Disini et al., 1998; Claveria et al., 1999). However, temporal relationships between the two environments have yet to be quantified.

At Palinpinon, the low sulphidation alteration environment has either had a protracted development history, or it formed during discrete episodes of intrusive activity. Based on the available geochronological data (Zaide, 1984), the initial development of a low sulphidation alteration system probably occurred with the emplacement of the Nasuji Pluton at approximately 0.8 Ma. It probably developed contemporaneously with the magmatic-hydrothermal system, but physically separate from it in a distal location. The low sulphidation system would have lasted for as long as a thermal anomaly from the cooling pluton could maintain a hydrothermal convection cell. Work by Cathles et al. (1997) indicates a pluton 2 km wide by 3 km high (the Nasuji Pluton is at least 4 km wide by 1.5 km high) would cool conductively within about 100,000 yr, and in considerably less time by convective cooling. Emplacement of a blind intrusion in the Puhagan area apparently shifted the thermal anomaly eastwards. Depending on the timing of this emplacement, the intrusion either reinitiated a hydrothermal convection cell, or transferred the focus of convection towards the Puhagan area.

With emplacement of the blind intrusion in the Puhagan area, it appears that any dense, saline, aqueous magmatic fluid failed to reach shallow crustal levels. The lack of any hypogene advanced argillic alteration in the Puhagan area also implies that : (1) the flux of degassed magmatic volatiles was low; (2) the fluids were sufficiently neutralised by water-rock interaction in the overlying stratigraphy; or (3) permeability in the deeper parts of the system were insufficient to provide a focus for fluid flow. Hence, shallow regions of the system were dominated by meteoric waters that enabled low sulphidation style alteration assemblages to develop above deeper, high temperature magmatic-hydrothermal assemblages. These relationships suggest that the present-day geothermal system at Palinpinon is an example where there has been synchronous development of low sulphidation and magmatic-hydrothermal-style alteration assemblages (i.e., biotite, calc-silicate) that were genetically related to a common intrusion.

5.2. BASE AND PRECIOUS METAL ORE DEPOSITION AT PALINPINON?

The previous section establishes that the geological and hydrothermal settings at Palinpinon are comparable to many porphyry epithermal base and precious metal ore deposits. However, a question that needs to be addressed is whether or not the Palinpinon hydrothermal system is, or has ever been, a base and/or precious metal mineralising system.

Based on the assay results and sulphide mineral petrography, significant mineralised zones of copper, zinc, lead, gold and silver have not been detected at Palinpinon. Samples from biotite, hypogene advanced argillic and illite alteration zones contain no more than 0.1 modal % base metal sulphide minerals. Furthermore, geochemical assays of drillcores and drillcuttings show that base and precious metals are one to two orders of magnitude below ore grade (< 0.02 wt. % Cu, < 0.03 wt. % Pb, < 0.01 wt. % Zn, < 0.01 wt. % Mo, < 8 g/t Ag and <0.05 g/t Au). It may be that geothermal wells drilled to date have failed to intersect mineralised ore zones, or that such zones associated with shallow alteration environments (i.e., hypogene advanced argillic alteration) have since been eroded. Until any evidence to the contrary is obtained, based on the assay results and sulphide mineral petrography, Palinpinon is interpreted to be a barren hydrothermal system with respect to base and precious metal minerals.

However, because Palinpinon does have the characteristic alteration assemblages of porphyry, high sulphidation and low sulphidation environments, reasons need to be proposed why it lacks any significant 'ore' zones. Such reasons could be : (1) poor permeability necessary to create a focus for fluid flow and ore deposition; (2) insufficient fluid flux for the accumulation of large amounts of base and/or precious metals; and/or (3) a lack of significant volumes of metals derived from the intrusions.

The emplacement depth of the Nasuji Pluton is estimated to be between 2.5-3 km (Figure 3.22). As the intrusion cooled to approximately 400°C, there was a transition from lithostatic to hydrostatic pressures and low density vapour and high density, saline aqueous fluids were expelled from the intrusion into the surrounding country rock. Permeability in the surrounding host rock must have been sufficient enough for the low density vapour to permeate to shallow crustal levels, but not necessarily enough for the high density brines to migrate upward. It is possible that by the time the transition to hydrostatic pressures had occurred, most of the pluton had crystallised, trapping the two-phase fluids in the equigranular portions of the intrusion. Therefore, there may have been a paucity of metalliferous brines and fluid flux necessary to create high grade ore zones that are typically characterised by intense quartz stockwork in porphyry metal deposits (e.g., 20-30 vol.% at Grasberg).

In the Puhagan area, without knowing the size or depth ofthe blind intrusion, the pressure regime affecting the intrusive body, or how much magmatic-derived fluids have been expelled from the confines of the intrusion, it is difficult to comment on the reasons why this intrusion

has not produced any significant base and precious metal mineralisation. But all the reasons just described for the Nasuji Pluton could be just as valid. That is, poor permeability, lack of sufficient fluid flux and/or volumes of metals and fluids derived from the intrusions.

Regarding the present-day geothermal system, results of the trace metal chemistry and scale deposit study show that the modern geothermal fluids are capable of transporting and depositing precious (and to a lesser extent) base metals. Measured gold concentrations (1-4 μg/kg Au) in the deep neutral chloride waters are comparable to those from other geothermal systems. These Au concentrations are not particularly enriched and are equivalent to background gold concentrations for island arc igneous rocks. This implies that there is no need to invoke a magmatic source for gold, because wallrock leaching can provide sufficient amounts of gold. Consequently, effective leaching combined with a high fluid flux and effective trapping mechanisms are most important for gold ore deposition in low sulphidation epithermal environments.

The minerals identified in scale deposits from geothermal wells at Palinpinon include anhydrite, calcite, clay minerals and amorphous silica, along with the base and precious metal minerals, chalcopyrite, sphalerite, galena, electrum and gold. The 'gangue minerals' (anhydrite, calcite, clays, amorphous silica) can occur in a low sulphidation epithermal environment, although anhydrite is unusual. At Palinpinon, with the exception of amorphous silica, these minerals are associated with the illite alteration assemblage. Amorphous silica has not been recognised in any of the Palinpinon drillcores and drillcuttings. Its occurrence in geothermal wells is due to reaction kinetics that allows only amorphous silica to precipitate, rather than any of the other silica polymorphs (Simmons and Browne, 2000). Therefore, amorphous silica scale can be considered a proxy for quartz in the illite alteration assemblage.

Reaction path modelling involving boiling, mixing, conductive cooling and heating have attempted to simulate scale mineral deposition in the geothermal wells. Results showed that the minerals predicted to deposit during boiling simulations most closely match those seen in the well scales. Mixing involving acid sulphate water predicted similar mineral assemblages. However, boiling was found to be the more efficient process in terms of higher quantities of metal deposited over a narrower temperature interval.

The implications for ore deposition in the low sulphidation epithermal environment at Palinpinon is that gas separation, or boiling, appears to be the most effective mechanism for the precipitation of base and precious metals. Significant metal deposition is most likely to occur in regions of high permeability where fluid pressures have decreased enough to promote high fluid flux and gas separation. At Palinpinon, such zones are mostly restricted to fault zones close to the upflow zone. These areas are predicted to be the most prospective exploration targets for future drilling.

Despite the parallels that can be drawn between Palinpinon and mineralised porphyry and epithermal ore deposits, important features that characterise the high grade ore zones of these deposit types are apparently absent at Palinpinon. These include high density quartz stockwork veining (porphyry), a core zone of vuggy silica (high sulphidation epithermal) and massive crustiform veins or mineralised breccia complexes (low sulphidation epithermal). All of these features intimate that high grade ore deposition at these deposit types has been promoted by large volumes of fluid and highly permeable wallrock. The absence of these features at Palinpinon indicates that permeability and/or fluid flux have been insufficient and that an upsurge in magmatic activity, large fault movements, or catastrophic decompression and breccia formation would be required to promote ore deposition.

5.3. CONCLUSIONS

The following are the major conclusions from this study :

- The Palinpinon geothermal field (Negros Island, Philippines) is a high temperature, liquid-dominated geothermal system in an active island arc volcanic setting.
- Rock formations at Palinpinon have been regionally correlated with the Visayas stratigraphy. The igneous rock formations in southern Negros Island have medium K, calc-alkaline basaltic to dacitic compositions with adakitic and Nb-enriched basaltic geochemical signatures. This is interpreted to indicate that magmatism in this region has been influenced by the melting of subducted oceanic basalt.
- During Early Pliocene to Recent times, diorites to quartz diorites of the Puhagan dikes (4.2-4.1 Ma) and the Nasuji Pluton (0.7-0.3 Ma) intruded the Middle Miocene, Late Miocene and Early-Late Pliocene rock units.
- The Nasuji Pluton is thought to have been emplaced at minimum depths of 2-2.5 km under lithostatic pressure and ductile deformation. The hydrothermal alteration assemblages spatially associated with the pluton are biotite, calc-silicate, hypogene advanced argillic, propylitic, illite and steam-heated advanced argillic.
- Ages of hydrothermal biotite (0.7-0.6 Ma), hypogene alunite (0.9-0.8 Ma) and illite (0.7 Ma) are interpreted to demonstrate that these assemblages all formed contemporaneously with the Nasuji Pluton (0.7-0.3 Ma), implying a genetic link between intrusion emplacement and their formation. The older age for the advanced argillic assemblage, compared to the intrusion and biotite ages, is interpreted to reflect closure temperatures and relative depths of formation.
- The transition from lithostatic to hydrostatic conditions occurred as the pluton cooled to 400°C. Hydrostatic conditions resulted in the exsolution of a low density vapor and a high density brine and the quenching of the magma to a porphyritic quartz diorite. Fluid

inclusions record temperatures of 267° to > 600°C and salinities of 40 to 79 eq.wt.% NaCl. These brines are endowed with base metals (< 0.2 wt. % Cu at room temperature).

- The exsolved magmatic volatiles ascended to shallow crustal levels to condense and form acidic aquifers, which altered the host rocks to hypogene advanced argillic alteration assemblages. The occurrence of high temperature (> 250°C) minerals at the surface implies at least 450 m of erosion over the past 800 000 years. This suggests a minimum rate of erosion of 0.56 mm/yr.

- The emplacement of a blind intrusion beneath the Puhagan dikes (i.e., > 2.5 km depth) at the intersection of the Ticala and Lagunao Faults occurred within the last 0.8 Ma. This shifted the focus of hypogene alteration to the Puhagan area and provided a heat source for the present-day geothermal system. Hypogene hydrothermal alteration types in this area are : calc-silicate (garnet, clinopyroxene, scapolite); biotite; propylitic (tremolite-actinolite, epidote); and illite. With the exception of the calc-silicate assemblage, all are in apparent thermal equilibrium with the present-day geothermal system. The occurrence of clinopyroxene and garnet in the calc-silicate assemblage implies that the hydrothermal system has cooled by at least 70°-100°C.

- At shallow levels, illite alteration assemblages overprint the biotite, propylitic and hypogene advanced argillic alteration assemblages associated with the Nasuji pluton. Perched aquifers of steam-heated acid sulphate water have altered regions above the water table to an advanced argillic (steam-heated) alteration assemblage. The percolation of these waters down near-vertical permeable structures (i.e., faults and joints) results in steeply dipping zones of steam-heated advanced argillic alteration.

- The chemistry of the present-day geothermal reservoir is influenced by boiling, mixing and conductive cooling. Proposed end-member mixing solutions are meteoric water and shallow derived, steam-heated sulphate water. Steam-heated sulphate waters are sourced from perched aquifers beneath areas of high elevation.

- Wells discharging mixed chloride-sulphate waters have chemistries influenced by host rock dissolution and have not attained chemical equilibrium. Wells discharging water that have mixed with meteoric waters are located peripheral to the upflow zone and have chemistries that indicate they are closer to chemical equilibrium with the host rocks.

- Boiling and mixing are mainly restricted to permeable zones, such as faults and lithologic boundaries. Conductive cooling occurs in the easterly flowing outflow zone. Water chemistries influenced by conductive cooling are close to chemical equilibrium with the host rocks.

- Trace metal analyses of the deep reservoir fluids shows they are undersaturated with respect to gold (i.e., 1-4 μg/kg relative to 100 μg/kg). The measured Cu and Zn concentrations are

high (5-6 mg/kg and 2 mg/kg, respectively) and may reflect contamination from the sampling equipment. The measured Au contents are considered to be accurate.

- The occurrence of base and precious metals as well scale deposits demonstrates that the deep reservoir fluid at Palinpinon is capable of transporting and depositing base and precious metals.
- Fluid modelling predicts that boiling will produce sulphide assemblages most similar to those seen in well scale deposits. Mixing with acid sulphate waters can also produce these sulphide assemblages, but the deposition of gold and silver occurs at much lower temperatures in association with galena, covellite and acanthite. Based on fluid modelling results, neither mixing with meteoric water or conductive cooling can be considered effective deposition mechanisms for base or precious metals.
- Results of this study show that gas separation is the most effective process for depositing base and precious metals from dilute neutral chloride waters like those at Palinpinon. However, significant quantities of metals will only deposit in zones where fluid pressures are low enough to promote high fluid flux and gas separation. Such zones are most likely to be in the present-day upflow zone.
- The distribution and ages of hydrothermal alteration assemblages are comparable to those associated with coupled porphyry-epithermal ore deposits. There has been synchronous development of coupled porphyry and high sulphidation epithermal alteration assemblages, and coupled low sulphidation and magmatic-hydrothermal-style alteration assemblages (biotite, calc-silicate).
- Despite similarities with mineral deposits, Palinpinon is interpreted to be a barren hydrothermal system due to either low permeabilities and/or fluid flux.

5.4. FUTURE WORK

Some suggested avenues for future research are :

- Further radiometric dating of mineral separates from the Nasuji Pluton using $^{40}Ar/^{39}Ar$ geochronology is needed. Textural and compositional variations of the Nasuji Pluton may be due to the intrusion being a composite pluton consisting of multiple intrusive events. A detailed radiometric dating study of rocks from different compositional and textural groups may resolve this and also the discrepancy between the results presented in this (0.7-0.3 Ma) and a previous study (10.5-5.6 Ma; Zaide, 1984). The use of $^{40}Ar/^{39}Ar$ geochronology is recommended as this provides better qualitative information.
- The influence of various hydrothermal fluid types (i.e., magmatic, meteoric, connate) on the formation of the different hydrothermal alteration assemblages is not well understood. A stable isotope ($\delta^{18}O$, δH) study of the alteration minerals (i.e., biotite, illite and alunite)

would provide a better understanding of the proportions of discrete fluid types and the amount of mixing that occurred during the formation of biotite, illite and advanced argillic alteration assemblages.

- The stable isotope study could be augmented with analysis of fluid inclusions for their halogen contents. Any potential influences of connate brines on the formation of the Puhagan hydrothermal alteration assemblages, in particular the propylitic, tremolite-actinolite and epidote subzones, could be tested using this technique. The Cl/Br ratios of the population A and B fluid inclusions from these subzones may prove useful for determining the origins of the trapped fluids.
- In terms of the present-day geothermal system, the source of the hydrothermal fluids is poorly constrained. The noble gas geochemistry of the geothermal waters would be useful for determining the various fluid sources (meteoric, magmatic, crustal), providing a better understanding of fluid types and helping to identify the fluid flow paths at Palinpinon.

REFERENCES

Acharya, H.K. & Aggarwal, Y.P., 1980. Seismicity and tectonics of the Philippine Islands. *Journal of Geophysical Research* **85**, 3239-3250.

Ahmad, S.N. & Rose, A.W., 1980. Fluid inclusions in porphyry and skarn ore at Santa Rita, New Mexico. *Economic Geology* **75**, 229-250.

Amistoso, A.E., Aquino, B.G., Aunzo, Z.P., Jordan, O.T., Sta. Ana, F.X.M., Bodvarsson, G.S. & Doughty, C., 1993. Reservoir analysis of the Palinpinon geothermal field, Negros Oriental, Philippines. *Geothermics* **22**, 555-574.

Aoki, M., Comsti, E.C., Lazo, F.B. & Matsuhisa, Y., 1993. Advanced argillic alteration and geochemistry of alunite in an evolving hydrothermal system at Baguio, northern Luzon, Philippines. *Resource Geology* **43**, 155-164.

Archibald, S.M. & Williams-Jones, A.E., 1999. Precious metal precipitation in wellhead scales at the Momotombo geothermal field, Nicaragua. *GAC/MAC Joint Annual Meeting,* Sudbury.

Arevalo, E.M., 1987. Mineralisation associated with Tongonan well ejecta, blockage materials and discharge line precipitates. *9th N.Z. Geothermal Workshop,* Auckland, New Zealand, 259-264.

Arribas, A., 1995. Characteristics of high-sulfidation epithermal deposits, and their relation to magmatic fluid. In: J. F H. Thompson (ed) *Magmas, Fluids and Ore Deposits.* Mineralogical Association of Canada, Short Course Series. **23.** 419-454.

Arribas, A., Hedenquist, J.W., Itaya, T., Okada, T., Concepcion, R.A. & Garcia, J., J.S., 1995. Contemporaneous formation of adjacent porphyry and epithermal Cu-Au deposits over 300 ka in northern Luzon, Philippines. *Geology* **23**, 337-340.

Asami, N. & Britten, R.M., 1980. The porphyry copper deposits at the Frieda River prospect, Papua New Guinea. *Mining Geology, Special Issue* **8**, 117-139.

Aurelio, M.A., Barrier, E., Rangin, C. & Müller, C., 1991. The Philippine Fault in the Late Cenozoic tectonic evolution of the Bondoc-Masbate-N. Leyte area, central Philippines. *Journal of Southeast Asian Earth Sciences* **6**, 221-248.

Baksi, A.K., Archibald, D.A. & Farrar, E., 1996. Intercalibration of 40Ar/39Ar dating standards. *Chemical Geology* **129**, 307-324.

Barrier, E., Huchon, P. & Aurelio, M., 1991. Philippine fault: a key for Philippine kinematics. *Geology* **19**, 32-35.

Batayola, G.J., 1983. *A Simulation Study of the Puhagan Section of the Southern Negros Geothermal Reservoir, Philippines.* Unpublished Report. Geothermal Institute, University of Auckland. 77p.

Bodnar, R.J., 1995. Fluid-inclusion evidence for a magmatic source for metals in porphyry copper deposits. In: J. F. H. Thompson (ed). *Magmas, Fluids, and Ore Deposits.* Mineralogical Association of Canada Short Course Series. **23.** 139-152.

Bodnar, R.J., Burnham, C.W. & Sterner, S.M., 1985. Synthetic fluid inclusions in natural quartz. III. Determination of phase equilibrium properties in the system H_2O-NaCl to 1000°C and 1500 bars. *Geochimica et Cosmochimica Acta* **49**, 1861-1873.

Bodnar, R.J., Sterner, S.M. & Hall, D.L., 1989. SALTY: a FORTRAN program to calculate compositions of fluid inclusions in the system NaCl-KCl-H_2O. *Computers and Geosciences* **15**, 19-41.

Bogie, I., Lawless, J.V. & Pornuevo, J.B., 1987. Kaipohan: an apparently nonthermal manifestation of hydrothermal systems in the Philippines. *Journal of Volcanology and Geothermal Research* **31**, 281-292.

Bromley, C.J., Rigor Jr., D.M., Rodriguez, R.C., Layugan, D.B. & Ignacio, C.P., 1984. Geophysical modelling and reservoir monitoring studies of Southern Negros geothermal field. *6th N.Z. Geothermal Workshop,* Auckland, N.Z., 101-106.

Bromley, C.J., Pearson, C.F., Rigor Jr., D.M. & PNOC-EDC, 1987. Microearthquakes at the Puhagan geothermal field, Philippines - a case of induced seismicity. *Journal of Volcanology and Geothermal Research* **31**, 293-311.

Brown, K.L., 1986. Gold deposition from geothermal discharges in New Zealand. *Economic Geology* **81**, 979-983.

Brown, K.L., Webster, J.G. & Christenson, B.W., 1996. Precious metal sampling at the Ohaaki geothermal field. *18th N.Z. Geothermal Workshop,* Auckland, N.Z., 169-174.

Burnham, C.W., 1979. Magmas and hydrothermal fluids. In: H. L. Barnes (ed). *Geochemistry of Hydrothermal Ore Deposits.* Wiley. 71-136.

Cardwell, R.K., Isacks, B.L. & Karig, D.E., 1980. The spatial distribution of earthquakes, focal mechanism solutions, and subducted lithosphere in the Philippines and northeastern Indonesian islands. In: D. E. Hayes (ed). *The Tectonic and Geologic Evolution of Southeast Asian Seas and Islands.* American Geophysical Union. **23.** 1-35.

Castillo, P.R., 1996. Origin and geodynamic implication of the Dupal isotopic anomaly in volcanic rocks from the Philippine island arcs. *Geology* **24**, 271-273.

Castillo, P.R , Janney, P.E. & Solidum, R.U., 1999. Petrology and geochemistry of Camiguin Island, southern Philippines: insights to the source of adakites and other lavas in a complex arc setting. *Contributions to Mineralogy and Petrology* **134**, 33-51.

Castro, C.C., Estero, J.L., Fragata, J.J., Licup, J., A.C. & Tan, E.S., 1979. *Geology of the Okoy Valley and Tibanglan area, southern Negros geothermal project.* Unpublished Report. PNOC-EDC Geothermal Division.

Cathles, L.M., Erendi, A.H.J. & Barrie, T., 1997. How long can a hydrothermal system be sustained by a single intrusive event? *Economic Geology* **92**, 766-771.

Celenk, H., Flores, R.A.L. & Dela Cruz, A.P., 1987. Geochemical characterisation of epithermal alteration in southeast Negros, Philippines. *Journal of Geochemical Exploration* **27**, 189-211.

Clark, J.R. & Williams-Jones, A.E., 1990. Analogues of epithermal gold-silver deposition in geothermal well scales. *Nature* **346**, 644-645.

Claveria, R.J.R , Cuison, A.G. & Andam, B.V., 1999. The Victoria gold deposit in the Mankayan mineral district, Luzon, Philippines. *PACRIM '99,* Bali, Indonesia, 73-80.

Clemente, V.C., 1981. *Geochemistry and related geology of the Southern Negros geothermal field, Philippines.* Unpublished Report. Geothermal Institute, University of Auckland.

Cooke, D.R. & Bloom, M.S., 1990. Epithermal and subjacent porphyry mineralization, Acupan, Baguio district, Philippines: a fluid inclusion and paragenetic study. *Journal of Geochemical Exploration* **35**, 297-340.

Cooke, D.R. & McPhail, D.C., 2001. Epithermal Au-Ag-Te mineralisation, Acupan, Baguio District, Philippines: numerical simulations of mineral deposition. *Economic Geology* **96**, 109-131.

Cooke, D.R. & Simmons, S.F., 2000. Characteristics and genesis of epithermal gold deposits. In: S. G. Hagemann and P. E. Brown (ed). *Gold in 2000.* Society of Economic Geology. **13.** 221-244.

Cooke, D.R., McPhail, D.C. & Bloom, M.S., 1996. Epithermal gold mineralisation, Acupan, Baguio district, Philippines: geology, mineralisation, alteration and the thermochemical environment of ore deposition. *Economic Geology* **91**, 243-272.

Corbett, G.J. & Leach, T.M., 1998. *Southwest Pacific Rim gold-copper systems: structure, alteration and mineralization.* Society of Economic Geologists Special Publication 6, Kansas City, pp.237.

Crocket, J.H., 1993. Distribution of gold in the Earth's crust. In: R. P. Foster (ed). *Gold Metallogeny and Exploration.* Chapman and Hall. 1-36.

D'Amore, F.D., Ramos-Candellaria, M.N., Seastres Jr., J.S., Ruaya, J.R. & Nuti, S., 1993. Applications of gas chemistry in evaluating physical processes in the Southern Negros (Palinpinon) geothermal field, Philippines. *Geothermics* **22**, 535-553.

Defant, M.J. & Drummond, M.S., 1990. Derivation of some modern arc magmas by melting of young subducted lithosphere. *Nature* **347**, 662-665.

Defant, M.J. & Drummond, M.S., 1993. Mount St. Helens: Potential example of the partial melting of the subducted lithosphere in a volcanic arc. *Geology* **21**, 547-550.

Defant, M.J , Clark, L.F., Stewart, R.H., Drummond, M.S., de Boer, J.Z., Maury, R.C., Bellon, H., Jackson, T.E. & Restrepo, J.F., 1991a. Andesite and dacite genesis via contrasting processes: The geology and geochemistry of El Valle Volcano, Panama. *Contributions to Mineralogy and Petrology* **106**, 309-324.

Defant, M.J., Richerson, P.M., de Boer, J.Z., Stewart, R.H., Maury, R.C., Bellon, H., Drummond, M.S., Feigenson, M.D. & Jackson, T.E., 1991b. Dacite genesis via both slab melting and differentiation: Petrogenesis of La Yegunda Volcanic Complex, Panama. *Journal of Petrology* **32**, 1101-1142.

Defant, M.J., Jackson, T.E., Drummond, M.S., de Boer, J.Z., Bellon, H., Feigenson, M.D., Maury, R C. & Stewart, R.H., 1992. The geochemistry of young volcanism throughout western Panama and southeastern Costa Rica: An overview. *Geological Society of London Journal* **149**, 569-579.

Dilles, J H., Einaudi, M.T., Proffett, J. & Barton, M.D., 2000. Overview of the Yerington porphyry copper deposit : magmatic to nonmagmatic sources of hydrothermal fluids : their flow paths and alteration effects on rocks and Cu-Mo-Fe-Au ores. In: J. H. Dilles, M. D. Barton, D. A. Johnson, J. M. Proffett and M. T. Einaudi (ed). *Part I. Contrasting Styles of Intrusion-Associated Hydrothermal Systems*. Society of Economic Geologists, Guidebook Series. **32.** 55-66.

Disini, A.F., Robertson, B.M. & Claveria, R.J.R., 1998. The Mankayan mineral district, Luzon, Philippines. *Porphyry and Hydrothermal Copper and Gold Deposits: a global perspective,* Perth, Australia, 75-86.

Drummond, M.S. & Defant, M.J., 1990. A model for trondhjemite-tonalite-dacite genesis and crustal growth via slab melting: Archean to modern comparisons. *Journal of Geophysical Research* **95**, 21,501-21,521.

Drummond, S.E. & Ohmoto, H., 1985. Chemical evolution and mineral deposition in boiling hydrothermal systems. *Economic Geology* **80**, 126-147.

Eastoe, C.J., 1978. A fluid inclusion study of the Panguna porphyry copper deposit, Bougainville, Papua New Guinea. *Economic Geology* **73**, 721-748.

Ellis, A.J. & Mahon, W.A.J., 1977. *Chemistry and Geothermal Systems.* Academic Press, Inc., London, pp.392.

Ewart, A., 1982. The mineralogy and petrology of Tertiary-Recent orogenic volcanic rocks: with special reference to the andesitic-basaltic compositional range. In: R. S. Thorpe (ed). *Andesites: Orogenic Andesites and Related Rocks*. John Wiley & Sons. 25-95.

Fleck, R.J., Sutter, J.F. & Elliot, D.H., 1977. Interpretation of discordant 40Ar/39Ar age spectra of Mesozoic tholeiites from Antarctica. *Geochimica et Cosmochimica Acta* **41**, 15-32.

Fournier, R.O., 1981. Application of water geochemistry to geothermal exploration and reservoir engineering. In: L. Rybach and L. J. P. Muffler (ed). *Geothermal Systems*. John Wiley & Sons. . 109-144.

Fournier, R.O., 1985. The behavior of silica in hydrothermal solutions. In: B. R. Berger and P. M. Bethke (ed). *Geology and Geochemistry of Epithermal Systems*. Society of Economic Geologists. **2.** 45-61.

Fournier, R.O., 1987. Conceptual models of brine evolution in magmatic-hydrothermal systems. *U.S. Geological Survey Professional Paper 1350* **2**, 1487-1506.

Fournier, R.O., 1999. Hydrothermal processes related to movement of fluid from plastic into brittle rock in the magmatic-epithermal environment. *Economic Geology* **94**, 1193-1211.

Fournier, R.O. & Truesdell, A.H., 1973. An empirical Na-K-Ca geothermometer for natural waters. *Geochimica et Cosmochimica Acta* **37**, 1255-1275.

Fragata, J.J., 1983a. *Downhole Geology of Well PN16D.* Unpublished Report. PNOC-EDC Geothermal Division.

Fragata, J.J., 1983b. *Downhole Geology of Well PN18D.* Unpublished Report. PNOC-EDC Geothermal Division.

Gallup, D.L., 1998. Geochemistry of geothermal fluids and well scales, and potential for mineral recovery. *Ore Geology Reviews* **12**, 225-236.

Gerardo, J.Y., Nuti, S., D'Amore, F., Seastres, J.S. & Gonfiantini, R., 1993. Isotopic evidence for magmatic and meteoric water recharge and the processes affecting reservoir fluids in the Palinpinon geothermal system, Philippines. *Geothermics* **22**, 521-533.

Gervasio, F.C., 1971. Geotectonic development of the Philippines. In: P. J. Coleman (ed). *The Western Pacific: Island Arcs, Marginal Seas, Geochemistry.* University of Western Australia Press. 307-324.

Giggenbach, W.F., 1980. Geothermal gas equilibria. *Geochimica et Cosmochimica Acta* **44**, 2021-2032.

Giggenbach, W.F., 1988. Geothermal solute equilibria. Derivation of Na-K-Mg-Ca geoindicators. *Geochimica et Cosmochimica Acta* **52**, 2749-2765.

Giggenbach, W.F., 1992. Isotopic shifts in waters from geothermal and volcanic systems along convergent plate boundaries and their origin. *Earth and Planetary Science Letters* **113**, 495-510.

Giggenbach, W.F., 1997. The origin and evolution of fluids in magmatic-hydrothermal systems. In: H. L. Barnes (ed). *Geochemistry of Hydrothermal Ore Deposits*. John Wiley & Sons, Inc. 737-796.

Giggenbach, W.F. & Corrales, R., 1992. Isotopic and chemical composition of water and steam discharges from volcanic-magmatic-hydrothermal systems of the Guanacaste Geothermal Province, Costa Rica. *Applied Geochemistry* **7**, 309-332.

Giggenbach, W.F. & Goguel, R.L., 1989. *Collection and analysis of geothermal and volcanic water and gas discharges*. Unpublished Report. D.S.I.R., Chemistry Division.

Gill, J., 1981. *Orogenic Andesites and Plate Tectonics*. **16.** Springer-Verlag, pp.390.

Glover, R.B., 1975. *Chemical analysis of waters from Negros Oriental, Philippines, and their geothermal significance*. Unpublished Report. D.S.I.R., Chemistry Division.

Gustafson, L.B. & Hunt, J.P., 1975. The porphyry copper deposit at El Salvador, Chile. *Economic Geology* **70**, 857-912.

Gutscher, M.A., Maury, R., Eissen, J.P. & Bourdon, E., 2000. Can slab melting be caused by flat subduction? *Geology* **28**, 535-538.

Hamilton, W., 1979. Tectonics of the Indonesian region. *U.S. Geological Survey Professional Paper* **1078**, 345.

Harper, R.T. & Jordan, O.T., 1985. Geochemical changes in response to production and reinjection for Palinpinon I geothermal field, Negros Oriental, Philippines. *7th N.Z. Geothermal Workshop,* Auckland, NZ, 39-44.

Hayba, D.O., Bethke, P.M., Heald, P. & Foley, N.K., 1985. Geologic, mineralogic, and geochemical characteristics of volcanic-hosted epithermal precious-metal deposits. In: B. R. Berger and P. M. Bethke (ed). *Geology and Geochemistry of Epithermal Systems*. Society of Economic Geologists. **2.** 249-272.

Heald, P., Foley, N.K. & Hayba, D.O., 1987. Comparative anatomy of volcanic-hosted epithermal deposits: acid-sulfate and adularia-sericite types *Economic Geology* **82**, 1-26

Hedenquist, J.W., 1986. Geothermal systems in the Taupo Volcanic Zone: their characteristics and relation to volcanism and mineralisation. *Bulletin of the Royal Society of New Zealand* **23**, 134-168.

Hedenquist, J.W., 1986. Mineralization associated with volcanic-related hydrothermal systems in the Circum-Pacific basin. In: M. K. Horn (ed). *Transactions of the 4th Circum-Pacific Energy & Mineral Resources Conference*. American Association of Petroleum Geology, 513-524.

Hedenquist, J.W., 1990. The thermal and geochemical structure of the Broadlands-Ohaaki geothermal system, New Zealand. *Geothermics* **19**, 151-185.

Hedenquist, J.W. & Henley, R.W., 1985. The importance of CO_2 freezing point measurements of fluid inclusions: evidence from active geothermal systems and implications for epithermal ore deposition. *Economic Geology* **80**, 1379-1406.

Hedenquist, J.W. & Lowenstern, J.B., 1994. The role of magmas in the formation of hydrothermal ore deposits. *Nature* **370**, 519-527.

Hedenquist, J.W., Arribas, A. & Reynolds, T.J., 1998. Evolution of an intrusion-centred hydrothermal system: Far Southeast-Lepanto porphyry and epithermal Cu-Au deposits, Philippines. *Economic Geology* **93**, 373-404.

Hedenquist, J.W., Arribas, A. & Gonzalez-Urien, E., 2000. Exploration for epithermal gold deposits. In: S. G. Hagemann and P. E. Brown (ed). *Gold in 2000*. Society of Economic Geologists. **13.** 245-277.

Heinrich, C.A., Ryan, C.G., Mernagh, T.P. & Eadington, P.J., 1992. Segregation of ore metals between magmatic brine and vapor: a fluid inclusion study using PIXE microanalysis. *Economic Geology* **87**, 1566-1583.

Heinrich, C A., Gunther, D., Audetat, D., Ulrich, T. & Frischnecht, R., 1999. Metal fractionation between magmatic brine and vapor, determined by microanalysis of fluid inclusions. *Geology* **27**, 755-758.

Henley, R.W. & Ellis, A.J., 1983. Geothermal systems ancient and modern: a geochemical review. *Earth Science Reviews* **19**, 1-50.

Henley, R.W. & McNabb, A., 1978. Magmatic vapor plumes and ground-water interaction in porphyry copper emplacement. *Economic Geology* **73**, 1-19.

Henley, R.W., Truesdell, A.H. & Barton, J., P.B., 1984. *Fluid-Mineral Equilibria in Hydrothermal Systems*. **1.** Society of Economic Geologists, Chelsea, Missouri, pp.267.

Hermoso, D.Z., 1983. *Preliminary Geological Report of Well PN26*. Unpublished Report. PNOC-EDC Geothermal Division.

Hinz, H. & Block, M., 1990. Summary of geophysical data from the Sulu and Celebes Seas. In: E. A. Silver, C. Rangin and M. T. von Breymann, et al. (ed). *Proceedings, Ocean Drilling Program, initial reports*. Ocean Drilling Program. **124.** 87-92.

Hochstaedter, A.G., Kepezhinskas, P.K., Defant, M.J., Drummond, M.S. & Bellon, H., 1994. On the tectonic significance of arc volcanism in northern Kamchatka. *Journal of Geology* **102**, 639-654.

Hochstein, M.P. & Browne, P.R.L., 2000. Surface manifestations of geothermal systems with volcanic heat sources. In: H. Sigurdsson (ed). *Encyclopedia of Volcanoes*. Academic Press. 835-855.

Hofstra, A.H., Leventhal, J.S., Northrop, H.R., Landis, G.P., Rye, R.O., Birak, D.J. & Dahl, A.R., 1991. Genesis of sediment-hosted disseminated-gold deposits by fluid mixing and sulphidisation: chemical-reaction-path modelling of ore-depositional processes documented in the Jerritt Canyon district, Nevada. *Geology* **19**, 36-40.

Hsu, L.C., 1986 The stability relationships of zunyite under hydrothermal conditions. *Mining Geology* **36**, 219-230.

Hulston, J.R., 1984. *Potassium Argon dating of Philippine geothermal rocks*. Unpublished Report. DSIR, Nuclear Sciences, Lower Hutt, N.Z. 1p.

Imai, H., Adachi, M., Takahashi, M., Yamaguchi, M. & Yashiro, K., 1988. Sulphide mineralisation in Oku-Aizu geothermal field, with the genetical relation to the epithermal gold deposits. *Mining Geology* **38**, 291-301.

Johnson, J.W., Oelkers, E.H. & Helgeson, H.C., 1992. SUPCRT92: A software package for calculating the standard molal thermodynamic properties of minerals, gases, aqueous species and reactions from 1 to 5000 bars and 0deg to 1000degC. *Computers and Geosciences* **18**, 899-947.

Jones, B.K., 1992. Application of metal zoning to gold exploration in porphyry copper systems. *Journal of Geochemical Exploration* **43**, 127-155.

Jordan, O.T., 1983. *Interpretation of the reservoir geochemistry of the Southern Negros geothermal field, Philippines (an update)*. Unpublished Report. PNOC-EDC.

Kavalieris, I., 1994. *The Grasberg Superporphyry*. Unpublished Report. CODES Key Centre, MEcon. Geol. Short Course Notes. University of Tasmania. 3.1-3.29 (unpublished).

Kay, R.W., 1978. Aleutian magnesian andesites: melts from subducted Pacific ocean crust. *Journal of Volcanology and Geothermal Research* **4**, 117-132.

Kay, S.M., Ramos, V.A. & Marquez, M., 1993. Evidence in Cerro Pampa volcanic rocks for slab melting prior to ridge-trench collision in southern South America. *Journal of Geology* **101**, 703-714

Kepezhinskas, P.K., 1989. Origin of the hornblende andesites of northern Kamchatka. *International Geology Reviews* **31**, 246-252.

KRTA, 1977. *Review of geothermal potential and recommendations for exploration wells Okoy 1 and Okoy 2, Southern Negros, Philippines*. Unpublished Report. Kingston Reynolds Thom & Allardice Ltd.

Leach, T.M. & Bogie, I., 1982. Overprinting of hydrothermal regimes in the Palinpinon geothermal field, Southern Negros, Philippines. *4th New Zealand Geothermal Workshop,* Auckland, New Zealand, 179-183.

Lindgren, W., 1933. *Mineral Deposits*. McGraw Hill, New York, pp.929.

Lister, C.R.B., 1974. On the penetration of water into hot rock. *Geophysical Journal of the Royal Astronomical Society* **39**, 465-509.

Losada-Calderon, A.J. & McPhail, D.C., 1996. Porphyry and high-sulphidation epithermal mineralisation in the Nevados del Famatina mining district, Argentina. In: F. Camus, Sillitoe, R.H., Petersen, R. (eds). *Andean copper deposits: new discoveries, mineralisation, styles and metallogeny.* Society of Economic Geology. **5.** 91-118.

Maglambayan, V.B., Ishiyama, D., Mizuta, T., Imai, A. & Ishikawa, Y., 1998. Geology, alteration, mineralogy and formation environment of the disseminated gold-silver telluride Bulawan deposit, Negros Occidental, Philippines. *Resource Geology* **48**, 87-104.

Maunder, B.R., Brodie, A.J. & Tolentino, B.S., 1982. The Palimpinon geothermal resource, Negros, Republic of the Philippines. An exploration case history. *4th N.Z. Geothermal Workshop,* Auckland, N.Z., 87-92.

McCabe, R., Almasco, J. & Diegor, W., 1982. Geologic and paleomagnetic evidence for a possible Miocene collision in western Panay, central Philippines. *Geology* **10**, 325-329.

McDougall, I., 1985. K-Ar and $^{40}Ar/^{39}Ar$ dating of the hominid-bearing Pliocene-Pleistocene sequence at Koobi Fora, Lake Turkana, northern Kenya. *Geological Society of America Bulletin* **96**, 159-175.

McDougall, I & Harrison, T.M., 1999. *Geochronology and Thermochronology by the $^{40}Ar/^{39}Ar$ Method.* Oxford University Press, pp.212.

McKibben, M.A., Williams, A.E. & Hall, G.E.M., 1989. Precious metals in the Salton Sea geothermal brines. *Geothermal Resources Council, Transactions* **13**, 45-48.

McKibben, M.A., Williams, A.E. & Hall, G.E., 1990. Solubility and transport of platinum-group elements and Au in saline hydrothermal fluids: constraints from geothermal brine data. *Economic Geology* **85**, 1926-1934.

Meyer, C. & Hemley, J.J., 1967. Wall rock alteration. In: H. L. Barnes (ed). *Geochemistry of hydrothermal ore deposits.* Holt, Rhinehart & Winston. 166-235.

Mitchell, A.H.G., Hernandez, F. & dela Cruz, A.P., 1986. Cenozoic evolution of the Philippine archipelago. *Journal of Southeast Asian Earth Sciences* **1**, 3-22.

Mitchell, A.H.G. & Leach, T.M.L., 1991. *Epithermal Gold in the Philippines: Island Arc Metallogenesis, Geothermal Systems and Geology.* Academic Press, London, pp.457.

Moore, J.N., Powell, T.S., Heizler, M.T. & Norman, D.I., 2000. Mineralisation and hydrothermal history of the Tiwi geothermal system, Philippines. *Economic Geology* **95**, 1001-1023.

Moyle, A.J., Doyle, B.J., Hoogvliet, H. & Ware, A.R., 1990. Ladolam gold deposit, Lihir Island. In: F. E. Hughes (ed). *Geology of the mineral deposits of Australia and Papua New Guinea.* Australasian Institute of Mining and Metallurgy, Monograph 14. **2.** 1793-1806.

Muntean, J.L. & Einaudi, M.T., 2001. Porphyry-epithermal transition: Maricunga belt, northern Chile. *Economic Geology* **96**, 743-772.

Norman, D.K., Parry, W.T. & Bowman, J.R., 1991. Petrology and geochemistry of propylitic alteration at southwest Tintic, Utah. *Economic Geology* **86**, 13-28.

Norrish, K. & Chappell, B.W., 1977. X-ray fluorescence spectrometry. In: J. Zussman (ed). *Physical Methods in Determinative Mineralogy.* Academic Press. 201-272.

Norrish, K. & Hutton, J.T., 1969. An accurate X-ray spectrographic method for analysis of a wide range of geological samples. *Geochimica et Cosmochimica Acta* **33**, 431-453.

Norton, D.L. & Cathles, L.M., 1973. Breccia pipes, products of exsolved vapour from magmas. *Economic Geology* **68**, 540-546.

Peacock, S.M., Rushmer, T. & Thompson, A.B., 1994. Partial melting of subducting oceanic crust. *Earth and Planetary Science Letters* **121**, 227-244.

Peccerillo, R. & Taylor, S.R., 1976. Geochemistry of Eocene calc-alkaline volcanic rocks from the Kastamonu area, northern Turkey. *Contributions to Mineralogy and Petrology* **58**, 63-81.

Plumlee, G.S., 1994. Fluid chemistry evolution and mineral deposition in the main-stage Creede epithermal system. *Economic Geology* **89**, 1860-1882.

PNOC-EDC, 1992. Structural map, Southern Negros Geothermal Project. *Unpublished internal report.* 1:20 000.

Pornuevo, J.B., 1984. Lithologic map of Southern Negros geothermal project. *Unpublished internal report.* 1:50 000.

Porth, H., Müller, C. & von Daniels, C.H., 1989. The sedimentary formations of the Visayan Basin, Philippines. In: H. Porth and C. H. von Daniels (ed). *On the Geology and Hydrocarbon Prospects of the Visayan Basin, Philippines.* Geologisches Jahrbuch. **B70.** 7-27.

Potter, R.W., Clynne, M.A. & Brown, D.L., 1978. Freezing point depression of aqueous sodium chloride solutions. *Economic Geology* **73**, 284-285.

Prouteau, G., Maury, R.C., Sajona, F.G., Cotten, J. & Joron, J.L., 2000. Behaviour of niobium, tantalum and other high field strength elements in adakites and related lavas from the Philippines. *The Island Arc* **9**, 487-498.

Pubellier, M., Quebral, R., Rangin, C., Deffontaines, B., Müller, C., Butterlin, J. & Manzano, J., 1991. The Mindanao collision zone: a soft collision event within a continuous Neogene strike-slip setting. *Journal of Southeast Asian Earth Sciences* **6**, 239-248.

Pubellier, M., Quebral, R., Aurelio, M. & Rangin, C., 1996. Docking and post-docking escape tectonics in the southern Philippines. In: R. Hall and D. J. Blundell (ed). *Tectonic Evolution of Southeast Asia.* Geological Society Special Publication. **106.** 511-523.

Rae, A.J., Brown, K.L., Leach, T.L., Jordan, O.T. & Hermoso, D.Z., 1998. Trace metals in deep geothermal water, Palinpinon geothermal field, Southern Negros, Philippines. *20th N.Z. Geothermal Workshop,* Auckland, N.Z., 233-238.

Rangin, C., 1989. The Sulu Sea: a back-arc basin setting within a Neogene collision zone. *Tectonophysics* **161**, 119-141.

Rangin, C., 1991. The Philippine mobile belt: a complex plate boundary. *Journal of Southeast Asian Earth Sciences* **6**, 209-220.

Rangin, C. & Silver, E.A., 1991. Neogene tectonic evolution of the Celebes-Sulu Basins: new insights from Leg 124 drilling. In: E. A. Silver, C. Rangin and M. T. von Breymann, et al. (ed). *Proceedings, Ocean Drilling Program, scientific results.* Ocean Drilling Program. **124.** 51-63.

Rangin, C., Stephan, J.F. & Müller, C., 1985. Middle Oligocene oceanic crust of South China Sea jammed into Mindoro collision zone (Philippines). *Geology* **13**, 425-428.

Rangin, C., Müller, C. & Porth, H., 1989. Neogene geodynamic evolution of the Visayan region. In: H. Porth and C. H. v. Daniels (ed). *On the Geology and Hydrocarbon Prospects of the Visayan Basin, Philippines.* Geologisches Jahrbuch. **B70.** 7-27.

Rangin, C., Jolivet, L. & Pubellier, M., 1990. A simple model for the tectonic evolution of southeast Asia and Indonesia region for the past 43 m.y. *Bulletin of the Geological Society of France* **8**, 889-905.

Reagan, M.K. & Gill, J.B., 1989. Coexisting calcalkaline and high-niobium basalts from Turrialba volcano, Costa Rica: implications for residual titanites in arc magma sources. *Journal of Geophysical Research* **94**, 4619-4633.

Reed, M.H., 1982. Calculation of multicomponent chemical equilibria and reaction processes in systems involving minerals, gases and an aqueous phase. *Geochimica et Cosmochimica Acta* **46**, 513-528.

Reed, M.H., 1994. Hydrothermal alteration in active continental hydrothermal systems. In: D. R. Lentz (ed). *Alteration and alteration processes associated with ore-forming systems.* Geological Association of Canada. **11.** 315-337.

Reed, M.H. & Spycher, N.F., 1985. Boiling, cooling, and oxidation in epithermal systems: a numerical modeling approach. In: B. R. Berger and P. M. Bethke (ed). *Geology and Geochemistry of Epithermal Systems.* Society of Economic Geologists. **2.** 249-272.

Reyes, A.G., 1990. Petrology of Philippine geothermal systems and the application of alteration mineralogy. *Journal of Volcanology and Geothermal Research* **43**, 279-309.

Reyes, A.G., 1995. Geothermal systems in New Zealand and the Philippines - why are they so different? *PACRIM Congress 1995,* Auckland, New Zealand, 485-490.

Reyes, A.G. & Cardile, C.M., 1989. Characterisation of clay scales forming in Philippine geothermal wells. *Geothermics* **18**, 429-446.

Reynolds, T.J & Beane, R.E., 1985. Evolution of hydrothermal fluid characteristics at the Santa Rita, New Mexico, porphyry copper deposit. *Economic Geology* **80**, 1328-1347.

Richards, J.P., 1992. Magmatic-epithermal transitions in alkalic systems: Porgera gold deposit, Papua New Guinea. *Geology* **20**, 547-550.

Roedder, E., 1984. *Fluid Inclusions.* **12.** Mineralogical Society of America, Chelsea, Michigan, pp.646.

Roedder, E. & Bodnar, R.J., 1980. Geologic pressure determinations from fluid inclusion studies. *Annual Reviews of Earth & Planetary Sciences* **8**, 263-301.

Roeser, H.A., 1991. Age of the crust of the southeast Sulu Sea basin based on magnetic anomalies and age determined at site 768. In: E. A. Silver, C. Rangin and M. T. von Breymann, et al. (ed). *Proceedings, Ocean Drilling Program, scientific results.* Ocean Drilling Program. **124.** 339-343.

Rohrlach, B., Madera, A. & Watt, R., 1999. Geology, alteration and mineralisation of the Tampakan copper deposit. *PACRIM,* Bali, Indonesia, 517-525.

Ruaya, J.R., 1980. *Comments on the geology and geochemistry of Kaipohan areas, Southern Negros geothermal Project.* Unpublished Report. PNOC-EDC.

Rutherford, M.J. & Hill, P.M., 1993. Magma ascent rates from amphibole breakdown: an experimental study applied to the 1980-1986 Mount St. Helens eruptions. *Journal of Geophysical Research* **98**, 19,667-19,685.

Ryan, C.G., Jamieson, D.N., Griffin, W.L., Cripps, G. & Szymanski, R., 2001. The new CSIRO-GEMOC nuclear microprobe: first results, performance and recent publications. *Nuclear Instruments & Methods B*, in press.

Rye, R.O., 1993. The evolution of magmatic fluids in the epithermal environment: the stable isotope perspective. *Economic Geology* **88**, 733-752.

Rye, R.O., Bethke, P.M. & Wasserman, M.D., 1992. The stable isotope geochemistry of acid sulphate alteration. *Economic Geology* **87**, 225-262.

Sajona, F.G. & Maury, R.C., 1998. Association of adakites with gold and copper mineralisation in the Philippines. *Comptes Rendus de l'Academie des Sciences, Sciences de la Terre et Des Planetes* **326**, 27-34.

Sajona, F.G., Bellon, H., Maury, R.C., Pubellier, M., Cotten, J. & Rangin, C., 1994. Magmatic response to abrupt changes in tectonic setting: Pliocene-Quaternary calc-alkaline lavas and Nb-enriched basalts of Leyte and Mindanao, Philippines. *Tectonophysics* **237**, 47-72.

Sajona, F.G., Maury, R.C., Bellon, H., Cotten, J., Defant, M.J. & Pubellier, M., 1993. Initiation of subduction and the generation of slab melts in western and eastern Mindanao, Philippines. *Geology* **21**, 1007-1010.

Sajona, F.G., Maury, R.C., Bellon, H., Cotten, J. & Defant, M., 1996. High field strength element enrichment of Pliocene-Pleistocene island arc basalts, Zamboanga Peninsula, Western Mindanao (Philippines). *Journal of Petrology* **37**, 693-726.

Sajona, F.G., Maury, R.C., Prouteau, G., Cotton, J., Schiano, P., Bellon, H. & Fontaine, L., 2000a. Slab melt as metasomatic agent in island arc magma mantle sources, Negros and Batan (Philippines). *The Island Arc* **9**, 472-486.

Sajona, F.G., Maury, R C., Pubellier, M., Leterrier, J., Bellon, H. & Cotten, J., 2000b. Magmatic source enrichment by slab-derived melts in a young post-collision setting, central Mindanao Philippines. *Lithos* **54**, 173-206.

Sarewitz, D.R. & Karig, D.E., 1986a. Geologic evolution of western Mindoro Island and the Mindoro suture zone, Philippines. *Journal of Southeast Asian Earth Sciences* **1**, 117-141.

Sarewitz, D.R. & Karig, D.E., 1986b. Processes of allochthonous terrane evolution, Mindoro Island, Philippines. *Tectonics* **5**, 525-552.

Schiano, P., Clocchiatti, R., Shimizu, N., Maury, R.C., Jochum, K.P. & Hofmann, A.W., 1995. Hydrous, silica-rich melts in the sub-arc mantle and their relationship with erupted arc lavas. *Nature* **377**, 595-600.

Seastres, J.S., 1982. Subsurface geology of the Nasuji-Sogongon sector, Southern Negros geothermal field, Philippines. *4th N.Z. Geothermal Workshop,* Auckland, N.Z., 173-178.

Seastres, J.S., 1985. *Hydrothermal alteration and chemistry of sulphate-rich wells in the Southern Negros geothermal field, Philippines.* Unpublished Report. Geothermal Institute, University of Auckland.

Shepherd, T.J., Rankin, A.H. & Alderton, D.H.M., 1985. *A practical guide to fluid inclusion studies.* Blackie & Son Ltd, London, pp.239.

Shinohara, H., Kazahaya, K. & Lowenstern, J.B., 1995. Volatile transport in a convecting magma column: implications for porphyry Mo mineralisation. *Geology* **23**, 1091-1094.

Sillitoe, R.H., 1973. The tops and bottoms of porphyry copper deposits. *Economic Geology* **68**, 799-815.

Sillitoe, R.H., 1989. Gold deposits in western Pacific island arcs: the magmatic connection. *Economic Geology* Monograph 6, 266-283.

Sillitoe, R.H., 1994. Erosion and collapse of volcanoes: causes of telescoping in intrusion-centred ore deposits. *Geology* **22**, 945-948.

Sillitoe, R.H., 1999. Styles of high-sulphidation gold, silver and copper mineralisation in porphyry and epithermal environments. *PACRIM,* Bali, Indonesia, 29-44.

Sillitoe, R.H. & Gappe, I.M., 1984. *Philippine porphyry copper deposits : geologic setting and characteristics.* Unpublished Report. CCOP Technical Publication.

Silver, E.A. & Rangin, C., 1991. Leg 124 tectonic synthesis. In: E. A. Silver, C. Rangin and M. T. von Breymann, et al. (ed). *Proceedings, Ocean Drilling Program, scientific results.* Ocean Drilling Program. **124.** 3-9.

Simmons, S.F. & Browne, P.R.L., 1997. Saline fluid inclusions in sphalerite from the Broadlands-Ohaaki geothermal system: a coincidental trapping of fluids being boiled toward dryness. *Economic Geology* **92**, 485-489.

Simmons, S.F. & Browne, P.R.L., 2000. Hydrothermal minerals and precious metals in the Broadlands-Ohaaki geothermal system: implications for understanding low-sulphidation epithermal environments. *Economic Geology* **95**, 971-999.

Skinner, B.J., White, D.E., Rose, H.J. & Mays, R.E., 1967. Sulfides associated with the Salton Sea geothermal brine. *Economic Geology* **62**, 316-330.

Spycher, N.F. & Reed, M.H., 1989. Evolution of a Broadlands-type epithermal ore fluid along alternative P-T paths: implications for the transport and deposition of base, precious, and volatile metals. *Economic Geology* **84**, 328-359.

Steiger, R.H. & Jager, E., 1977. Subcommission on geochronology: convention on the use of decay constants in geo- and cosmochronology. *Earth and Planetary Science Letters* **36**, 359-362.

Stephan, J.F., Blanchet, R., Rangin, C., Pelletier, B , Letouzey, J. & Müller, C., 1986. Geodynamic evolution of the Taiwan-Luzon-Mindoro belt since the late Eocene. *Tectonophysics* **125**, 245-268.

Stern, C.R. & Kilian, R., 1996. Role of the subducted slab, mantle wedge and continental crust in the generation of adakites from the Andean Austral Volcanic Zone. *Contributions to Mineralogy and Petrology* **123**, 263-281.

Tetley, N., MacDougall, I. & Heydegger, H.R., 1980. Thermal neutron interferences in the $^{40}Ar/^{39}Ar$ dating technique. *Journal of Geophysical Research* **85**, 7201-7205.

Thompson, J.F.H., Abidin, H.Z., Both, R.A., Martosuroyo, S., Rafferty, W.J. & Thompson, A.J.B., 1994. Alteration and mineralisation in the Masupa Ria volcanic center. Central Kalimantan, Indonesia. *Journal of Geochemical Exploration* **50**, 429-456.

Titley, S.R., 1975. Geological characteristics and environment of some porphyry copper occurrences in the southwestern Pacific. *Economic Geology* **70**, 499-514.

Titley, S.R., 1982. The style and progress of mineralisation and alteration in porphyry copper systems. In: S. R. Titley (ed). *Advances in Geology of the Porphyry Copper Deposits, Southwestern North America.* University of Arizona Press. 93-116.

Tracy, R.J & Frost, B.R., 1991. Phase equilibria and thermobarometry of calcareous, ultramafic and mafic rocks, and iron formations. In: D. M. Kerrick (ed). *Reviews in Mineralogy, Contact Metamorphism.* Mineralogical Society of America. **26.** 207-289.

Urbino, M.E.G., Zaide, M.C., Malate, R.C.M. & Bueza, E.L., 1986. Structural flowpaths of reinjected fluids based ion tracer tests - Palinpinon I, Philippines. *8th N.Z. Geothermal Workshop,* Auckland, N.Z., 53-58.

Verbeeten, A., 1996. *Petrology, geochemistry and tectonic implications of magmatism along the northern Hunter Ridge and Kadavu Island group, Fiji.* Unpublished PhD thesis. University of Tasmania

von Biedersee, H. & Pichler, H., 1995. The Canlaon and its neighbouring volcanoes in the Negros Belt/Philippines. *Journal of Southeast Asian Earth Sciences* **11**, 111-123.

Ward, C.W., 1980. Exploration of the Okoy geothermal field. *2nd N.Z Geothermal Workshop,* Auckland, N.Z., 105-108.

Watson, 1996. Fast, simple method of powder pellet preparation for X-ray fluorescence analysis. *X-Ray Spectrometry* **25**, 174-174.

Weissberg, B.G., 1969. Gold-silver ore-grade precipitates from New Zealand thermal waters. *Economic Geology* **64**, 95-108.

Weissberg, B G., Browne, P.R.L. & Seward, T.M., 1979. Ore metals in active geothermal systems. In: H. L. Barnes (ed). *Geochemistry of Hydrothermal Ore Deposits.* Wiley-Interscience. 739-780.

Werre, R.W., Bodnar, R.J., Bethke, P.M. & Barton, P.B., 1979. A novel gas-flow fluid inclusion heating/freezing stage. *Geological Society of America, Abstracts with Programs* **11**, 540.

White, D.E., 1955. Thermal springs and epithermal ore deposits. *Economic Geology* **50**, 99-154.

White, D.E., 1981. Active geothermal systems and hydrothermal ore deposits. *Economic Geology* **75**, 392-423.

White, N.C. & Hedenquist, J.W., 1990. Epithermal environments and styles of mineralization: variations and their causes, and guidelines for exploration. *Journal of Geochemical Exploration* **36**, 445-474.

White, N.C., Leake, M.J., McCaughey, S.N. & Parris, B.W., 1995. Epithermal gold deposits of the southwest Pacific. *Journal of Geochemical Exploration* **54**, 87-136.

Wood, C.P., 1982. *Report of the DSIR scientific mission to the Philippines.* Unpublished Report. Department of Scientific and Industrial Research.

Woods, T.L., Bethke, P.M., Bodnar, R.J. & Werre, R.W., 1981. Supplementary components and operation of the U.S. Geological Survey gas-flow heating/freezing stage. *U.S.G.S. Open File Report* **81-954**, pp. 12.

Yogodzinski, G.M., Kay, R.W., Volynets, O.N., Koloskov, A.V. & Kay, S.M., 1995. Magnesian andesite in the western Aleutian Komandorsky region: Implications for slab melting and processes in the mantle wedge. *Geological Society of American Bulletin* **107**, 505-519.

Yumul Jr., G.P., Dimalanta, C.B., Bellon, H., Faustino, D.V., De Jesus, J.V., Tamayo Jr., R.A. & Jumawan, F.T., 2000. Adakitic lavas in the Central Luzon back-arc region (Philippines): lower crust melting products. *The Island Arc* **9**, 499-512.

Zaide, M.C., 1984. *Interpretation of rock-dating results in the Southern Negros geothermal field.* Unpublished Report. PNOC-EDC Geothermal Division.

APPENDIX 1: ANALYTICAL TECHNIQUES

A1.1: RADIOMETRIC DATING

K-Ar Analysis

The alunite sample was prepared for conventional K-Ar analysis, as described by McDougall (1985). Separate aliquots of the sample were selected for duplicate potassium and argon analyses. Two aliquots were dissolved in sulphuric acid and hydrofluoric acid and the potassium concentrations were determined by standard flame photometric methods. A third weighed aliquot of the sample was loaded into a degassed Mo bucket and placed into a glass bottle connected to a high vacuum system. The sample was heated by radio-frequency induction to a temperature of ~1450°C to ensure complete outgassing. Argon measurements were carried out on splits of the same sample, using an MS10 mass spectrometer and standard isotope dilution methods with a ^{38}Ar spike

$^{40}Ar/^{39}Ar$ Analysis

The $^{40}Ar/^{39}Ar$ dating technique is described in detail by McDougall and Harrison (1999). Approximately 200 mg of each sample was wrapped in aluminium packets and placed into an aluminium irradiation canister together with interspersed aliquots of the flux monitor Fish Canyon Tuff biotite (FCT-1, Age = 27 95 Ma; Baksi et al., 1996). This canister was irradiated for 48 hours in position X34 of the HIFAR reactor, Lucas Heights, Sydney, Australia. After irradiation, the sample was removed from its packaging and ~40 – 150 mg aliquots were loaded into tin foil packets for analysis. The samples were then dropped into a Tantalum resistance furnace and heated to progressively higher temperatures, with temperatures maintained for fifteen minutes per step. The $^{40}Ar/^{39}Ar$ step-heating analyses were carried out on a VG MM12 mass spectrometer using an electron multiplier detector at the Australian National University (ANU). Mass discrimination was monitored by analyses of standard air volumes. Correction factors for interfering reactions are as follows:

$(^{36}Ar/^{37}Ar)_{Ca} = 3.20\ (\pm\ 0.02) \times 10^{-4}$

$(^{39}Ar/^{37}Ar)_{Ca} = 7.86\ (\pm\ 0\ 5) \times 10^{-4}$ (Tetley et al., 1980)

$(^{40}Ar/^{39}Ar)_{K} = 0.051\ (\pm\ 0\ 010)$

The K/Ca ratios were determined from the ANU laboratory hornblende standard 77-600 and were calculated as follows

$K/Ca = 1.90 \times {}^{39}Ar/{}^{37}Ar$

The reported data have been corrected for system backgrounds, mass discrimination and radioactive decay. The $^{40}Ar^*/^{39}Ar$ ratios and ages have also been corrected for fluence gradients

and atmospheric contamination. Errors associated with the age determinations are one sigma uncertainties and exclude errors in the J-value estimates. The error on the J-value is ±0.5%, excluding the uncertainty in the age of FCT-1 (which is ~1%). Decay constants are those of Steiger and Jager (1977)

A1.2: X-RAY FRACTIONATION TECHNIQUES AND WHOLE ROCK METAL ANALYSES

Analytical Methods for Whole-Rock Geochemistry

Samples selected for analysis were crushed in a hydraulic press between tungsten carbide plates. Any fragments with altered or weathered surfaces, or surfaces containing saw marks from thin section preparation, were discarded. The fragments were then passed through a sample splitter until about ~100 g remained (generally two passes). Twenty grams of the ~100 g sample fraction was then ground to a fine powder in a tungsten carbide mill.

Powders were reserved for major and trace element analysis at the University of Tasmania. Gold was analysed by neutron activation analysis at Becquerel Laboratory.

Major Element Analyses

Major element oxide abundances for each sample were measured on a Philips PW 1480 automated X-ray fluorescence (XRF) spectrometer at the University of Tasmania (School of Earth Sciences). Spectrometer calibration was maintained using international and in-house standards and pure silica blanks. Elements were analysed on fused glass discs, made using the method described by Norrish and Hutton (1969). Ignition losses (LOI) were determined by heating ~1 g of powdered sample to 1000°C for twelve hours in a pure vitreosil silica or platinum crucible, followed by cooling the sample to 400°C for five hours, and subsequently calculating the weight percent loss. Net weight gain (positive LOI) for some samples results from the oxidation of FeO to Fe_2O_3 during ignition being greater than the total volatile loss for the sample. Instrument operating conditions and counting times are outlined in Table A1.1.

Table A1.1. Instrument operating conditions and counting times for major element oxide analysis on the Philips PW1480 XRF spectrometer.

OXIDE	OPERATING CONDITIONS	EMISSION LINE	COLLIMATOR	X-RAY TUBE	CRYSTAL	COUNTING TIME (secs.)
SiO_2	40 kV, 70 mA	K-alpha	coarse	Sc-Mo	PE	50
TiO_2	40 kV, 70 mA	K-alpha	fine	Sc-Mo	LiF200	40
Al_2O_3	40 kV, 70 mA	K-alpha	coarse	Sc-Mo	PE	50
Fe_2O_3	90 kV, 30 mA	K-alpha	fine	Sc-Mo	Lif200	10
MnO	90 kV, 30 mA	K-alpha	fine	Sc-Mo	LiF200	20
MgO	40 kV, 70 mA	K-alpha	coarse	Sc-Mo	PX-1	50
CaO	40 kV, 70 mA	K-alpha	fine	Sc-Mo	LiF200	10
Na_2O	40 kV, 70 mA	K-alpha	coarse	Sc-Mo	PX-1	100 + 50(bgd.*)
K_2O	40 kV, 70 mA	K-alpha	fine	Sc-Mo	LiF200	20
P_2O_5	40 kV, 70 mA	K-alpha	coarse	Sc-Mo	GE	40

*bgd is background counting time for Na_2O analysis

Trace Element Analyses

X-Ray Fluorescence (XRF)

Trace element abundances were measured on pressed powder pills using the Philips PW 1480 automated X-ray fluorescence (XRF) spectrometer at the University of Tasmania (School of Earth Sciences). Spectrometer calibration was maintained using international and in-house standards and pure silica blanks. Mass absorption coefficients calculated from major element analyses and Compton Scattering were used to correct trace element concentrations. Powdered basalt samples were made into 10 g pressed pellets with a PVP-MC binder, following the method of Norrish and Chappell (1977) and Watson (1996). Elements analysed, analytical conditions and detection limits are outlined in Table A1.2.

Table A1.2. Instrument operating conditions and detection limits for trace element analysis on the Philips PW1480 XRF spectrometer.

ELEMENT	OPERATING CONDITIONS	EMISSION LINE	X-RAY TUBE	DETECTION LIMIT (ppm)
Rb	90 kV, 30 mA	K-alpha	Sc-Mo	1
Sr	80 kV, 35 mA	K-alpha	Au	1
Ba	40 kV, 70 mA	L alpha	Au	4
Sc	40 kV, 70 mA	K-alpha	Au	2
V	40 kV, 70 mA	K-alpha	Au	1.5
Cr	40 kV, 70 mA	K-alpha	Au	1
Ni	90 kV, 30 mA	K-alpha	Sc-Mo	1
Cu	90 kV, 30 mA	K-alpha	Sc-Mo	1
Zn	90 kV, 30 mA	K-alpha	Sc-Mo	1
La	70 kV, 40 mA	L-alpha	Au	2
Sb	100 kV, 30 mA	K-alpha	Au	2
As	100 kV, 30 mA	K-beta	Sc-Mo	3
Y	90 kV, 30 mA	K-alpha	Sc-Mo	1
Zr	80 kV, 35 mA	K-alpha	Au	1
Nb	80 kV, 35 mA	K-alpha	Au	1
Pb	90 kV, 30 mA	L-beta	Sc-Mo	1.5
Mo	100 kV, 30 mA	K-alpha	Rh	1
Ag	100 kV, 30 mA	K-alpha	Au	2

Detection limits are 3σ (99 %) confidence levels

Table A1.3.a Bulk rock, base and precious metal analyses of drillcuttings and drillcores from wells OK1 and OK4. Drillcore depth intervals are shown in italics. For each sample, the rock formation and dominant alteration type are also presented. A key for the abbreviations is listed in Table A1.3.b

Well	Depth Interval (m)	Rock Form.	Alter. Type	Cu	Pb	Zn (ppm)	Mo	Ag	Au (ppb)
OK1	35-40	SNF	I	130	8	107	1 7	-	-
	100-105	SNF	I	154	11	87	1.7	-	-
	200-205	SNF	I	113	170	144	10.1	-	-
	299-302	SNF	I	87	19	87	3.3	-	-
	300-305	SNF	I	85	7	66	2.2	-	-
	400-405	SNF	I	99	9	67	3.3	-	-
	500-505	SNF	I	75	10	63	3.3	-	-
	600-605	SNF	I	62	7	61	2.3	-	-
	700-705	SNF	I	84	7	71	1 4	-	-
	760	SNF	AA	66	12	55	2 3	-	-
	800-805	SNF	I	82	9	64	2 1	-	-
	900-905	SNF	I	63	7	52	7 5	3.1	-
	1000-1005	OF	I	81	8	51	1.4	2.4	-
	1100-1105	OF	I	55	11	52	6 2	6	-
	1200-1205	OF	I	72	10	58	2 5	3 7	-
	1207.8	OF	I	108	20	55	15.1	3.7	-
	1300-1305	OF	I	67	13	57	1.4	2.7	-
	1353	OF	unalt	55	-	66	2.3	5.4	-
	1400-1405	OF	I	88	7	64	1.1	-	-
	1500-1505	OF	I	81	11	62	3	2.3	-
	1600-1605	OF	I	82	7	54	2.7	-	-
	1700-1705	OF	I	40	5	41	3.1	8	-
	1800-1805	OF	I	38	5	54	2	7.4	-
	1843.5	OF	I	79	4	65	1.3	3.7	-
	1900-1905	OF	I	66	8	61	1.9	3.9	-
	1982	OF	unalt	71	9	72	2.3	4.7	-

Well	Depth Interval (m)	Rock Form.	Alter. Type	Cu	Pb	Zn (ppm)	Mo	Ag	Au (ppb)
OK4	0-15	SNF	I	81	8	69	1 2	-	-
	100-105	SNF	I	89	18	73	1.9	-	-
	200-205	SNF	I	49	6	69	-	-	-
	300-305	SNF	I	212	8	67	1.1	-	8.5
	400-405	SNF	I	131	7	84	1.5	-	-
	500-505	SNF	I	96	8	80	-	-	-
	600-605	SNF	I	85	10	63	1.2	-	-
	700-705	SNF	AA	88	59	6	1.8	2.3	-
	725-728	SNF	I	33	5	144	-	-	-
	800-805	SNF	I	97	8	50	1.2	-	-
	900-905	SNF	I	116	12	57	1 4	-	-
	1000-1005	SNF	I	85	8	56	-	-	-
	1100-1105	SNF	I	36	8	66	1 6	-	-
	1200-1205	SNF	I	58	8	57	2 6	-	-
	1300-1305	SNF	I	101	8	54	1.9	-	-
	1400-1405	SNF	I	100	6	57	1.5	-	-
	1500-1505	OF	I	68	7	67	2.4	-	-
	1600-1605	OF	I	78	2	80	-	-	-
	1678-1681	OF	P (chl)	90	8	62	2.2	3.2	-
	1700-1705	OF	P (chl)	145	7	74	2.3	-	-
	1800-1805	OF	P (chl)	87	10	102	-	-	-
	1900-1905	OF	unalt	66	7	72	2.5	2.4	-
	1981-1984	OF	unalt	40	8	79	2.4	4.3	-
	2000-2005	OF	unalt	29	3	60	3.3	-	-
	2100-2105	OF	unalt	71	6	79	4.1	2.5	-
	2133-2137	OF	unalt	43	7	92	3.2	2.7	-

Table A1.3.b Bulk rock, base and precious metal analyses of drillcuttings and drillcores from well SG2. Drillcore depth intervals are shown in italics. Also presented are 30 rocks samples from surface outcrops and drillcore from 20 other geothermal wells. For each sample, the rock formation and dominant alteration are also presented.

Well	Depth Interval (m)	Rock Form.	Alter. Type	Cu	Pb	Zn (ppm)	Mo	Ag	Au (ppb)
SG2	27-30	SNF	I	101	5	68	-	-	-
	98-104	SNF	AA	69	22	35	3.2	-	-
	198-204	SNF	AA	75	21	89	1.6	2.3	-
	298-304	SNF	AA	90	29	47	1.6	2.7	-
	399-405	SNF	AA	78	27	77	-	-	-
	500-506	SNF	AA	106	14	51	7.2	-	-
	597-603	SNF	AA	114	41	31	7.3	-	-
	698-704	SNF	AA	91	81	44	3.3	2.5	-
	796-804	SNF	AA	42	60	5	7.6	-	7 2
	899-905	SNF	AA	50	106	6	2.8	-	8.9
	1000-1006	SNF	AA	28	110	8	2 2	-	-
	1097-1103	SNF	AA	53	311	18	2 7	-	-
	1198-1204	SNF	AA	27	115	5	2 8	-	-
	1298-1304	SNF	I	180	45	131	9 4	2.1	14.4
	1381-1387	SNF	I	188	24	117	10.7	3	-
	1700-1701	*NP*	B	103	20	127	20 6	2.3	-
	2660-2662	*NP*	P (tr-act	12	8	28	0.7	-	-
	2869-2871	*NP*	P (tr-act	12	9	35	-	-	-

Sample	Rock Form.	Alter. Type	Cu	Pb	Zn (ppm)	Mo	Ag	Au (ppb)
96001	SNF	unalt	105	9	65	1 4	-	-
96006	CVF	unalt	53	7	53	1.3	-	-
96008	CVF	unalt	34	4	57	1.4	-	-
96010	CVF	unalt	87	8	67	1.2	-	-
96014	CVF	unalt	51	7	56	1.5	-	-
PN1RD/3	PD	I	37	2	78	-	-	-
PN20D/2	PD	I	20	4	57	-	-	-
SG1/1	NP	I	24	14	58	1 4	-	-
NJ4D/2	NP	P (epi)	23	8	52	1 1	-	-
NJ6D/4	NP	P (epi)	218	6	104	-	-	-
OK9/6-2	PD	P (epi)	19	2	45	-	-	-
OK10D/6	PD	P (epi)	59	3	54	1 6	-	-
PN1RD/6	PD	P (epi)	57	6	54	1 7	-	-
PN30D/1	PD	P (epi)	107	3	75	3 6	-	-
NJ1D/5	NP	P (tr-act)	32	9	35	3	-	-
NJ2D/1	NP	P (tr-act)	47	6	29	2.4	-	-
NJ3D/3	NP	P (tr-act)	1025	10	54	4.9	2.6	45.3
NJ7D/1 (2)	NP	P (tr-act)	230	8	37	2.8	-	-
OK7/7	PD	P (tr-act)	116	4	72	1.2	-	-
OK8RD/2	NP	P (tr-act)	33	6	37	1.8	-	-
OK11D/3	NP	P (tr-act)	59	12	73	1.1	-	-
PN21D/4	PD	P (tr-act)	81	5	68	1.1	-	-
PN31D/4	PD	P (tr-act)	169	3	81	-	-	-
SG1RD/1 (2)	NP	P (tr-act)	159	24	123	1.3	-	-
SG3RD/1	NP	P (tr-act)	26	5	37	-	-	-
NJ3D/1	NP	B	142	12	105	3	-	-
NJ5D/3	NP	B	101	6	55	2.2	-	-
NJ5D/4 (2)	NP	B	202	3	44	3.5	-	50.3
NJ5D/5 (2)	LPV	B	42	8	76	-	-	-
PN25D/2	LPV	B	46	10	82	1	-	-

Key:

Rock Form. = Rock Formation
CVF = Cuernos Volcanic Formation
OF = Okoy Formation
LPV = Lower Puhagan Volcanics
NP = Nasuji Pluton
PD = Puhagan dikes
SNF = Southern Negros Formation

Alter. Type = Alteration Type
AA = advanced argillic
B = biotite
I = illite
P (chl) = propyltic (chlorite)
P (epi) = propylitic (epidote)
P (tr-act) = tremolite-actinolite
unalt = unaltered

A1.3: ANALYTICAL TECHNIQUES FOR ELECTRON MICROPROBE ANALYSES

Electron microprobe analyses were obtained using the Cameca Camebax SX-50 automated electron microprobe located at the University of Tasmania's Central Science Laboratory. This machine was equipped with three wavelength-dispersive spectrometers used for quantitative analysis and one energy-dispersive spectrometer used for qualitative spectral analysis. X-ray lines used for analyses were calibrated against international and in-house natural minerals, synthetic simple oxides and glass standards.

Sulphide and electrum scale analyses were collected with operating conditions set at 20 kV accelerating voltage, a 20 nA beam current and a 2-5 μm diameter beam. Peak and background counting times, analysing crystal used, and working detection limits for each element are given in Table A1.4. Background counting times were measured twice, once on either side of the peak. For elements where peak and background counting times are the same, the background was measured once only, on one side of the peak for analytical reasons.

Table A1.4. Peak and background counting times for elements analysed in sulphide and electrum scales.

ELEMENT	S	Fe	Cu	Zn	Pb	As	Sb	Bi	Se	Au	Hg
Analysing crystal	PET	LiF	LiF	LiF	PET	TAP	PET	PET	TAP	LiF	PET
Peak (s)	10	10	10	10	10	10	10	10	10	10	10
Background (s)	5	5	5	5	5	10	5	5	5	5	5
Detection limit (wt%)	0 09	0.04	0.05	0 07	0 07	0.05	0.04	0.09	0.04	0.07	0.06

A1.4: INDUCTIVELY COUPLED PLASMA MASS SPECTROMETRY (ICP-MS)

Trace metals in the downhole water and aqua regia samples were analysed on the "Element" Finnigan Magnetic Sector ICP-MS (Central Science Laboratory, 1998). Water samples were analysed as received and Indium (In) was added as an internal standard at a concentration of 10 ppb or 100 ppb. All aqua regia samples were diluted 1 in 10 with In added. No acid was added to any samples (aqua regia or waters) so as not to change the pH or cause other associated problems. An external calibration was performed (5 standards, top standard 50 ppb).

Sample	Chip	Class	Type	Population	Alteration Type	Te	Tm-H2O	Tm-other	Th	Tdissol.1	Tdissol.2	NaCl (<23.3wt%)	CaCl2 (wt%)	NaCl (>23.3wt%)	KCl (wt%)	TotalSalinity
N3/1	A	P	1a	B	Illite		-1.0		217.3			1.7				1.7
N3/1	C	P	1a	B	Illite		-0.3		217.0			0.5				0.5
N3/1	C	P	1a	B	Illite		-0.2		221 1			0.4				0.4
N3/1	D	P	1a	B	Illite		-0.8		216.5			1.4				1.4
N3/1	D	P	1a	B	Illite		-0.7		214 3			1.2				1.2
N3/4	A	P	1a	B	Illite		-0.9		251.9			1.6				1.6
N3/4	A	P	1a	B	Illite		-0.9		244.9			1.6				1.6
N3/4	A	P	1a	B	Illite		-0.8		247.5			1.4				1.4
N3/4	B	P	1a	B	Illite		-0.8		246.0			1.4				1.4
N3/4	B	P	1a	B	Illite		-0.7		246.1			1.2				1.2
N3/4	C	P	1a	B	Illite		-0.4		235.4			0.7				0.7
N3/4	D	P	1a	B	Illite		-2.0		251.6			3.4				3.4
N3/4	D	P	1a	B	Illite		-2 4		248 6			4 0				4 0
N3/6	C	P	1a	A	propylitic (chlorite)		-1.4		269.0			2.4				2 4
N3/6	B	S	1a	A	propylitic (chlorite)		-0 4		188.5			0 7				0 7
N3/6	B	P	1a	A	propylitic (chlorite)		-0.4		203.0			0.7				0.7
N3/6	B	P	1a	A	propylitic (chlorite)		-0.4		236 9			0.7				0.7
N3/6	B	S	1a	A	propylitic (chlorite)		-0.3		188.5			0 5				0.5
N3/6	A2	P	1a	A	propylitic (chlorite)		-0 4		241.4			0 7				0 7
N3/6	A2	P	1a	A	propylitic (chlorite)		-0.4		243.3			0.7				0 7
N3/6	A2	P	1a	A	propylitic (chlorite)		-0.4		247 0			0.7				0 7
N3/6	B2	P	1a	A	propylitic (chlorite)		-0.4		252.7			0.7				0.7
N3/6	B2	P	1a	A	propylitic (chlorite)		-0.2		250.0			0.4				0.4
N3/6	B2	P	1a	A	propylitic (chlorite)		-0.2		257.9			0.4				0.4
N3/6	B2	P	1a	A	propylitic (chlorite)		-0.4		262.0			0.7				0.7
N3/6	B2	P	1a	A	propylitic (chlorite)		-0.4		276.2			0.7				0.7
N3/6	B2	P	1a	A	propylitic (chlorite)		-0 4		263.4			0.7				0.7
NJ2D/1	A	P	1a	B	propylitic (epidote)		0.0		290.6			0.0				
NJ2D/1	A	P	1a	B	propylitic (epidote)		-		290.6							
NJ2D/1	A	P	1a	B	propylitic (epidote)		0.0		290.2			0.0				
NJ2D/1	A	P	1a	B	propylitic (epidote)		-1.0		287.8			1.7				1.7
NJ2D/1	A	P	1a	B	propylitic (epidote)		-1.0		268.8			1.7				1.7
NJ2D/1	B	P	1a	B	propylitic (epidote)		-0.3		309.2			0.5				0.5
NJ2D/1	B	P	1a	B	propylitic (epidote)		-0.4		297.3			0.7				0.7
NJ2D/1	B	P	1a	B	propylitic (epidote)		-0.3		294.1			0.5				0.5

Sample	Chip	Class	Type	Population	Alteration Type	Te	Tm-H2O	Tm-other	Th	Tdissol.1	Tdissol.2	NaCl (<23.3wt%)	CaCl2 (wt%)	NaCl (>23.3wt%)	KCl (wt%)	TotalSalinity
NJ2D/1	E	P	1a	B	propylitic (epidote)		0.0		278.8			0.0				
NJ2D/1	E	P	1a	B	propylitic (epidote)		-0 1		283.8			0.2				0.2
NJ2D/1	E	P	1a	B	propylitic (epidote)		0.0		282.8			0.0				
NJ2D/1	E	P	1a	B	propylitic (epidote)		0.0		284.7			0 0				
NJ2D/1	B	S	3ad	C	equigran qtz dio				396.0	431.8				49 1		49 1
NJ2D/1	B	S	3ad	C	equigran. qtz dio				304.6	414.1				47.4		47.4
NJ2D/1	B	S	3al	C	equigran qtz dio				>600	471 3				53 2		53 2
NJ2D/1	B	S	3al	C	equigran. qtz dio				420.6	418 5				47.8		47.8
NJ2D/1	B	S	3al	C	equigran. qtz dio				>600	454 0				51.3		51 3
NJ2D/1	B	S	2	C	equigran. qtz dio				-							
NJ2D/1	B	S	2	C	equigran. qtz dio				-							
NJ2D/1	B	S	2	C	equigran. qtz dio				-							
NJ2D/1	B	S	2	C	equigran. qtz dio				-							
NJ3D/3	1-inclus b	S	1b	C	porphyritic qtz dio		decrepitated		-							
NJ3D/3	1-inclus c	S	3bl	C	porphyritic qtz dio				429.7	347 7				41 5		41 5
NJ3D/3	2-inclus.a	S	3bd	C	porphyritic qtz dio				292 8	416 7				47 6		47 6
NJ3D/3	2-inclus c	S	3bd	C	porphyritic qtz dio				327 0	384.5				44.7		44 7
NJ3D/3	3-inclus d	S	3bd	C	porphyritic qtz dio				278 6	380 6				44 3		44 3
NJ3D/3	3-inclus.d	S	2	C	porphyritic qtz dio				-							
OK6/2	A	P	4	C	biotite				529.5	575.9	267 9			59.5	19.9	79 4
OK6/2	A	P	4	C	biotite				450 5	541.1	143.2			58.4	13.3	71.7
OK6/2	A	P	3bd	C	biotite				367.8	537.3				60.7		60.7
OK6/2	A	P	4	C	biotite				286.5	462.5	79.7			48.9	11.8	60.7
OK6/2	A	P	3bd	C	biotite				269.3	386				44.8		44.8
OK6/2	A	P	3al	C	biotite				435.0	403.6				46.4		46.4
OK6/2	B	S	1a	A	illite		-0.1		271.1			0.2				0.2
OK6/2		S	1a	A	illite		-0.1		237.9			0.2				0.2
OK6/2		S	1a	A	illite		-0.1		276.7			0.2				0.2
OK6/2		S	1a	A	illite		-0.1		266.2			0.2				0.2
OK6/2		P	3bd	C	biotite				416.3	559.5	135.0			61.6	11.9	73.5
OK7/7	1	P	1a	B	propylitic (epidote)	-69.1		-30.7	288.4			-				
OK7/7	1	P	1a	B	propylitic (epidote)	-		-	306.4							
OK7/7	1	P	1a	B	propylitic (epidote)	-		-	296.1			-				
OK7/7	1	P	1a	B	propylitic (epidote)	-60.1		-25.6	299.5			-				
OK7/7	1	P	1a	B	propylitic (epidote)	-61.1		-25.9	299.0			-				

Sample	Chip	Class	Type	Population	Alteration Type	Te	Tm-H2O	Tm-other	Th	Tdissol.1	Tdissol.2	NaCl (<23.3wt%)	CaCl2 (wt%)	NaCl (>23.3wt%)	KCl (wt%)	TotalSalinity
OK7/7	1	P	1a	B	propylitic (epidote)	-		-	299.2							
OK7/7	1	P	1a	B	propylitic (epidote)	-		-	283.5							
OK7/7	1	P	1a	B	propylitic (epidote)	-		-	285.8							
OK7/7	1	P	2	B	propylitic (epidote)				-							
OK7/7	1	P	2	B	propylitic (epidote)				-							
OK7/7	1	P	1a	B	propylitic (epidote)	-		-	290.3							
OK7/7	1	P	1a	B	propylitic (epidote)	-		-	308.4							
OK7/7	1	P	1a	B	propylitic (epidote)	-61.1		-25.0	301.7			-				
OK7/7	1	P	1a	B	propylitic (epidote)	-56.3		-26.2	301.8			-				
OK7/7	1	P	1a	B	propylitic (epidote)	-61.1		-26.8	295.8			-				
OK7/7	1	P	1a	B	propylitic (epidote)	-55.8		-24 9	300.2			-				
OK7/7	1	P	1a	B	propylitic (epidote)		-7.0		304.2			10 5				10.5
OK7/7	1	P	1a	B	propylitic (epidote)	-68 8	-3 2	-28 8	288.4			1.6	3 8			5.4
OK7/7	1	P	1a	B	propylitic (epidote)		-0.3		306.4			0.5				0.5
OK7/9	2	P	1a	B	propylitic (epidote)		-1 6		308.4			2 7				2.7
OK7/9	2	P	1a	B	propylitic (epidote)		-2 1		305.5			3.5				3.5
OK7/9	2	P	1a	B	propylitic (epidote)		-1 9		311.0			3 2				3.2
OK7/9	2	P	1a	B	propylitic (epidote)		-2 0		299 4			3 4				3.4
OK7/9	2	P	1a	B	propylitic (epidote)		-2 0		301.4			3.4				3.4
OK7/9	2	P	1a	B	propylitic (epidote)		-2 0		296.4			3.4				3.4
OK7/9		P	2		propylitic (epidote)				-							
OK7/9	2	P	1a	B	propylitic (epidote)		-2.0		300.5			3.4				3.4
OK8/5		S	1a	A	illite		-0.6		230.0			1.0				1.0
OK8/5		P	1a	A	illite		-		282.5			-				
OK8/5	A	S	1a	A	illite		-2.5		223.1			4.2				4.2
OK8/5		S	1b	A	illite	-23.5	-2.7		223.4			4.5				4.5
OK8/5		S	1a	A	illite		-2.7		224.3			4.5				4.5
OK8/5		S	1a	A	illite		0.0		225.7			0.0				
OK8/5		S	1a	A	illite		-1.8		224.6			3.1				3.1
OK8/5		S	1a	A	illite		-		200.8			-				
OK8/5	E	S	3ad	C	biotite				219.7	391.5				45.3		45.3
OK8/5		S	1a	A	illite		-		259.0			-				
OK8/5	D	S	1a	A	illite		0.0		226.3			0.0				
OK8/5		S	3ad	C	biotite				217.6	334.0				40.4		40.4
OK8/5		S	1a	A	illite		0.0		231.0			0.0				

Sample	Chip	Class	Type	Population	Alteration Type	Te	Tm-H2O	Tm-other	Th	Tdissol.1	Tdissol.2	NaCl (<23.3wt%)	CaCl2 (wt%)	NaCl (>23.3wt%)	KCl (wt%)	TotalSalinity
OK8/5	C	S	3ad	C	biotite				201.2	349.6				41.7		41.7
OK8/5		S	1a	A	illite		-0.1		344.7			0.2				0.2
OK8/5		S	1a	A	illite		-0.1		323.3			0.2				0.2
OK8/5		S	1a	A	illite		-0 1		313.1			0 2				0 2
OK8/5		S	1a	A	illite		-0.1		290.5			0.2				0 2
OK12D/5	A	P	1a	B	propylitic (epidote)	-19.0	-2.2		261.5			3.7				3.7
OK12D/5	F	P	1a	B	propylitic (epidote)		-1.7		268 0			2.9				2.9
PN1RD/2	2	P	1a	B	illite		-1 5		337 0			2.6				2.6
PN1RD/2	2	P	1a	B	illite		-		337.0							
PN1RD/2	2	P	1a	B	illite		-1.7		335.6	Boiling		2.9				2.9
PN1RD/2	2	P	1a	B	illite		-1.7		309.5	Zone		2.9				2.9
PN1RD/2	2	P	1a	B	illite		-1.8		308.0			3.1				3.1
PN1RD/2	2	P	1a	B	illite		-1 6		336 8			2.7				2.7
PN5RD/1	A	P	1a	B	illite		-1.0		280 8			1.7				1.7
PN5RD/1	A	P	1a	B	illite		-		319.0							
PN5RD/1	B	P	1a	B	illite		-1 6		266 8			2.7				2.7
PN5RD/1	C	P	1a	B	illite		-4.1		329 9			6.6				6 6
PN5RD/1	unmarked	P	1a	B	illite		-1 4		290.0			2 4				2.4
PN5RD/1	unmarked	P	1a	B	illite		-2.1		280.7			3.5				3.5
PN5RD/1	unmarked	P	1a	B	illite		-2.1		274.8			3.5				3.5
PN5RD/1	unmarked	P	1a	B	illite		-2.4		274 0			4 0				4.0
PN5RD/1	unmarked	S	1a	B	illite		-1.7		264.5			2.9				2.9
PN5RD/1	unmarked	S	1a	B	illite		-2.2		251.5			3.7				3.7
PN7RD/1	A	P	1a	B	propylitic (tre-act)		-1.2		298.1			2.1				2.1
PN7RD/1	A	P	1a	B	propylitic (tre-act)		-1.5		306.0			2.6				2.6
PN7RD/1	A	P	1a	B	propylitic (tre-act)		-1.6		308.8			2.7				2.7
PN7RD/1	A	P	1a	B	propylitic (tre-act)		-1.3		305.0			2.2				2.2
PN7RD/1	D	P	1a	B	propylitic (tre-act)		-1.4		310.2			2.4				2.4
PN7RD/1	D	P	1a	B	propylitic (tre-act)		-2.1		308.2			3.5				3.5
PN7RD/1	D	P	1a	B	propylitic (tre-act)		-1.3		309.6			2.2				2.2
PN7RD/1	D	P	1a	B	propylitic (tre-act)		-2.1		306.3			3.5				3.5
PN7RD/1	D	P	1a	B	propylitic (tre-act)		-		306.2							
PN16D/2	4	P	1a	B	propylitic (epidote)	-23.0	-3.4		309 9			5.5				5.5
PN16D/2	4	P	1a	B	propylitic (epidote)		-2.2		311.7			3.7				3.7
PN16D/2	4	P	1a	B	propylitic (epidote)		-6.4		311.0			9.7				9.7

Sample	Chip	Class	Type	Population	Alteration Type	Te	Tm-H2O	Tm-other	Th	Tdissol.1	Tdissol.2	NaCl (<23.3wt%)	CaCl2 (wt%)	NaCl (>23.3wt%)	KCl (wt%)	TotalSalinity
PN16D/2	4	P	1a	B	propylitic (epidote)		-		307.4							
PN16D/2	4	P	1a	B	propylitic (epidote)		-1.5		283.6			2.6				2.6
PN16D/2	4	P	1a	B	propylitic (epidote)		-1.5		289.0			2.6				2.6
PN16D/2	1	P	1a	B	propylitic (epidote)		-1 5		339 5			2.6				2.6
PN16D/2	1	P	1a	B	propylitic (epidote)		-0 5		274 6			0.9				0.9
PN16D/2	1	P	1a	B	propylitic (epidote)		-0 5		277.2			0.9				0.9
PN16D/2	1	P	1a	B	propylitic (epidote)		-0.8		281 8			1.4				1.4
PN16D/2	1	P	1a	B	propylitic (epidote)		-2.7		356.0			4 5				4 5
PN16D/2	1	P	1a	B	propylitic (epidote)		-0.3		314.9			0.5				0.5
PN16D/2	1	P	1a	B	propylitic (epidote)		-0.3		291 0			0.5				0.5
PN16D/2	1	P	1a	B	propylitic (epidote)		-0.3		289.2			0.5				0 5
PN16D/2	1	P	1a	B	propylitic (epidote)		-0.3		268.0			0.5				0 5
PN16D/2	1	P	1a	B	propylitic (epidote)		-0 3		268 0			0 5				0 5
PN16D/2	1	P	1a	B	propylitic (epidote)		-0 5		281.8			0.9				0.9
PN20D/2	5		1a	B	propylitic (tre-act)		-2 0		334.9			3 4				3 4
PN20D/2	5		1a	B	propylitic (tre-act)		-		351 2							
PN20D/2	5		1a	B	propylitic (tre-act)		-2 0		326 2			3 4				3 4
PN20D/2	5		1a	B	propylitic (tre-act)		-1.6		333 7			2 7				2.7
PN20D/2	4		1a	B	propylitic (tre-act)		-2 4		341.5			4 0				4.0
PN20D/2	4		1a	B	propylitic (tre-act)		-		269.3							
PN20D/2	4		3al	C	propylitic (tre-act)				267.4	262.7				35.4		35.4
PN20D/2	4		3al	C	propylitic (tre-act)				271.3	266.6				35 7		35.7
PN20D/2	4		3al	C	propylitic (tre-act)				271.3	268.5				35.8		35.8
PN20D/2	4		3ad	C	propylitic (tre-act)				262.7	276.7				36.3		36.3
PN20D/2	4		1a	B	propylitic (tre-act)				350.5							
PN20D/2	4		1a	B	propylitic (tre-act)				334.0							
PN20D/2	4		1a	B	propylitic (tre-act)				333.9							
PN20D/2	4		1a	B	propylitic (tre-act)				334.7							
PN20D/2	4		1a	B	propylitic (tre-act)				322.6							
PN22D/1	2	P	1a	B	propylitic (epidote)		-1.8		296.2			3.1				3.1
PN22D/1	2	P	1a	B	propylitic (epidote)		-1.2		288.4			2.1				2.1
PN22D/1	2	P	1a	B	propylitic (epidote)		-1.4		287.2			2.4				2.4
PN22D/1	2	P	1a	B	propylitic (epidote)		-1.4		262.5			2.4				2.4
PN22D/1	2	P	1a	B	propylitic (epidote)		-1.6		290.4			2.7				2.7
PN22D/1	2	P	1a	B	propylitic (epidote)		-1.6		294.2			2.7				2.7

Sample	Chip	Class	Type	Population	Alteration Type	Te	Tm-H2O	Tm-other	Th	Tdissol.1	Tdissol.2	NaCl (<23.3wt%)	CaCl2 (wt%)	NaCl (>23.3wt%)	KCl (wt%)	TotalSalinity
PN22D/1	2	P	1a	B	propylitic (epidote)		-1.2		281.2			2.1				2.1
PN22D/1	2	P	1a	B	propylitic (epidote)		-1.7		310.2			2.9				2.9
PN22D/1	5	P	1a	B	propylitic (epidote)		-2.0		312.4			3.4				3.4
PN22D/1	5	P	1a	B	propylitic (epidote)		-1 3		308.2			2 2				2 2
PN22D/1	5	P	1a	B	propylitic (epidote)		-2.1		293.0			3 5				3 5
PN22D/1	5	P	1a	B	propylitic (epidote)		-0.9		334.5			1.6				1.6
PN22D/1	5	P	1a	B	propylitic (epidote)		-2.1		294 4			3 5				3.5
PN22D/1	5	P	1a	B	propylitic (epidote)		-2 3		286.3			3.9				3.9
PN22D/1	5	P	1a	B	propylitic (epidote)		-1.9		283.5			3.2				3.2
PN22D/1	5	P	1a	B	propylitic (epidote)		-1.8		290.7			3.1				3.1
PN22D/1	5	P	1a	B	propylitic (epidote)		-1.5		283.8			2.6				2.6
PN22D/1	5	P	1a	B	propylitic (epidote)		-2.3		289.2			3.9				3.9
PN22D/1	5	P	1a	B	propylitic (epidote)		-2 5		299 7			4 2				4 2
PN22D/1	5	P	1a	B	propylitic (epidote)		-1 7		296 6			2.9				2.9
PN22D/1	5	P	1a	B	propylitic (epidote)		-3 0		289.4			4 9				4.9
PN25D/2	3	P	3a1	C	biotite				299 5	244 1		0.0		34 3		34.3
PN25D/2	4	P	1b	C	biotite				299.5							
PN25D/2	4	P	1b	C	biotite				298 5							
PN25D/2	4	P	1b	C	biotite				300.0							
PN25D/2	4	P	1b	C	biotite				299.4							
PN25D/2	4	P	1a	C	biotite				299.7							
PN25D/2	4	P	1b	C	biotite				300.6							
PN25D/2	4	P	1b	C	biotite				300 1							
PN25D/2	4	P	1a	C	biotite				298.4							
PN25D/2	5		1b	C	biotite				299.5							
PN30D/1	2	P	1a	B	propylitic (epidote)		-1.9		338.3			3.2				3.2
PN30D/1	2	P	1a	B	propylitic (epidote)		-2.4		337.5			4.0				4.0
PN30D/1	2	P	1a	B	propylitic (epidote)				345.7							
PN30D/1	1		1a	B	propylitic (epidote)		-1.8		326.4			3.1				3.1
PN30D/1	1		1a	B	propylitic (epidote)		-2.5		317.4			4.2				4.2
PN30D/1	1		1a	B	propylitic (epidote)		-1.8		314.2			3.1				3.1
PN30D/1			2	B	propylitic (epidote)											
PN30D/1			2	B	propylitic (epidote)											
PN30D/1	1		1a	B	propylitic (epidote)		-1.8		309.5			3.1				3.1
PN30D/1	1		1a	B	propylitic (epidote)		-2.4		320.1			4.0				4.0

Sample	Chip	Class	Type	Population	Alteration Type	Te	Tm-H2O	Tm-other	Th	Tdissol.1	Tdissol.2	NaCl (<23.3wt%)	CaCl2 (wt%)	NaCl (>23.3wt%)	KCl (wt%)	TotalSalinity
PN30D/1	1		1a	B	propylitic (epidote)		-1.8		317.2			3.1				3.1
PN30D/1	1		1a	B	propylitic (epidote)		-1.9		332.1			3.2				3.2
PN30D/1	1		1a	B	propylitic (epidote)		-1.9		330.6			3.2				3.2
SG1RD/2	F	P	1a	A	illite		-0 3		205.9			0.5				0.5
SG1RD/2	F	P	1a	A	illite		-0 3		208.9			0.5				0 5
SG1RD/2	F	P	1a	A	illite		-0 3		209.0			0 5				0.5
SG1RD/2	F	P	1a	A	illite		-0.1		207.5			0 2				0.2
SG1RD/2	F	P	1a	A	illite		-0.1		207.8			0.2				0.2
SG1RD/2	F	P	1a	A	illite		-0.1		207.8			0.2				0.2
SG1RD/2	F	P	1a	A	illite		-0.3		206.8			0.5				0.5
SG1RD/2	F	P	1a	A	illite		-0.1		207.6			0.2				0.2
SG1RD/2	A	P	1a	A	illite	-24.3	-1.3		212 3			2.2				2.2
SG1RD/2		P	1a	A	illite	-27.9	-1.2		231 6			2 1				2 1
SG1RD/2		P	1a	A	illite		-1.4		228 5			2.4				2.4
SG1RD/2	G	P	1a	A	illite		-0 2		238 7			0.4				0 4
SG1RD/2		P	1a	A	illite		-0 2		218 3			0 4				0 4
SG1RD/2		P	1a	A	illite		-0 1		213.9			0 2				0.2
SG1RD/2		P	1a	A	illite		0.0		205 6			0 0				
SG1RD/2		P	1a	A	illite		-0 1		206 3			0.2				0 2
SG1RD/2		P	1a	A	illite		-0.2		207.4			0.4				0.4
SG1RD/2	D	P	1a	A	illite		0.0		210.0			0.0				
SG1RD/2		P	1a	A	illite		-0.1		210.3			0.2				0.2
SG1RD/2		P	1a	A	illite		0 0		209.8			0.0				
SG1RD/2		P	1a	A	illite		-0.1		210 3			0.2				0.2
SG1RD/2		P	1a	A	illite		0.0		208.6			0.0				
SG1RD/2		P	1a	A	illite		0.0		210.8			0.0				
SG1RD/2		P	1a	A	illite		0.0		221.0			0.0				
SG1RD/2		P	1a	A	illite		0.0		228.8			0.0				

APPENDIX 3: SCALE DEPOSIT DESCRIPTIONS

Scale Deposits

The 26 scale samples, mounted as polished sections for microscopic examination, are described below. A summary of the mineralogy of each specimen is represented in Figure 4.7. The composition of the clay mineral referred to in the following descriptions was not determined during this study. It is a fine grained (< 40 μm) white mica and assumed to be the same as that identified by Reyes and Cardile (1989).

BL1D

1075 m

Scales are from a measured depth (MD) of 1075 m, close to the topmost aquifer and the top of the production casing (Figure 4.9b). They consist almost entirely of clay chips, but a few crystal fragments of carbonate (< 0.6 mm) and anhydrite (< 0.4 mm) are present. Both have tabular habits.

NJ6D

2065.3 m

These scales are from the middle section of the production casing, just above an aquifer (2100-2200 m MD; Figure 4.9b), and consist of anhydrite crystal fragments (0.1-2 mm) and minor chips of clay. A few scale chips are crystal aggregates of anhydrite with clay lining grain boundaries. Some coarser anhydrite crystals have well-developed growth bands defined by vapour- and liquid-rich fluid inclusion trails.

OK3

0 to 264 m, 270 m, 300 m, 355 m, 409 m, 451 m and 505 m

Scales are mostly from above the production casing, in the unslotted regions of the well (Figure 4.9c). The deepest, from 505 m depth, is the only sample from the production casing, approximately 500 m above the only aquifer, or production zone in this well. The shallowest sample (0-264 m) represents mineral deposit build-up over an interval from surface to 264 m depth. The other six samples were collected from spot depths. The mineralogy of each sample is similar, consisting mainly of amorphous silica. Variation is seen at shallowest levels, with samples 0-264 m, 270 m and 300 m also containing minor amounts of carbonate. A few chips of clay scale are seen at depths of 300 m and 505 m depths. Sulphide minerals are present only as fine inclusions (< 15 μm) in amorphous silica. These consist of pyrite, chalcopyrite, sphalerite and galena. Minute grains (< 5 μm) of electrum are seen at 0-264 m, 270 m, 355 m and 505 m depths.

OK10D

2144.5 to 2835.5 m

Scales are from a 691 m measured interval, spanning two production zones (Figure 4.9b). Chips represented in polished thin section consist of clays (60%) and anhydrite crystal fragments (40%) with tabular and bladed habits. Those with a bladed habit contain fine grained dendrites of sphalerite and chalcopyrite. However, most sulphide minerals (pyrite, chalcopyrite, sphalerite and galena) occur as fine grained inclusions (< 10 μm) in clay chips.

2835.5 to 3000.0 m

This 164.5 m interval represents the lowermost region of the well, that includes one aquifer (Figure 4.9b). Scale chips are mineral aggregates of anhydrite-gypsum-clay and anhydrite-alunite-clay, but also tabular anhydrite crystal fragments (< 4 mm). Sulphide minerals are present in the anhydrite-alunite-clay chips as fine (< 15 μm) dendritic intergrowths interstitial to alunite. These intergrowths consist mainly of chalcopyrite, pyrite and sphalerite but also minor amounts of galena, bornite and rare electrum (< 5 μm).

PN13D

1464 to 1499 m and 1499 to 1529 m

Both samples are from the top of the production casing in the topmost aquifer (Figure 4.9a). The mineralogy of the chips consist mostly of clay (50%) and carbonate (50%). Carbonate chips are aggregates of fine (< 0.1 mm) anhedral crystals. A few clay chips contain fine tabular crystals of anhydrite (< 0.2 mm) with minute (< 25 μm) grains of pyrite.

1529 to 1816 m

This 287 m interval includes, and extends approximately 200 m below, the topmost aquifer (Figure 4.9a). Scale minerals consist of anhydrite (20%), carbonate (20%), clay (60%) and sulphide minerals (< 1%). Scale chips are aggregates of either clay and anhydrite, or clay and carbonate. Anhydrite-clay aggregates consist of loosely interlocking, fine grained anhydrite needles (< 0.3 mm) enclosed in clay masses. Carbonate-clay chips are intergrowths of clay masses with fine (< 0.1 mm), anhedral carbonate crystals. Sulphide minerals consist of pyrite, chalcopyrite and sphalerite. Fine tabular pyrite crystals (< 0.1 mm) occur in clay masses in carbonate-clay chips. The anhydrite-clay chips contain fine (< 25 μm) grains of pyrite, chalcopyrite and sphalerite.

1477.7 to 1746.0 m

This 268.3 m scale interval is close to the 1529-1816 m scale interval described above (Figure 4.9a) and has a similar mineralogy. Scales are discrete chips of carbonate (60%), clay (20%), and anhydrite (20%). Carbonate chips are aggregates of fine grained (< 0.1 mm)

anhedral crystals. Anhydrite chips are tabular crystal fragments (< 0.8 mm) with a few containing dendritic inclusions of chalcopyrite and pyrite (< 25 μm). Minute pyrite grains (< 10 μm) are present in the clay chips.

1746 to 2767 m

Scales represented in this sample are from a 1021 m interval that spans one aquifer and extends to close to the bottom of the well and the lowermost aquifer (Figure 4.9a). Chips present are aggregates of carbonate and clay, and tabular anhydrite crystal fragments (< 1.0 mm). Carbonate-clay aggregates consist of fine (< 0.1 mm) anhedral carbonate crystals with clays lining carbonate grain boundaries. Minute pyrite grains (< 25 μm) are present in the clay masses.

2000 to 2200 m and 2200 to 2767 m

The shallower sample spans a 200 m thick production zone, whereas the deeper sample is from a 567 m interval that extends to the top of the lowermost production zone (Figure 4.9a). Both samples share the same mineralogies. Scales are chips of anhydrite (40%), carbonate (50%) and clay (10%). Anhydrite chips are tabular crystal fragments (< 1 mm), but a few acicular aggregates are present. Tabular anhydrite crystals commonly have liquid and vapour-rich fluid inclusions. Carbonate chips are aggregates of fine (< 0.1 mm) anhedral crystals. Fine (< 25 μm), dendritic intergrowths of pyrite and chalcopyrite occur in both anhydrite crystals and clay chips.

PN15D

1320 m

This sample is from the uppermost production zone, close to the top of the production casing (Figure 4.9c). Scale chips are mostly aggregates of carbonate, clay and sulphides. Carbonate is most common as equant, rhombic crystals, but an aggregate of platey crystals is also present. Sulphide minerals are present either as anhedral grains in clay-carbonate aggregates, or as discrete grains. Bornite is the most abundant sulphide mineral and is partly replaced by digenite/covellite. In some chips, bornite encloses rectangular voids which are interpreted to have been anhydrite crystals. Chalcopyrite is minor and only occurs as rounded grains partly enclosed by bornite. Small grains of electrum (< 10 μm) occur in one bornite chip.

PN17D

993 m

This sample is from the unslotted well lining, approximately 600 m above the production casing (Figure 4.9c). The mineralogy of the scale chips is clay (50%) and carbonate (50%). Sulphide minerals are not present. The chips are either monomineralic clay and carbonate, or aggregates

of both. Texturally, the aggregates consist of linear bands of clay and carbonate, or have clays occurring along carbonate grain boundaries. Carbonate in the aggregates is fine grained (< 0.2 mm) with an anhedral mosaic fabric. Discrete carbonate chips are coarser grained (< 3 mm) with a tabular habit.

PN21D

1171 m

This sample is from the top of the production zone, above a production zone (Figure 4.9c). Scale chips are composed mainly of clays (95%). These are massive with a few containing banded structures. They also contain inclusions of minute pyrite grains (< 20 μm) and fine (< 5 μm) dendritic chalcopyrite Carbonate aggregates consist of fine, anhedral grains (5-300 μm). Scale chips comprising both calcite and clay are rare.

PN22D

1654.4 m

Scales are from the topmost production zone, approximately 100 m below the top of the production casing (Figure 4 9a). Chips are composed of clays and discrete tabular crystal fragments of anhydrite (< 10%; < 0.5 mm). There are no sulphide minerals.

2445.5 m to 2620.5 m

This 175 m interval spans the lowermost production zone (Figure 4.9a). Scale chips consist mostly of anhydrite and clay, and occur as discrete chips or together as aggregates with bladed anhydrite crystals aligned perpendicular to bands of clay. Discrete anhydrite chips are either crystal aggregates or single crystals. Sulphide minerals are dominated by pyrite and chalcopyrite, with less abundant sphalerite and galena. Chalcopyrite, sphalerite and galena occur as fine grained (< 5 μm across) dendrites enclosed in anhydrite crystals or clay masses. Pyrite is more commonly present as fine subhedral grains (< 20 μm). A few scale chips consist of amorphous silica. These contain sparse, fine grained (< 15 μm) inclusions of chalcopyrite, sphalerite and pyrite.

2620.5 to 2726 5 m

This sample is from a 106 m interval below the lowermost production zone (Figure 4.9a) and consists mainly of anhydrite and clay scales. Anhydrite scales are mostly discrete tabular crystals; only a few clay-anhydrite aggregates are present. Pyrrhotite, the only sulphide mineral present, occurs as crystal fragments that are partly replaced by hydrous Fe-oxides.

PN29D

1680 m

Scale deposits from well PN29D are from approximately 100 m below the topmost production zone (Figure 4.9a). They consist of clays (80%), anhydrite (19%) and sulphide minerals (< 1%). Anhydrite occurs as either tabular or acicular crystals. Fine grained (< 5-20 μm) sulphide minerals occur in clay chips as banded or linear aggregates. These aggregates consist mostly of chalcopyrite, with minor fine grained (< 2.5 μm) intergrowths of sphalerite, galena, bornite and electrum.

SG3D

1797.1 m

Scales are from a production zone, approximately 500 m below the top of the production casing (Figure 4.9b). They are mostly chips of clay, but are a few aggregates of clay and tabular anhydrite (< 0.3 mm) are present. Clay occurs interstitial to anhydrite. No sulphide minerals are present.

Table A3.1. Collection depths and elevations of scale deposits and the location of production zones.

Well	Well location	Scale Deposits				Aquifer Elevation (m)	
		Collection Date	Collection Depth (m)	Elevation (m) from	to	from	to
BL1D	western upflow margin	11/84	1075	-107	-	-107 0	-218.0
						-395.0	-567.0
						-648.0	-732.0
						-1066.0	-1231.0
						-1360 0	-1449.0
NJ6D	western upflow margin	-	2065.3	-836.3	-	-235.0	-325.0
						-547.0	-683.0
						-868.0	-961.0
						-1184.0	-1358 0
OK3	eastern outflow	-	0-264	468.3	204.3	-531.7	-631.7
		-	270	198.3	-		
		-	300	168.3	-		
		-	355	113.3	-		
		-	409	59.3	-		
		-	451	17.3	-		
		-	505	-36.7	-		
OK10D	eastern upflow margin	18/04/97	2144 5-2835 5	-948.9	-1542.1	-549.0	-746.0
		15/04/87	2835 5-3000.0	-1542.1	-1666.9	-784.0	-855.0
						-1022.0	-1126.0
						-1438 0	-1589.0
PN13D	upflow	-	1464-1499	-648.2	-681.1	-634.9	-774.9
		-	1478-1746	-660 8	-912.3	-1152.9	-1338 9
		-	1499-1529	-681.1	-709.0	-1890.9	-1941.9
		-	1529-1816	-709.0	-978 4		
		-	1746-2767	-912.3	-1860.8		
		-	2000-2200	-1152.4	-1339.0		
		-	2200-2767	-1339.0	-1860.8		
PN15D	eastern upflow margin	19/08/86	1320	-571.5	-	-456.0	-584.0
						-838.0	-1026.0
						-1314.0	-1410.0
						-1602.0	-1699.0
						-1894.0	-2000.0
PN17D	eastern outflow	-	993	-267.3	-	-840.2	-934.2
						-1219.2	-1364.2
						-1899.2	-1998.2
PN21D	eastern upflow margin	29/07/96	1171	-412 0	-	-485.0	-624.0
						-906.0	-1091.0
						-1185.0	-1378.0
						-1475.0	-1671.0
						-1968.0	-2066.0
PN22D	upflow	21/01/89	1656 4	-757.5	-	-710.0	-876.0
			2445.5-2620 5	-1431.9	-1587.4	-1041.0	-1138.0
			2620.5-2726 5	-1587.4	-1686.8	-1304.0	-1392.0
						-1480.0	-1570.0
PN29D	upflow	19/02/96	1680	-926.1	-	-658.0	-853.0
						-1327.0	-1517.0
						-1991.0	-2088.0
SG3D	western outflow	-	1797	-623.3	-	-109.4	-194.4
						-324.4	-455.4
						-540.4	-711.4
						-881.4	-968.4
						-1507.4	-1633.4

Rock catalogue Catalog#	Field#	Rock Name	Lat	Long	AMG Northing	AMG Easting	Full Map Title	Map Scale	Map comments	DDH	Depth (m)	Area	Country	Lithostratigraphy	Formation	Preps	Comments
148534	BL1D/1 1	andesite breccia	9 15'	123 10'	1026485 84	517908 85	Southern Negros Geothermal Project	1 20 000	unpublished PNOC EDC company map	BL1D		1719 Southern Negros Island	Philippines	Late Pliocene	Southern Negros Formation	R PS	core 1
148535	BL1D/1 2	andesite breccia	9 15'	123 10'	1026485 84	517908 85	Southern Negros Geothermal Project	1 20 000	unpublished PNOC-EDC company map	BL1D		1719 Southern Negros Island	Philippines	Late Pliocene	Southern Negros Formation	R PS	core 1
148536	BL1D/2	andesite breccia	9 15'	123 10'	1026485 84	517908 85	Southern Negros Geothermal Project	1 20 000	unpublished PNOC-EDC company map	BL1D		2019 Southern Negros Island	Philippines	Late Pliocene	Southern Negros Formation	R 2PS	core 2
148537	BL1D/5	andesite breccia	9 15'	123 10'	1026485 84	517908 85	Southern Negros Geothermal Project	1 20 000	unpublished PNOC-EDC company map	BL1D		2693 Southern Negros Island	Philippines	Late Pliocene	Southern Negros Formation	R PS	core 5
148538	LG1D/1 1	andesite breccia	9 15'	123 10'	1026685 81	518645 50	Southern Negros Geothermal Project	1 20 000	unpublished PNOC-EDC company map	LG1D		1749 Southern Negros Island	Philippines	Late Pliocene	Southern Negros Formation	R PS	core 1
148539	LG1D/1 2	andesite breccia	9 15'	123 10'	1026685 81	518645 50	Southern Negros Geothermal Project	1 20 000	unpublished PNOC-EDC company map	LG1D		1749 Southern Negros Island	Philippines	Late Pliocene	Southern Negros Formation	R PS	core 1
148540	N3/1 1	andesite breccia	9 15'	123 10'	1029223 60	519942 00	Southern Negros Geothermal Project	1 20 000	unpublished PNOC-EDC company map	N3		367 Southern Negros Island	Philippines	Late Pliocene	Southern Negros Formation	R PS FI	core 1
148541	N3/1 2	andesite breccia	9 15'	123 10'	1029223 60	519942 00	Southern Negros Geothermal Project	1 20 000	unpublished PNOC-EDC company map	N3		367 Southern Negros Island	Philippines	Late Pliocene	Southern Negros Formation	R PS	core 1
148542	N3/1 3	andesite breccia	9 15'	123 10'	1029223 60	519942 00	Southern Negros Geothermal Project	1 20 000	unpublished PNOC-EDC company map	N3		367 Southern Negros Island	Philippines	Late Pliocene	Southern Negros Formation	R PS	core 1
148543	N3/2 1	andesite breccia	9 15'	123 10'	1029223 60	519942 00	Southern Negros Geothermal Project	1 20 000	unpublished PNOC-EDC company map	N3		855 Southern Negros Island	Philippines	Late Pliocene	Southern Negros Formation	R PS	core 2
148544	N3/2 3	andesite breccia	9 15'	123 10'	1029223 60	519942 00	Southern Negros Geothermal Project	1 20 000	unpublished PNOC-EDC company map	N3		855 Southern Negros Island	Philippines	Late Pliocene	Southern Negros Formation	R PS	core 2
148545	N3/3	andesite breccia	9 15'	123 10'	1029223 60	519942 00	Southern Negros Geothermal Project	1 20 000	unpublished PNOC EDC company map	N3		882 Southern Negros Island	Philippines	Late Pliocene	Southern Negros Formation	R PS	core 3
148546	N3/4 1	andesite breccia	9 15'	123 10'	1029223 60	519942 00	Southern Negros Geothermal Project	1 20 000	unpublished PNOC EDC company map	N3		915 Southern Negros Island	Philippines	Late Pliocene	Southern Negros Formation	R PS	core 4
148547	N3/4 2	andesite breccia	9 15'	123 10'	1029223 60	519942 00	Southern Negros Geothermal Project	1 20 000	unpublished PNOC EDC company map	N3		915 Southern Negros Island	Philippines	Late Pliocene	Southern Negros Formation	R 2PS FI	core 4
148548	N3/5	andesite breccia	9 15'	123 10'	1029223 60	519942 00	Southern Negros Geothermal Project	1 20 000	unpublished PNOC EDC company map	N3		941 Southern Negros Island	Philippines	Late Pliocene	Southern Negros Formation	R PS	core 5
148549	N3/6	andesite breccia	9 15'	123 10'	1029223 60	519942 00	Southern Negros Geothermal Project	1 20 000	unpublished PNOC EDC company map	N3		973 Southern Negros Island	Philippines	Late Pliocene	Southern Negros Formation	R PS FI	core 6
148550	NJ1D/1 1	andesite breccia	9 16'	123 10'	1026134 60	516790 40	Southern Negros Geothermal Project	1 20 000	unpublished PNOC-EDC company map	NJ1D		1547 Southern Negros Island	Philippines	Late Pliocene	Southern Negros Formation	R PS	core 1
148551	NJ1D/1 2	andesite breccia	9 15'	123 10'	1026134 60	516790 40	Southern Negros Geothermal Project	1 20 000	unpublished PNOC-EDC company map	NJ1D		1547 Southern Negros Island	Philippines	Late Pliocene	Southern Negros Formation	R PS	core 1
148552	NJ1D/2 1	andesite breccia	9 15'	123 10'	1026134 60	516790 40	Southern Negros Geothermal Project	1 20 000	unpublished PNOC-EDC company map	NJ1D		1794 Southern Negros Island	Philippines	Late Pliocene	Southern Negros Formation	R PS	core 2
148553	NJ1D/2 2	andesite breccia	9 15'	123 10'	1026134 60	516790 40	Southern Negros Geothermal Project	1 20 000	unpublished PNOC-EDC company map	NJ1D		1794 Southern Negros Island	Philippines	Late Pliocene	Southern Negros Formation	R PS	core 2
148554	NJ1D/4	andesite breccia	9 15'	123 10'	1026134 60	516790 40	Southern Negros Geothermal Project	1 20 000	unpublished PNOC-EDC company map	NJ1D		2127 Southern Negros Island	Philippines	Late Pliocene	Southern Negros Formation	R PS	core 4
148555	NJ1D/5	quartz diorite	9 15'	123 10'	1026134 60	516790 40	Southern Negros Geothermal Project	1 20 000	unpublished PNOC-EDC company map	NJ1D		2374 Southern Negros Island	Philippines	Pleistocene	Nasuji Pluton	R PS PD CR	core 5
148556	NJ1D/6-1	quartz diorite	9 15'	123 10'	1026134 60	516790 40	Southern Negros Geothermal Project	1 20 000	unpublished PNOC EDC company map	NJ1D		2556 Southern Negros Island	Philippines	Pleistocene	Nasuji Pluton	R PS	core 6
148557	NJ1D/6-2	quartz diorite	9 15'	123 10'	1026134 60	516790 40	Southern Negros Geothermal Project	1 20 000	unpublished PNOC EDC company map	NJ1D		2556 Southern Negros Island	Philippines	Pleistocene	Nasuji Pluton	R PS	core 6
148558	NJ1D/7	quartz diorite	9 15'	123 10'	1026134 60	516790 40	Southern Negros Geothermal Project	1 20 000	unpublished PNOC EDC company map	NJ1D		2777 Southern Negros Island	Philippines	Pleistocene	Nasuji Pluton	R PS	core 7
148559	NJ2D/1	quartz diorite	9 15'	123 10	1026015 80	516850 10	Southern Negros Geothermal Project	1 20 000	unpublished PNOC-EDC company map	NJ2D		2906 Southern Negros Island	Philippines	Pleistocene	Nasuji Pluton	R 3PS PD CR FI	core 1
148560	NJ2D/2 1	quartz diorite	9 15'	123 10'	1026015 80	516850 10	Southern Negros Geothermal Project	1 20 000	unpublished PNOC EDC company map	NJ2D		3127 Southern Negros Island	Philippines	Pleistocene	Nasuji Pluton	R PS	core 2
148561	NJ2D/2 2	quartz diorite	9 15'	123 10	1026015 80	516850 10	Southern Negros Geothermal Project	1 20 000	unpublished PNOC EDC company map	NJ2D		3127 Southern Negros Island	Philippines	Pleistocene	Nasuji Pluton	R PS	core 2
148562	NJ2D/2 3	quartz diorite	9 15'	123 10	1026015 80	516850 10	Southern Negros Geothermal Project	1 20 000	unpublished PNOC EDC company map	NJ2D		3127 Southern Negros Island	Philippines	Pleistocene	Nasuji Pluton	R PS	core 2
148563	NJ3D/1 1	quartz diorite	9 15'	123 10'	1026428 40	515879 50	Southern Negros Geothermal Project	1 20 000	unpublished PNOC EDC company map	NJ3D		1556 Southern Negros Island	Philippines	Pleistocene	Nasuji Pluton	R PS	core 1
148564	NJ3D/1 2	quartz diorite	9 15'	123 10'	1026428 40	515879 50	Southern Negros Geothermal Project	1 20 000	unpublished PNOC EDC company map	NJ3D		1556 Southern Negros Island	Philippines	Pleistocene	Nasuji Pluton	R PS	core 1
148565	NJ3D/1 3	quartz diorite	9 15'	123 10'	1026428 40	515879 50	Southern Negros Geothermal Project	1 20 000	unpublished PNOC EDC company map	NJ3D		1556 Southern Negros Island	Philippines	Pleistocene	Nasuji Pluton	R PS PD CR	core 1
148566	NJ3D/2	quartz diorite	9 15'	123 10	1026428 40	515879 50	Southern Negros Geothermal Project	1 20 000	unpublished PNOC EDC company map	NJ3D		1891 Southern Negros Island	Philippines	Pleistocene	Nasuji Pluton	R PS	core 2
148567	NJ3D/3-1	quartz diorite	9 15'	123 10'	1026428 40	515879 50	Southern Negros Geothermal Project	1 20 000	unpublished PNOC EDC company map	NJ3D		2397 Southern Negros Island	Philippines	Pleistocene	Nasuji Pluton	R PS PD CR FI	core 3
148568	NJ3D/3-2	quartz diorite	9 15'	123 10'	1026428 40	515879 50	Southern Negros Geothermal Project	1 20 000	unpublished PNOC-EDC company map	NJ3D		2397 Southern Negros Island	Philippines	Pleistocene	Nasuji Pluton	R PS	core 3
148569	NJ3D/3-3	quartz diorite	9 15'	123 10'	1026428 40	515879 50	Southern Negros Geothermal Project	1 20 000	unpublished PNOC EDC company map	NJ3D		2397 Southern Negros Island	Philippines	Pleistocene	Nasuji Pluton	R PS	core 3
148570	NJ3D/4-1	quartz diorite	9 15'	123 10	1026428 40	515879 50	Southern Negros Geothermal Project	1 20 000	unpublished PNOC EDC company map	NJ3D		2810 Southern Negros Island	Philippines	Pleistocene	Nasuji Pluton	R PS	core 4
148571	NJ3D/4 2	quartz diorite	9 15'	123 10	1026428 40	515879 50	Southern Negros Geothermal Project	1 20 000	unpublished PNOC EDC company map	NJ3D		2810 Southern Negros Island	Philippines	Pleistocene	Nasuji Pluton	R PS	core 4
148572	NJ4D/1 1	quartz diorite	9 15'	123 10	1025924 10	516758 20	Southern Negros Geothermal Project	1 20 000	unpublished PNOC EDC company map	NJ4D		2257 Southern Negros Island	Philippines	Pleistocene	Nasuji Pluton	R PS	core 1
148573	NJ4D/1 2	quartz diorite	9 16'	123 10	1025924 10	516758 20	Southern Negros Geothermal Project	1 20 000	unpublished PNOC EDC company map	NJ4D		2257 Southern Negros Island	Philippines	Pleistocene	Nasuji Pluton	R PS	core 1
148574	NJ4D/1 3	quartz diorite	9 15'	123 10	1025924 10	516758 20	Southern Negros Geothermal Project	1 20 000	unpublished PNOC EDC company map	NJ4D		2257 Southern Negros Island	Philippines	Pleistocene	Nasuji Pluton	R PS	core 1
148575	NJ4D/2	quartz diorite	9 15'	123 10'	1025924 10	516758 20	Southern Negros Geothermal Project	1 20 000	unpublished PNOC EDC company map	NJ4D		3045 Southern Negros Island	Philippines	Pleistocene	Nasuji Pluton	R PS PD CR	core 2
148576	NJ5D/1 1	andesite breccia	9 15'	123 10	1026340 20	516764 60	Southern Negros Geothermal Project	1 20 000	unpublished PNOC EDC company map	NJ5D		1552 Southern Negros Island	Philippines	Late Pliocene	Southern Negros Formation	R PS	core 1
148577	NJ5D/1 2	andesite breccia	9 15'	123 10	1026340 20	516764 60	Southern Negros Geothermal Project	1 20 000	unpublished PNOC EDC company map	NJ5D		1552 Southern Negros Island	Philippines	Late Pliocene	Southern Negros Formation	R PS	core 1
148578	NJ5D 2 1	andesite breccia	9 15'	123 10	1026340 20	516764 60	Southern Negros Geothermal Project	1 20 000	unpublished PNOC EDC company map	NJ5D		1873 Southern Negros Island	Philippines	Late Pliocene	Southern Negros Formation	R PS	core 2
148579	NJ5D/2 2	andesite breccia	9 15'	123 10	1026340 20	516764 60	Southern Negros Geothermal Project	1 20 000	unpublished PNOC EDC company map	NJ5D		1873 Southern Negros Island	Philippines	Late Pliocene	Southern Negros Formation	R	core 2
148580	NJ5D/2 3	andesite breccia	9 15'	123 10	1026340 20	516764 60	Southern Negros Geothermal Project	1 20 000	unpublished PNOC EDC company map	NJ5D		1873 Southern Negros Island	Philippines	Late Pliocene	Southern Negros Formation	R PS	core 2
148581	NJ5D/3-1	quartz diorite	9 15'	123 10'	1026340 20	516764 60	Southern Negros Geothermal Project	1 20 000	unpublished PNOC EDC company map	NJ5D		2162 Southern Negros Island	Philippines	Pleistocene	Nasuji Pluton	R PS PD CR	core 3
148582	NJ5D/3 2	quartz diorite	9 15'	123 10'	1026340 20	516764 60	Southern Negros Geothermal Project	1 20 000	unpublished PNOC-EDC company map	NJ5D		2162 Southern Negros Island	Philippines	Pleistocene	Nasuji Pluton	R PS	core 3
148583	NJ5D/4 1	quartz diorite	9 15'	123 10'	1026340 20	516764 60	Southern Negros Geothermal Project	1 20 000	unpublished PNOC-EDC company map	NJ5D		2532 Southern Negros Island	Philippines	Pleistocene	Nasuji Pluton	R PS PD CR	core 4
148584	NJ5D/4 2	quartz diorite	9 15'	123 10	1026340 20	516764 60	Southern Negros Geothermal Project	1 20 000	unpublished PNOC-EDC company map	NJ5D		2532 Southern Negros Island	Philippines	Pleistocene	Nasuji Pluton	R PS	core 4
148585	NJ5D/4-3	quartz diorite	9 15'	123 10'	1026340 20	516764 60	Southern Negros Geothermal Project	1 20 000	unpublished PNOC EDC company map	NJ5D		2532 Southern Negros Island	Philippines	Pleistocene	Nasuji Pluton	R PS PD CR	core 4
148586	NJ5D/5-1	basalt	9 15'	123 10'	1026340 20	516764 60	Southern Negros Geothermal Project	1 20 000	unpublished PNOC EDC company map	NJ5D		2922 Southern Negros Island	Philippines	Middle Miocene	Lower Puhagan Volcanic Formation	R PS PD CR	core 5
148587	NJ5D/5 2	basalt	9 15'	123 10'	1026340 20	516764 60	Southern Negros Geothermal Project	1 20 000	unpublished PNOC EDC company map	NJ5D		2922 Southern Negros Island	Philippines	Middle Miocene	Lower Puhagan Volcanic Formation	R PS	core 5
148588	NJ5D/5-3	basalt	9 15'	123 10'	1026340 20	516764 60	Southern Negros Geothermal Project	1 20 000	unpublished PNOC EDC company map	NJ5D		2922 Southern Negros Island	Philippines	Middle Miocene	Lower Puhagan Volcanic Formation	R PS PD CR	core 5
148589	NJ6D/1	andesite breccia	9 15'	123 10'	1026179 90	516836 20	Southern Negros Geothermal Project	1 20 000	unpublished PNOC-EDC company map	NJ6D		1486 Southern Negros Island	Philippines	Late Pliocene	Southern Negros Formation	R PS	core 1
148590	NJ6D/2 1	andesite breccia	9 15'	123 10'	1026179 90	516836 20	Southern Negros Geothermal Project	1 20 000	unpublished PNOC-EDC company map	NJ6D		1614 Southern Negros Island	Philippines	Late Pliocene	Southern Negros Formation	R PS	core 2
148591	NJ6D/2 2	andesite breccia	9 15'	123 10	1026179 90	516836 20	Southern Negros Geothermal Project	1 20 000	unpublished PNOC-EDC company map	NJ6D		1614 Southern Negros Island	Philippines	Late Pliocene	Southern Negros Formation	R PS	core 2
148592	NJ6D/2 3	andesite breccia	9 15'	123 10'	1026179 90	516836 20	Southern Negros Geothermal Project	1 20 000	unpublished PNOC-EDC company map	NJ6D		1614 Southern Negros Island	Philippines	Late Pliocene	Southern Negros Formation	R 2PS PD,CR	core 2
148593	NJ6D/3	andesite breccia	9 15'	123 10'	1026179 90	516836 20	Southern Negros Geothermal Project	1 20 000	unpublished PNOC-EDC company map	NJ6D		2133 Southern Negros Island	Philippines	Late Pliocene	Southern Negros Formation	R PS	core 3
148594	NJ6D/4-1	quartz diorite	9 15'	123 10'	1026179 90	516836 20	Southern Negros Geothermal Project	1 20 000	unpublished PNOC EDC company map	NJ6D		2453 Southern Negros Island	Philippines	Pleistocene	Nasuji Pluton	R PS	core 4
148595	NJ6D/4 2	quartz diorite	9 15'	123 10'	1026179 90	516836 20	Southern Negros Geothermal Project	1 20 000	unpublished PNOC EDC company map	NJ6D		2453 Southern Negros Island	Philippines	Pleistocene	Nasuji Pluton	R PS	core 4
148596	NJ7D/1 1	quartz diorite	9 15'	123 10'	1026059 07	516789 53	Southern Negros Geothermal Project	1 20 000	unpublished PNOC-EDC company map	NJ7D		1808 Southern Negros Island	Philippines	Pleistocene	Nasuji Pluton	R PS PD,CR	core 1
148597	NJ7D/1-2	quartz diorite	9 15'	123 10'	1026059 07	516789 53	Southern Negros Geothermal Project	1 20 000	unpublished PNOC-EDC company map	NJ7D		1808 Southern Negros Island	Philippines	Pleistocene	Nasuji Pluton	R PS PD,CR	core 1
148598	NJ7D/2	quartz diorite	9 15'	123 10'	1026059 07	516789 53	Southern Negros Geothermal Project	1 20 000	unpublished PNOC-EDC company map	NJ7D		2212 Southern Negros Island	Philippines	Pleistocene	Nasuji Pluton	R PS	core 2
148599	NJ7D/3	quartz diorite	9 15'	123 10'	1026059 07	516789 53	Southern Negros Geothermal Project	1 20 000	unpublished PNOC-EDC company map	NJ7D		2441 Southern Negros Island	Philippines	Pleistocene	Nasuji Pluton	R PS	core 3
148600	NJ7D/4	quartz diorite	9 15'	123 10'	1026059 07	516789 53	Southern Negros Geothermal Project	1 20 000	unpublished PNOC-EDC company map	NJ7D		2716 Southern Negros Island	Philippines	Pleistocene	Nasuji Pluton	R PS	core 4
148601	NJ8D/1	quartz diorite	9 15'	123 10'	1025924 60	516734 70	Southern Negros Geothermal Project	1 20 000	unpublished PNOC EDC company map	NJ8D		1888 Southern Negros Island	Philippines	Pleistocene	Nasuji Pluton	R 2PS	core 1
148602	NJ9D/1	quartz diorite	9 15'	123 10'	1026500 17	515934 78	Southern Negros Geothermal Project	1 20 000	unpublished PNOC EDC company map	NJ9D		1635 Southern Negros Island	Philippines	Pleistocene	Nasuji Pluton	R PS	core 1
148603	NJ10D/1 1	quartz diorite	9 15'	123 10'	1026485 58	515916 15	Southern Negros Geothermal Project	1 20 000	unpublished PNOC-EDC company map	NJ10D		1427 Southern Negros Island	Philippines	Pleistocene	Nasuji Pluton	R PS	core 1
148604	NJ10D/1-2	quartz diorite	9 16'	123 10'	1026485 58	515916 15	Southern Negros Geothermal Project	1 20 000	unpublished PNOC-EDC company map	NJ10D		1427 Southern Negros Island	Philippines	Pleistocene	Nasuji Pluton	R PS	core 1
148605	NJ10D/1 3	quartz diorite	9 16'	123 10'	1026485 58	515916 15	Southern Negros Geothermal Project	1 20 000	unpublished PNOC-EDC company map	NJ10D		1427 Southern Negros Island	Philippines	Pleistocene	Nasuji Pluton	R PS	core 1
148606	NJ10D/2 1	quartz diorite	9 16'	123 10'	1026485 58	515916 15	Southern Negros Geothermal Project	1 20 000	unpublished PNOC-EDC company map	NJ10D		1736 Southern Negros Island	Philippines	Pleistocene	Nasuji Pluton	R PS	core 2
148607	NJ10D/2 2	quartz diorite	9 15'	123 10'	1026485 58	515916 15	Southern Negros Geothermal Project	1 20 000	unpublished PNOC-EDC company map	NJ10D		1736 Southern Negros Island	Philippines	Pleistocene	Nasuji Pluton	R PS	core 2
148608	OK1/1-1	andesite breccia	9 15'	123 10'	1030550 60	520384 40	Southern Negros Geothermal Project	1 20 000	unpublished PNOC-EDC company map	OK1		760 Southern Negros Island	Philippines	Late Pliocene	Southern Negros Formation	R PS PD	core 1
148609	OK1/1 2	andesite breccia	9 15'	123 10'	1030550 60	520384 40	Southern Negros Geothermal Project	1 20 000	unpublished PNOC-EDC company map	OK1		760 Southern Negros Island	Philippines	Late Pliocene	Southern Negros Formation	R PS	core 1
148610	OK1/2 1	limestone	9 15'	123 10'	1030550 60	520384 40	Southern Negros Geothermal Project	1 20 000	unpublished PNOC-EDC company map	OK1		1208 Southern Negros Island	Philippines	Late Miocene-Early Pliocene	Okoy Formation	R PS	core 2
148611	OK1/2 2	limestone	9 15'	123 10'	1030550 60	520384 40	Southern Negros Geothermal Project	1 20 000	unpublished PNOC-EDC company map	OK1		1208 Southern Negros Island	Philippines	Late Miocene-Early Pliocene	Okoy Formation	R PS	core 2
148612	OK1/3	limestone	9 15'	123 10'	1030550 60	520384 40	Southern Negros Geothermal Project	1 20 000	unpublished PNOC-EDC company map	OK1		1353 Southern Negros Island	Philippines	Late Miocene-Early Pliocene	Okoy Formation	R PS	core 3
148613	OK1/4 1	limestone	9 15'	123 10'	1030550 60	520384 40	Southern Negros Geothermal Project	1 20 000	unpublished PNOC-EDC company map	OK1		1844 Southern Negros Island	Philippines	Late Miocene-Early Pliocene	Okoy Formation	R PS	core 4
148614	OK1/4 2	limestone	9 15'	123 10'	1030550 60	520384 40	Southern Negros Geothermal Project	1 20 000	unpublished PNOC EDC company map	OK1		1844 Southern Negros Island	Philippines	Late Miocene-Early Pliocene	Okoy Formation	R PS	core 4
148615	OK1/4 3	limestone	9 15'	123 10	1030550 60	520384 40	Southern Negros Geothermal Project	1 20 000	unpublished PNOC EDC company map	OK1		1844 Southern Negros Island	Philippines	Late Miocene-Early Pliocene	Okoy Formation	R PS	core 4
148616	OK1/5	limestone	9 15'	123 10	1030550 60	520384 40	Southern Negros Geothermal Project	1 20 000	unpublished PNOC-EDC company map	OK1		1982 Southern Negros Island	Philippines	Late Miocene-Early Pliocene	Okoy Formation	R PS PD	core 5
148617	OK2/1-1	andesite breccia	9 15'	123 10	1027785 10	518742 70	Southern Negros Geothermal Project	1 20 000	unpublished PNOC-EDC company map	OK2		605 Southern Negros Island	Philippines	Late Pliocene	Southern Negros Formation	R PS	core 1
148618	OK2/1 2	andesite breccia	9 15'	123 10'	1027785 10	518742 70	Southern Negros Geothermal Project	1 20 000	unpublished PNOC EDC company map	OK2		605 Southern Negros Island	Philippines	Late Pliocene	Southern Negros Formation	R PS	core 1
148619	OK2/2 1	andesite breccia	9 15'	123 10'	1027785 10	518742 70	Southern Negros Geothermal Project	1 20 000	unpublished PNOC-EDC company map	OK2		971 Southern Negros Island	Philippines	Late Pliocene	Southern Negros Formation	R PS	core 2
148620	OK2/2 2	andesite breccia	9 15'	123 10'	1027785 10	518742 70	Southern Negros Geothermal Project	1 20 000	unpublished PNOC-EDC company map	OK2		971 Southern Negros Island	Philippines	Late Pliocene	Southern Negros Formation	R PS	core 2

148621 OK3/1	andesite breccia	9 15	123 10'	1029345 70	519210 90	Southern Negros Geothermal Project	1 20 000	unpublished PNOC EDC company map	OK3		763	Southern Negros Island	Philippines	Late Pliocene	Southern Negros Formation	R PS	core 1
Catalog# Field#	Rock Name	Lat.	Long	AMG Northing	AMG Easting	Full Map Title	Map Scale	Map comments	DDH	Depth (m)	Area		Country	Lithostratigraphy	Formation	Preps	Comments
148622 OK3/2 1	limestone	9 15	123 10	1029345 70	519210 90	Southern Negros Geothermal Project	1 20 000	unpublished PNOC EDC company map	OK3		978	Southern Negros Island	Philippines	Late Miocene-Early Pliocene	Okoy Formation	R PS	core 2
148623 OK3/2 2	limestone	9 15	123 10'	1029345 70	519210 90	Southern Negros Geothermal Project	1 20 000	unpublished PNOC EDC company map	OK3		978	Southern Negros Island	Philippines	Late Miocene-Early Pliocene	Okoy Formation	R PS	core 2
148624 OK3/2 3	limestone	9 15'	123 10	1029345 70	519210 90	Southern Negros Geothermal Project	1 20 000	unpublished PNOC EDC company map	OK3		978	Southern Negros Island	Philippines	Late Miocene-Early Pliocene	Okoy Formation	R PS	core 2
148625 OK3/2-4	limestone	9 15'	123 10	1029345 70	519210 90	Southern Negros Geothermal Project	1 20 000	unpublished PNOC EDC company map	OK3		978	Southern Negros Island	Philippines	Late Miocene-Early Pliocene	Okoy Formation	R PS	core 2
148626 OK3/3 1	limestone	9 15	123 10	1029345 70	519210 90	Southern Negros Geothermal Project	1 20 000	unpublished PNOC EDC company map	OK3		1526	Southern Negros Island	Philippines	Late Miocene-Early Pliocene	Okoy Formation	R PS	core 3
148627 OK3/3-2	limestone	9 15	123 10'	1029345 70	519210 90	Southern Negros Geothermal Project	1 20 000	unpublished PNOC EDC company map	OK3		1526	Southern Negros Island	Philippines	Late Miocene-Early Pliocene	Okoy Formation	R	core 3
148628 OK4/1 1	andesite breccia	9 15'	123 10'	1027170 40	518280 30	Southern Negros Geothermal Project	1 20 000	unpublished PNOC EDC company map	OK4		727	Southern Negros Island	Philippines	Late Pliocene	Southern Negros Formation	R PS PD	core 1
148629 OK4/1 2	andesite breccia	9 15'	123 10'	1027170 40	518280 30	Southern Negros Geothermal Project	1 20 000	unpublished PNOC EDC company map	OK4		727	Southern Negros Island	Philippines	Late Pliocene	Southern Negros Formation	R PS	core 1
148630 OK4/2 1	limestone	9 15'	123 10'	1027170 40	518280 30	Southern Negros Geothermal Project	1 20 000	unpublished PNOC EDC company map	OK4		1678	Southern Negros Island	Philippines	Late Miocene-Early Pliocene	Okoy Formation	R PD	core 2
148631 OK4/2 2	limestone	9 15'	123 10'	1027170 40	518280 30	Southern Negros Geothermal Project	1 20 000	unpublished PNOC EDC company map	OK4		1678	Southern Negros Island	Philippines	Late Miocene-Early Pliocene	Okoy Formation	R PS	core 2
148632 OK4/3	limestone	9 15'	123 10'	1027170 40	518280 30	Southern Negros Geothermal Project	1 20 000	unpublished PNOC EDC company map	OK4		1982	Southern Negros Island	Philippines	Late Miocene-Early Pliocene	Okoy Formation	R PS PD	core 3
148633 OK4/4	limestone	9 15'	123 10'	1027170 40	518280 30	Southern Negros Geothermal Project	1 20 000	unpublished PNOC EDC company map	OK4		2134	Southern Negros Island	Philippines	Late Miocene-Early Pliocene	Okoy Formation	R,PS,PD	core 4
148634 OK5/1 1	andesite breccia	9 15'	123 10'	1027300 00	518050 00	Southern Negros Geothermal Project	1 20 000	unpublished PNOC EDC company map	OK5		915	Southern Negros Island	Philippines	Late Pliocene	Southern Negros Formation	R PS	core 1
148635 OK5/1-2	andesite breccia	9 15'	123 10'	1027300 00	518050 00	Southern Negros Geothermal Project	1 20 000	unpublished PNOC EDC company map	OK5		915	Southern Negros Island	Philippines	Late Pliocene	Southern Negros Formation	R PS	core 1
148636 OK5/2	andesite breccia	9 15	123 10'	1027300 00	518050 00	Southern Negros Geothermal Project	1 20 000	unpublished PNOC EDC company map	OK5		1164	Southern Negros Island	Philippines	Late Pliocene	Southern Negros Formation	R PS	core 2
148637 OK5/3	andesite breccia	9 15'	123 10'	1027300 00	518050 00	Southern Negros Geothermal Project	1 20 000	unpublished PNOC EDC company map	OK5		1354	Southern Negros Island	Philippines	Late Pliocene	Southern Negros Formation	R 2PS	core 3
148638 OK5/4 1	limestone	9 15'	123 10'	1027300 00	518050 00	Southern Negros Geothermal Project	1 20 000	unpublished PNOC EDC company map	OK5		1825	Southern Negros Island	Philippines	Late Miocene-Early Pliocene	Okoy Formation	R,TS	core 4
148639 OK5/4 2	limestone	9 15'	123 10'	1027300 00	518050 00	Southern Negros Geothermal Project	1 20 000	unpublished PNOC EDC company map	OK5		1825	Southern Negros Island	Philippines	Late Miocene-Early Pliocene	Okoy Formation	R PS	core 4
148640 OK5/4 3	limestone	9 15	123 10'	1027300 00	518050 00	Southern Negros Geothermal Project	1 20 000	unpublished PNOC EDC company map	OK5		1825	Southern Negros Island	Philippines	Late Miocene-Early Pliocene	Okoy Formation	R PS	core 4
148641 OK5/5	limestone	9 15'	123 10'	1027300 00	518050 00	Southern Negros Geothermal Project	1 20 000	unpublished PNOC EDC company map	OK5		1974	Southern Negros Island	Philippines	Late Miocene-Early Pliocene	Okoy Formation	R PS	core 5
148642 OK6/1 1	andesite breccia	9 15'	123 10'	1026100 00	516740 00	Southern Negros Geothermal Project	1 20 000	unpublished PNOC EDC company map	OK6		1065	Southern Negros Island	Philippines	Late Pliocene	Southern Negros Formation	R PS	core 1
148643 OK6/1 2	andesite breccia	9 15'	123 10'	1026100 00	516740 00	Southern Negros Geothermal Project	1 20 000	unpublished PNOC EDC company map	OK6		1065	Southern Negros Island	Philippines	Late Pliocene	Southern Negros Formation	R PS	core 1
148644 OK6/2 1	andesite breccia	9 15	123 10'	1026100 00	516740 00	Southern Negros Geothermal Project	1 20 000	unpublished PNOC EDC company map	OK6		1328	Southern Negros Island	Philippines	Late Pliocene	Southern Negros Formation	R PS FI	core 2
148645 OK6/2 2	andesite breccia	9 15'	123 10	1026100 00	516740 00	Southern Negros Geothermal Project	1 20 000	unpublished PNOC EDC company map	OK6		1328	Southern Negros Island	Philippines	Late Pliocene	Southern Negros Formation	R PS	core 2
148646 OK6/3 1	andesite breccia	9 15	123 10'	1026100 00	516740 00	Southern Negros Geothermal Project	1 20 000	unpublished PNOC EDC company map	OK6		1517	Southern Negros Island	Philippines	Late Pliocene	Southern Negros Formation	R,PS	core 3
148647 OK6/3 2	andesite breccia	9 15	123 10	1026100 00	516740 00	Southern Negros Geothermal Project	1 20 000	unpublished PNOC EDC company map	OK6		1517	Southern Negros Island	Philippines	Late Pliocene	Southern Negros Formation	R PS	core 3
148648 OK6/5 1	quartz diorite	9 15'	123 10	1026100 00	516740 00	Southern Negros Geothermal Project	1 20 000	unpublished PNOC EDC company map	OK6		1868	Southern Negros Island	Philippines	Pleistocene	Nasuji Pluton	R PS	core 5
148649 OK6/5 2	quartz diorite	9 15	123 10'	1026100 00	516740 00	Southern Negros Geothermal Project	1 20 000	unpublished PNOC EDC company map	OK6		1868	Southern Negros Island	Philippines	Pleistocene	Nasuji Pluton	R PS	core 5
148650 OK6/7	quartz diorite	9 15'	123 10	1026100 00	516740 00	Southern Negros Geothermal Project	1 20 000	unpublished PNOC EDC company map	OK6		2510	Southern Negros Island	Philippines	Pleistocene	Nasuji Pluton	R PS	core 7
148651 OK6/9	quartz diorite	9 15	123 10	1026100 00	516740 00	Southern Negros Geothermal Project	1 20 000	unpublished PNOC EDC company map	OK6		2770	Southern Negros Island	Philippines	Pleistocene	Nasuji Pluton	R PS	core 9
148652 OK7/1-1	andesite breccia	9 15	123 10	1027476 90	518863 30	Southern Negros Geothermal Project	1 20 000	unpublished PNOC EDC company map	OK7		1166	Southern Negros Island	Philippines	Late Pliocene	Southern Negros Formation	R PS	core 1
148653 OK7/1 2	andesite breccia	9 15	123 10	1027476 90	518863 30	Southern Negros Geothermal Project	1 20 000	unpublished PNOC EDC company map	OK7		1166	Southern Negros Island	Philippines	Late Pliocene	Southern Negros Formation	R PS	core 1
148654 OK7/1 3	andesite breccia	9 15	123 10	1027476 90	518863 30	Southern Negros Geothermal Project	1 20 000	unpublished PNOC EDC company map	OK7		1186	Southern Negros Island	Philippines	Late Pliocene	Southern Negros Formation	R PS	core 1
148655 OK7/1 4	andesite breccia	9 15	123 10	1027476 90	518863 30	Southern Negros Geothermal Project	1 20 000	unpublished PNOC EDC company map	OK7		1189	Southern Negros Island	Philippines	Late Pliocene	Southern Negros Formation	R PS	core 1
148656 OK7/2	andesite breccia	9 15	123 10	1027476 90	518863 30	Southern Negros Geothermal Project	1 20 000	unpublished PNOC EDC company map	OK7		1342	Southern Negros Island	Philippines	Late Pliocene	Southern Negros Formation	R PS	core 2
148657 OK7/3	andesite breccia	9 15	123 10	1027476 90	518863 30	Southern Negros Geothermal Project	1 20 000	unpublished PNOC EDC company map	OK7		1576	Southern Negros Island	Philippines	Late Pliocene	Southern Negros Formation	R PS	core 3
148658 OK7/6	andesite breccia	9 15	123 10	1027476 90	518863 30	Southern Negros Geothermal Project	1 20 000	unpublished PNOC EDC company map	OK7		2255	Southern Negros Island	Philippines	Middle Miocene	Lower Puhagan Volcanic Formation	R PS	core 6
148659 OK7/7	diorite	9 15	123 10	1027476 90	518863 30	Southern Negros Geothermal Project	1 20 000	unpublished PNOC EDC company map	OK7		2410	Southern Negros Island	Philippines	Early Pliocene	Puhagan dikes	R 2PS PD CR FI	core 7
148660 OK7/9	diorite	9 15'	123 10	1027476 90	518863 30	Southern Negros Geothermal Project	1 20 000	unpublished PNOC EDC company map	OK7		2744	Southern Negros Island	Philippines	Early Pliocene	Puhagan dikes	R PS FI	core 9
148661 OK7/10	andesite breccia	9 15'	123 10	1027476 90	518863 30	Southern Negros Geothermal Project	1 20 000	unpublished PNOC EDC company map	OK7		2882	Southern Negros Island	Philippines	Middle Miocene	Lower Puhagan Volcanic Formation	R 2PS	core 10
148662 OK8/1 1	andesite breccia	9 15	123 10	1027402 70	516742 40	Southern Negros Geothermal Project	1 20 000	unpublished PNOC EDC company map	OK8		333	Southern Negros Island	Philippines	Late Pliocene	Southern Negros Formation	R PS	core 1
148663 OK8/1 2	andesite breccia	9 15	123 10	1027402 70	516742 40	Southern Negros Geothermal Project	1 20 000	unpublished PNOC EDC company map	OK8		333	Southern Negros Island	Philippines	Late Pliocene	Southern Negros Formation	R PS	core 1
148664 OK8/2 1	andesite breccia	9 15	123 10	1027402 70	516742 40	Southern Negros Geothermal Project	1 20 000	unpublished PNOC EDC company map	OK8		750	Southern Negros Island	Philippines	Late Pliocene	Southern Negros Formation	R PS	core 2
148665 OK8/2 2	andesite breccia	9 15'	123 10	1027402 70	516742 40	Southern Negros Geothermal Project	1 20 000	unpublished PNOC EDC company map	OK8		750	Southern Negros Island	Philippines	Late Pliocene	Southern Negros Formation	R PS	core 2
148666 OK8/3 1	andesite breccia	9 15	123 10	1027402 70	516742 40	Southern Negros Geothermal Project	1 20 000	unpublished PNOC EDC company map	OK8		1685	Southern Negros Island	Philippines	Late Pliocene	Southern Negros Formation	R PS	core 3
148667 OK8/3 2	andesite breccia	9 15	123 10	1027402 70	516742 40	Southern Negros Geothermal Project	1 20 000	unpublished PNOC EDC company map	OK8		1685	Southern Negros Island	Philippines	Late Pliocene	Southern Negros Formation	R PS	core 3
148668 OK8/3 3	andesite breccia	9 15'	123 10	1027402 70	516742 40	Southern Negros Geothermal Project	1 20 000	unpublished PNOC EDC company map	OK8		1685	Southern Negros Island	Philippines	Late Pliocene	Southern Negros Formation	R,PS	core 3
148669 OK8/5	andesite breccia	9 15	123 10'	1027402 70	516742 40	Southern Negros Geothermal Project	1 20 000	unpublished PNOC EDC company map	OK8		2304	Southern Negros Island	Philippines	Middle Miocene	Lower Puhagan Volcanic Formation	R,2PS FI	core 5
148670 OK8/6	andesite breccia	9 15'	123 10	1027402 70	516742 40	Southern Negros Geothermal Project	1 20 000	unpublished PNOC EDC company map	OK8		2451	Southern Negros Island	Philippines	Middle Miocene	Lower Puhagan Volcanic Formation	R PS	core 6
148671 OK8/7	andesite breccia	9 15'	123 10'	1027402 70	516742 40	Southern Negros Geothermal Project	1 20 000	unpublished PNOC EDC company map	OK8		2828	Southern Negros Island	Philippines	Middle Miocene	Lower Puhagan Volcanic Formation	R PS	core 7
148672 OK8/8	quartz diorite	9 15	123 10'	1027402 70	516742 40	Southern Negros Geothermal Project	1 20 000	unpublished PNOC EDC company map	OK8		2970	Southern Negros Island	Philippines	Pleistocene	Nasuji Pluton	R PS	core 8
148673 OK8RD/1	andesite breccia	9 15	123 10'	1027402 70	516742 40	Southern Negros Geothermal Project	1 20 000	unpublished PNOC EDC company map	OK8RD		2062	Southern Negros Island	Philippines	Middle Miocene	Lower Puhagan Volcanic Formation	R 3PS	core 1
148674 OK8RD/2	quartz diorite	9 15	123 10'	1027402 70	516742 40	Southern Negros Geothermal Project	1 20 000	unpublished PNOC EDC company map	OK8RD		2284	Southern Negros Island	Philippines	Pleistocene	Nasuji Pluton	R 2PS PD,CR	core 2
148675 OK9D/1	andesite breccia	9 15'	123 10'	1027486 30	516539 00	Southern Negros Geothermal Project	1 20 000	unpublished PNOC EDC company map	OK9D		925	Southern Negros Island	Philippines	Late Pliocene	Southern Negros Formation	R PS	core 1
148676 OK9D/2	andesite breccia	9 15'	123 10	1027486 30	516539 00	Southern Negros Geothermal Project	1 20 000	unpublished PNOC EDC company map	OK9D		1560	Southern Negros Island	Philippines	Late Pliocene	Southern Negros Formation	R PS	core 2
148677 OK9D/3-1	limestone	9 15'	123 10'	1027486 30	516539 00	Southern Negros Geothermal Project	1 20 000	unpublished PNOC EDC company map	OK9D		1982	Southern Negros Island	Philippines	Late Miocene - Early Pliocene	Okoy Formation	R,PS,FI	core 3
148678 OK9D/3 2	limestone	9 15'	123 10	1027486 30	516539 00	Southern Negros Geothermal Project	1 20 000	unpublished PNOC EDC company map	OK9D		1982	Southern Negros Island	Philippines	Late Miocene - Early Pliocene	Okoy Formation	R,2PS	core 3
148679 OK9D/4	limestone	9 15'	123 10'	1027486 30	516539 00	Southern Negros Geothermal Project	1 20 000	unpublished PNOC EDC company map	OK9D		2184	Southern Negros Island	Philippines	Late Miocene - Early Pliocene	Okoy Formation	R PS	core 4
148680 OK9D/5	limestone	9 15'	123 10	1027486 30	516539 00	Southern Negros Geothermal Project	1 20 000	unpublished PNOC EDC company map	OK9D		2350	Southern Negros Island	Philippines	Late Miocene - Early Pliocene	Okoy Formation	R,2PS	core 5
148681 OK9D/6	diorite	9 15'	123 10'	1027486 30	516539 00	Southern Negros Geothermal Project	1 20 000	unpublished PNOC EDC company map	OK9D		2530	Southern Negros Island	Philippines	Early Pliocene	Puhagan dikes	R,2PS,PD CR	core 6
148682 OK9D/7	andesite breccia	9 15	123 10'	1027486 30	516539 00	Southern Negros Geothermal Project	1 20 000	unpublished PNOC EDC company map	OK9D		2897	Southern Negros Island	Philippines	Middle Miocene	Lower Puhagan Volcanic Formation	R PS	core 7
148683 OK10D/1 1	andesite breccia	9 15'	123 10'	1027464 30	518843 20	Southern Negros Geothermal Project	1 20 000	unpublished PNOC EDC company map	OK10D		1667	Southern Negros Island	Philippines	Late Pliocene	Southern Negros Formation	R PS	core 1
148684 OK10D/1-1	andesite breccia	9 15	123 10'	1027464 30	518843 20	Southern Negros Geothermal Project	1 20 000	unpublished PNOC EDC company map	OK10D		1882	Southern Negros Island	Philippines	Late Pliocene	Southern Negros Formation	R PS	core 3
148685 OK10D/3-2	andesite breccia	9 15'	123 10'	1027454 30	518843 20	Southern Negros Geothermal Project	1 20 000	unpublished PNOC EDC company map	OK10D		1882	Southern Negros Island	Philippines	Late Pliocene	Southern Negros Formation	R	core 3
148686 OK10D/4-1	andesite breccia	9 15	123 10'	1027464 30	518843 20	Southern Negros Geothermal Project	1 20 000	unpublished PNOC EDC company map	OK10D		2135	Southern Negros Island	Philippines	Late Pliocene	Southern Negros Formation	R,2PS	core 4
148687 OK10D/5	andesite breccia	9 15	123 10'	1027464 30	518843 20	Southern Negros Geothermal Project	1 20 000	unpublished PNOC EDC company map	OK10D		2420	Southern Negros Island	Philippines	Middle Miocene	Lower Puhagan Volcanic Formation	R,2PS	core 5
148688 OK10D/6	diorite	9 15'	123 10'	1027464 30	518843 20	Southern Negros Geothermal Project	1 20 000	unpublished PNOC EDC company map	OK10D		2704	Southern Negros Island	Philippines	Early Pliocene	Puhagan dikes	R,PS PD CR	core 6
148689 OK11D/1 1	andesite breccia	9 15	123 10	1025749 80	517023 10	Southern Negros Geothermal Project	1 20 000	unpublished PNOC EDC company map	OK11D		1980	Southern Negros Island	Philippines	Late Pliocene	Southern Negros Formation	R PS	core 1
148690 OK11D/1 2	andesite breccia	9 15'	123 10	1025749 80	517023 10	Southern Negros Geothermal Project	1 20 000	unpublished PNOC EDC company map	OK11D		1980	Southern Negros Island	Philippines	Late Pliocene	Southern Negros Formation	R,3PS	core 1
148691 OK11D/2 1	quartz diorite	9 15'	123 10	1025749 80	517023 10	Southern Negros Geothermal Project	1 20 000	unpublished PNOC EDC company map	OK11D		2309	Southern Negros Island	Philippines	Pleistocene	Nasuji Pluton	R 4PS	core 2
148692 OK11D/3 2	quartz diorite	9 15'	123 10'	1025749 80	517023 10	Southern Negros Geothermal Project	1 20 000	unpublished PNOC EDC company map	OK11D		2825	Southern Negros Island	Philippines	Pleistocene	Nasuji Pluton	R 2PS,PD,CR	core 3
148693 OK12D/1	andesite breccia	9 15	123 10'	1026087 00	518969 80	Southern Negros Geothermal Project	1 20 000	unpublished PNOC EDC company map	OK12D		1325	Southern Negros Island	Philippines	Late Pliocene	Southern Negros Formation	R PS	core 1
148694 OK12D/2	limestone	9 15'	123 10'	1026087 00	518969 80	Southern Negros Geothermal Project	1 20 000	unpublished PNOC EDC company map	OK12D		1950	Southern Negros Island	Philippines	Late Miocene - Early Pliocene	Okoy Formation	R PS	core 2
148695 OK12D/3-1	limestone	9 15'	123 10'	1026087 00	518969 80	Southern Negros Geothermal Project	1 20 000	unpublished PNOC EDC company map	OK12D		2192	Southern Negros Island	Philippines	Late Miocene - Early Pliocene	Okoy Formation	R PS	core 3
148696 OK12D/4	limestone	9 15'	123 10'	1026087 00	518969 80	Southern Negros Geothermal Project	1 20 000	unpublished PNOC EDC company map	OK12D		2473	Southern Negros Island	Philippines	Late Miocene - Early Pliocene	Okoy Formation	R PS	core 4
148697 OK12D/5	andesite breccia	9 15'	123 10'	1026087 00	518969 80	Southern Negros Geothermal Project	1 20 000	unpublished PNOC EDC company map	OK12D		2877	Southern Negros Island	Philippines	Middle Miocene	Lower Puhagan Volcanic Formation	R,3PS,FI	core 5
148698 OK12D/6-1	andesite breccia	9 15'	123 10'	1028087 00	518969 80	Southern Negros Geothermal Project	1 20 000	unpublished PNOC EDC company map	OK12D		2800	Southern Negros Island	Philippines	Middle Miocene	Lower Puhagan Volcanic Formation	R,3PS	core 6
148699 PN1RD/1 2	andesite breccia	9 15'	123 10'	1028095 40	518949 20	Southern Negros Geothermal Project	1 20 000	unpublished PNOC EDC company map	PN1RD		1460	Southern Negros Island	Philippines	Late Pliocene	Southern Negros Formation	2PS	core 1
148700 PN1RD/2-1	limestone	9 15'	123 10'	1028095 40	518949 20	Southern Negros Geothermal Project	1 20 000	unpublished PNOC EDC company map	PN1RD		1804	Southern Negros Island	Philippines	Late Miocene - Early Pliocene	Okoy Formation	R,2PS FI	core 2
148701 PN1RD/3	diorite	9 15'	123 10'	1028095 40	518949 20	Southern Negros Geothermal Project	1 20 000	unpublished PNOC EDC company map	PN1RD		2127	Southern Negros Island	Philippines	Early Pliocene	Puhagan dikes	R 3PS,PD CR	core 3
148702 PN1RD/6	diorite	9 15'	123 10	1028095 40	518949 20	Southern Negros Geothermal Project	1 20 000	unpublished PNOC EDC company map	PN1RD		2518	Southern Negros Island	Philippines	Early Pliocene	Puhagan dikes	R PS PD CR	core 6
148703 PN1RD/7-1	andesite breccia	9 15'	123 10'	1028095 40	518949 20	Southern Negros Geothermal Project	1 20 000	unpublished PNOC EDC company map	PN1RD		2780	Southern Negros Island	Philippines	Middle Miocene	Lower Puhagan Volcanic Formation	R,PS	core 7
148704 PN1RD/7 2	andesite breccia	9 15'	123 10'	1028095 40	518949 20	Southern Negros Geothermal Project	1 20 000	unpublished PNOC EDC company map	PN1RD		2780	Southern Negros Island	Philippines	Middle Miocene	Lower Puhagan Volcanic Formation	R PS	core 7
148705 PN2RD/1	diorite	9 15'	123 10	1028103 20	518928 80	Southern Negros Geothermal Project	1 20 000	unpublished PNOC EDC company map	PN2RD		3490	Southern Negros Island	Philippines	Early Pliocene	Puhagan dikes	R PS	core 1
148706 PN4RD/1	andesite breccia	9 15'	123 10	1028224 70	519029 90	Southern Negros Geothermal Project	1 20 000	unpublished PNOC EDC company map	PN4RD		2854	Southern Negros Island	Philippines	Middle Miocene	Lower Puhagan Volcanic Formation	R PS	core 1
148707 PN4RD/2	andesite breccia	9 15'	123 10'	1028224 70	519029 90	Southern Negros Geothermal Project	1 20 000	unpublished PNOC EDC company map	PN4RD		3211	Southern Negros Island	Philippines	Middle Miocene	Lower Puhagan Volcanic Formation	R	core 2
148708 PN5RD/1	andesite breccia	9 15'	123 10'	1028243 90	518988 50	Southern Negros Geothermal Project	1 20 000	unpublished PNOC EDC company map	PN5RD		2853	Southern Negros Island	Philippines	Middle Miocene	Lower Puhagan Volcanic Formation	R,PS	core 1

146709	PN6RD/1	limestone	9 15'	123 10'	1028234 30	519009.20	Southern Negros Geothermal Project	1:20 000	unpublished PNOC-EDC company map	PN6RD		1870	Southern Negros Island	Philippines	Late Miocene - Early Pliocene	Okoy Formation		R PS	core 1
146710	PN7RD/1	andesite breccia	9 15	123 10'	1028349 60	516949 40	Southern Negros Geothermal Project	1 20 000	unpublished PNOC EDC company map	PN7RD		2551	Southern Negros Island	Philippines	Middle Miocene	Lower Puhagan Volcanic Formation		R PS	core 1
Catalog#	Field#	Rock Name	Lat.	Long	AMG Northing	AMG Easting	Full Map Title	Map Scale	Map comments	DDH	Depth (m)	Area		Country	Lithostratigraphy	Formation		Prepa	Comments
146711	PN8RD/1	andesite breccia	9 15'	123 10'	1028355 20	518868 50	Southern Negros Geothermal Project	1 20 000	unpublished PNOC EDC company map	PN8RD		3042	Southern Negros Island	Philippines	Middle Miocene	Lower Puhagan Volcanic Formation		R PS	core 1
146712	PN9RD/1	andesite breccia	9 15	123 10'	1028361 30	518911 70	Southern Negros Geothermal Project	1:20 000	unpublished PNOC-EDC company map	PN9RD		2710	Southern Negros Island	Philippines	Middle Miocene	Lower Puhagan Volcanic Formation		R PS	core 1
146713	PN9RD/2 1	andesite breccia	9 15'	123 10'	1028361 30	518911 70	Southern Negros Geothermal Project	1:20 000	unpublished PNOC-EDC company map	PN9RD		3123	Southern Negros Island	Philippines	Middle Miocene	Lower Puhagan Volcanic Formation		R PS	core 2
146714	PN9RD/2 2	andesite breccia	9 15	123 10	1028361 30	518911 70	Southern Negros Geothermal Project	1 20 000	unpublished PNOC-EDC company map	PN9RD		3123	Southern Negros Island	Philippines	Middle Miocene	Lower Puhagan Volcanic Formation		R,2PS	core 2
146715	PN13D/1	limestone	9 15'	123 10'	1027452 50	516825 30	Southern Negros Geothermal Project	1:20 000	unpublished PNOC-EDC company map	PN13D		2059	Southern Negros Island	Philippines	Late Miocene - Early Pliocene	Okoy Formation		R PS	core 1
146716	PN13D/2	diorite	9 15	123 10	1027452 50	516825 30	Southern Negros Geothermal Project	1:20 000	unpublished PNOC EDC company map	PN13D		2169	Southern Negros Island	Philippines	Early Pliocene	Puhagan dikes		R,2PS	core 2
146717	PN13D/3A	andesite breccia	9 15'	123 10	1027452 50	516825 30	Southern Negros Geothermal Project	1:20 000	unpublished PNOC-EDC company map	PN13D		2529	Southern Negros Island	Philippines	Middle Miocene	Lower Puhagan Volcanic Formation		R PS	core 3
146718	PN13D/5	diorite	9 15'	123 10	1027452 50	516825 30	Southern Negros Geothermal Project	1:20 000	unpublished PNOC EDC company map	PN13D		2855	Southern Negros Island	Philippines	Early Pliocene	Puhagan dikes		R PS	core 5
146719	PN14/2 1	andesite breccia	9 15'	123 10	1027656 10	518681 90	Southern Negros Geothermal Project	1:20 000	unpublished PNOC EDC company map	PN14		2719	Southern Negros Island	Philippines	Middle Miocene	Lower Puhagan Volcanic Formation		R 3PS	core 2
146720	PN14/3-1	andesite breccia	9 15'	123 10	1027656 10	518681 90	Southern Negros Geothermal Project	1:20 000	unpublished PNOC EDC company map	PN14		3000	Southern Negros Island	Philippines	Middle Miocene	Lower Puhagan Volcanic Formation		R,PS	core 3
146721	PN14/3-2	andesite breccia	9 15	123 10'	1027656 10	518681 90	Southern Negros Geothermal Project	1:20 000	unpublished PNOC EDC company map	PN14		3000	Southern Negros Island	Philippines	Middle Miocene	Lower Puhagan Volcanic Formation		R PS	core 3
146722	PN15D/3	andesite breccia	9 15	123 10'	1027623 50	518851 70	Southern Negros Geothermal Project	1:20 000	unpublished PNOC-EDC company map	PN15D		1464	Southern Negros Island	Philippines	Late Pliocene	Southern Negros Formation		R,PS	core 3
146723	PN16D/1	diorite	9 15'	123 10'	1027433 10	518713 10	Southern Negros Geothermal Project	1:20 000	unpublished PNOC EDC company map	PN16D		2349	Southern Negros Island	Philippines	Early Pliocene	Puhagan dikes		R PS	core 1
146724	PN16D/2 1	diorite	9 15	123 10'	1027433 10	518713 10	Southern Negros Geothermal Project	1:20 000	unpublished PNOC EDC company map	PN16D		2744	Southern Negros Island	Philippines	Early Pliocene	Puhagan dikes		R PS	core 2
146725	PN16D/2 2	diorite	9 15'	123 10'	1027433 10	518713 10	Southern Negros Geothermal Project	1:20 000	unpublished PNOC EDC company map	PN16D		2744	Southern Negros Island	Philippines	Early Pliocene	Puhagan dikes		R 2PS,FI	core 2
146726	PN16D/3	andesite breccia	9 15	123 10'	1027433 10	518713 10	Southern Negros Geothermal Project	1:20 000	unpublished PNOC EDC company map	PN16D		3216	Southern Negros Island	Philippines	Middle Miocene	Lower Puhagan Volcanic Formation		R,PS	core 3
146727	PN17D/1 1	limestone	9 15	123 10'	1027633 60	518872 00	Southern Negros Geothermal Project	1:20 000	unpublished PNOC EDC company map	PN17D		2014	Southern Negros Island	Philippines	Late Miocene - Early Pliocene	Okoy Formation		R PS	core 1
146728	PN17D/2	andesite breccia	9 15	123 10'	1027633 60	518872 00	Southern Negros Geothermal Project	1:20 000	unpublished PNOC EDC company map	PN17D		2746	Southern Negros Island	Philippines	Middle Miocene	Lower Puhagan Volcanic Formation		R PS	core 2
146729	PN17D/3-1	andesite breccia	9 15'	123 10	1027633 60	518872 00	Southern Negros Geothermal Project	1:20 000	unpublished PNOC EDC company map	PN17D		3049	Southern Negros Island	Philippines	Middle Miocene	Lower Puhagan Volcanic Formation		R PS	core 3
146730	PN17D/3-2	andesite breccia	9 15'	123 10'	1027633 60	518872 00	Southern Negros Geothermal Project	1:20 000	unpublished PNOC EDC company map	PN17D		3049	Southern Negros Island	Philippines	Middle Miocene	Lower Puhagan Volcanic Formation		R PS	core 3
146731	PN18D/1	andesite breccia	9 15	123 10'	1027440 40	518756 90	Southern Negros Geothermal Project	1:20 000	unpublished PNOC EDC company map	PN18D		2835	Southern Negros Island	Philippines	Middle Miocene	Lower Puhagan Volcanic Formation		R PS	core 1
146732	PN18D/2 2	diorite	9 15'	123 10'	1027440 40	518756 90	Southern Negros Geothermal Project	1:20 000	unpublished PNOC EDC company map	PN18D		3151	Southern Negros Island	Philippines	Early Pliocene	Puhagan dikes		R 2PS	core 2
146733	PN18D/3	andesite breccia	9 15	123 10	1027440 40	518756 90	Southern Negros Geothermal Project	1:20 000	unpublished PNOC EDC company map	PN18D		3265	Southern Negros Island	Philippines	Middle Miocene	Lower Puhagan Volcanic Formation		R,2PS	core 3
146734	PN19D/1 2	limestone	9 15	123 10'	1027638 80	518669 30	Southern Negros Geothermal Project	1:20 000	unpublished PNOC EDC company map	PN19D		2390	Southern Negros Island	Philippines	Late Miocene - Early Pliocene	Okoy Formation		R,2PS	core 1
146735	PN19D/2	diorite	9 15'	123 10	1027638 80	518669 30	Southern Negros Geothermal Project	1:20 000	unpublished PNOC EDC company map	PN19D		2580	Southern Negros Island	Philippines	Early Pliocene	Puhagan dikes		R PS	core 2
146736	PN19D/3	andesite breccia	9 15'	123 10'	1027638 80	518669 30	Southern Negros Geothermal Project	1:20 000	unpublished PNOC EDC company map	PN19D		2875	Southern Negros Island	Philippines	Middle Miocene	Lower Puhagan Volcanic Formation		R PS	core 3
146737	PN20D/1 2	andesite breccia	9 15'	123 10	1027444 10	518779 40	Southern Negros Geothermal Project	1:20 000	unpublished PNOC EDC company map	PN20D		2713	Southern Negros Island	Philippines	Middle Miocene	Lower Puhagan Volcanic Formation		R 3PS	core 1
146738	PN20D/2	diorite	9 15'	123 10	1027444 10	518779 40	Southern Negros Geothermal Project	1:20 000	unpublished PNOC EDC company map	PN20D		3013	Southern Negros Island	Philippines	Early Pliocene	Puhagan dikes		R 2PS 2PD CR FI	core 2
146739	PN21D/4	diorite	9 15	123 10	1027618 20	518870 00	Southern Negros Geothermal Project	1:20 000	unpublished PNOC EDC company map	PN21D		2740	Southern Negros Island	Philippines	Early Pliocene	Puhagan dikes		R PS PD CR	core 4
146740	PN21D/5	andesite breccia	9 15	123 10	1027618 20	518830 00	Southern Negros Geothermal Project	1:20 000	unpublished PNOC EDC company map	PN21D		2981	Southern Negros Island	Philippines	Middle Miocene	Lower Puhagan Volcanic Formation		R PS	core 5
146741	PN22D/1	diorite	9 15	123 10	1027447 60	518801 50	Southern Negros Geothermal Project	1:20 000	unpublished PNOC EDC company map	PN22D		2427	Southern Negros Island	Philippines	Early Pliocene	Puhagan dikes		R,2PS FI	core 1
146742	PN23D/1	diorite	9 15	123 10	1027465 50	518551 10	Southern Negros Geothermal Project	1:20 000	unpublished PNOC-EDC company map	PN23D		2134	Southern Negros Island	Philippines	Early Pliocene	Puhagan dikes		R,3PS	core 1
146743	PN23D/2	diorite	9 15	123 10	1027465 50	518551 10	Southern Negros Geothermal Project	1:20 000	unpublished PNOC EDC company map	PN23D		2787	Southern Negros Island	Philippines	Early Pliocene	Puhagan dikes		R,2PS	core 2
146744	PN23D/3	andesite breccia	9 15	123 10	1027465 50	518551 10	Southern Negros Geothermal Project	1:20 000	unpublished PNOC EDC company map	PN23D		3091	Southern Negros Island	Philippines	Middle Miocene	Lower Puhagan Volcanic Formation		R,PS	core 3
146745	PN24D/1	andesite breccia	9 15	123 10	1027620 80	518656 10	Southern Negros Geothermal Project	1:20 000	unpublished PNOC EDC company map	PN24D		2995	Southern Negros Island	Philippines	Middle Miocene	Lower Puhagan Volcanic Formation		R,2PS	core 1
146746	PN24D/2	andesite breccia	9 15	123 10	1027620 80	518656 10	Southern Negros Geothermal Project	1:20 000	unpublished PNOC EDC company map	PN24D		3222	Southern Negros Island	Philippines	Middle Miocene	Lower Puhagan Volcanic Formation		R PS	core 2
146747	PN25D/2	basaltic andesite	9 15'	123 10	1027749 30	518519 10	Southern Negros Geothermal Project	1:20 000	unpublished PNOC-EDC company map	PN25D		3469	Southern Negros Island	Philippines	Middle Miocene	Lower Puhagan Volcanic Formation		R PS PD CR FI	core 2
146748	PN28/1	andesite breccia	9 15	123 10'	1027619 90	519916 80	Southern Negros Geothermal Project	1:20 000	unpublished PNOC EDC company map	PN28		2892	Southern Negros Island	Philippines	Middle Miocene	Lower Puhagan Volcanic Formation		R 2PS	core 1
146749	PN29D/1	andesite breccia	9 15'	123 10	1027653 00	518703 60	Southern Negros Geothermal Project	1:20 000	unpublished PNOC EDC company map	PN29D		1555	Southern Negros Island	Philippines	Late Pliocene	Southern Negros Formation		R,PS	core 1
146750	PN29D/2	limestone	9 15	123 10	1027653 00	518703 60	Southern Negros Geothermal Project	1:20 000	unpublished PNOC EDC company map	PN29D		2056	Southern Negros Island	Philippines	Late Miocene - Early Pliocene	Okoy Formation		R 2PS	core 2
146751	PN29D/3	andesite breccia	9 15	123 10	1027653 00	518703 60	Southern Negros Geothermal Project	1:20 000	unpublished PNOC EDC company map	PN29D		2910	Southern Negros Island	Philippines	Middle Miocene	Lower Puhagan Volcanic Formation		R 3PS	core 3
146752	PN30D/1	diorite	9 15	123 10	1027474 00	518501 00	Southern Negros Geothermal Project	1:20 000	unpublished PNOC EDC company map	PN30D		2021	Southern Negros Island	Philippines	Early Pliocene	Puhagan dikes		R PS,PD CR	core 1
146753	PN31D/3	limestone	9 15'	123 10'	1027653 00	518703 60	Southern Negros Geothermal Project	1:20 000	unpublished PNOC EDC company map	PN31D		1625	Southern Negros Island	Philippines	Late Miocene - Early Pliocene	Okoy Formation		R,2PS	core 3
146754	PN31D/4	diorite	9 15	123 10	1027653 00	518703 60	Southern Negros Geothermal Project	1:20 000	unpublished PNOC EDC company map	PN31D		2354	Southern Negros Island	Philippines	Early Pliocene	Puhagan dikes		R PS PD CR	core 4
146755	SG1/1	quartz diorite	9 15	123 10	1026552 90	515392.50	Southern Negros Geothermal Project	1:20 000	unpublished PNOC EDC company map	SG1		1501	Southern Negros Island	Philippines	Pleistocene	Nasuji Pluton		R,3PS PD CR	core 1
146756	SG1/2 1	quartz diorite	9 15	123 10'	1026562 90	515392 50	Southern Negros Geothermal Project	1:20 000	unpublished PNOC-EDC company map	SG1		1825	Southern Negros Island	Philippines	Pleistocene	Nasuji Pluton		R 4PS	core 2
146757	SG1/3	quartz diorite	9 15'	123 10'	1026562 90	515392 50	Southern Negros Geothermal Project	1:20 000	unpublished PNOC-EDC company map	SG1		2285	Southern Negros Island	Philippines	Pleistocene	Nasuji Pluton		R,PS	core 3
146758	SG1/4 1	quartz diorite	9 15'	123 10'	1026562 90	515392.50	Southern Negros Geothermal Project	1:20 000	unpublished PNOC-EDC company map	SG1		2293	Southern Negros Island	Philippines	Pleistocene	Nasuji Pluton		R 3PS	core 4
146759	SG1/5	quartz diorite	9 15'	123 10	1026562 90	515392.50	Southern Negros Geothermal Project	1:20 000	unpublished PNOC-EDC company map	SG1		2769	Southern Negros Island	Philippines	Pleistocene	Nasuji Pluton		R PS	core 5
146760	SG1RD/1-3	diorite	9 15	123 10	1027561 71	515650 50	Southern Negros Geothermal Project	1:20 000	unpublished PNOC EDC company map	SG1RD		2026	Southern Negros Island	Philippines	Pleistocene	Nasuji Pluton		R 3PS,2PD CR	core 1
146761	SG1RD/2 1	diorite	9 15	123 10'	1027561 71	515650 50	Southern Negros Geothermal Project	1:20 000	unpublished PNOC EDC company map	SG1RD		2344	Southern Negros Island	Philippines	Pleistocene	Nasuji Pluton		R 3PS FI	core 2
146762	SG2/2	quartz diorite	9 15	123 10	1025766 80	515648 90	Southern Negros Geothermal Project	1:20 000	unpublished PNOC EDC company map	SG2		1392	Southern Negros Island	Philippines	Pleistocene	Nasuji Pluton		R 4PS PD	core 2
146763	SG2/5	quartz diorite	9 15'	123 10	1025766 80	515648 90	Southern Negros Geothermal Project	1:20 000	unpublished PNOC EDC company map	SG2		1700	Southern Negros Island	Philippines	Pleistocene	Nasuji Pluton		R PS PD CR	core 5
146764	SG2/6	quartz diorite	9 15	123 10	1025766 80	515648 90	Southern Negros Geothermal Project	1:20 000	unpublished PNOC EDC company map	SG2		2141	Southern Negros Island	Philippines	Pleistocene	Nasuji Pluton		R PS PD	core 6
146765	SG3D/1	quartz diorite	9 15'	123 10'	1025723 80	515659 60	Southern Negros Geothermal Project	1:20 000	unpublished PNOC EDC company map	SG3D		1255	Southern Negros Island	Philippines	Pleistocene	Nasuji Pluton		R,2PS	core 1
146766	SG3D/2	andesite breccia	9 15	123 10	1025723 80	515659 60	Southern Negros Geothermal Project	1:20 000	unpublished PNOC EDC company map	SG3D		1765	Southern Negros Island	Philippines	Late Pliocene	Southern Negros Formation		R PS	core 2
146767	SG3D/3	quartz diorite	9 15'	123 10'	1025723 80	515659 60	Southern Negros Geothermal Project	1:20 000	unpublished PNOC-EDC company map	SG3D		2235	Southern Negros Island	Philippines	Pleistocene	Nasuji Pluton		R 3PS	core 3
146768	SG3D/4	quartz diorite	9 15	123 10'	1025723 80	515659 60	Southern Negros Geothermal Project	1:20 000	unpublished PNOC-EDC company map	SG3D		2678	Southern Negros Island	Philippines	Pleistocene	Nasuji Pluton		R PS	core 4
146769	SG3D/6	quartz diorite	9 15'	123 10	1025723 80	515659 60	Southern Negros Geothermal Project	1:20 000	unpublished PNOC-EDC company map	SG3D		2835	Southern Negros Island	Philippines	Pleistocene	Nasuji Pluton		R PS	core 6
146770	SG3RD/1	quartz diorite	9 15'	123 10'	1027330 97	515819 35	Southern Negros Geothermal Project	1:20 000	unpublished PNOC-EDC company map	SG3RD		2401	Southern Negros Island	Philippines	Pleistocene	Nasuji Pluton		R,PS PD CR	core 1
146771	96001	andesite	9 15'	12 . 10	1029580	520360	Southern Negros Geothermal Project	1:20 000	unpublished PNOC-EDC company map				Southern Negros Island	Philippines	Late Pliocene	Southern Negros Formation		R PS,PD CR	
146772	96002	andesite	9 15'	123 10'	1029730	520960	Southern Negros Geothermal Project	1:20 000	unpublished PNOC-EDC company map				Southern Negros Island	Philippines	Late Pliocene	Southern Negros Formation		R PS	
146773	96006	andesite	9 15	123 10'	1022600	518940	Southern Negros Geothermal Project	1:20 000	unpublished PNOC-EDC company map				Southern Negros Island	Philippines	Pleistocene	Cuernos Volcanic Formation		R PS,PD CR	
146774	96007	andesite	9 15'	123 10'	1023150	519300	Southern Negros Geothermal Project	1:20 000	unpublished PNOC-EDC company map				Southern Negros Island	Philippines	Pleistocene	Cuernos Volcanic Formation		R PS	
146775	96008	basaltic andesite	9 15	123 10	1023200	519500	Southern Negros Geothermal Project	1:20 000	unpublished PNOC-EDC company map				Southern Negros Island	Philippines	Pleistocene	Cuernos Volcanic Formation		R PS FD CR	
146776	96009	andesite	9 15'	123 10	1022600	520630	Southern Negros Geothermal Project	1:20 000	unpublished PNOC-EDC company map				Southern Negros Island	Philippines	Pleistocene	Cuernos Volcanic Formation		R PS	
146777	96010	andesite	9 15'	123 10'	1026000	519340	Southern Negros Geothermal Project	1:20 000	unpublished PNOC EDC company map				Southern Negros Island	Philippines	Pleistocene	Cuernos Volcanic Formation		R,2PS,PD CR	
146778	96011	andesite	9 15'	123 10'	1026000	519340	Southern Negros Geothermal Project	1:20 000	unpublished PNOC EDC company map				Southern Negros Island	Philippines	Pleistocene	Cuernos Volcanic Formation		PS	
146779	96013	andesite	9 15'	123 10	1026000	519340	Southern Negros Geothermal Project	1:20 000	unpublished PNOC-EDC company map				Southern Negros Island	Philippines	Pleistocene	Cuernos Volcanic Formation		R PS	
146780	96014	andesite	9 15	123 10	1025460	519100	Southern Negros Geothermal Project	1:20 000	unpublished PNOC EDC company map				Southern Negros Island	Philippines	Pleistocene	Cuernos Volcanic Formation		R,PS,PD CR	
146781	96015	andesite	9 15'	123 10	1024740	519500	Southern Negros Geothermal Project	1:20 000	unpublished PNOC-EDC company map				Southern Negros Island	Philippines	Pleistocene	Cuernos Volcanic Formation		PS	
146782	96017	andesite	9 15	123 10'	1024480	519760	Southern Negros Geothermal Project	1:20 000	unpublished PNOC-EDC company map				Southern Negros Island	Philippines	Pleistocene	Cuernos Volcanic Formation		R PS	
146783	96020	andesite	9 15'	123 10'	1024480	519760	Southern Negros Geothermal Project	1:20 000	unpublished PNOC-EDC company map				Southern Negros Island	Philippines	Pleistocene	Cuernos Volcanic Formation		R PS	
146784	96025	andesite	9 15	123 10'	1023900	520100	Southern Negros Geothermal Project	1:20 000	unpublished PNOC-EDC company map				Southern Negros Island	Philippines	Pleistocene	Cuernos Volcanic Formation		R PS	
146785	96027	andesite	9 15'	123 10'	1027940	515960	Southern Negros Geothermal Project	1:20 000	unpublished PNOC-EDC company map				Southern Negros Island	Philippines	Late Pliocene	Southern Negros Formation		R PS	
146786	96027-1	andesite	9 15'	123 10'	1027940	515960	Southern Negros Geothermal Project	1:20 000	unpublished PNOC-EDC company map				Southern Negros Island	Philippines	Late Pliocene	Southern Negros Formation		R,PS	
146787	96029	andesite	9 15	123 10'	1027820	516140	Southern Negros Geothermal Project	1:20 000	unpublished PNOC-EDC company map				Southern Negros Island	Philippines	Late Pliocene	Southern Negros Formation		R,2PS	
146788	96030	andesite	9 15	123 10'	1027870	516210	Southern Negros Geothermal Project	1:20 000	unpublished PNOC-EDC company map				Southern Negros Island	Philippines	Late Pliocene	Southern Negros Formation		R,2PS	
146789	96032	andesite	9 15	123 10	1029000	518900	Southern Negros Geothermal Project	1:20 000	unpublished PNOC-EDC company map				Southern Negros Island	Philippines	Late Pliocene	Southern Negros Formation		R PS	
146790	96033	andesite	9 15'	123 10	1030000	521500	Southern Negros Geothermal Project	1:20 000	unpublished PNOC EDC company map				Southern Negros Island	Philippines	Late Pliocene	Southern Negros Formation		R PS	
146791	97003	andesite	9 15	123 10'	1028040	518100	Southern Negros Geothermal Project	1:20 000	unpublished PNOC EDC company map				Southern Negros Island	Philippines	Late Pliocene	Southern Negros Formation		R PS	
146792	97005	andesite	9 15'	123 10	1028140	516000	Southern Negros Geothermal Project	1:20 000	unpublished PNOC EDC company map				Southern Negros Island	Philippines	Late Pliocene	Southern Negros Formation		R PS	
146793	97008	andesite	9 15'	123 10	1028180	516080	Southern Negros Geothermal Project	1:20 000	unpublished PNOC EDC company map				Southern Negros Island	Philippines	Late Pliocene	Southern Negros Formation		R PS	
146794	97021	andesite	9 15'	123 10	1026700	516600	Southern Negros Geothermal Project	1:20 000	unpublished PNOC EDC company map				Southern Negros Island	Philippines	Late Pliocene	Southern Negros Formation		R,PS	
146795	BL1D 1075		9 15'	123 10'	1026485 84	517908 85				BL1D		1075	Southern Negros Island	Philippines				PS	Geothermal well scale deposit
146796	NJ6D 2065.3		9 15	123 10	1026179.90	516836.20				NJ6D		2065.3	Southern Negros Island	Philippines				PS	Geothermal well scale deposit

146797	OK3 0-264		9 15'	123 10	1029345 70	519210 90				OK3	0-264		Southern Negros Island	Philippines			PS	Geothermal well scale deposit
146798	OK3 270		9 15	123 10	1029345 70	519210 90				OK3		270	Southern Negros Island	Philippines			PS	Geothermal well scale deposit
146799	OK3 300		9 15	123 10'	1029345 70	519210 90				OK3		300	Southern Negros Island	Philippines			PS	Geothermal well scale deposit
Catalog#	Field	Rock Name	Lat.	Long	AMG Northing	AMG Easting	Full Map Title	Map Scale	Map comments	DDH	Depth (m)		Area	Country	Lithostratigraphy	Formation	Prep	Comments
146800	OK3 355		9 15	123 10	1029345 70	519210 90				OK3		355	Southern Negros Island	Philippines			PS	Geothermal well scale deposit
146801	OK3 409		9 15'	123 10'	1029345 70	519210 90				OK3		409	Southern Negros Island	Philippines			PS	Geothermal well scale deposit
146802	OK3 451		9 15	123 10	1029345 70	519210 90				OK3		451	Southern Negros Island	Philippines			PS	Geothermal well scale deposit
146803	OK3 505		9 15	123 10	1029345 70	519210 90				OK3		505	Southern Negros Island	Philippines			PS	Geothermal well scale deposit
146804	OK10D 2835-3000		9 15	123 10	1027464 30	518843 20				OK10D	2835-3000		Southern Negros Island	Philippines			PS	Geothermal well scale deposit
146805	OK10D 2144 5-2835 5		9 15'	123 10'	1027464 30	518843 20				OK10D	2144 5-2835.5		Southern Negros Island	Philippines			PS	Geothermal well scale deposit
146806	PN13D 1464 1499		9 15	123 10'	1027452 50	518825 30				PN13D	1464 1499		Southern Negros Island	Philippines			PS	Geothermal well scale deposit
146807	PN13D 1499-1529		9 15'	123 10	1027452 50	518825 30				PN13D	1499 1529		Southern Negros Island	Philippines			PS	Geothermal well scale deposit
146808	PN13D 1529-1816		9 15	123 10	1027452 50	518825 30				PN13D	1529-1816		Southern Negros Island	Philippines			PS	Geothermal well scale deposit
146809	PN13D 1477 7 1746 0		9 15'	123 10	1027452 50	518825 30				PN13D	1477 7-1746 0		Southern Negros Island	Philippines			PS	Geothermal well scale deposit
146810	PN13D 1746-2767		9 15'	123 10	1027452 50	518825 30				PN13D	1746-2767		Southern Negros Island	Philippines			PS	Geothermal well scale deposit
146811	PN13D 2000-2200		9 15	123 10'	1027452 50	518825 30				PN13D	2000-2200		Southern Negros Island	Philippines			2PS	Geothermal well scale deposit
146812	PN13D 2200-2767		9 15'	123 10'	1027452 50	518825 30				PN13D	2200-2767		Southern Negros Island	Philippines			PS	Geothermal well scale deposit
146813	PN15D 1320		9 15'	123 10'	1027623 50	518651 70				PN15D		1320	Southern Negros Island	Philippines			PS	Geothermal well scale deposit
146814	PN17D 993		9 15'	123 10'	1027633 60	518872 00				PN17D		993	Southern Negros Island	Philippines			PS	Geothermal well scale deposit
146815	PN21D 1171		9 15'	123 10'	1027818 20	518830 00				PN21D		1171	Southern Negros Island	Philippines			2PS	Geothermal well scale deposit
146816	PN22D 2445 5 2620.5		9 15'	123 10	1027447 90	518801 50				PN22D	2445.5-2620.5		Southern Negros Island	Philippines			PS	Geothermal well scale deposit
146817	PN22D 1650 4		9 15'	123 10	1027447 90	518801 50				PN22D		1650 4	Southern Negros Island	Philippines			PS	Geothermal well scale deposit
146818	PN22D 2620.5-2726 5		9 15	123 10	1027447 90	518801 50				PN22D	2620 5 2726.5		Southern Negros Island	Philippines			PS	Geothermal well scale deposit
146819	PN29D 1680		9 15'	123 10'	1027653 00	518703 60				PN29D		1680	Southern Negros Island	Philippines			PS	Geothermal well scale deposit
146820	SG3D 1797 1		9 15'	123 10	1025723 80	515659 60				SG3D		1797 1	Southern Negros Island	Philippines			PS	Geothermal well scale deposit